REMOTE SOUNDING OF THE ATMOSPHERE OF TITAN

Conor A. Nixon

Wolfson College

A thesis submitted to the Faculty of Physical Sciences for the degree of Doctor of Philosophy in the University of Oxford.

Trinity Term 1998

Figure 1: **The launch of Cassini/Huygens aboard a Titan IV rocket from Cape Canaveral Air Station at 4:43 EDT on 15th October 1997.**

REMOTE SOUNDING OF THE ATMOSPHERE OF TITAN

A thesis submitted to the Faculty of Physical Sciences by C.A. Nixon, Wolfson College in Trinity term 1998 for the degree of Doctor of Philosophy in the University of Oxford.

Abstract

The Composite Infrared Spectrometer (CIRS) instrument onboard the Cassini spacecraft will be used to probe the atmosphere and surface of Saturn's giant moon Titan. This thesis describes an investigation of the capabilities of CIRS as a remote sounding instrument.

To enable infrared spectra to be computed, a radiative transfer code has been adapted for Titan's atmosphere. The atmospheric model, including gases and aerosol particles, was refined by comparison of synthetic spectra with results from the IRIS instrument of the Voyager 1 spacecraft.

Characteristics of the instrument have been deduced from laboratory measurements. The size and shape of the field of view was found for the mid-infrared detectors. A Fourier code was developed to transform the raw data (interferograms). Blackbody spectra taken with the flight instrument were analysed to calculate the noise equivalent radiance for the detectors of all three focal planes.

Finally, the data regarding instrument performance was used in combination with the predictive radiative transfer code to consider in detail the extent to which gaseous bands and other spectral features will be observable for a variety of limb and nadir viewing modes. Current observing strategies are reviewed and recommendations for scientific emphasis in the light of the actual instrument performance are made.

Contents

Acknowledgements

I would like to thank all those who have helped me in one way or another during the last three years while researching and writing this thesis:

Prof. F.W. Taylor and Dr. C.L. Hepplewhite, my supervisors who have directed me into a very interesting field of study, guided my research, and also proof-read my thesis and provided helpful feedback.

Dr. S.B. Calcutt, for getting me involved in the CIRS project, and explaining many aspects of the instrument to me.

Ish Aslam, for helpful conversations during the CIRS field of view measurements, and some tough squash matches.

Tim Vellacott, Nick O'Donnell and Jon Temple of AOPP, who constructed the CIRS MIR FPA and kept the ATR running.

Dr. P.G.J. Irwin, for helping me to get `Radtran` converted to handle the Titan atmosphere.

Virgil Kunde (P.I.), J. Brasunas, R. Carlson and D. Jennings, of the GSFC CIRS team for making the CIRS radiometric calibration data available to me, and helpful comments and feedback during the analysis.

Dr A. Coustenis of the Observatoire de Paris, Meudon, for making her atmospheric temperature profiles and IRIS spectra available.

Francis Reininger and Chris Palmer for useful conversations about interferometers, Fourier Transforms and phase corrections.

Phil, Kam, Miguel, Paul, Chris, and the other AOPP students for lunches, coffees, cocktails, punting, barbeques and other necessary diversions, and enthusiasm in the face of thesis-writing.

Bob Wells, Anu Dudhia, Alan Darbyshire and the other Mansfield Road running club stalwarts, for introducing me to muddy towpaths of Oxford that I may never otherwise have known.

Dave Waters, Shond Laha, John Linstroth and Anthony Leonard, my housemates

who helped me keep my sanity.

Andy, Jezza, Louise, Jillian, and the rest at Wolfson Bar Co. and Ents Ctte. for a wide-spectrum graduate social life: there were never any dull moments.

Ang and Pete, and the rest of the staff at the Victoria Arms Public House, for many great evenings behind the bar, and in front of the bar.

My father and the rest of my family; Patrick, Gareth, Siobhan, Robert, Cara and Aunt Lily for much support. Most especially to my late grandfather, Andrew Watterson, for his many years of interest and enthusiasm, and without whose encouragement I would never have completed this academic voyage.

I was supported during the first two years of this work by a grant from the Particle Physics and Astronomy Research Council.

Foreword

This thesis describes the work which I personally have contributed to the CIRS project. This is a large international collaboration between NASA Goddard Space Flight Center, Oxford Univeristy and other British, French and German groups. A large number of people have been involved in the project, so my efforts have inevitably been intertwined with the work of other project members, which I outline here.

The CIRS mid-IR focal plane integration, alignment and test was carried out by a team at Oxford led by S. Calcutt, of which I was a member. My contribution included using the alignment test rig to conduct the focal plane alignment and detector field of view measurements, which I analyse in chapter 4.

The radiometric calibration data was recorded by a team at GSFC led by V. Kunde and included members of the Oxford team. The code which I used to unpack the raw instrument data was written by S. Calcutt. The code which I used to bring about the phase correction and Fourier Transform of the interferograms to power spectra was written by myself. The subsequent radiometric analysis of the power spectra described in chapter 5 is my own.

The `Radtran` radiative transfer code used in chapters 3 and 6 was written and developed by S. Calcutt, P. Irwin and others at AOPP. Several necessary extensions were then made by myself, as described in the text. The `FORTRAN` routines used to compute the CIA absorption are due to A. Borysow and collaborators, of the University of Michigan.

The final interpretation of results and recommendations are my own.

Mathematical Symbols

$A_{\rm b}$	Bond albedo
A	area ($\rm cm^2$)
B	Planck radiance ($\rm W\,cm^{-2}\,sr^{-1}\,/cm^{-1}$)
C	power spectrum (counts)
D^*	detector figure of merit
E	energy (J)
$F_{\rm s}$	solar flux ($\rm W\,cm^{-2}$)
H	scale height (km)
$\mathcal{I}$	detected interferogram (counts)
I	radiance ($\rm W\,cm^{-2}\,sr^{-1}\,/cm^{-1}$)
J	source radiance ($\rm W\,cm^{-2}\,sr^{-1}\,/cm^{-1}$)
$M_{\rm r}$	relative molecular mass ($\rm g\,mol^{-1}$)
N	number density of particles ($\rm cm^{-3}$)
$N_{\rm g}$	number of gases
P	power spectrum ($\rm W\,cm^{-2}\,sr^{-1}\,/cm^{-1}$)
$Q_{\rm D}$	the detector quantum efficiency
R	detector responsivity (counts/ unit radiance)
$\rm R_g$	ideal gas constant
$\rm R_S$	Saturn radius (=60330 km)
$\rm R_T$	Titan radius (=2575 km)
S	line strength
T	temperature (K)
$X_{\rm IR}$	absorption co-efficient infrared scaling factor
$X_{\rm vis}$	absorption co-efficient visible scaling factor
T	temperature (K)
$\hat{W}$	instrumental spatial weighting function

a	planetary radius (km)
c	speed of light ($\mathrm{m\,s^{-1}}$)
c_{FP}	focal plane resampling constant
d	distance to planet (km)
e_{c}	saturation vapour pressure of condensable species (bar)
g	acceleration due to gravity
h	relative humidity (%)
k_{a}	absorption co-efficient ($\mathrm{g^{-1}}$)
l	longitude
n	refractive index real part
p	pressure (bar)
q_{m}	mass mixing ratio of gas species
q_{v}	volume mixing ratio of gas species
r	particle radius (μm)
s	supersaturation fraction
w	vertical wind velocity ($\mathrm{cm\,s^{-1}}$)
z	altitude (km)
Ω	detector solid angle (steradians)
Γ	resolution scaling factor due to apodisation function type
α	CIA co-efficient ($\mathrm{cm^{-1}}$/ $\mathrm{amagat^{-2}}$)
α_{D}	half-width of Doppler line broadening
α_{L}	half-width of Lorentz line broadening
β	instrumental emission warm fraction
γ	temperature dependence of width parameter
ϵ_{s}	planetary surface emissivity

θ	angle of elevation (in spherical co-ordinate system)
η	system optical efficiency
κ	refractive index imaginary part
λ	wavelength (μm)
ν	frequency (Hz)
$\tilde{\nu}$	wavenumber (cm^{-1})
ρ	mass density ($\mathrm{g\ cm}^{-3}$)
σ	total extinction cross-section (cm^2)
σ_a	absorption cross-section (cm^2)
σ_s	scattering cross-section (cm^2)
σ_SB	Stefan-Boltzmann constant
τ	transmission
ϕ	angle of azimuth (in spherical co-ordinate system)
χ	opacity or optical depth
ω	single-scattering albedo

Abbreviations

a.c.	alternating current
ACP	Aerosol Collector Pyrolyser
AOPP	Atmospheric, Oceanic and Planetary Physics
	(of the Department of Physics at the University of Oxford)
ASTR	Alignment Scan Test Rig; another name for the ATR
ATR	Alignment Test Rig
CIA	Collisionally Induced Absorption
CIRS	Composite Infra-Red Spectrometer
EM	Engineering Model
ESA	European Space Agency
FIR	Far Infra-Red
FMA	Flight Model A
FMB	Flight Model B
FP1	Focal Plane 1 (thermopile detector; 16.7–100 μm)
FP3	Focal Plane 3 (PC detectors; 9.1–16.7 μm)
FP4	Focal Plane 4 (PV detectors; 6.7–9.1 μm)
FPA	Focal Plane Assembly
FT	Fourier Transform
FTS	Fourier Transform Spectrometer
FWHM	Full Width to Half Maximum
GCM	General Circulation Model
GSFC	Goddard Space Flight Center (NASA; in Greenbelt, MD, USA)
`IDL`	Interactive Display Language (data analysis software)
IFM	Interferogram
IFOV	Instantaneous Field Of View
ILS	Instrumental Line Shape

IR	Infra-Red
IRIS	Infra-Red Interferometer-Spectrometer (on Voyagers 1 & 2)
ISO	Infrared Space Observatory
ISS	Imaging Science Subsystem
LHe	Liquid Helium
LN2	Liquid Nitrogen
MIR	Mid Infra-Red
NASA	National Aeronautical and Space Administration
NESR	Noise Equivalent Spectral Radiance
PC	Photo-Conductive
p.d.	potential difference
P.I.	Principal Investigator
ppb	parts per billion
ppm	parts per million
PV	Photo-Voltaic
RTI	Real Time Interrupt (unit increment of CIRS scan time)
SIL	Space Instruments Laboratory (AOPP)
S.T.P.	Standard Temperature and Pressure
SVP	Saturation Vapour Pressure
SWS	Short Wavelength Spectrometer (instrument of ISO)
UKIRT	United Kingdom Infra-Red Telescope (U.K.; on Mauna Kea, Hawaii)
VIMS	Visual and Infrared Mapping Spectrometer
VMR	Volume Mixing Ratio
UV	Ultra-Violet
UVIS	Ultraviolet Imaging Spectrograph
ZPD	Zero Path Difference

Chapter 1

The Atmosphere of Titan

1.1 Introduction

Titan, the largest moon of the planet Saturn, was discovered in 1655 by the Dutch astronomer Christiaan Huygens. It was the sixth planetary moon to be observed; after the Earth's Moon and the four Gallilean satellites of Jupiter.

Since then, terrestrial observers of Titan in visible light have seen it as a very homogeneous orange-yellow orb. The lack of visible surface features is now known to be due to a haze of organic particles which obscures the surface: Titan has an atmosphere.

In fact, Titan's true size was not finally confirmed until the Voyager 1 encounter of 1980, which sent radio waves back to the Earth from behind Titan, penetrating the atmosphere and revealing the level of the surface. Its solid diameter of 5150 km makes it the second largest moon in the solar system. Only Jupiter's Ganymede is larger, by 120 km. In contrast, the planet Mercury is 272 km smaller, although neither of these worlds has a significant atmosphere.

The mean density of Titan is comparable to that of Callisto and Ganymede, and it is probable that Titan is similarly composed of a rocky core (52% by mass) surrounded by a water ice envelope (48%) (Tyler et al., 1981).

Titan's orbit around Saturn takes almost sixteen days (table 1.1), however the length

Physical:	
Mean Diameter (R_T)	5150±1 km
Mass (M_T)	1.346 $\times 10^{26}$ g
Mean Density	1.881±0.002 g cm^{-3}
Surface Temperature[a]	93.0±0.5 K
Effective Temperature	86 K
Solar Flux	1.1% earth's
Surface Pressure	1496 ± 20 mbar
Orbital:	
Mean distance from Saturn	1.226 $\times 10^6$ km
Mean distance from Sun	9.546 AU
Orbital period around Saturn	15.95 days
Orbital period around Sun	29.5 years

Table 1.1: Titan's physical statistics. All data taken from Hunten et al. (1984) except where otherwise indicated. [a] Equatorial range of probable temperatures, including argon uncertainty, from Courtin et al. (1995).

of its 'day' or rotational period has proved elusive, due to the lack of features with which to track rotation. Observations of the surface in infrared 'window' regions in the last few years (Lemmon et al., 1995) have been able to demonstrate that synchronous rotation is very likely: *i.e.* its 'day' and 'year' of its orbit of Saturn are the same.

1.2 Atmospheric Composition

The presence of an atmosphere was first suggested by Comas-Solá (1908) on the basis of dubious sightings of limb-darkening. However, the first firm evidence came when Kuiper (1944) spectroscopically detected gaseous methane at 726 nm. Subsequent spectroscopy with ground-based telescopes revealed the presence of several other organic molecules.

The widths of the methane absorption features implied that there was a major, unseen atmospheric constituent which was hypothesised to be nitrogen from slow photolysis of outgased NH_3 over geological timescales (Lewis, 1971; Hunten, 1973; Atreya et al., 1978). Voyager 1 confirmed this suspicion in two ways: (i) by finding that the mean molecular

weight of the atmosphere is close to 28 (Tyler et al., 1981; Lindal et al., 1983) and (ii) by the direct observation of significant UV emission from N and N^+ (Broadfoot et al., 1981; Smith et al., 1982b). Although the composition varies from the troposphere to the stratosphere and beyond, the atmosphere is known to be mainly composed of N_2, with CH_4 at 2–6% being the next largest detected constituent.

Argon is probably also present at some level, due to it being cosmically abundant and would not condense under Titan's atmospheric conditions. A 3σ upper limit, equal to $\sim$6% was placed on its abundance by Courtin et al. (1995).

Infrared spectroscopy of the atmosphere, by Voyager and ground based telescopes, has also revealed a rich cocktail of lesser constituents of which molecular hydrogen and ethane are the most significant, but many other hydrocarbons and nitriles have also been detected (see table 1.2).

Oxygen-bearing species are quite rare: most atmospheric oxygen is in the form of carbon monoxide which has been detected by ground-based observations in the near-infrared and millimeter/sub-millimeter wavelength ranges. Estimates of its abundance vary from 2 ppm to 75 ppm (see §3.1.2 for discussion). The other oxygen-bearing molecules detected to date are CO_2, which at $\sim$10 ppb is much rarer than CO, and even less abundant is the recently-detected H_2O at $\sim$0.4 ppb (Coustenis et al., 1998b).

1.3 Stratospheric Haze

Sagan (1974) first suggested that solid organic aerosols were being produced in Titan's upper atmosphere, in order to explain the visible extinction and reddish-orange colour of the satellite. The Voyager 1 and Voyager 2 images (Smith et al., 1981, 1982a) confirmed that Titan's atmosphere is opaque at visible wavelengths ($\chi > 5$), obscuring the surface. This also causes its apparent optical radius, defined as the altitude of photometric inflection, to be some $\sim$240 km greater than its actual surface radius (Smith et al., 1981).

The haze layer at first glance appears to be very homogeneous, and indeed no small-

Molecule	Equator (7°N)	N. Pole (70°N)
H_2 [a]	1.0×10^{-3}	n/a
CH_4	$\sim 2.0 \times 10^{-2}$	$\sim 2.0 \times 10^{-2}$
CH_3D [b]	1.1×10^{-5}	n/a
C_2H_2	3.0×10^{-6}	6.5×10^{-6}
C_2H_4	1.5×10^{-7}	1.5×10^{-6}
C_2H_6	1.3×10^{-5}	1.7×10^{-5}
C_3H_4	5.0×10^{-9}	3.7×10^{-8}
C_3H_8	5.0×10^{-7}	1.2×10^{-6}
C_4H_2	1.4×10^{-9}	2.7×10^{-8}
HCN	1.7×10^{-7}	1.5×10^{-6}
C_2N_2 [c]	$< 1.5 \times 10^{-9}$	2.2×10^{-8}
HC_3N [c]	$< 1.5 \times 10^{-9}$	4.5×10^{-8}
CO [d]	$2–75 \times 10^{-6}$	n/a
CO_2	1.4×10^{-8}	1.3×10^{-8}
H_2O [e]	4.0×10^{-10}	n/a

Table 1.2: Equatorial and North Polar mole fractions of minor atmospheric constituents in the stratosphere at the time of the Voyager 1 encounter. All values are taken from Coustenis and Bézard (1995) except where otherwise indicated. Molecular nitrogen is assumed to constitute the remaining $\sim 98\%$ of the atmosphere, although some argon may also be present. Notes: [a] Hydrogen mole fraction determined for -60°$< l <$ +60° by Courtin *et al.* (1995). [b] Mono-deuterated methane mole fraction determined for equator only (Coustenis *et al.* 1989). [c] Not detected in equatorial spectra. [d] Carbon monoxide mole fraction is a disk-average value from unresolved ground-based observations. Estimates vary widely: see text. [e] Water mole fraction determined from unresolved ISO SWS spectra (Coustenis *et al.* 1998b).

scale clouds or storms, or breaks in the cloud layer have ever been observed. However, closer examination of the images, and in particular contrast-stretching, has revealed at least four large-scale features of the global haze which require explanation.

Firstly, the northern hemisphere was visibly darker and redder than the southern hemisphere. This was a surprising discovery, in view of the fact that Voyager passed Titan close to the time of the northern vernal equinox, when both hemispheres would be equally illuminated by the sun. This asymmetry was also present in the derived temperature profiles, with the northern latitudes appearing colder than their southern counterparts (Coustenis and Bézard, 1995).

This asymmetry may be due, at least in part, to the large radiative time constant for Titan's massive atmosphere,[1] estimated at 138 years, which would cause the effective atmospheric season to lag behind the season of insolation by a phase angle of $\sim 90^{\circ}$ (Smith et al., 1981). Therefore, Titan's northern hemisphere would be close to winter solstice rather than vernal equinox.

This seasonal temperature lag is likely to have an influence on the distribution of aerosol particles which could then cause the observed colour and brightness asymmetry between hemispheres. Atmospheric transport of haze particles is therefore probably a more important effect than a seasonal variation in their production rates (Toon et al., 1992; Hutzell et al., 1993, 1996; Lorenz et al., 1997). A similar type of explanation may hold for the second feature, the 'North Polar Hood', seen as a distinct darker crown to the northern hemisphere.

Also seen was mid-latitude banding (Voyager 1) and the North Polar Collar (Voyager 2, and see figure 1.1). These zonal colour effects are not yet understood, but they are likely to be related to planetary rotation, similar to the banding of the giant planets.

Finally, there is the detached haze layer, seen on the limb of high-phase angle images of the Voyager cameras. This is separated from and above the main haze layer by as much as 100 km at equatorial and southern latitudes, but merged with the main haze

[1] Defined as the ratio of atmospheric thermal energy content to the mean solar heating rate for the atmosphere.

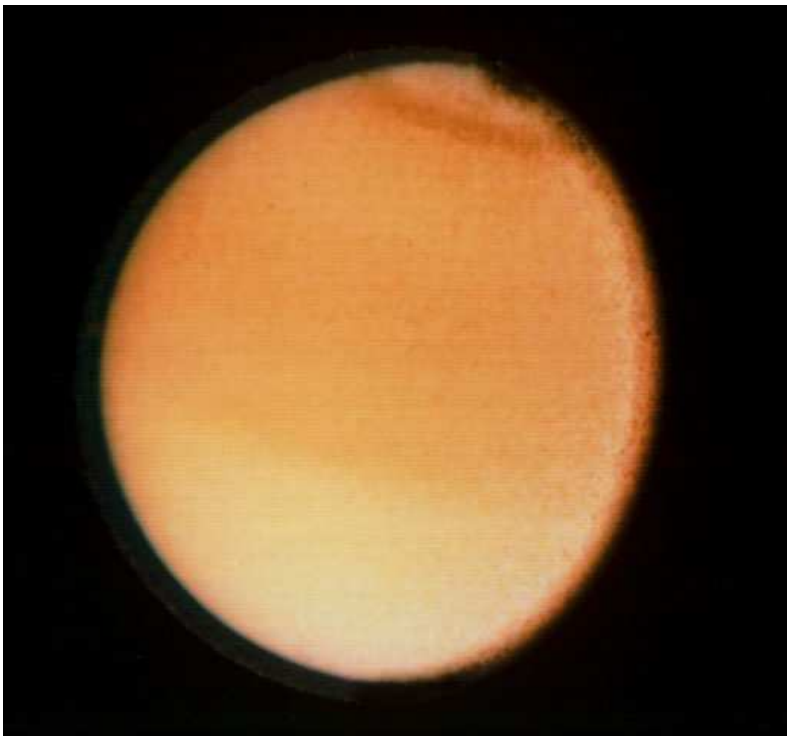

Figure 1.1: Voyager 2 image of Titan taken August 23rd 1981 from a range of 2.3 million km. This image is composed of blue, green and violet frames. The southern hemisphere is lighter in contrast, and the N. Polar collar is evident. The atmosphere can be discerned around the limb.

layer at high northern latitudes.

The detached layer is probably caused by dynamical effects. Toon et al. (1992) have suggested that Hadley-type motions above 300 km with velocities of order 1 $\mathrm{cm\,s^{-1}}$ could reproduce the observations. In this scenario, rising motions in the warmer hemisphere (the southern hemisphere at the time of the Voyager encounters) lift the haze particles, which then sink again in the winter hemisphere where the detached layer merges with the main haze layer.

1.4 Clouds

The question of condensed methane or other hydrocarbons in the atmosphere of Titan has been especially controversial since the Voyager probes, which returned ambiguous and even contradictory signs of clouds. The 'traditional' arguments for and against clouds are reviewed in Toon et al. (1988). The main lines of evidence are examined in the following paragraphs.

Circumstantial evidence for tropospheric clouds is due to the idea of surface hydrocarbon oceans (see §1.9). If there are hydrocarbon oceans on Titan, there would be a high relative humidity of methane near the surface (Flasar, 1983). In any case, the mixing ratio of methane in the troposphere is almost certainly high enough that its partial pressure exceeds the SVP, at least for part of the ascent. For a probable humidity of 60% at the surface (McKay et al., 1997), the saturation region is between about 5 and 30 km in the troposphere.

The strongest evidence so far for clouds is a broad absorption feature seen in the IRIS spectra between 200 and 600 $\mathrm{cm^{-1}}$, which has two likely explanations. The first is the pressure induced opacity of the various N_2 and CH_4 collisional combinations, however at the time of the first analysis of the data this was thought to be insufficient to fully account for the absorption (Samuelson et al., 1981). Instead, the extinction was attributed to the opacity of liquid or solid methane (Samuelson et al., 1981; Courtin, 1982; Samuelson,

1983; Thompson and Sagan, 1984; Toon et al., 1988), which was thought plausible as it is consistent with the proposed 'ocean' scenario.

More recently however, models in which methane reaches super-saturation in the troposphere have been favoured (Courtin et al., 1995; McKay et al., 1997; Samuelson et al., 1997b). If methane is up to a factor of two above the condensation mixing ratio near the cold trap, then sufficient collisionally-induced absorption (CIA) occurs to match the IRIS spectrum extremely well. Indeed, Courtin et al. (1995) argue that a condensed cloud is only admissible if it is at 40 km, much higher than expected.

Several other condensed organics are likely to exist in Titan's polar atmosphere. Emission features at 503 and 478 cm^{-1} have been attributed to condensed HC_3N (Samuelson, 1985) and solid C_4N_2 (Khanna et al., 1987; Samuelson et al., 1997a).

1.5 Photochemistry

The observed composition of the atmosphere can be attributed to a complex photochemistry, by which most species are derived from a few parent molecules; namely, the major atmospheric gases CH_4 and N_2, and presumably H_2O and CO as sources of oxygen. The many different reaction pathways have been described in literature, and used to construct 1-dimensional (vertical) models of chemical composition (Sagan and Thompson, 1984; Yung et al., 1984; Yung, 1987; Toublanc et al., 1995; Lara et al., 1996).

The chain of reactions starts in the exosphere ($z \sim 1000$ km and above) with the dissociation of N_2 into N and N^+ by bombardment with high-energy electrons from Saturn's magnetosphere and, to a lesser extent, cosmic rays (Broadfoot et al., 1981; Strobel and Shemansky, 1982). About 40% of these fragments escape and the majority of the remainder react with hydrocarbons to form HCN.

Lower down, in the thermosphere and mesosphere, CH_4 is dissociated by ultraviolet light at $\lambda < 145$ nm and the reactive radicals CH_n (n=1,2,3) form. Hydrogen atoms and molecules are produced, which can easily escape to space to form the 'hydrogen torus' of

Saturn (Broadfoot et al., 1981). The low hydrogen abundance limits re-cycling to CH_4, and because the radicals do not react with N_2, they diffuse downwards and inter-react, forming increasingly longer-chain hydrocarbons.

Ethylene (C_2H_4) is formed by addition of the CH radical to CH_4, and can undergo subsequent photolysis to acetylene (C_2H_2). Ethane also forms at $z < 800$ km through the combination of two CH_3 radicals, and becomes the second most plentiful hydrocarbon. Methyl acetylene (C_3H_4) is created through production of the $^1CH_2$ radical (Lara et al., 1996), and propane (C_3H_8) is produced in the stratosphere by addition of CH_4 to C_2H_6.

Acetylene diffuses downwards, and may eventually be dissociated to C_2H and thence to C_4H_2. Both acetylene and diacetylene undergo polymerisation in the mesosphere, leading the the polyynes C_6H_2, C_8H_2 and higher, catalysed by C_2H and C_4H. HCN is also a likely candidate for polymerisation. Finally, these polymers may stick together and coagulate, forming the ubiquitous stratospheric haze particles. The net effect of all the hydrocarbon reaction pathways is a significant consumption of methane, and a loss of hydrogen.

Sources of oxygen in the atmosphere may include H_2O, continually supplied at a low level from meteoric debris (Samuelson et al., 1983; Ip, 1990) or CO from the surface and/or interior of the planet. Water is dissociated by $\lambda < 198$ nm forming the OH radical, which reacts with atmospheric CO to form CO_2, some of which is recycled to CO by reaction with C_2H_2.

1.6 Thermal Profile

The close encounter of Voyager 1 with Titan in November 1980 used the technique of radio occultation to measure equatorial vertical profiles of atmospheric refractivity from 0–200 km. These measurements have been inverted to yield temperature profiles, by assuming a mean molecular weight and atmospheric composition (Tyler et al., 1981; Lindal et al., 1983; Lellouch et al., 1989).

These calculations led to surface temperatures in the range 94–100 K, largely dependent on the uncertainty in the amount of argon. However more recent modelling of the troposphere points towards the lower end of the range at 93–95 K (Courtin et al., 1995; McKay et al., 1997).

The ν_4 band of methane at 7.7 μm has been used, as for Jupiter and Saturn previously, to sound the atmospheric temperature in Titan's stratosphere. The wavelength of the centre and sides of the band are sensitive to different heights (this is the same as saying that the peak of the weighting function moves up and down in altitude, with changing wavelength), and so the temperature may be retrieved by an iterative technique for $110 < z < 450$ km.

Coustenis and Bézard (1995) have re-analysed spectra from the Voyager IRIS instrument using this method to retrieve temperature profiles from latitudes of 53°S to 70°N.

Finally, Yelle (1991) has modelled the upper atmosphere of Titan, from the stratosphere through the mesosphere and thermosphere to the exobase at ∼1250 km. He derives a range of models, depending on uncertain parameters, such as the abundances of C_2H_2, C_2H_6 and HCN which are important to the thermal structure, and the amount of heating by haze. Many of these models agree well with the limited data available to constrain the profiles; in particular the temperature measurement of the exobase 180 ± 20 K by the Voyager UVS instrument, and the retrieved IRIS profiles at the lower end.

Figure 1.2 shows a typical equatorial temperature profile which has been synthesised from the three data sources.

The atmosphere is probably divided into four distinct physical regions (which are analogous to similar regions in the Earth's atmosphere):

1. *The Troposphere.* The temperature at ground level is ∼94 K, which falls through the troposphere, as heat is transported upwards by convection and adiabatic gaseous expansion. A minimum of ∼71 K is reached at the *tropopause*, which occurs at

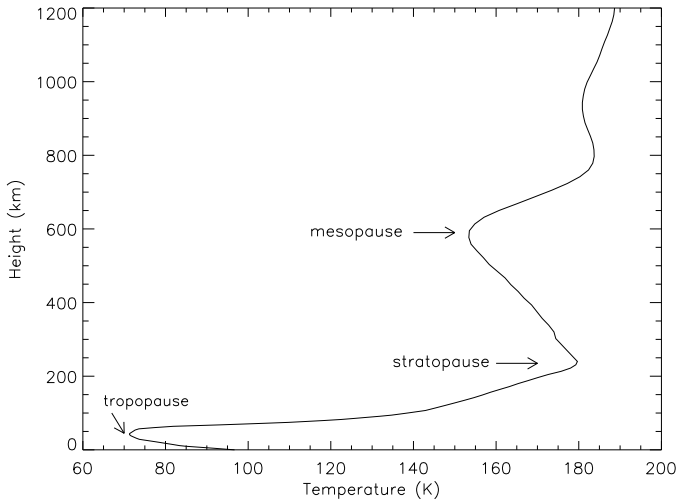

Figure 1.2: Equatorial temperature profile of Titan. Three data sets have been combined to produce the profile: (i) a radio occultation retrieval for heights less than 100 km (Lellouch *et al.* 1989) (ii) A methane band retrieval for 100–300 km (Coustenis and Bézard 1995) (iii) A model prediction for $z > 300$ km (Yelle 1991).

($\sim$45 km, $\sim$130 mbar).

2. *The Stratosphere.* The temperature rises again above 45 km due to strong absorption of solar UV, primarily by the opacity of haze particles and collisional opacity of gases (a role played by ozone above the Earth). At ($\sim$250 km, 1 mbar) the heating becomes balanced by cooling to space and a second temperature inversion is reached (*the stratopause*).

3. *The Mesosphere.* Modelling of the mesosphere by Yelle shows that it is expected to have a negative temperature gradient, due to cooling to space in the rotational-vibrational bands of certain molecules (primarily HCN, C_2H_2 and C_2H_6). A well-developed *mesopause* is predicted at ($\sim$600 km, 10^{-7} bar).

4. *The Thermosphere.* The thermosphere extends from the mesopause to the exobase at ($\sim 10^{-11}$ bar, 1250 km) defined as the level where the mean free path of molecules escaping to space becomes $\sim$1. Solar EUV heating, primarily of CH_4 and C_2H_2 below 1000 km and N_2 above, causes a moderate temperature rise in this region (Lellouch et al., 1990).

Note that the low surface gravity of Titan means that the atmosphere is greatly extended compared to that of the Earth, the pressure scale height at the surface ($\mathrm{R_g}T/M_\mathrm{r}g$) is ∼21 km,[2] compared to ∼8.5 km on the Earth, and the tropopause and exopause are both significantly higher in proportion on Titan (45 km, ∼1600 km) than on the Earth (16 km, 400 km).

At the time of the Voyager encounter, the temperatures in the northern hemisphere were significantly cooler than at equatorial and southern latitudes, by as much as 17 K at 0.4 mbar (Coustenis and Bézard, 1995). Two explanations have been proposed for the asymmetry: (i) a radiative origin, due to radiative equilibrium in the presence of seasonally varying aerosol production (Bézard et al., 1995), (ii) a dynamical origin where the atmospheric state lags behind the solar radiative forcing by 1 season, due to dynamical inertia (Flasar and Conrath, 1990).

1.7 Global Heat Balance and Greenhouse Effect

The global heat balance is determined by the amounts of solar heating and radiative cooling of the atmosphere, since there is not likely to be a significant internal heat source (Neff et al., 1985). The absorption of solar energy can be characterised by the effective temperature T_eff, and the emission of energy by the bolometric temperature T_bol, which should be equal if there is no net heating or cooling of the planet. A planet with an internal energy source for example would have $T_\mathrm{bol} > T_\mathrm{eff}$, and radiate in excess of what it absorbs from the sun.

The effective temperature of a planet is the temperature of blackbody emission required for it to remain in equilibrium with solar radiation:

$$4\pi a^2 \cdot \sigma_\mathrm{SB} {T_\mathrm{eff}}^4 = \frac{\pi a^2 (1 - A_\mathrm{b}) F_\mathrm{s}}{d^2} \tag{1.1}$$

[2]From integration of the hydrostatic equilibrium formula.

	% of radiation on Titan	% of radiation on Earth
Reflected to space	30	35
Absorbed in atmosphere	60	18
Absorbed at surface	10	47

Table 1.3: Atmospheric all wavelength radiation budget comparison for the Earth and Titan. Titan sources McKay *et al.* (1989) and McKay *et al.* (1991); Earth source is Emiliani (1992) p257.

where a is the radius of the planet, $\sigma_{\rm SB}$ is the Stefan-Boltzmann constant, $A_{\rm b}$ is the Bond albedo, $F_{\rm s}$ is the solar flux and d is the distance to the planet. The main problem in determining a value for $T_{\rm eff}$ is to obtain a value for the Bond albedo: an extensive discussion is given by Neff et al. (1985). I adopt their value of $A_{\rm b} \simeq 0.27$, which leads to a $T_{\rm eff} \simeq 83 \pm 2$ K for Titan.

The fact that the surface temperature on Titan is warmer than $T_{\rm eff}$ indicates a greenhouse effect, which has been examined by McKay et al. (1989) and McKay et al. (1991).

The $\sim$10% of incident solar radiation reaching the ground on Titan is absorbed in roughly equal amounts from photons of $\lambda < 0.7$ μm and $\lambda > 1.0$ μm (see table 1.3) in the model of McKay et al. (1989). Although a higher fraction of the longer wavelength radiation is passed by the atmosphere, the higher energy photons are more efficient at heating the surface.

The greenhouse effect is caused by blocking of surface re-radiation of this heat to space in the thermal IR. The absorption is dominated by the collision-induced opacity of tropospheric N_2–N_2, CH_4–N_2 and H_2–N_2, particularly longward of 400 cm^{-1}. This effect tends to raise the surface temperature of Titan by 21 K.

On the other hand the greenhouse effect is limited by the stratospheric haze, which is strongly absorbing at short wavelengths, blocking incoming solar radiation, but is also transparent in the thermal IR. This so-called 'anti-greenhouse' effect allows a cooling of the surface by $\sim$9 K. Taken together, the present balance of the greenhouse and anti-greenhouse effects cause a net increase of 12 K in surface temperature over the effective

temperature.

The heat balance is stable with respect to a change in either effect. If the temperature decreases, the peak of the thermal Planck function (at ∼200 cm^{-1}) would move into a spectral region of even greater opacity at ∼100–200 cm^{-1}, limiting the decrease in temperature. On the other hand, if the peak moves to higher wavenumbers, the relatively transparent 'window' at 400–600 cm^{-1} allows more radiation to escape and the surface is cooled. Hence these competing effects tend to reduce the impact of any change.

H_2 and CH_4 on Titan play a similar role to CO_2 and H_2O respectively on the Earth. For comparison, the temperature increase due to the greenhouse effect of H_2O and CO_2 in the Earth's atmosphere is ∼30 K, 523 K on Venus with its thick CO_2 blanket, and 7 K on Mars with its thin CO_2 atmosphere.

Note that on Titan, the stratosphere is significantly hotter (by 80 K) than the surface, whereas on the Earth the stratopause (temperature maximum) is somewhat cooler (15 K) than the surface. Titan's stratosphere is unable to heat the lower atmosphere at thermal wavelengths due to the low opacity of its gases and haze particles at these wavelengths.

Finally, McKay et al. (1989) argue that the thermal structure of Titan's atmosphere can be modelled fairly well without CH_4/C_2H_6 condensate clouds. This is not to say that such clouds are not present, merely that their effect on the overall temperature profile may be small.

1.8 Dynamics

At the time of the Voyager 1 encounter, Titan exhibited a substantial meridional temperature gradient, with the northern hemisphere being substantially cooler than the southern. In the stratosphere, the difference was up to 20 K at ∼1 mbar, although less at lower altitudes (Coustenis and Bézard, 1995).

Due to Saturn's obliquity of 26.7°, Titan experiences seasonal changes over the Saturnian year of $\simeq$ 30 terrestial years (Hunten et al., 1984). In November 1980 the northern

vernal equinox had just passed, and so Titan was moving into northern spring. The fact therefore that the northern hemisphere was cooler implies that the atmospheric temperature lags the cycle of insolation by as much as one season, despite the expectation that radiative time constants should be much shorter than 7.5 years (Flasar et al., 1981).

The two possible explanations for this are: (i) a radiative origin due to photochemical processes; *i.e.* a seasonal cycle of aerosol production, or; (ii) a dynamical origin, related to a high thermal heat capacity. In any event, the thermal gradient at 1 mbar implies a meridional gradient in geopotential, which must be dynamically balanced. For example, the formation of an equator-to-pole Hadley cell would effectively transport angular momentum northwards. However, this is very efficient at transporting heat and would produce a much smaller temperature contrast than observed (Hanel et al., 1981).

It has previously been suggested that Titan, which is a slowly rotating planet like Venus, may similarly exhibit super-rotation in the upper atmosphere (Golitsyn, 1975). Also, evidence from the stellar occultation of the star 28 Sagittarii by Titan (Sicardy et al., 1990; Hubbard et al., 1993) suggests winds of the order 100 $\mathrm{m\,s^{-1}}$ in the high stratosphere.

Hourdin et al. (1995) have adapted a terrestial GCM and applied it to the Titanian atmosphere. As expected for a planet with significant obliquity, their model predicts a pair of equator-to-pole Hadley cells near equinox, and a global pole-to-pole Hadley cell near the solstices (figure 1.3). Their simulations also support the idea of a cyclostrophic zonal flow, with prograde stratospheric winds of order $\sim$80–100 $\mathrm{m\,s^{-1}}$ (a super-rotation factor of $\sim$6–8). However, the temperature contast predicted by the model is 5–10 K less than the Voyager observations.

1.9 Surface

The surface of any planet necessarily interacts with the atmosphere; thermodynamically, physically, chemically, radiatively etc. so it is appropriate to add a brief discussion here.

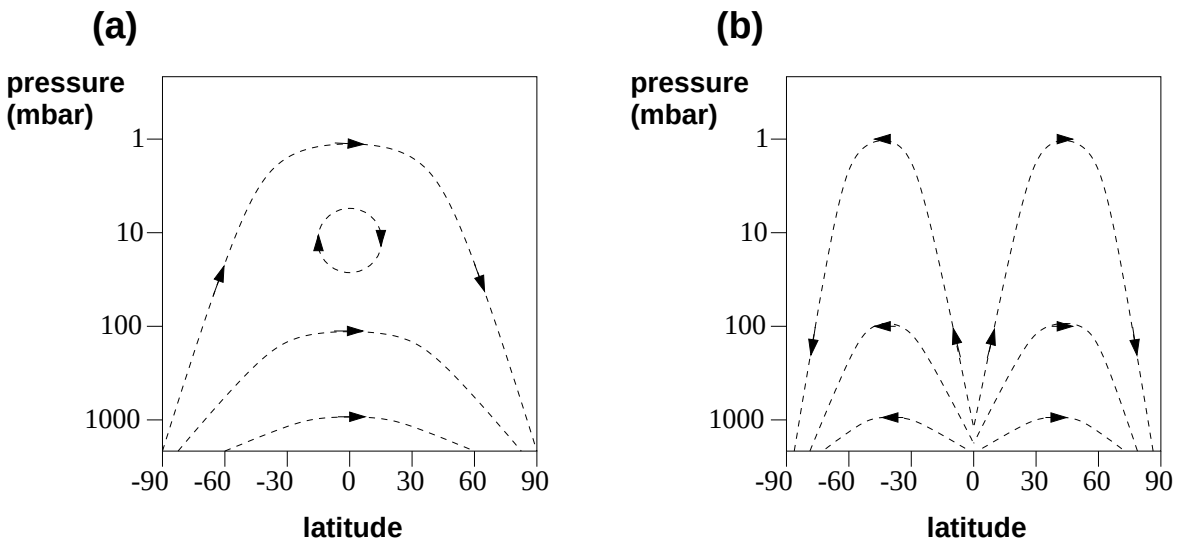

Figure 1.3: Schematic diagram showing a simplified version of the zonally averaged meridional circulation: (a) for northern winter solstice, and (b) at northern equinox. In fact the equinoxal circulation is not quite symmetric (see figure 6 of Hourdin *et al.* 1995).

The surface of Titan remains almost completely unknown. Until recently, no direct images of the surface were available, and only indirect evidence from the Voyager missions coupled with theoretical considerations gave any clues as to its nature. At present, many uncertainties remain unresolved.

Tyler *et al.* (1981) proposed a surface ocean or ice layer of methane to explain the under-representation of carbon with respect to nitrogen in the atmosphere, by a factor of $\sim$100, compared to the solar ratio. Methane is close to its triple point (90.7 K, 117 mbar) in the lower atmosphere of Titan and hence might be expected to form clouds and precipitate to the surface. Some sort of vast surface or sub-surface reservoir of methane would also appear to be required to continuously resupply the atmosphere- the present content of CH_4 would be destroyed by photolytic and catalytic processes in the mesosphere in a relatively short time compared to the satellite's presumed age of $\sim$4.3 Gyr (Strobel, 1982).

Constraints were already being imposed on this possibility by the Voyager radio occultation measurements. Flasar (1983) pointed out that the relative humidity of methane above an ocean of liquid methane must be at least 98%, corresponding to a 'wet' CH_4

lapse rate of 0.6 K/km (Lunine et al., 1983). This would appear to be incompatible with the experimental lapse rate of 1.38 ± 0.10 K/km in the lowest 3.5 km of the atmosphere, derived from the radio profile. The experimental lapse rate however is in good agreement with the dry lapse rate of 1.40 K/km predicted from non-ideal gas calculations for a pure nitrogen composition (Lindal et al., 1983).

Therefore surface oceans of pure CH_4 are ruled out, at least at the locations of the ingress and egress radio occultations, although Lunine et al. (1983) proposed that a predominantly ethane ocean of depth up to 1 km with lesser amounts of CH_4 and C_3H_8 could have the required lapse rate.

Tidal effects have also been used to constrain surface ocean models. Dermott and Sagan (1995) have studied the relation of ocean coverage to tidal effects on Titan. Titan has a significant ($\sim$3%) eccentricity in its orbit about Saturn which implies that tidal dissipation, which tends to circularise the orbit, is small. They find that either a deep, global ocean or an intermittent, insignificant coverage would produce the low dissipation rate. A recent review of surface models is by Lunine (1993).

The first observational refutation of the 'ocean' hypothesis was due to radar reflectivity measurements made by Muhleman et al. (1990). The experiment demonstrated that Titan is much too reflective, by an order of magnitude, to be largely covered in hydrocarbon seas, and is more comparable in this respect to the icy Gallilean satellites.

More recently, observations of Titan through methane 'windows' of low opacity in the near-IR (0.94, 1.08, 1.28, 1.6, 2.0 μm) using ground-based telescopes have been used to sense the surface (Griffith et al., 1991). Repeated observations over a complete orbital period have revealed a cyclical modulation in albedo, with the leading hemisphere appearing more reflective than the trailing one (Griffith, 1993; Lemmon et al., 1993, 1995; Coustenis et al., 1995). This not only constrains Titan to be in synchronously locked orbit about its parent, but provides the first evidence for surface heterogeneity.

In addition, the first surface images have now been produced using the HST (Smith et al., 1996) and ground based adaptive optics (Combes et al., 1997) which have confirmed

that the leading hemisphere contains a large bright feature centred at a latitude of 114°. The surrounding terrain is less reflective, but still bright compared to other icy satellites such as Hyperion (Coustenis et al., 1995).

These albedos are much too high to reasonably allow a global liquid hydrocarbon surface, although smaller expanses: such as 'lakes', or underground 'aquifers' are still possible, in agreement with the second option of Dermott and Sagan. The high overall albedo is more compatible with a water-ice coverage, possibly mixed with smaller amounts of tholin (Coustenis et al., 1995).

1.10 Current Unanswered Questions

There are currently significant uncertainties surrounding all aspects of Titan's nature:

- **Temperature Profile:** how does the temperature vary away from the equator, particularly in the lower atmosphere at $z < 100$ km?
- **Gas profiles:** what is the vertical variation of mixing ratios of methane and ethane in the lower atmosphere; do they reach super-saturation and by how much?
- **Condensates:** which species condense in the atmosphere; at what levels do the droplets form and what is their composition and size; how are they removed (rain-out, re-evaporation)?
- **Aerosols:** what is the nature of the stratospheric haze particles; at what levels and from what do they form; how does their size and composition vary with latitude, and relate to the hemispheric brightness difference and detached layer; how are the particles removed?
- **Upper atmosphere:** what is the vertical temperature variation of the atmosphere above 450 km; what are the profiles of minor species in the mesosphere; what are the photo-sensitised and catalytic reactions taking place; what are the timescales for return to chemical equilibrium after, *e.g.* meteoric disruption?

- **Dynamics:** what is the global circulation; what are the timescales for vertical and horizontal transport of haze and gaseous species; what is the interaction of the troposphere with the stratosphere; what is the dynamical response to seasonal forcing?

- **Evolution:** how did the original atmosphere come into being; how did it then evolve to its present composition over geologic time?

- **Surface:** what is the state of Titan's surface; in particular is there a mixture of substances and phases; and what is the interaction of the atmosphere with the surface, especially regarding re-supply of methane to the atmosphere?

The major new scientific endeavour to answer these queries is the Cassini-Huygens space mission to the Saturnian system. Amongst other instruments, Cassini carries the Composite Infrared Spectrometer (CIRS), the capabilities of which are the subject of this thesis. Both Cassini and CIRS are discussed in the next chapter.

Chapter 2

The Cassini-Huygens Mission and CIRS

In 1982, a working group of planetary scientists drawn from the European Space Sciences Committee and the US National Academy of Sciences Space Sciences Board proposed a new co-operative mission to the Saturnian system, which was to include both an orbiter and a Titan probe. At this time, the Voyager 1 and 2 missions had just passed Saturn and, although answering some questions, had raised many more, and so scientific interest was high. Funding was allocated for the mission in 1988 by ESA and 1989 by NASA, and the instrument payloads were simultaneously selected in 1990. Design, construction and testing continued for the next seven years.

The first part of this chapter gives an overview of this new mission to the Saturnian system, which is composed of the Cassini orbiter and the Huygens atmospheric descent probe and lander for Titan.

The second part of the chapter concerns the Composite Infrared Spectrometer (CIRS) which is carried on-board Cassini. The main aim of this thesis is to calibrate and understand the capibilities of CIRS, with particular emphasis on the study of Titan's atmosphere. Before discussing CIRS however, there is a brief description of the IRIS instrument which flew on both Voyager spacecraft. This is instructive, both because

data from the IRIS mission have been the main source of information concerning Titan's infrared spectrum to date, but also because CIRS has evolved technically from the IRIS design.

The specification of IRIS is summarised, and it is shown how this technical background, in parallel with the scientific background detailed in chapter 1, has given rise to the desired capabilities for the Cassini infrared spectrometer. Lastly the design and operation of CIRS is discussed.

2.1 The Cassini-Huygens Mission

The Cassini-Huygens mission is a joint NASA-ESA project, with NASA assuming the lead role in designing and building the orbiter, and ESA the probe. In all, seventeen countries contributed to the spacecraft and instruments. An overview of the mission has appeared in the literature (Lebreton and Matson, 1992).

Cassini is the sister spacecraft of the Gallileo mission to Jupiter, currently in Jovian orbit and still sending back data. Like Gallileo, Cassini has a descent probe, Huygens. Unlike Gallileo however, the target for the probe is not the main planetary body of the system. Instead, Huygens will be dropped into the atmosphere of Titan to make *in situ* measurements, and will hopefully also be functional for a short time on the surface. Figure 2.1 shows the configuration of the spacecraft.

Cassini was launched on October 15, 1997, at 4:43 a.m. Eastern USA Time from Cape Canaveral Air Force Station, aboard a Titan IVB/ Centaur launch vehicle (see frontispiece).

Figure 2.2 illustrates the trajectory of the spacecraft. The seven-year cruise phase of the mission includes four gravity-assist manoeuvers, in which the spacecraft makes a close pass to a planet and is accelerated. The first three passes are in the inner solar system: twice close to Venus, and then the Earth, after which Cassini heads for the outer solar system and a swing past Jupiter. Until Jupiter is passed, none of the instruments

are intended to be fully powered up in operational mode.

Unlike earlier 'fly-by' missions Cassini will go into orbit around Saturn upon arrival in July 2004, and then spend four years sending back vastly greater quantities of data than all the earlier missions combined.

2.1.1 The Cassini Orbiter

The science objectives for Cassini can be divided into five main groups: Saturn, Rings, Magnetosphere, Icy Satellites and Titan. The specific objectives for Titan science are to:

- Determine the abundances of gases in the atmosphere, establish isotope ratios for the most abundant elements, provide information that might help to constrain formation and evolution models.
- Observe vertical and horizontal distributions of trace gases, search for more complex organic molecules, investigate energy sources for atmospheric chemistry, study the formation and composition of aerosols.
- Measure winds and global temperatures, investigate cloud properties, investigate circulation and seasonal effects in the atmosphere, search for evidence of lightning.
- Determine the phase of the surface (liquid or solid), determine the topology and composition of the surface, collect data that will help determine the internal structure.
- Investigate the upper atmosphere and ionosphere of Titan and their roles as sources of neutral and ionized material in the magnetosphere of Saturn, such as the hydrogen torus.

To achieve these goals, Cassini carries onboard 12 scientific experiments, which can be divided into three broad categories (which also relates to their mounting position on the spacecraft).

Figure 2.1: The Cassini spacecraft (NASA).

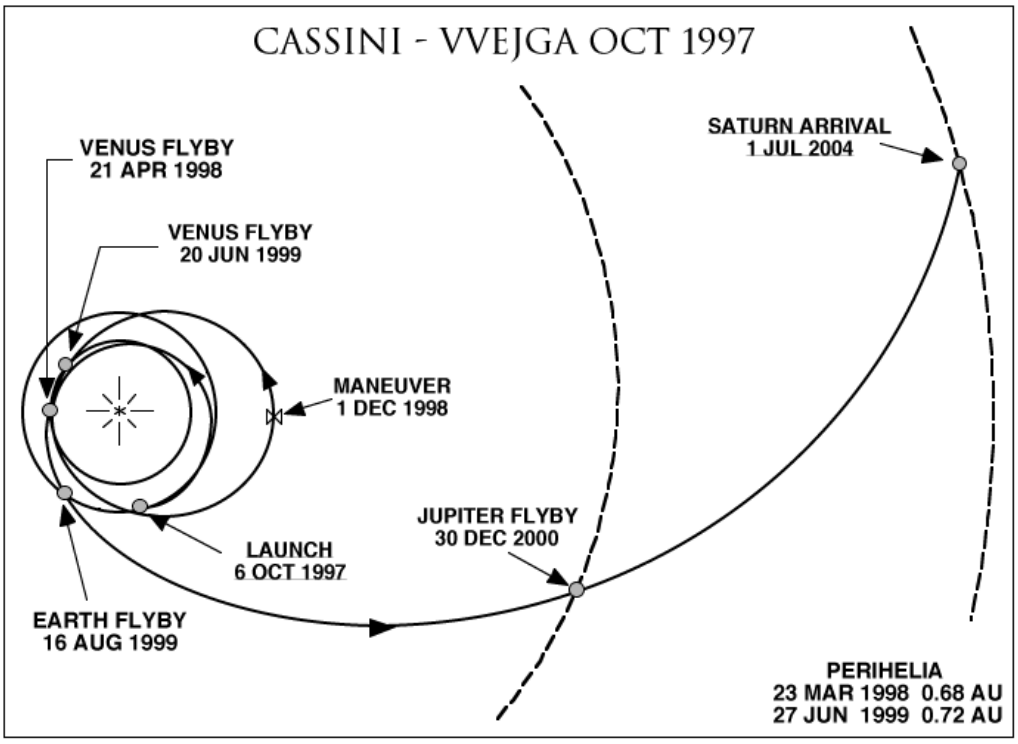

Figure 2.2: The cruise trajectory of Cassini spacecraft (NASA). Note that the dates of the manoeuvers will be somewhat later than indicated on this plot, due to the nine-day delay in the launch.

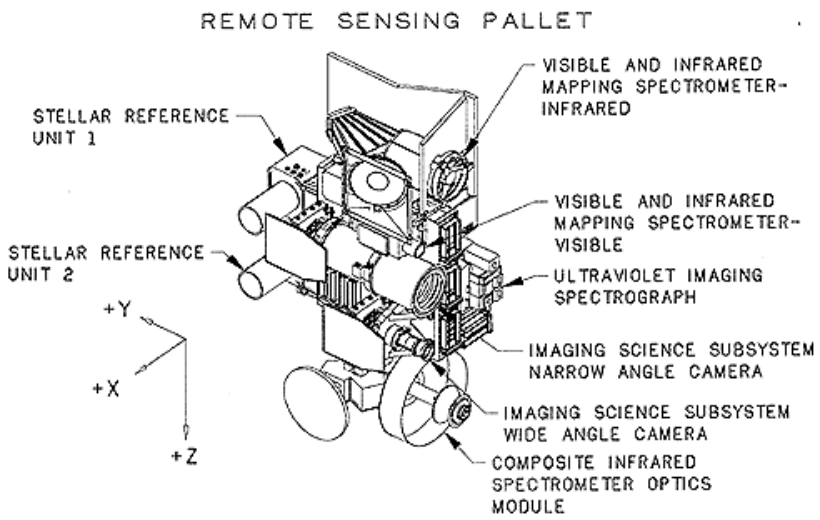

Figure 2.3: Optical Remote Sensing Pallette of Cassini (NASA).

The Optical Remote Sensing Palette (figure 2.3), which is fixed to the spacecraft carries four instruments: the Composite Infrared Spectrometer (CIRS), the Imaging Science Subsystems (ISS), the Ultraviolet Imaging Spectrograph (UVIS) and the Visual and Infrared Mapping Spectrometer (VIMS). Two further experiments, sometimes grouped together as Microwave Remote Sensing investigations, are attached to the spacecraft directly: the Cassini Radar (RADAR), and the Radio Science Subsystem (RSS).

Finally, the Fields, Particles, and Waves experiments are mounted on the fields & particles palette which is attached to the main spacecraft (figure 2.1). They are the Cassini Plasma Spectrometer (CAPS), the Cosmic Dust Analyzer (CDA), the Ion and Neutral Mass Spectrometer (INMS), the Dual Technique Magnetometer (MAG), the Magnetospheric Imaging Instrument (MIMI) and the Radio & Plasma Wave Science experiment (RPWS).

2.1.2 The Huygens Probe

The Huygens probe was built by the European Space Agency, and is designed to enter and decelerate in Titan's atmosphere and parachute a fully instrumented robotic laboratory down to the surface. The probe will separate from the orbiter four months after Saturn

orbit insertion, in November 2004. Twenty-two days later the probe reaches Titan, and the instruments will be switched on 15 minutes before encountering the atmosphere, at a distance of ∼4500 km.

After the initial entry phase, the front heat shield will be ejected. The probe will then use three different parachutes to descend over a period of about 2.5 hrs to the surface, during which atmospheric data will be collected. When the probe reaches the surface, if it survives impact, it will function and relay data back to the orbiter for up to half an hour, depending on battery life, at which point Cassini goes over the horizon.

The six experiments carried onboard Huygens cover a full range of investigations into atmospheric composition, dynamics and surface nature. They are the Aerosol Collector Pyrolyser (ACP), the Descent Imager and Spectral Radiometer (DISR), the Doppler Wind Experiment (DWE), the Gas Chromatograph and Mass Spectrometer (GCMS), the Huygens Atmospheric Structure Instrument (HASI) and the Surface Science Package (SSP).

2.2 Voyager IRIS

Much of the information we possess about Titan has come from the Voyager 1 mission, which made a close pass to Titan on 12 November 1980. During this time the Infrared Interferometer Spectrometer (IRIS) recorded ∼3000 spectra in 11 hours, including on-disk and limb spectra of the equator and poles.

The instrument consisted of a 20 *in.* Cassegrain telescope, a single Michelson interferometer, and a single thermopile detector with a field of view (FOV) of 4.3 mrad. The detector was sensitive from 200–1400 cm^{-1}, with a spectral resolution of 4.3 cm^{-1} (see figure 2.4).

IRIS operated in a continuously scanning mode rather than sampling at discrete path differences. In this method the signal is sampled at small, equal intervals, which must

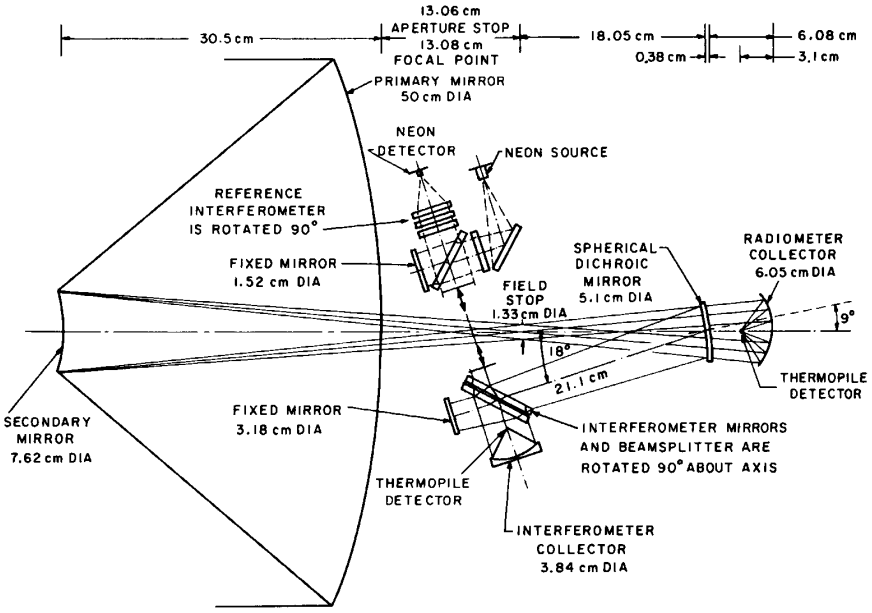

Figure 2.4: IRIS optical layout (after Hanel *et al.* 1992).

be less than one half of the shortest wavelength to be measured, to avoid aliasing.[1] The continuous scan mode is usually prefered for space instruments due to simplicity, and slightly greater efficiency than the alternative, mirror-stepping method. The maximum path difference determines the maximum resolution obtainable from the interferogram before apodisation (see §5.1.6). IRIS had no chopping mechanism, and was periodically aimed at deep space to subtract out the instrumental background radiation.

The IRIS dataset has played a pivotal role in increasing our understanding of Titan. Its analysis has provided a wealth of information (see chapter 1), including the abundances of minor molecular species in the stratosphere, the stratospheric temperature profile, variation of both temperatures and abundances with latitude, the D/H ratio, and constraints on the size and optical nature of haze and cloud particles. It has also been an important guide when interpreting the results of other datasets (*e.g.* the radio occultation data).

Figure 2.5 shows a typical IRIS equatorial spectrum. The emission signatures of

[1] This is essential if the spectrometer is operating in the first order. For the second and higher orders, the sampling rate may be reduced if longer wavelengths are not required to be measured, and are filtered out.

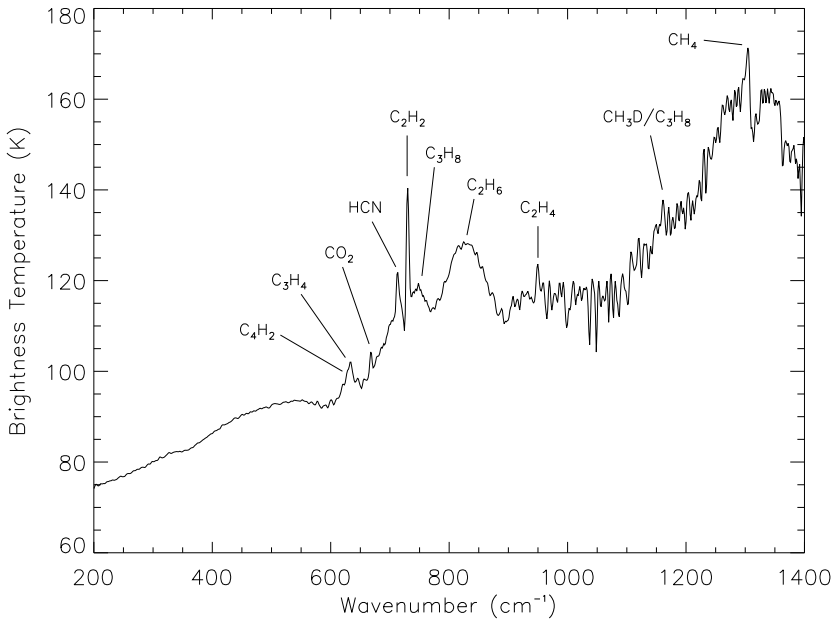

Figure 2.5: Voyager 1 IRIS equatorial spectrum at a nominal resolution of 4.3 cm^{-1}. Obtained by co-adding 31 nadir spectra at a mean airmass of 1.03 (Coustenis *et al.* 1989). Some of the more prominent molecular bands are marked.

methane and many other minor species are evident, as is the continuum absorption below 600 cm^{-1}.

However, the IRIS dataset is limited in many respects. Titan experiences seasonal changes over the course of 30 terrestial years, and since Voyager passed by the Saturnian system in a matter of days, we only have one close-up 'snapshot' in time of the state of the atmosphere, which is constantly evolving.

IRIS was also limited in technical respects, partly due to the limits imposed on its mass, cost and development time. Its wavelength coverage did not reach to the far-infrared region, in which there are many potentially important molecular bands, including H_2O, CO and also the collision-induced bands of N_2 and H_2, which allow tropospheric sounding on Titan and Saturn respectively. Finally, the spectral resolution (4.3 cm^{-1}), spatial resolution (4.3 mrad) and sensitivity were all moderate by present-day standards.

2.3 The Composite Infrared Spectrometer

2.3.1 Scientific Objectives

When a new infrared spectrometer instrument was proposed for Cassini, its broad mission objectives for Titan science were:

- To continue and extend the investigation begun by Voyager IRIS of Titan's infrared spectrum, especially into the far-IR region.
- To provide spatially resolved infrared mapping over a substantial fraction of one Titanian year, which will permit investigation of seasonal changes in temperature, gaseous composition and haze.
- To provide an independent, contemporaneous dataset to help interpret observations by other Cassini instruments.
- To help extend *in situ* results from the Huygens probe to the whole globe, and at later times.

The far-IR coverage was important for a number of reasons. Firstly, important molecular species such as H_2O and CO have rotational bands in this region. Secondly, the wide collision-induced absorption band due to N_2–N_2 interactions, and also rotational lines of methane at $\sim$100 cm^{-1} can both be used for temperature sounding of the lower stratosphere and troposphere.

A detailed set of objectives at Titan for the new spectrometer was then drawn up. This was based on the current scientific uncertainties about Titan (see §1.10) and were chosen to increase our understanding of its nature in every possible area, whilst remaining within the realms of practicality. The key scientific observations required to be made are as follows (adapted from Kunde et al., 1990):

- **Temperature profiles:** To make global maps of the atmospheric thermal structure from 0.01 mbar (stratosphere) to $\sim$100 mbar (upper troposphere). This will

aid understanding of atmospheric dynamics, energetics and transport processes, and their seasonal variations.

- **Methane:** To measure the latitudinal variation in methane abundance, using the 1304 cm^{-1} band to sound the 1-5 mbar region, in order to more fully understand the greenhouse effect and global heat balance.

- **Vertical Mixing Ratios of minor species:** To globally map the vertical distributions of trace gases including hydrocarbons, nitriles and oxygen-bearing compounds, to constrain photochemical models of the stratosphere.

- **Oxygen chemistry:** Measure the latitudinal change in the mean abundance of carbon monoxide in the stratosphere, to help understand sources and sinks of oxygen in the atmosphere.

- **New species:** To search for new atmospheric constituents, in particular higher order hydrocarbons which have been predicted by photochemical models such as allene (CH_2CCH_2) and benzene (C_6H_6). These will help to constrain evolutionary and equilibrium models of Titan and its atmosphere.

- **Isotopic ratios:** To measure isotopic ratios, such as D/H , $^{12}C/^{13}C$ and $^{14}N/^{15}N$, which will aid understanding of Titan's origin.

- **Particles and droplets:** To globally map tropospheric and stratospheric cloud and aerosol distribution and properties. From these data inferences can be made about the aerosol composition, size and production/loss mechanisms. The aerosols play a major role in atmospheric thermodynamics.

- **Upper atmosphere:** To map non-LTE emissions in the upper atmosphere (10^{-6} and 10^{-7} bar). These will contribute to the understanding of the mesosphere and thermosphere, in association with data from other instruments such as UVIS.

- **Surface:** To make global maps of the surface temperature through the infrared window at 400–600 cm^{-1}, to more fully understand the nature of the surface and the interaction of the surface with the atmosphere through dynamical, thermodynamical and chemical processes.

2.3.2 Design Considerations

A design for the new instrument which would be able to carry out the observations listed was proposed by a GSFC-led team (Kunde et al., 1990). The design was partly based on the older Voyager IRIS instruments, but is more advanced in almost every respect.

It was obvious from early on that two separate interferometers would be required (IRIS had one) one for the mid and one for the far infrared. This layout would allow the engineers to take the maximum advantage of technological advances for the optics and detectors in the different wavelength regimes. Therefore the instrument was named the Composite Infrared Spectrometer (CIRS).

There were other important constraints on the design. Cassini will approach Titan closely, to within an altitude of 1000 km or 40% of its radius. On the contrary, the spacecraft will only be able to approach Saturn to a distance of 5 R_S due to the rings. Nevertheless, it is important that the infrared spectrometer is able to resolve distances on the limb comparable to the scale height. This necessitated a much smaller field of view, over at least part of the spectrum, than that of IRIS. This was achieved by using high-efficiency photo-electronic detectors.

Higher spectral resolution than IRIS was a further requirement, to enable the separation of bands which are blended together on the IRIS spectra (*e.g.* C_4H_2 and C_3H_4 at $\sim$630 cm^{-1}), and also to increase the accuracy of the temperature profile and abundance retrievals.

Finally, the small field of view in the mid-IR and the high spectral resolution both combined to reduce the signal to noise ratio. In order to reduce any instrumental noise therefore cooled detectors were required, which was achieved by means of a passive

Telescopes:	Primary	Secondary
Diameter (cm):	50.8	7.6
F-number:	F/6	
Interferometers:	**Mid-IR**	**Far-IR**
Type:	Michelson	Polarising
Spectral Range (cm^{-1}):	10–600	600–1400
Spectral Resolution (cm^{-1}):	0.5–20	0.5–20
Integration time (s):	50–2	50–2

Focal Planes:†	FP1	FP3	FP4
Spectral Range:	10–600	600–1100	1100-1400
Detectors:	Thermopile (dual)	Photoconductive (1×10 array)	Photovoltaic (1×10 array)
Pixel FOV (mrad):	4.3	0.27	0.27
Pixel AΩ (cm^2):	2.4×10^{-2}	1.5×10^{-4}	1.5×10^{-4}
Peak D* ($cm\,Hz^{\frac{1}{2}}\,W^{-1}$):	4×10^{9}	2×10^{10}	7×10^{11}
Temperature (K):	170	70, 75, 80, 85	70, 75, 80, 85

Table 2.1: CIRS Instrument Technical Specification. † In the original proposal, the far-IR was covered by two focal planes, with FP1 covering 10–300 cm^{-1} and FP2 covering 300–600 cm^{-1}. These were later combined into a single focal plane 1, covering the full range 10–600 cm^{-1}.

radiative cooler.

2.3.3 Description of Flight Instrument

The instrument was designed, built and tested by an international partnership, led by NASA Goddard Space Flight Center (GSFC) and including the CEN/Saclay and Observatoire de Paris-Meudon in France, Queen Mary and Westfield College of the University of London, the University of Oxford, and the Universität Karlsruhe, Germany. The principal investigator is V. Kunde (GSFC).

The final design has evolved considerably since the original conception (Kunde et al., 1990). A description of the flight model of the instrument is given here; the reader is referred to technical publications in the literature (Calcutt et al., 1992; Kunde et al., 1996, and references therein) for further technical details.

Table 2.1 summarises the principal instrument parameters. The optics assembly is

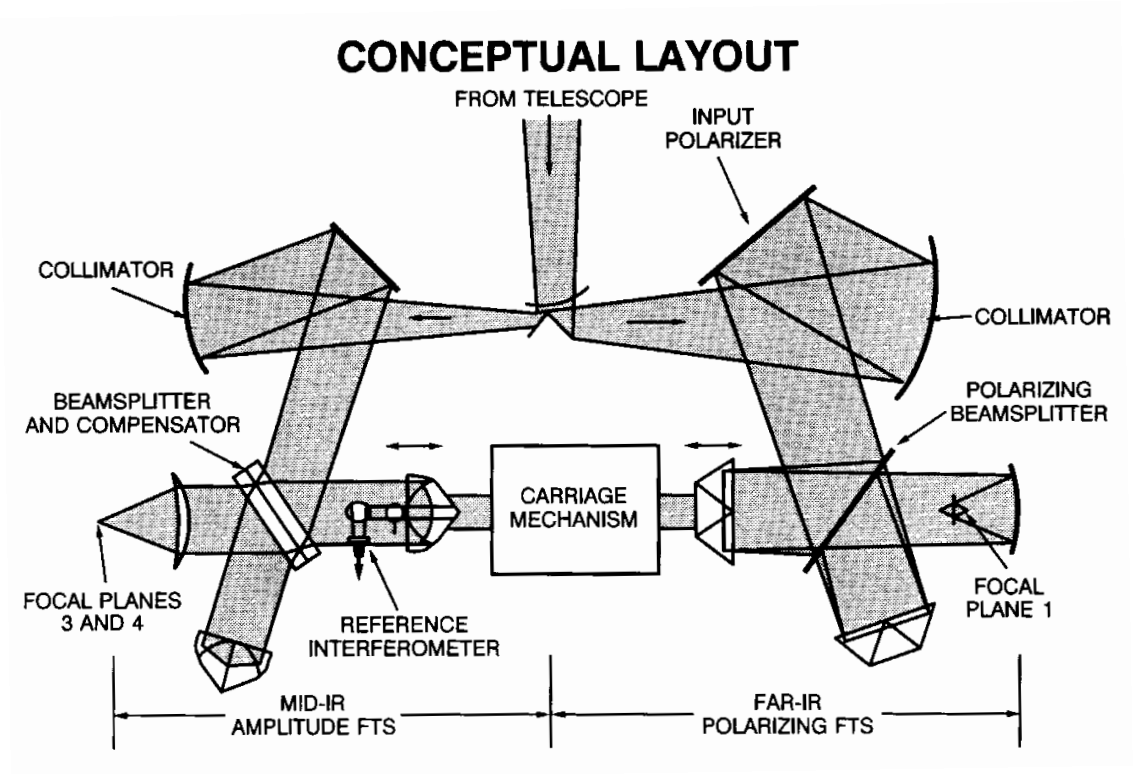

Figure 2.6: CIRS optical schematic (NASA).

comprised of a telescope, relay optics, and a pair of interferometers, covering the mid and far-IR spectral regions. Both interferometers share a common scan mechanism, as does a reference interferometer which controls the sampling rate and mirror movement. The other main components of CIRS are the detectors, the electronics assembly, and the passive radiative cooler. The entire instrument is maintained at 170 K, except for the mid-IR detectors which are at ∼80 K.

The berylium telescope is a Cassegrain type, consisting of a 50.8 cm F/6 parboloidal primary and a 7.6 cm hyperboloidal secondary, the same sizes as used by IRIS. The primary mirror has a gold-enhanced surface for low-scattering. The beam then passes to two field stops, where one part of the field is relayed to the far-IR interferometer and the other to the mid-IR interferometer, via collimators and folding mirrors (see figures 2.6 and 2.7). A shutter may be commanded into the light path of the mid-IR fore-optics for internal calibration.

The far-infrared interferometer (FIR) is of the Martin-Puplett type (Martin and Pu-

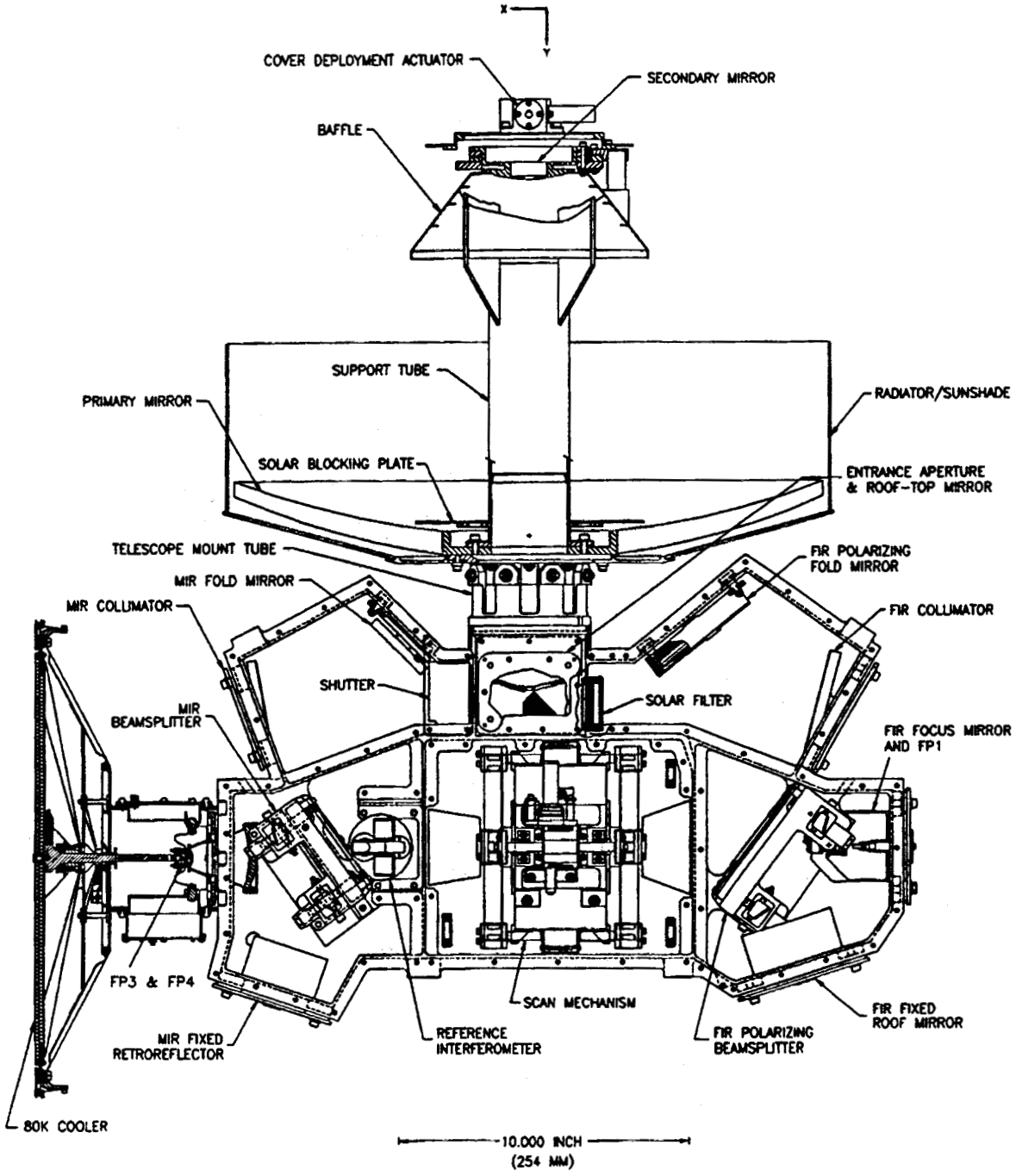

Figure 2.7: CIRS mechanical configuration (NASA).

plett, 1969), which uses wire-grid polarisers to split, recombine and analyse the radiation. This technique takes advantage of nearly ideal-response wire-grid polarisers, which have reflection and transmission co-efficients approaching 100% for both linear planes of polarisation, and over a wide spectral range. The 2 μm centre to centre wire spacing used in CIRS gives good response from 0–300 cm^{-1} and then decreasing response to 600 cm^{-1}. The far-infrared focal plane assembly (FP1) uses two thermopile detectors to measure the final transmitted and reflected beams at the polariser-analyser, however if one fails the interferometer can still operate, albeit with a lower efficiency.

The 4.3 mrad diameter field of view (FOV) of the FIR detector is the same as the IRIS detector. CIRS represents an improvement however in terms of spectral range (10–200 cm^{-1} now being accessible) and also in throughput, due to the greater efficiency of the polarising grids over conventional mirrors in the far-IR.

The mid-infrared interferometer (MIR) is a conventional Michelson design which has a KBr beamsplitter and cube-corner retroreflectors. A germanium lens focuses the recombined beams onto the mid-IR focal plane, which covers the range 600–1400 cm^{-1} using two photodetector arrays. The FP3 array of 1×10 photoconductive detectors measures from 600–1100 cm^{-1}, which includes prominent bands of acetylene, ethane, propane and nitriles. The FP4 array of 1×10 photovoltaic detectors covers 1100–1400 cm^{-1}. This range includes the important 1304 cm^{-1} band of methane.

CIRS sensitivity is improved substantially over the IRIS instrument in the MIR due to the use of cooled HgCdTe detectors rather than a thermopile. The mid-infrared focal plane is thermally isolated from the rest of the instrument by a tripod of low-conductance titanium alloy supports. At the rear of the focal plane, a flexible copper link connects to a cold finger, which extends from the passive radiative cooler. This patch is of aluminium honeycomb painted with conductive black paint, which radiates to a 2π field of view of deep space.

The temperature of the mid-IR focal plane can be set via ground control to temperatures between 70 and 90 K, by balancing the cooling effect of the patch with the

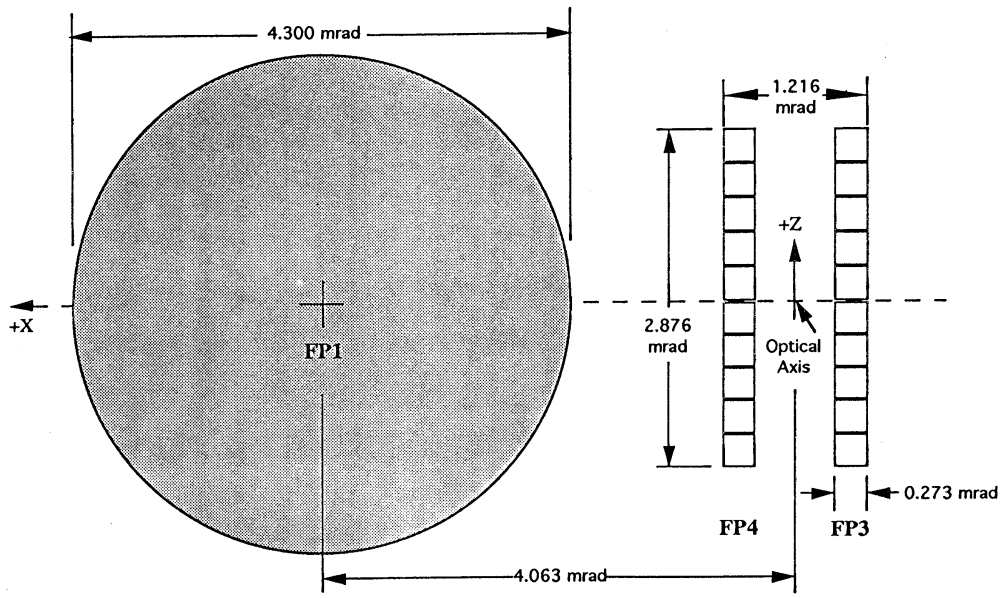

Figure 2.8: CIRS field of view (NASA).

application of a small heater, to an accuracy of 0.1 K. The noise performance of the final flight instrument is determined from experimental data in chapter 5.

This improved sensitivity allows for a much smaller FOV: each pixel has a 0.273 mrad square field of view, (*c.f.* IRIS 4.3 mrad) although the response across this field is not flat. The spatial response function of the MIR detectors is determined in chapter 4. This much smaller FOV allows for much higher spatial resolution on the limb than IRIS, with a resolution of less than one scale height in the stratospheres of both Saturn and Titan.

The relative sizes and alignment of the FIR and MIR fields of view is depicted in figure 2.8. Due to constraints on the available mass for electronics, the ten detectors on each of the mid-IR focal planes may not be used at once. Instead, five from each array can be used simultaneously, in one of four modes (see figure 2.9): odd detectors, even detectors, reduced field of view (centre detectors only), or reduced resolution mode. This allows considerable versatility in operation.

Both the FIR and the MIR interferometers share a common scan mechanism and Reference Interferometer (RI), which is a red light laser (785 nm) diode source. This provides the reference fringes used to create timing signals for data logging, and for

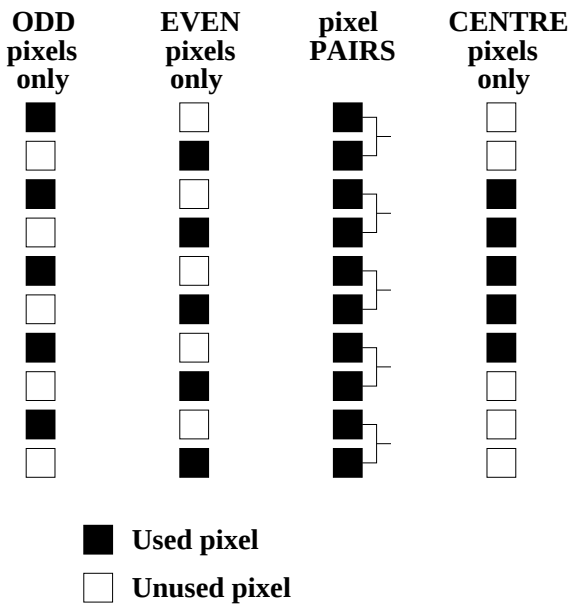

Figure 2.9: CIRS mid-infrared pixel switching modes.

feedback control of the mirror speed (see §5.1.5). The scan time is set in units of 1/8 second (=1 RTI) from 2–52 s, which takes the mechanism to the maximum mirror travel distance of 1.04 cm. The scan time controls the spectral resolution (see §5.1.6), from 20–0.5 cm^{-1}.

CIRS also provides an option for co-adding two consequtive spectra in an on-board buffer before downlink, which halves the data rate. To enable this, the zero path difference (ZPD) of each interferogram must be determined on board, which requires an additional white light interferogram to be produced for reference. A white light source is provided in the RI for this purpose, which is an LED of centre wavelength 870 nm and FWHM 70 nm, and shares the optics with the laser.

Decontamination heaters are also provided which can increase the instrument temperature to ∼270 K to drive off contaminants which may have condensed on the optics or detectors.

2.3.4 Flight Model Performance

The purpose of this thesis is to investigate the capability of CIRS for scientific investigation. The final performance of the flight instrument was expected to differ somewhat from the specification. Therefore it is very important not only to measure the performance parameters, but to see how these may affect the measurements which will be made.

One previous study of the capabilities of CIRS for Titan science has been published in the literature. Coustenis et al. (1993) predicted synthetic spectra at the resolution of CIRS, including the long wavelength region 10–200 cm^{-1} which CIRS will investigate for the first time. Their study includes rotational lines of H_2O, CO, HCN and CH_4 which may be detectable on CIRS FIR spectra, as well as lines of benzene (C_6H_6) and allene (CH_2=C=CH_2, an isomer of methylacetylene C_3H_4), which are predicted to exist on Titan from photochemical models (Raulin et al., 1990; Thompson et al., 1991).

It is now possible to extend this study in a number of ways. In particular, key performance characteristics of the instrument: the spatial response function and the noise equivalent spectral radiance, can be deduced from laboratory measurements. Knowledge of these parameters can be used to put limits on the spectral signal-to-noise which can be attained for a given wavelength (or molecular band), in a given observing time and for a given spectral resolution.

Also, since the work of Coustenis et al. (1993), new determinations for the mole fractions of CO and H_2O, and also new co-efficients for collision-induced absorption bands have been published, which means that the spectral predictions must be revised.

The radiative transfer code and atmospheric model used in this work are described in chapter 3 which follows here. In chapters 4 & 5, the determination of the instrument characteristics from lab data is discussed. Then, in chapter 6, the implications of the measured performance for CIRS science at Titan are evaluated. Chapter 7 gives the concluding remarks and comments on mission planning.

Chapter 3

Titan Atmospheric Model and Radiative Transfer Code

In order to be able to make predictions of CIRS scientific capability at Titan, it was first necessary to develop a mathematical model of Titan's atmosphere (§3.1). A radiative transfer code was then used to calculate synthetic radiances which were compared to existing observations, *i.e.* IRIS spectra, in order to refine the atmospheric model (§3.2). Synthetic spectra for CIRS will be discussed in chapter 6.

3.1 Titan Model Atmosphere

The atmosphere of Titan has been qualitatively described in chapter 1. In this section, the creation of a quantitative description of the atmosphere is discussed. The basis of a model atmosphere is the physical profile, which describes the temperature and pressure variation with height at a particular latitude.[1] In addition, two other types of vertical profile must be included; the volume mixing ratios (VMRs) for each radiatively active gaseous species, and the profiles for particulate absorbers: aerosols or condensed vapour droplets, or both. Collectively, this set of profiles forms a one-dimensional description of

[1] In this work, the atmosphere is considered to be zonally symmetric, *i.e.* the same at all longitudes.

the atmosphere at a given latitude.

3.1.1 Physical Profile

The temperature-pressure profile of Titan has necessarily been deduced from a relatively limited amount of data (see §1.6). For the troposphere, the only data are the two refractivity profiles (ingress and egress) from radio occultation of the Voyager 1 spacecraft, which pertain to near-equatorial latitudes, and below 200 km. The derivation of temperature is dependent on the value used for the mean molecular weight of the atmosphere, which ranges from 27.8 to 29.4 depending on assumptions about composition. Lellouch et al. (1989) recommend a 'nominal profile' for Titan's equator, which falls midway between the extreme possible profiles.

Higher in the atmosphere, the IRIS dataset has been analysed to deduce the temperature profile from the ν_4 band of methane at $\sim$7.7 μm, at seven different northern and southern latitudes (Coustenis and Bézard, 1995).

These two datasets have been combined to form a basic equatorial profile. The Lellouch et al. (1989) profile was used for the troposphere, and the sample A (5°N) profile of Coustenis and Bézard (1995) was used for the stratosphere, up to z=300 km. The two profiles were grafted together at 55 km, where they are equal.

The profile was extended to 500 km (approximately 10^{-3} mbar) using vertical lapse rates of 0.08 K/km (from 300–400 km)and 0.09 K/km (from 400–500 km) from Model J of Yelle (1991). This model was chosen because it most closely agrees with the IRIS sample A temperature near 300 km, while remaining consistent with the Voyager UVS measurements (Smith et al., 1982a) and stellar occultation data (Hubbard et al., 1990). The final profile which was derived is shown in figure 3.1.

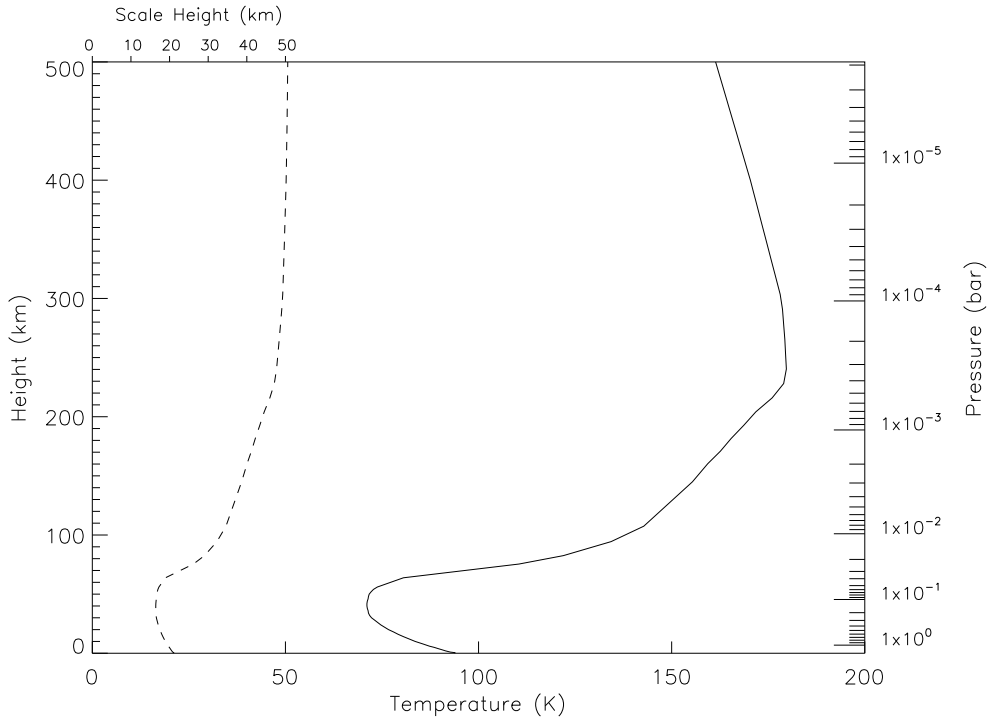

Figure 3.1: Equatorial temperature-pressure profile from combination of radio-occultation data, IRIS data and theoretical predictions for the upper atmosphere (see text). Also plotted is the variation in scale height with altitude.

3.1.2 Gas Profiles

Minor Species

There are no gases on Titan for which the abundance profiles are well-determined, because the data are too sparse. In principle, the best method for determining concentrations at different heights in the atmosphere is to make spectral observations of the limb at multiple altitudes, preferably with a spatial resolution of one scale height or less. This is one of the tasks for which CIRS has been designed.

To date however, the only limb observations of Titan have come from Voyager 1 IRIS, which took a sequence of 9 spectra near Titan's north pole, with a FOV width of ∼200 km (4–8 scale heights). These have been analysed by Coustenis et al. (1991), who derived crude vertical profiles (based on the only available data at two altitudes) for seven minor gases, at high northern latitudes.

IRIS also made many more observations of Titan over a wide range of latitudes in nadir-view. From these spectra, the mean stratospheric gas abundances for the hydro-

carbons C_2H_2, C_2H_4, C_2H_6, C_3H_4, C_3H_8, and C_4H_2, plus CO_2 and HCN, have been deduced by Coustenis and Bézard (1995). Strictly, these abundances apply only to the time of the encounter. For the nitriles C_2N_2 and HC_3N, abundances were found by the same authors for latitudes greater than 50°N, and upper limits thereof at other latitudes.

More recently, an analysis of Titan observations by the ISO Short Wavelength Spectrometer (SWS) over the same spectral range has yielded estimates of the disk-averaged abundances of these gases approximately half a Titan year later. These new figures, which largely reflect the present equatorial amounts, are not significantly different from the Voyager equatorial ones (Coustenis et al., 1998a). There has also been a detection of water vapour at a mole fraction of a 4×10^{-10} (Coustenis et al., 1998b), which has led to a preliminary equatorial profile. This band is too weak to be seen on the IRIS spectra and is discussed in the context of CIRS observations in chapter 6.

A vertical profile for HCN has recently been derived from millimeter and submillimeter spectra of the unresolved disk (Hidayat et al., 1997). This profile is in agreement with the stratospheric average of Coustenis et al. (1989) to within the level of uncertainty.

CO has been detected only from ground-based observations in the infrared (Lutz et al., 1983; Noll et al., 1996) and millimeter and submillimeter spectral regions (Paubert et al., 1988; Marten et al., 1988; Gurwell and Muhleman, 1995; Hidayat et al., 1998). These have resulted in a wide variety of estimates of the CO abundance, ranging from 2–75 ppm in the stratosphere, and from 10–60 ppm in the troposphere (see Hidayat et al., 1998, for review). Hence, the question as to whether CO is well-mixed, as predicted by photochemical models, or not, as indicated by some observations, is still wide open.

In the spectral modelling of this thesis, the hydrocarbons, plus CO_2 and HCN are taken to have constant VMRs in the stratosphere equal to the Voyager IRIS values. The VMRs then quickly drop as the gases condense out along their respective saturation vapour pressure curves near the top of the troposphere. In view of the present uncertainty in the CO abundance, a constant VMR of 1×10^{-5} equal to the result of Noll et al. (1996) has been adopted as an order-of-magnitude estimate. A constant volume mixing ratio

for hydrogen was set equal to 1×10^{-3} (Courtin et al., 1995).

Methane Model

For methane and deuterated methane (CH_3D), a slightly more sophisticated model is used to calculate the VMRs. Methane, which forms ∼2–8% of Titan's atmosphere depending on altitude, is sub-saturated both at the surface and in the stratosphere. However, for a region of the troposphere (roughly 5–30 km) the partial pressure of methane exceeds its saturation vapour pressure (SVP), and therefore either some of the gas must condense out, or it exists at super-saturated levels.

The simplest theoretical treatment is to consider a parcel of humid air moving upwards through the troposphere. Firstly, the humidity h or volume mixing ratio q_v of the condensable species is specified at the surface. The two quantities are related by the expression:

$$h(z) = \frac{q_\mathrm{v}(z)p(z)}{e_\mathrm{c}(T(z))} \times 100\% = \frac{p_\mathrm{c}(z)}{e_\mathrm{c}(T(z))} \times 100\% \tag{3.1}$$

where p is the atmospheric pressure and e_c is the SVP at the ambient temperature, which both vary with altitude. The parcel of 'moist' air is then considered at successively higher altitudes and the partial pressure of the condensable is compared to the SVP at that height. Where the h exceeds a maximum value h_MAX, condensation occurs to limit the rise in humidity.

A computer program was developed to simulate this model for tropospheric methane on Titan. This has two free parameters: firstly, the surface methane mole fraction $q_{\mathrm{CH_4}}(z_0)$ or relative humidity $h(z_0)$; and secondly, the maximum humidity before condensation occurs h_MAX. Note that if the surface humidity is specified, then the surface mole fraction of CH_4 is also then determined (or vice versa) because both the SVP curve for methane and the atmospheric T–p profile are fixed. The SVP curve was computed using an empirical formula from the literature (Armstrong et al., 1955; Lide and Kehiaian,

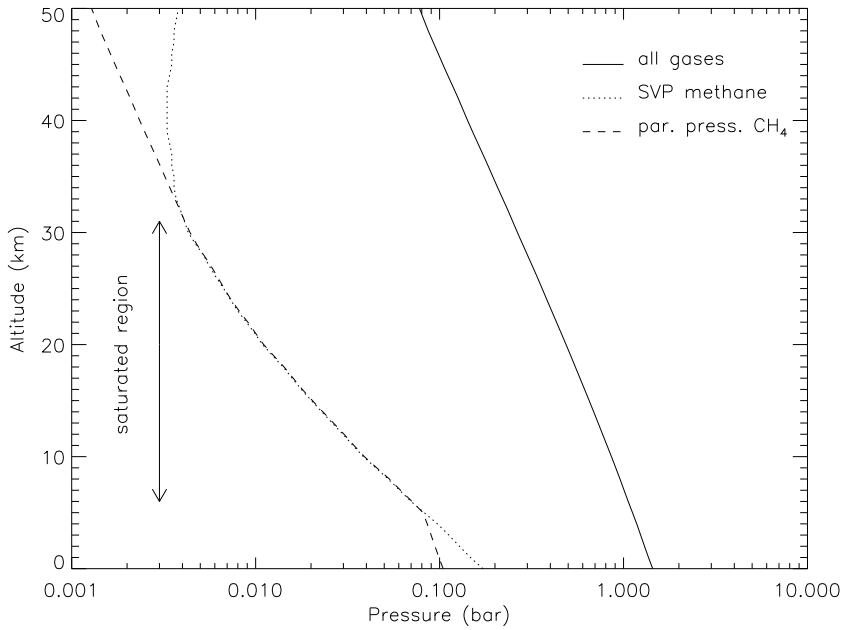

Figure 3.2: Comparison of methane partial pressure in the troposphere vs. saturated vapour pressure. The vertical extent of possible saturation, where condensation may occur, is also indicated. The surface methane mixing ratio of 7.3% gives a 60% relative humidity, which rises to 100% between 6 and 31 km. At the top of the condensation region the $q_{\mathrm{CH_4}}$ 'freezes out' at 1.7% . Physical profile is that of Lellouch *et al.*.

1994).[2]

Starting at z=0 km, the air parcel is raised upwards through the atmosphere, and the humidity calculated at each level. As z increases, the atmospheric temperature and pressure both decrease, and, because the VMR of methane is constant, its partial pressure decreases in line with the overall atmospheric pressure. At the same time, the SVP is also decreasing, and indeed falling more rapidly than $p_{\mathrm{CH_4}}$ (see figure 3.2), so the humidity rises.

When the relative h reaches h_{MAX} (the 'cloud base') it is fixed at this value, and above this level the $q_{\mathrm{CH_4}}$ is adjusted downwards to maintain h=h_{MAX}. This is equivalent to saying that condensation occurs, although the method of removal, particle seeding or

[2]Note that in the real atmosphere, the SVP curve would be altered by at least two factors. Firstly, nitrogen would probably also condense, along with methane, which would lower the condensation altitude level (McKay et al., 1997). Secondly, the SVP calculated here is strictly the saturated vapour pressure over an infinite plane surface of the condensed phase: $e = e_\infty$. In fact, when the condensation occurs onto a droplet or nucleus of some sort, then the SVP must be modified by the Kelvin factor, which accounts for the enhancement in SVP over curved surfaces. However, in this work, the actual microphysical condensation process is not modelled, and hence the droplet size is undetermined, and so e_∞ is used.

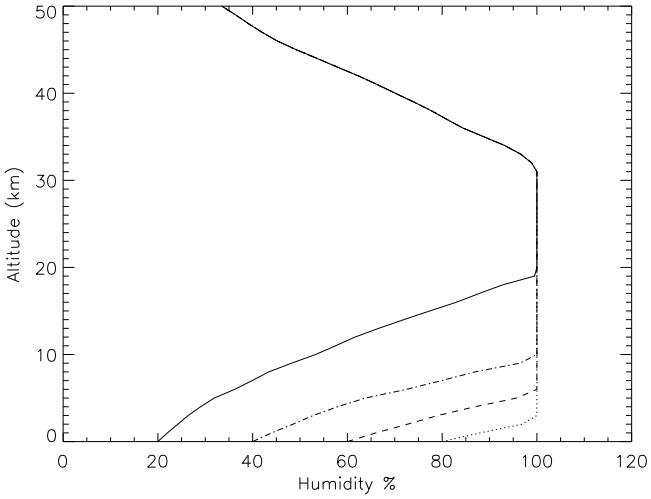

Figure 3.3: Methane humidity variation with height for a range of surface humidity values, as calculated using the simple ascent model described in the text. The saturated region is the altitudes which have 100% humidity.

sizes is not considered here. Eventually, as h drops below h_{MAX} again (the 'cloud top'), the $q_{\mathrm{CH_4}}$ becomes 'frozen out': this is the stratospheric value.

The program was used to calculate approximate levels of saturation for methane in Titan's atmosphere. Figure 3.3 shows the extent of the saturation region for a variety of surface humidity values, but for a fixed h_{MAX} of 100% . Although the altitude of the 'cloud base' varies substantially, the 'cloud top' occurs consistently at 30 km. This happens because, in this model, the partial pressure of methane inside the saturation region is the same in each calculation: it is simply the SVP at that altitude. Hence, the cloud top occurs where the SVP starts to increase again with altitude, irrespective of the starting humidity at the surface.

If we assume that some amount of methane condenses out in Titan's troposphere, then we would expect cloud droplets to form. Depending on amount and distribution, their presence should be observable to some extent, for example on the IRIS infrared spectra. However, if methane condensation were by some method inhibited, then *supersaturation* would occur, and the result would instead be increase in opacity at long wavelengths due to collision-induced absorption (CIA), particularly due to methane molecules. Both

supersaturation and condensation probably occur to some extent.

Measuring the relative importance of these two spectral absorptions, which should enable the relative importance of condensation vs supersaturation in Titan's atmosphere to be determined, has been difficult until recently when new and improved methods of calculating the collision-induced absorption have become available (see 3.2.4). Recent re-analyses of the IRIS dataset with the new spectral data have now been published.

Courtin et al. (1995) have calculated synthetic spectra for the 200–600 cm^{-1} region using several types of tropospheric model, including one with a thin methane cloud of 50 μm-sized droplets, and others where methane was supersaturated but there was no condensate. Comparison with IRIS data suggested that the calculations with the methane cloud failed to reproduce the long-wavelength end of the spectrum, from 200–350 cm^{-1}.

Although Courtin *et al.* were able to force a fit to the IRIS spectrum by decreasing the droplet size considerably, to $\sim$1 μm, the opacity of these drops then became so large in the visible that all sunlight would blocked out, completely incompatible with the observed greenhouse effect, as noted by Toon et al. (1988). Increasing the droplet size had a negligible effect since the relative opacities at 200–350 cm^{-1} and 400–500 cm^{-1} remained about equal.

A more recent study of IRIS data (Samuelson et al., 1997b) and one of the radio occultation data (McKay et al., 1997) also favour a scenario of significant supersaturation, combined with little or no cloud droplets being prevalent in the troposphere.

Two possible methods for supersaturation to exist and persist have been formulated (Courtin et al., 1995; McKay et al., 1997). The first is so-called 'kinetic' inhibition, which takes account of the fact that the likely condensation nucleii, the stratospheric aerosol particles, are relatively insoluble in CH_4 and C_2H_6 (McKay, 1996). An alternative idea is that eddy mixing of gases from the sub-saturated regions near the surface may more effectively transport methane upwards than the condensation process can remove it from the upper troposphere, resulting in a persistent supersaturation. In fact, both

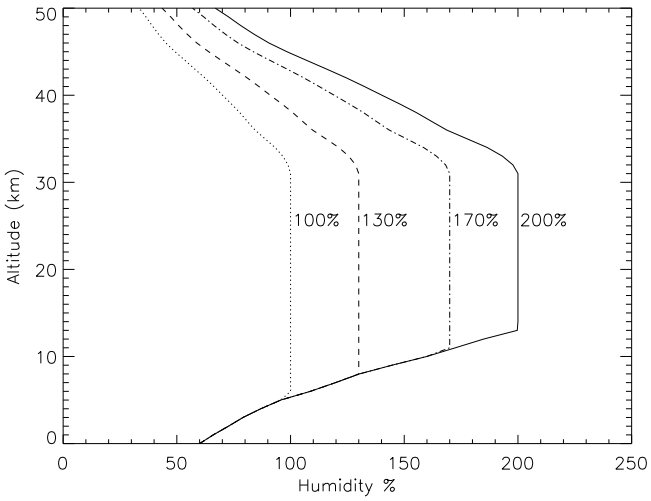

Figure 3.4: Humidity variation with height, where the maximum is allowed to exceed 100%, *i.e.* the methane is supersaturated to some extent. In all cases the surface humidity of CH_4 is 60%.

these processes may have some contribution.

In view of the recent findings, atmospheres with supersaturation ($h_{\rm MAX} > 100\%$) have also been calculated with the cloud model (see figure 3.4). Again, the 'cloud top' occurs near 30 km in each case, the altitude where the mixing ratio of methane would be required to increase again to maintain supersaturation.

Results from the program also indicate that saturated surface air could achieve a 440% supersaturation at the cold trap (30 km) in the total absence of condensation, for an initial $h_{\rm surf}$=60% . However, in many of the calculations presented in this chapter, the supersaturation fraction is less than this maximum possible value (see §3.3).

In these cases, it is implicit that methane condensation occurs, to limit the humidity to an imposed maximum value. However, in view of the evidence that clouds have a negligible effect on the observed spectrum, no cloud particle opacity is included in the spectral model.

CH_3D and N_2

Deuterated methane is treated simply by fixing the ratio of CH_3D to CH_4; the mixing ratio of CH_3D at a given altitude is then just the methane mole fraction times this ratio.

Nitrogen is assumed to constitute the bulk remainder of the atmosphere (along with the minor species), *i.e.* no argon is included in the model.

Gas Profiles

The final gas profiles for the equatorial region are shown in figure 3.5 for a methane maximum humidity of 100% .

3.1.3 Organic Haze Model

It was also necessary to create a quantitative model which describes Titan's stratospheric haze extinction for the radiative transfer calculations. The observed, large scale features of the haze have been outlined in §1.3. Note that, in addition to a distributed haze in the stratosphere, a distinct 'detached' haze layer was seen with a peak brightness at ∼300–350 km (Smith et al., 1981).

It is difficult to study the haze at infrared wavelengths, because there are competing effects such as collision-induced absorption which contribute opacity in the same region. This problem does not occur in the visible. Rages and Pollack (1983) have undertaken a quantitative analysis of a Voyager 2 image taken with a 0.5 μm filter, and inverted the measured radial intensity of the limb to obtain vertical extinction profiles at a range of latitudes 75°S to 75°N (see figure 3.6).

It can be seen that the log extinction per kilometer decreases approximately linearly from 200 to 500 km. Table 3.1 shows the calculation of the extinction per gram of atmosphere at two heights in the stratosphere, which turns out to be relatively constant (i.e. within a factor of two) between these widely-separated levels. As noted by Toon et al. (1992) this implies that the aerosols are almost uniformly mixed across the entire altitude range. This very important fact will be used to simplify the vertical model.

Outline of Method

The optical extinction data of Rages and Pollack (1983) is now analysed to construct

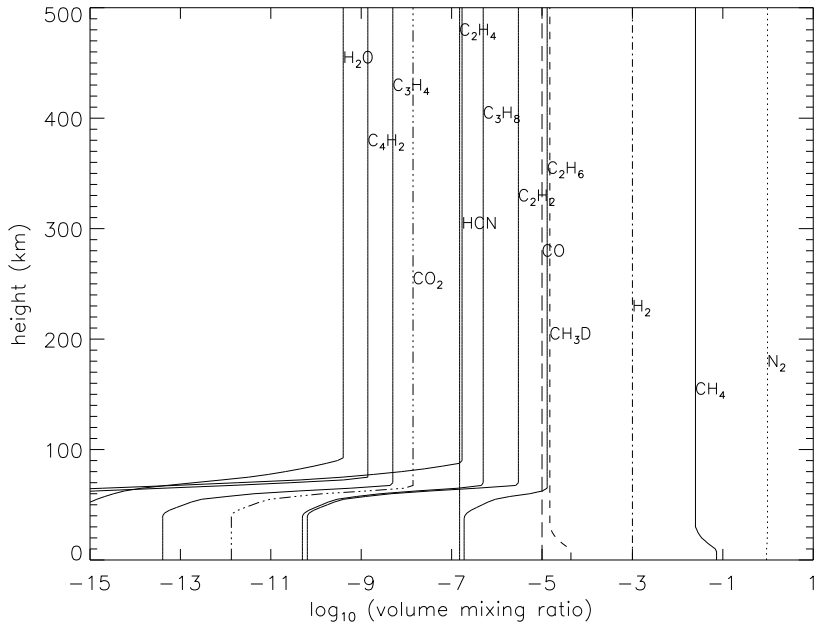

Figure 3.5: Sample A gas profiles (5°N).

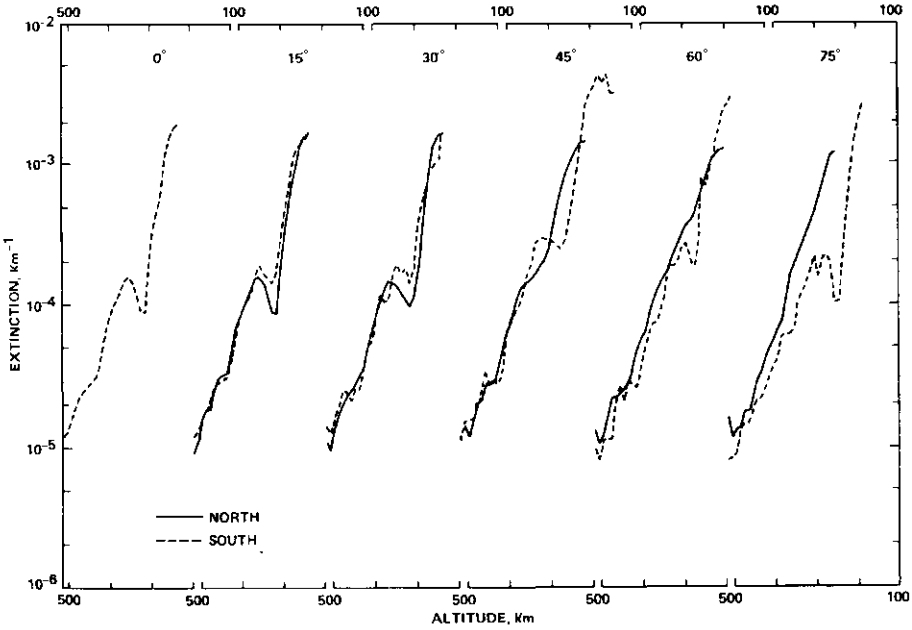

Figure 3.6: A comparison of extinction profiles from corresponding northern and southern latitudes. Extinction at the north pole is notably enhanced over that at the south pole. (After Fig. 5 of Rages *et al.*, (1983).

height z (km)	extinction $\frac{\delta k}{\delta z}$ (cm^{-1} per cm^2 column)	density ρ (g cm^{-3})	$\frac{\delta k}{\delta z}/\rho$ (g^{-1})
270	$\sim 10^{-8}$	3.32×10^{-7}	3.0×10^{-2}
530	$\sim 10^{-10}$	1.78×10^{-9}	5.6×10^{-2}

Table 3.1: The optical (0.5 μm) extinction per gram in the lower and upper stratosphere. This is calculated by dividing the extinction per kilometer at these heights (from Rages and Pollack 1983) by the local mass density.

simple vertical profiles of the stratospheric haze.

The main steps to obtaining a sufficient haze model are as follows. We start with some reasonable *a priori* assumptions about the size, shape and optical nature of the haze particles, which should be based as far as possible on clues from physical and chemical modelling, and on laboratory experiments. We then calculate the expected extinction of a typical haze particle. Finally, we can derive a volume mixing ratio of haze particles from the extinction per kilometer data, by dividing by the extinction per particle. To get the mass mixing ratio we also divide by the atmospheric density ρ.

Several simplifying assumptions are made. Firstly, that the haze particles are spherical, and can be well represented by a single particle size everywhere. It will be shown later that, due to the limited amount of constraining evidence, a single particle size gives a reasonable fit to the data. Secondly, that the haze particles are uniformly mixed in the stratosphere, as indicated by the Rages and Pollack (1983) extinction data. Finally, that the troposphere ($z < 42$ km) is devoid of particles, *i.e.* it is assumed that the aerosols act as condensation nucleii and are largely or totally rained out, or otherwise removed.

Particle Sizes

We wish to replace the distribution $N(r)$ where N is the number density of particles of radius r, with a population of uniform radius r_c which has the same overall extinction. Indeed, the assumption of a 'characteristic radius' reduces the number of free parameters in the model by one, compared to fitting with a Gaussian or log-normal distribution.

Toon et al. (1992) have constructed a detailed model of aerosol size distribution and its variation with altitude, taking into account particle charging effects, grain growth and vertical mixing. They then compared the optical properties of these particles, assumed to be spherical and calculated with Mie theory, against albedo measurements of Titan from the ultraviolet to the infrared. Their conclusion is that the mean particle size of Titan's main haze layer is near 0.15 μm.

This figure is slightly too small to be in agreement with the analysis of Rages and Pollack (1983) and Rages et al. (1983), which requires a single particle radius of 0.2 to 0.5 μm to fit high phase angle observations of Titan. The discrepancy may be explained by the detatched haze layer. A layer of particles which have a larger mean size, above 300 km, could be explained by rising air currents of $w \simeq 1$ cm s^{-1}. An alternative explanation is that the aerosols are asymmetric, possibly fractal in nature (Rannou et al., 1997) in which case a fit could also be made to the data. In this work, spherical aerosol particles of mean radius in the range $0.1 < r_c < 0.4$ μm are considered.

Optical Properties

In order to calculate the haze absorption, we must know the extinction cross section of the particles. This may be calculated theoretically if the refractive index properties of the substance are known.

Titan's haze substance has never been analysed directly, hence there have been numerous attempts to create a similar substance in the laboratory (*e.g.* Khare et al., 1984, 1986; Bar-Nun et al., 1988; Thompson et al., 1991; McDonald et al., 1994; Coll et al., 1995; McKay, 1996). Most of these experiments have attempted to duplicate the effects of cosmic ray irradiation on Titan's bulk atmospheric constituents, N_2 and CH_4, usually by electrical discharge in a pressure vessel.[3] After collection, chemical or physical analysis of the residue, a sticky organic material called *tholin*, is performed.

It is important to bear in mind that there is no single substance called 'tholin' -

[3]With the exception of Bar-Nun et al. (1988) who in a slightly different experiment used UV light on C_2H_2, C_2H_4, and HCN to form polymers.

rather it is an umbrella term applied to all H_x-C_y-N_z residues produced in this manner as analogs to Titan, Triton or Pluto atmospheric hazes. Indeed, the actual composition of the final substance is quite sensitive to the pressure (Thompson et al., 1991) and gaseous composition (McDonald et al., 1994) used in the reaction vessel.

To date, only one of the experiments in the post-Voyager era, due to Khare et al. (1984), has included a wide-range spectroscopic analysis of a tholin. These authors prepared a sample by cold plasma discharge in a simulated Titan atmosphere consisting of a 10% CH_4, 90% N_2 mixture, at standard temperature, and a pressure of 0.2 mbar appropriate to the stratosphere ($\sim$250 km). The substance resulting from this experiment formed a brown film on the inside of the reaction vessel, which was subsequently analysed by gas chromatography/mass spectroscopy (GC/MS) and found to contain over 75 different hydrocarbons and nitriles. Their results also include a determination of the real and imaginary (n, κ) parts of the refractive index in the wavelength range 250 Å–1000 μm.

These measured optical properties have since been widely utilised in atmospheric radiative transfer studies of Titan's atmosphere. McKay et al. (1989) determined the absorption required to fit the geometric albedo at a number of low methane absorption (or 'continuum') points across Titan's visible spectrum. The derived albedo values were found to be qualitatively and quantitatively similar to those of the laboratory tholins of Khare et al. (1984), although to obtain an exact match a scale factor of $\frac{4}{3}$ had to be applied to the tholin imaginary refractive index.

This led McKay et al. (1989) to attempt to fit the Voyager IRIS infrared spectrum from 400–600 cm^{-1} with the tholin properties as well, and found that a closest match was obtained when the imaginary refractive index co-efficient was scaled by a factor $\frac{1}{2}$. In summary therefore, McKay et al. (1989) found that in the visible the laboratory tholins were too bright, and in the thermal infrared they were too dark.

In this analysis, the absorption cross-section is calculated both with and without the scaling factors of McKay et al. (1989). In this way, I can expect to find the result of McKay *et al.* and then check to see whether I require a similar scaling factor, using a

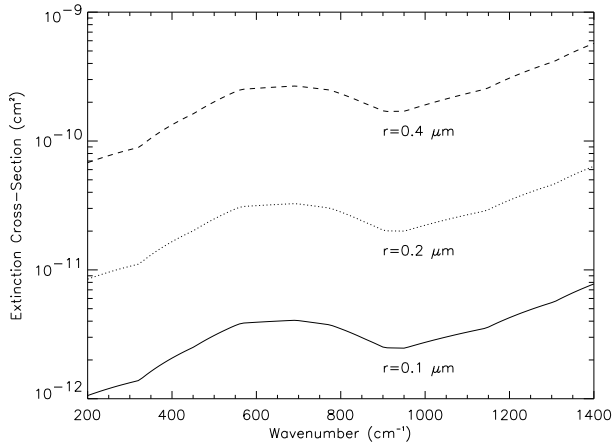

Figure 3.7: The extinction cross-section for tholin particles of various sizes over the IRIS wavenumber range, calculated using Mie theory. The scale factor $X_{\rm IR}$ is here set equal to 1.0, *i.e.* the optical coefficients of Khare *et al.* (1984) are used without the scaling of McKay *et al.* (1989). The effect of the scale factor $X_{\rm IR}$ is to cause a linear change of σ.

different radiative code. The results of are discussed in §3.3.

The wavelength variation of optical properties (Table 1 of Khare et al., 1984) was incorporated into an existing computer code : `Makephase` (Irwin and Calcutt, 1995). This code uses the Mie theory to calculate the extinction cross-section $\sigma(\lambda)$, which is the sum of a particle's scattering $\sigma_{\rm s}$ and absorption $\sigma_{\rm a}$ cross-sections, and the single scattering albedo $\omega(\lambda)$ over a specified wavelength range, given the particle size or size distribution. Figure 3.7 shows the variation of tholin σ across the IRIS wavenumber range for several typical particle sizes.

Aerosol Profiles

The extinction cross-section (σ), or extinction per particle can now be used to derive the number of particles per gram of atmosphere at a particular height, by dividing the extinction per gram by σ:

$$\frac{N}{\rho(z)} = \text{number/gram} = \frac{1}{\rho(z)\sigma(r_{\rm c})}\frac{\delta k}{\delta z}(z) \tag{3.2}$$

For $r_{\rm c}$=0.2 μm, σ=5.24$\times 10^{-9}$ cm^2 at 500 nm, and using $(\delta k/\delta z)$ from table 3.1, the

1	2	3	4	5	6
r_c (μm)	σ at 0.5 μm (cm^2)	particles/g at 270 km	particles /column	σ at 600 cm^{-1} (cm^2)	χ at 600 cm^{-1}
0.10	3.33×10^{-10}	9.01×10^{7}	1.433×10^{11}	1.97×10^{-12}	0.282
0.15	2.05×10^{-9}	1.46×10^{7}	2.455×10^{10}	6.65×10^{-12}	0.163
0.20	5.24×10^{-9}	5.73×10^{6}	9.755×10^{9}	1.58×10^{-11}	0.154
0.25	8.52×10^{-9}	3.52×10^{6}	5.773×10^{9}	3.10×10^{-11}	0.179
0.30	1.02×10^{-8}	2.94×10^{6}	4.977×10^{9}	5.38×10^{-11}	0.268
0.35	1.03×10^{-8}	2.91×10^{6}	4.927×10^{9}	8.58×10^{-11}	0.423
0.40	1.07×10^{-8}	2.80×10^{6}	4.479×10^{9}	1.29×10^{-10}	0.578

Table 3.2: Calculation of infrared column optical depth from 0.5 μm extinction data, for Titan's equator (Sample A). Column 3 is obtained by dividing the extinction per gram (fixed at 3×10^{-2}) by the σ at $\lambda = 0.5$ μm (column 2). Column 6 is obtained by multiplying together the two preceding columns.

number of particles per gram is $\sim 5.73\times10^{6}$ at 270 km. If we assume a density of 1 gcm^{-3} for the particles, this corresponds to a mass mixing ratio $q_m \sim 2\times10^{-7}$.

At this stage a further approximation is made; that the stratospheric mass mixing ratio of aerosol $q_m(z)$ is everywhere equal to the 270 km value $q_m(z{=}270$ km). In other words because the aerosol appears to be approximately uniformly mixed, as described earlier, the mid-stratosphere value is taken to be typical. The error introduced by this approximation is at most a factor 2 in overall opacity (by considering table 3.1), which will hence have a factor 2 effect on the derived extinction per particle (all particles are identical). However, it can readily be seen from figure 3.7 that an order-of-magnitude estimate of extinction per particle is sufficient to distinguish between a particle of $r{=}0.1$ μm and one of $r{=}0.2$ μm, so the crudeness of the model is justifiable, in view of the much greater simplicity of having uniform mixing.

A number of different aerosol profiles were created based on varying the value of r_c, deriving the particle concentration each time from the optical extinction and the calculated $\sigma(0.5$ μm) (see table 3.2 and figure 3.8).

Scattering Considerations

Before carrying out spectral synthesis calculations involving aerosols, it is important to consider whether the particles can be treated as simple thermal absorbers/emitters,

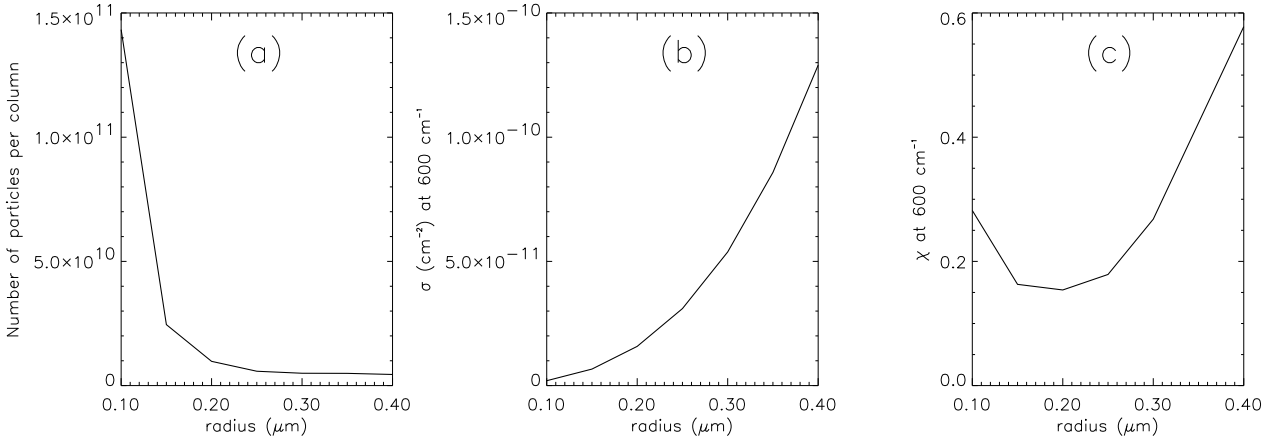

Figure 3.8: (a) plot of particles per column; (b) plot of extinction cross-section per particle at 600 cm^{-1}, and (c) plot of extinction per column at 600 cm^{-1}, *i.e.* the product of (a) and (b), as a function of particle radius. Column atmospheric density is equatorial (Sample A).

or whether scattering needs also be taken into account. The parameter which determines this is the single scattering albedo, which is defined as the ratio of the scattering cross-section to the total extinction cross-section:

$$\omega = \frac{\sigma_{\mathrm{s}}}{\sigma_{\mathrm{a}} + \sigma_{\mathrm{s}}}. \tag{3.3}$$

Therefore as $\omega \to 0$, scattering can neglected, but as $\omega \to 1$ scattering becomes increasingly important. However, the final impact of scattering on the spectrum also depends on the scattering angle. For example, if most of the radiation is being scattering out of the forward direction, then although ω may be high, it would still be sufficient to treat the particles as simple absorbers, using the appropriate absorption cross-section.

Using the complex refractivity data of Khare *et al.*, the `Makephase` program was used to calculate ω for tholin particles of a given size. Figure 3.9 shows the variation in ω for three typical particle sizes across the entire wavelength range for which refractivity has been determined.

Several important points can be gleaned from figure 3.9. Firstly, a small change in particle size can make a large difference to ω. In particular, longward of 3 μm, doubling

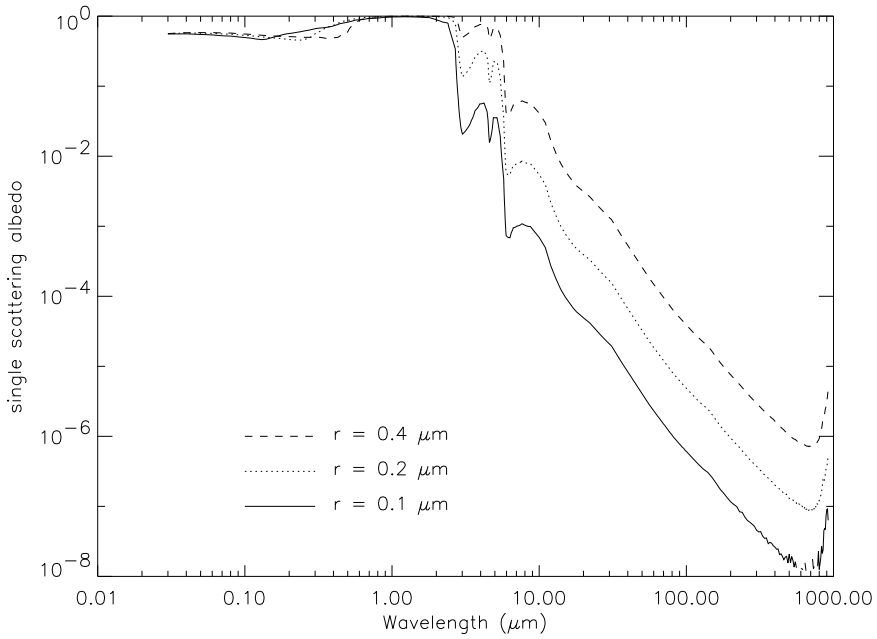

Figure 3.9: The variation with wavelength of the single scattering albedo (ω) for tholin particles of different radii. ω calculated using Mie theory for the tholin refractive index properties as measured by Khare *et al.* (1984).

the particle radius increases ω by up to an order of magnitude. Secondly, the overall trend is for high ω at optical wavelengths, when $\lambda \sim r$, but small ω when $\lambda >> r$. The transition region occurs when $1 < \lambda < 10$ μm.

In summary, when carrying out a spectral synthesis in the IRIS (200–1400 cm^{-1}) or CIRS (10–1400 cm^{-1}) ranges, it will normally be acceptable to ignore scattering (*i.e.* $\omega \leq 0.03$ for $r \leq 0.4$ μm and $\lambda \geq 6$ μm).

3.2 Radiative Transfer Code

This section describes the radiative transfer code `Radtran` which was used to generate synthetic Titan spectra. `Radtran` was developed in Atmospheric Physics at Oxford, principally by S. Calcutt and P. Irwin, and has been previously used successfully to model the atmosphere of the Jupiter for interpretation of IRIS and Galileo NIMS data (Irwin et al., 1997). However, before it could be applied to Titan, several important extensions were required, which were implemented by this author. In particular, the

treatment of collision-induced absorption (CIA) by the code was extended to include nitrogen and methane (§3.2.4).

3.2.1 Radiative Transfer in the Infrared

Radiative transfer in the infrared is governed by Schwarzchild's equation:

$$\frac{dI_{\tilde{\nu}}}{d\chi_{\tilde{\nu}}} = I_{\tilde{\nu}} - J_{\tilde{\nu}} \tag{3.4}$$

where $I_{\tilde{\nu}}$ is radiance and $J_{\tilde{\nu}}$ is the source term, both in units of W cm^{-2} sr^{-1} /cm^{-1}, and the increment of opacity is defined by:

$$d\chi_{\tilde{\nu}} = -k_{\tilde{\nu}}\rho_{\mathrm{a}}(z)dz \tag{3.5}$$

where $k_{\tilde{\nu}}$ is the absorption coefficient, ρ_{a} is the density of the absorber and z is the height above the surface. Note that χ has opposite sign to z. Normally there will be several different terms compounding the absorption, from lines, particles, and continuum opacity, as described below. The $\tilde{\nu}$ subscript for wavenumber will be implicit from here on. Equation 3.4 integrates to:

$$I_{\infty} = \int_0^{\infty} Je^{-\chi}d\chi \tag{3.6}$$

for an optically thick slab of atmosphere, where I_{∞} is the radiance seen at the top of the atmosphere. However, if the atmosphere is optically thin at any wavelengths we must include a contribution for emission from the surface. Defining $\tau_z = \exp(-\chi_z)$ to be the transmission to a level z, and including terms to represent surface emission and reflected atmospheric emission, equation 3.6 becomes:

$$I_\infty = \int_0^\infty J \frac{d\tau(\infty, z)}{dz} dz + \epsilon_s B_s \tau_s + (1 - \epsilon_s)\tau_s \int_\infty^0 J \frac{d\tau(0, z)}{dz} dz \tag{3.7}$$

where τ_s is the transmission from the surface to the top of the atmosphere, and the planetary surface is assumed to emit as a blackbody with an emissivity ϵ_s.

Usually, the atmospheric source function J is also taken to the Planck function, when Local Thermodynamic Equilibrium (LTE) applies in the atmosphere. Also, in all calculations for Titan's atmosphere in this work, the surface emissivity in the infrared is assumed to be unity, so the third term in 3.7 vanishes.

3.2.2 Numerical Integration over Path

The atmospheric model consists of a profile, which specifies the temperature, pressure and mixing ratios of all radiatively active gases over a range of altitudes. The creation of the profile has been described in §3.1. In order to compute equation 3.7 for an optical path in the atmosphere, the first step is to divide the atmosphere into layers.

Layers are equally spaced either in Δz (height), Δp (pressure), or $\Delta \log p$ (log pressure). The latter normally gives the most accurate results, because the layers are more closely spaced (in z) where the pressure and hence density of absorbers is changing most quickly, lower in the atmosphere, and further apart higher in the atmosphere where the pressure and opacity are changing more slowly. For the calculations in this chapter, 40 layers equally spaced in log pressure are used, a resolution equal to about a third of one scale height. This was found to be sufficient, *i.e.* the use of more layers produced a negligible effect on calculated radiance. Having split the atmosphere into equal log pressure layers, the altitudes of the top and bottom of each layer, and the thickness of each layer, were calculated in kilometers, z being the variable used in the integration.

The first step in the calculation is to compute the opacity from the top of the atmosphere to the bottom of each layer. Following from equation 3.5, the optical thickness

of the first (top) layer is:

$$\Delta\chi_1 = \sum_i (k_\mathrm{a} q_\mathrm{m}(z_1))_i \cdot \rho(z_1)\Delta z_1 \tag{3.8}$$

where the summation is over all sources of opacity in the layer. The density of absorbers is defined by: $\rho_\mathrm{a}(z_1) = q_\mathrm{m}(z_1) \cdot \rho(z_1)$, the mass mixing ratio of the species times the atmospheric density. Note that z_1 is taken to mean the altitude of the middle of the layer, and $q_\mathrm{m}(z_1)$ and $\rho(z_1)$ are the mean properties of that layer, calculated by an integral average.

In general the opacity from the n^{th} layer to the top is:

$$\chi_n = \sum_{i=1}^{n} \Delta\chi_i \tag{3.9}$$

Hence the radiance at the top of an atmosphere of N layers is the discrete version of equation 3.7:

$$I_\infty = B_s\tau_N + \sum_{n=1}^{N} B_n\tau_n \tag{3.10}$$

where $\tau_n = \exp(-\sum_{i=1}^{n}\Delta\chi_i)$.

It is now appropriate to consider how the calculation varies over frequency (wavenumber). `Radtran` divides up the frequency range into bins of equal width $\Delta\tilde{\nu}$. Then the opacity in each bin is calculated separately by equation 3.9 for each layer. The three sources of opacity are now discussed.

3.2.3 Spectral Lines

When a molecule interacts with the radiation field, either by absorption or emission of a photon, a spectral line results. Infrared spectral bands are groups of lines, which occur either due to pure rotational, or roto-vibrational transitions in a molecule. In the latter case, a rotational band structure is seen on either side of a central vibrational frequency. The quantum mechanical theory of molecular band spectra has been set out clearly in many textbooks (for example Atkins, 1983) and so is not described here.

However, it is relevant to discuss how the shape and strength of these lines may be quantified, for the purpose of numerical calculations. Any spectral line can be modelled by a magnitude or normalisation (the line strength) times a function (the line shape):

$$k_{\tilde{\nu}} = S.f(\tilde{\nu} - \tilde{\nu}_0) \tag{3.11}$$

where $\tilde{\nu}_0$ is the central frequency of the transition and the line strength S is defined as the integration of the line absorption co-efficient over all wavenumbers:

$$S(\tilde{\nu}_0) = \int_0^\infty k_{\tilde{\nu}} d\tilde{\nu}. \tag{3.12}$$

Line Shapes

Spectral 'lines' are not monochromatic, but have a shape and a finite width, collectively known as the line broadening. Broadening occurs due to three main processes: 'natural' broadening due to the Uncertainty Principle of quantum mechanics; thermal broadening due to the Doppler effect on frequency of the molecule's thermal motion; and pressure or Lorentz broadening due to collisions with other molecules.

Of these three effects, the first is always negligible in atmospheres in comparison to the other two, one of which is usually dominant depending on the temperature and

pressure regime. The shape of a Doppler line is described by;

$$f_{\mathrm{D}}(\tilde{\nu}) = \frac{S}{\sqrt{\pi}\alpha_{\mathrm{D}}} \exp\left[-\left(\frac{\tilde{\nu}-\tilde{\nu}_0}{\alpha_{\mathrm{D}}}\right)^2\right] \tag{3.13}$$

and that of a Lorentz line by:

$$f_{\mathrm{L}}(\tilde{\nu}) = \frac{S}{\pi}\frac{\alpha_{\mathrm{L}}}{(\tilde{\nu}-\tilde{\nu}_0)^2+\alpha_{\mathrm{L}}^2}, \tag{3.14}$$

where α_{L} and α_{D} are the half-widths due to Lorentz and Doppler broadening respectively. The Doppler width of a line depends on temperature and the mean molecular mass according to:

$$\alpha_{\mathrm{D}} = \frac{\tilde{\nu}_0}{c}\left(\frac{2\mathrm{R_g}T}{M_{\mathrm{r}}}\right)^{\frac{1}{2}} \tag{3.15}$$

while the Lorentz width of the line varies with temperature and pressure according to:

$$\alpha_{\mathrm{L}}(T,p) = \alpha_{\mathrm{L0}}\left(\frac{p}{p_0}\right)\left(\frac{T}{T_0}\right)^{-\gamma} \tag{3.16}$$

where the subscript 0's refer to S.T.P. The coefficient γ is the temperature dependence of width parameter, and is measured experimentally and tabulated for individual lines.

Figure 3.10 shows the changing Doppler and Lorentz half-widths for a typical line ($\alpha_{\mathrm{L0}} = 0.1$ cm^{-1}) for the ascent of a Titanian equatorial T–p profile. The altitude at which thermal broadening becomes dominant is around 115 km.

When both effects are important, a combined lineshape is observed. Providing the two mechanisms are uncorrelated and line coupling is negligible, this is a convolution of

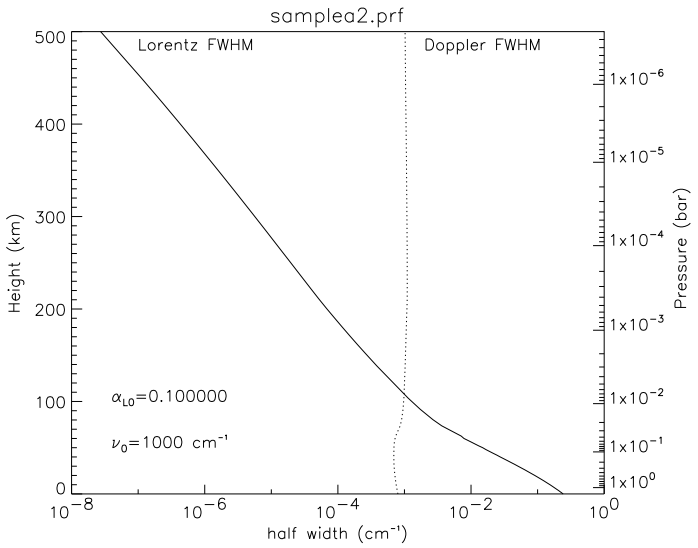

Figure 3.10: Comparison between the Doppler (thermal) and Lorentz (pressure) half-widths of a line in Titan's atmosphere at various altitudes. The cross-over point is 115 km.

the Doppler and Lorentz lineshapes:

$$f_{\mathrm{V}}(\tilde{\nu}-\tilde{\nu}_0) = \frac{1}{\alpha_{\mathrm{D}}}\frac{y}{\pi^{3/2}}\int_{-\infty}^{+\infty}\frac{\exp(-t^2)}{(x-t)^2+y^2}dt \tag{3.17}$$

where $x = (\tilde{\nu}-\tilde{\nu}_0)/\alpha_{\mathrm{D}}$ and $y = \alpha_{\mathrm{L}}/\alpha_{\mathrm{D}}$. This function, called the Voigt profile is commonly used for middle atmosphere calculations on the Earth and is used in `Radtran` for Titan atmosphere calculations. It has no analytic solution and so must be evaluated numerically.

Line database

In order to compute the line profile numerically, the strength and the parameters affecting the lineshape must be known for each individual line in the spectrum.

Several projects around the world have worked to create line parameter lists which are specially suited for numerical calculations of atmospheric radiative transfer. The two largest such publicly available databases are HITRAN, compiled by the Airforce Geophysical Laboratory (AFGL) in the USA, and the GEISA compendium due to the

wavenumber (cm^{-1})	species	transition	comments
220	C_4H_2	ν_9	
233	C_2N_2	ν_5	$l \geq 50°$ only
328	C_3H_4	ν_{10}	
499	HC_3N	ν_6	$l \geq 50°$ only
628	C_4H_2	ν_8	blended with ν_9 C_3H_4
633	C_3H_4	ν_9	blended with ν_8 C_4H_2
663	HC_3N	ν_5	$l \geq 50°$ only
667	CO_2	ν_2	
713	HCN	ν_2	
729	C_2H_2	ν_5	
748	C_3H_8	ν_{21}	
821	C_2H_6	ν_9	
950	C_2H_4	ν_7	
1161	CH_3D	ν_6	contribution from ν_7 and ν_{21} C_3H_8
1270	CH_4	ν_4	P-branch
1304	CH_4	ν_4	Q-branch
1330	CH_4	ν_4	R-branch

Table 3.3: The principal distinguishable bands seen on IRIS spectra.

Laboratoire de Meteorologie Dynamique du CNRS in France. Of the two, the GEISA database is more suited to non-terrestial atmospheric calculations, including Titan, as it contains more complete listings for certain gases which are found on the other planets.

The latest version, GEISA 97 is used in this study. The only modification to this database was the inclusion of additional parameters for the C_3H_4 ν_9 band at 633 cm^{-1} (Graner and Wagner, 1990). The main bands which contribute to the IRIS spectrum are listed in table 3.3.

The most important parameters in the database for each line of a given gaseous isotope are:

$\tilde{\nu}_0$	the line rest frequency (in cm^{-1}),
S	the line strength (in cm^{-1}/ (molecule cm^{-2})),
$\alpha_L(p_0, T_0)$	the Lorentz half-width at S.T.P. (cm^{-1}/atm),
E_l	lower state energy in cm^{-1},
γ	the exponent for temperature dependence of Lorentz line width.

Lines in Radtran

`Radtran` treats lines in the following way. The data for all lines of the appropriate molecules, for the entire wavenumber range of the calculation, are read into memory by the program at run-time.

Consider a bin from $\tilde{\nu}_1$ to $\tilde{\nu}_2$, where $\tilde{\nu}_2 - \tilde{\nu}_1 = \Delta\tilde{\nu}$. The absorption of all lines which have a centre frequency falling into the range $\tilde{\nu}_1 < \tilde{\nu}_c < \tilde{\nu}_2$ is calculated within the bin and added to the overall absorption. Because the calculation of the Voigt profile is computationally costly, the Voigt function is only evaluated within a central width (described by the parameter WING in `Radtran`). Outside of this region, the line shape is estimated by a quadratic function which approximates the far line wings.

In addition, nearby lines from outside the bin may have wings which contribute significant opacity, especially for strong lines. A further parameter $\Delta\tilde{\nu}_{\rm w}$ ('VREL' in `Radtran`) describes how far outside each bin to calculate contributions from far wings. The overall opacity of the bin due to lines is hence:

$$\chi_1(z_n, \tilde{\nu}_0) = \sum_{i=1}^{N_{\rm g}} \left[\sum_{\tilde{\nu}_{\rm c}} \left\{ S_i(\tilde{\nu}_{\rm c}) \int_{\tilde{\nu}'=\tilde{\nu}_1}^{\tilde{\nu}_2} f_i(\tilde{\nu}' - \tilde{\nu}_c) d\tilde{\nu}' \right\} \right] \cdot \rho_{{\rm a}i}(z_n) \Delta z_n \qquad (3.18)$$

where $N_{\rm g}$ is the number of gases, and $\tilde{\nu}_{\rm c}$ is the line centre wavenumber for each line, which takes discrete values in the range $\tilde{\nu}_1 - \Delta\tilde{\nu}_{\rm w}$ to $\tilde{\nu}_2 + \Delta\tilde{\nu}_{\rm w}$. Also $\rho_{{\rm a}i} = q_{{\rm m}i}\rho$, the product of the mass mixing ratio of the $i^{\rm th}$ gas times the density of the atmosphere (at a given height, z_n). $q_{{\rm m}i}$ for each gas is related to the volume mixing ratio by: $q_{{\rm m}i} = q_{{\rm v}i} \cdot (M_{{\rm r}i}/M_{\rm r})$. Equation 3.18 must be evaluated for each layer in the model.

3.2.4 Collision-Induced Absorption

A second important source of opacity in Titan's atmosphere is the pressure-induced or collision-induced absorption (PIA or CIA) of gaseous molecules in the far-infrared.

When two non-polar molecules collide, a transient dipole may be induced in one part-

ner by the permanent quadrupolar or higher order moment of the other. This dipole then allows temporary interaction with EM radiation. Participating molecular pairs may be 'free' (collisional complexes) or bound (van der Waals dimers) and undergo bound-bound, bound-free or free-free transitions between rotational or translational states. Due to the short lifetime of these states, the corresponding energy bands are wide, in accordance with the Uncertainty Principle.

In Titan's atmosphere, all the main atmospheric molecules: N_2, CH_4, H_2, and probably also atomic argon, contribute significant CIA absorption longward of 600 cm^{-1}, forming ten possible interaction pairs. Argon is not considered in this work, which reduces the interactions to six pairs.

CIA Data

A. Borysow and collaborators have undertaken a large project to compute exact quantum mechanical lineshapes for all the significant pair interactions in Titan's atmosphere, based on two functions of intermolecular separation; namely potential and induced dipole moment. For the first time dimer features were considered and accurate temperature dependence of line strength was included.

Because the computation of exact line shapes is very computationally intensive, Borysow *et al.* have reduced their results in each case to a six-parameter 'EBC' model, which has the same functional form but different parameters for each molecular pair. `FORTRAN` routines have kindly been provided by Ms. Borysow which calculate the absorption for a given temperature, pressure and frequency range (see table 3.4).

As can be seen from figure 3.11, the N_2–N_2 absorption dominates the opacity at frequencies below 100 cm^{-1}; from 150–500 cm^{-1} the opacity of N_2–CH_4 dominates, and above 550 cm^{-1} N_2–H_2 becomes the major opacity source. The region from 400–600 cm^{-1} is sometimes known as the 'window region', where the opacity is lower than at higher and lower wavenumbers to either side.

Pair	Temp. Range (K)	Model Reference
N_2–N_2	50–300	Borysow and Frommhold (1986a)
N_2–CH_4	70–300	Borysow and Tang (1993)
CH_4–CH_4	50–300	Borysow and Frommhold (1987)
N_2–H_2	50–300	Borysow and Frommhold (1986b)
CH_4–H_2	50–300	Borysow and Frommhold (1986c)
H_2–H_2 ν_0	40–300	Borysow et al. (1985)
H_2–H_2 ν_1	20–350	Borysow (1991); Meyer et al. (1989)
		Borysow (1993)
H_2–H_2 ν_2	20–500	Meyer et al. (1993); Zheng and Borysow (1995)

Table 3.4: Borysow Models.

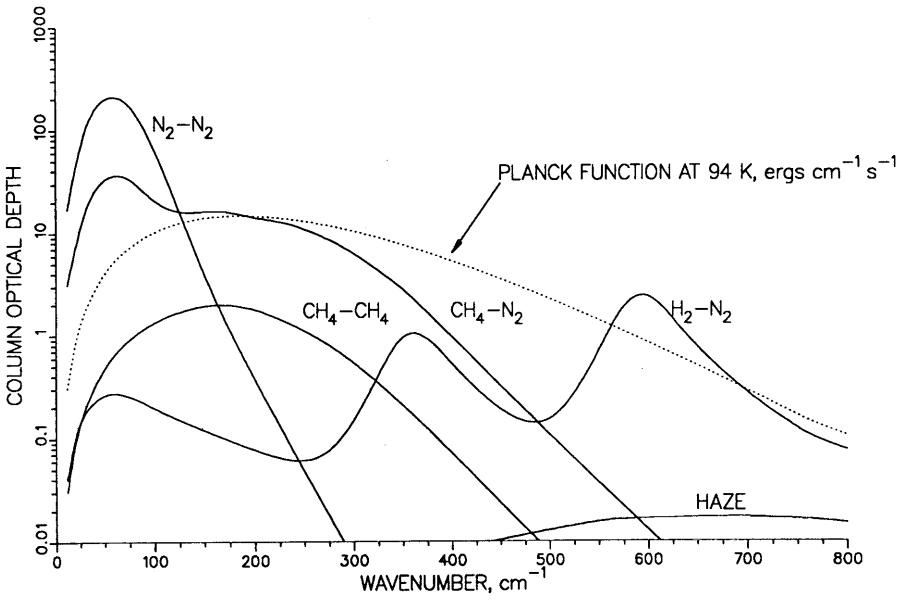

Figure 3.11: Optical depth in the far-infrared due to collision-induced absorption for Titan's atmosphere. The 400–600 cm^{-1} region of low opacity is the infrared 'window'. (Reproduced from Borysow and Tang, 1993).

CIA Treatment in Radtran

As part of the work for this thesis, the CIA routines of Borysow and collaborators were incorporated into `Radtran`. In order to speed up the spectral calculation, the absorption $\alpha(\tilde{\nu})$ in units of cm^{-1}/ amagat^{-2} is pre-computed for all the molecular species over a wide range of temperatures and pressures. This is the CIATABLE. When the spectral code runs, it then performs an interpolation for the exact temperature, pressure and mixing ratios for the layer centre and scales the absorption accordingly:

$$\chi_{\rm c}(z_n, \tilde{\nu}) = \sum_{i,j} (\alpha_{ij}(\tilde{\nu}) q_{{\rm v}i} q_{{\rm v}j}) \left(\frac{p(z_n)}{p_0}\right)^2 \left(\frac{T_0}{T(z_n)}\right)^2 \Delta z_n \tag{3.19}$$

where $\chi_c(z_n)$ is the CIA opacity of the $n^{\rm th}$ layer, which has thickness Δz_n; $q_{{\rm v}i}$ is the volume mixing ratio of the $i^{\rm th}$ gas, and $i = 1, 3$ and $j = 1, 3$ signifying N_2, H_2, and CH_4; and α_{ij} is the absorption of the $(i, j)^{\rm th}$ pair combination.

3.2.5 Treatment of Opacity due to Particles

The derivation of a haze model has already been described (§3.1.3). The haze properties, including the absorption cross-section variation with frequency of a single particle are pre-calculated in advance using the `Makephase` code.

When `Radtran` runs, the absorption due to particles in each layer is then simply the absorption due to each particle times the column number density of the particles (in the absence of scattering):

$$\chi_{\rm p}(z_n, \tilde{\nu}) = \sigma(\tilde{\nu}) N(z_n) \Delta z_n \tag{3.20}$$

where $N(z_n) = q_{\rm m}(z_n)\rho(z_n)$. Note that σ is independent of T and p.

3.3 Comparison of Model Runs with IRIS Data

The model is now compared to the equatorial sample A spectrum of Coustenis and Bézard (1995). This study has concentrated on the equatorial spectrum, because the measured (radio-occultation) tropospheric T–p profile is representative of the equatorial regions, and so the model is expected to be capable of a good fit to the data over the entire IRIS range of 200–1400 cm^{-1}.

For other latitudes, although spectra were measured by IRIS, there were no radio occultation measurements from which to derive the low-level temperature profile. This means that the 200–600 cm^{-1} spectral region, which sounds CIA in the troposphere could not be modelled, although in principle the 600–1400 cm^{-1} spectral region could be modelled using a stratospheric temperature profile derived from the ν_4 CH_4 band. This was not attempted in the present work, but would form a possible area of further work (see Chapter 7).

The atmospheric model described above has several variable parameters: the radius r of the stratospheric haze particles, the surface humidity h_{surf} and maximum humidity h_{max} (or supersaturation fraction, $s = h_{\mathrm{max}}/100$) in the troposphere. These are the parameters which were manipulated in order to optimise the model-data agreement.

In principle, the physical profile of temperature and pressure, and the VMRs of the minor gases are also variable parameters. However, both the physical and VMR profiles were derived by Coustenis and Bézard (1995) from the analysis of the exact same data, and so, even allowing for differences in the atmospheric model used, these parameters should already be close to optimal.

In addition, there are the two scaling factors, X_{vis} and X_{IR}, as first introduced by McKay et al. (1989) which scale the imaginary co-efficient of refractive index in the visible and IR respectively from the tholin values of Khare et al. (1984). In this study, both models with the original tholin k and models with the adjusted k are computed and then compared.

The calculation parameters in the radiative transfer code were all held constant. The atmosphere was divided into 40 layers, by equal increment of $\log p$. The zenith angle was 14°, which is the mean angle of the sample A spectrum. All models were calculated with a bin size and resolution of 1 cm^{-1}, and then smoothed to the nominal IRIS resolution of 4.3 cm^{-1} with a triangular function of that FWHM.

3.3.1 Humidity and Saturation of CH_4

Assuming that opacity in the spectral region 200–400 cm^{-1} due to stratospheric aerosols is small, then the continuum level is largely due to the collision-induced absorption of molecules. The principle absorption is due to CH_4–N_2 pairs, with a smaller contribution from CH_4–CH_4 and N_2–H_2 pairs . This spectral region can therefore be used to constrain the amount of methane in model calculations. Note that the hydrogen mole fraction is fixed at 0.1% and the nitrogen abundance is simply $1 - q_{CH_4} - q_{H_2}$.

In the model calculations, the amount of methane in the troposphere is controlled by two parameters: the surface humidity h_{surf}, and the maximum humidity h_{max}. Then the mole fraction of methane at each altitude is determined by the vapour pressure curve.

The surface humidity value was taken to be 60%, which has been indicated on the basis of a re-analysis of the radio occultation measurements (McKay et al., 1997). Figure 3.12 then shows the effect on the computed spectrum of varying h_{max} from 100 to 200%.

The model-data comparison indicates that a supersaturation fraction of 1.25–1.50 gives the closest match to the data.

3.3.2 Haze Particles

The tropospheric model was now fixed with h_{surf} =60% and h_{max} =150% , and the stratospheric haze added to the calculation. The spectral region 400–600 cm^{-1}, which has low opacity due to molecular collisions (the thermal 'window' region), was now used to constrain the haze model. The haze particle size was varied between 0.1 and 0.3

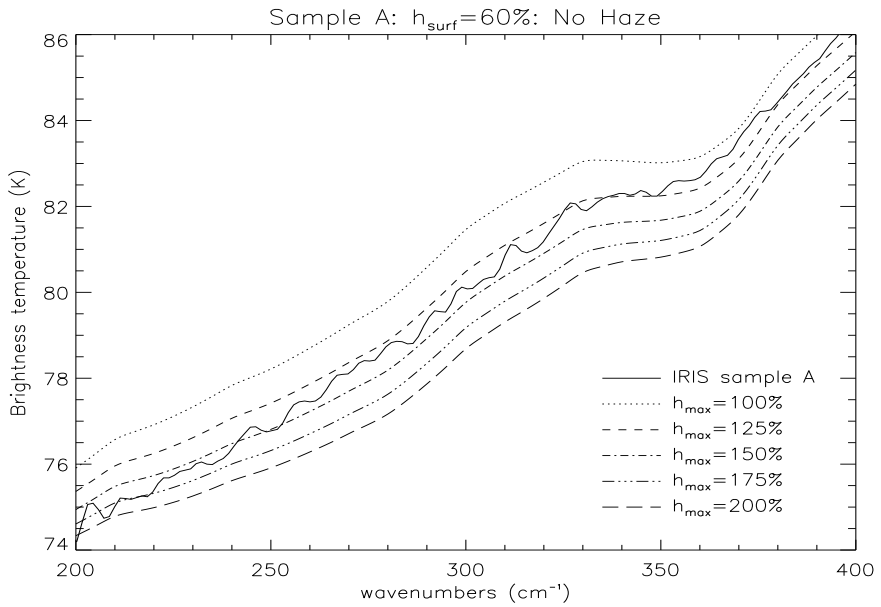

Figure 3.12: Comparison of IRIS Sample A spectrum to tropospheric supersaturation models. Surface humidity $h_{\rm surf}$=60% in all cases, and there is no stratospheric haze.

microns. Note that because the opacity per km is held constant according to the Rages and Pollack (1983) data, this means that as the particle size increases, the mass mixing ratio $q_{\rm m}$ decreases.

Figure 3.13 shows the model-data comparison, where the optical co-efficients are those measured for laboratory tholins by Khare et al. (1984). Note that the spectrum decreases in brightness as $r_{\rm c}$ increases from 0.1 to 0.2, and then increases in brightness again from $r_{\rm c}$=0.2 to $r_{\rm c}$=0.3. This corresponds to a decrease and then increase in the column extinction (*c.f.* figure 3.8 (c)). At the minimum, we see deepest into the atmosphere towards the tropopause.

This figure may be compared to figure 3.14, which is the same except that the scaling of the imaginary refractive index as recommended by McKay et al. (1989) has been used to derive the haze $q_{\rm m}$ from the Rages and Pollack (1983) data and compute the optical depth in the IR. Again, the absorption has a minimum at $r_{\rm c} = 0.2$ μm. However, the agreement between the model and the data is now improved.

It is important to remember that the laboratory tholins are not expected to give an exact fit to the data, yet it remains surprising that they approximate the Titan

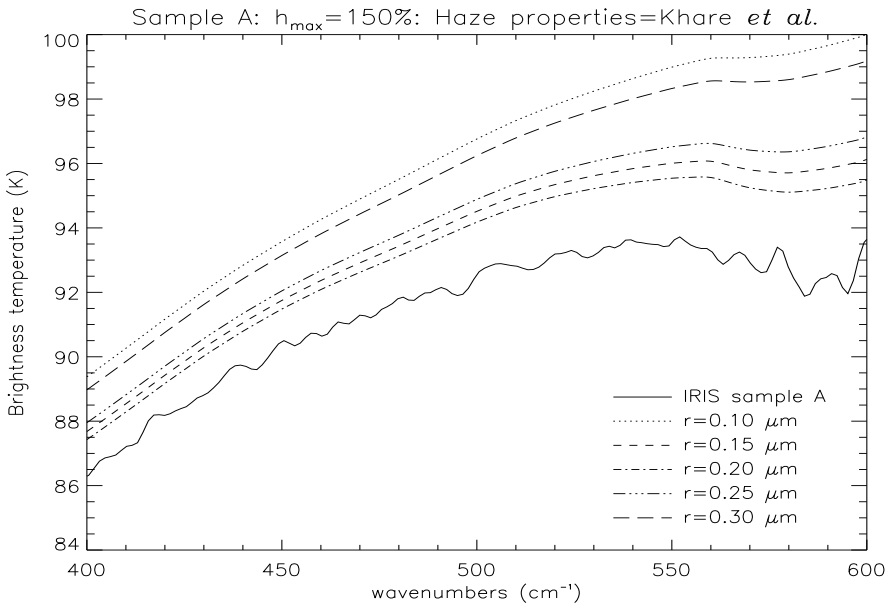

Figure 3.13: Comparison of IRIS Sample A spectrum to haze models with measured laboratory tholin optical properties (Khare *et al.* 1984). $h_{\rm surf} = 60\%$ and $h_{\rm max} = 150\%$.

stratospheric haze in this spectral region so well. The conclusion of this study is that the McKay et al. (1989) scaling tends to improve the agreement.

3.3.3 Rotational Bands

Figure 3.15 compares a model calculation to the sample A data over the entire IRIS range. The nominal mole fractions of the minor gases from Coustenis and Bézard (1995) have been used, along with the derived supersaturation $h_{\rm max} = 150\%$ and the $r_{\rm c}$=0.2 μm haze model with the McKay et al. (1989) optical scaling.

For most of the molecular bands, including the prominent bands of CH_4 ν_4, CH_3D ν_6, C_2H_2 ν_5, and HCN ν_2, a close fit to the data has been achieved. There appears to be two main discrepancies remaining. Firstly, the isolated C_3H_4 band centred on 633 cm^{-1} is underestimated.

Secondly, the entire region from 730–1100 cm^{-1} has too little opacity. The most likely explanation for this is that the continuum opacity, due to the aerosols, is too weak. This is hardly surprising, because the optical properties of laboratory tholins used in these

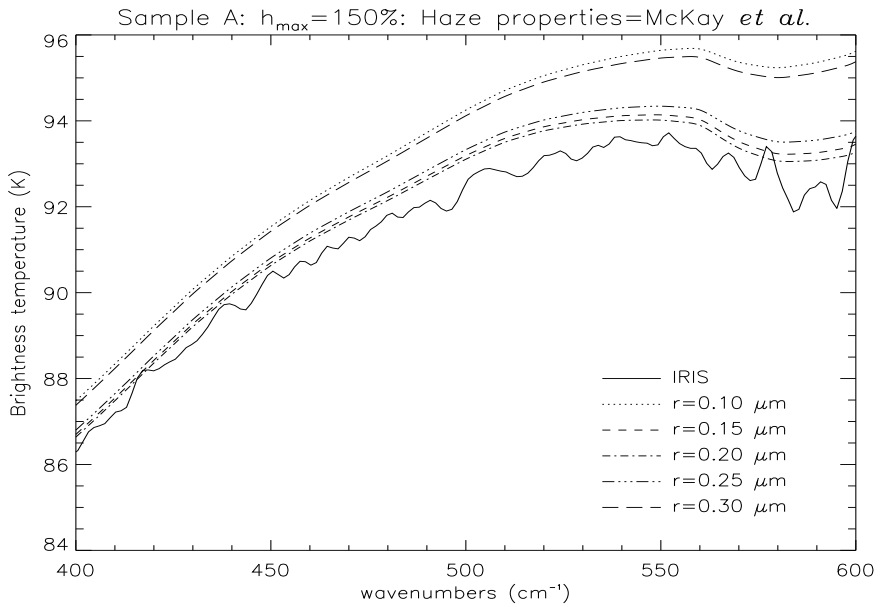

Figure 3.14: Comparison of IRIS Sample A spectrum to haze models with McKay *et al.* (1989) scaling of tholin imaginary refractive index. $h_{\rm surf} = 60\%$ and $h_{\rm max} = 150\%$.

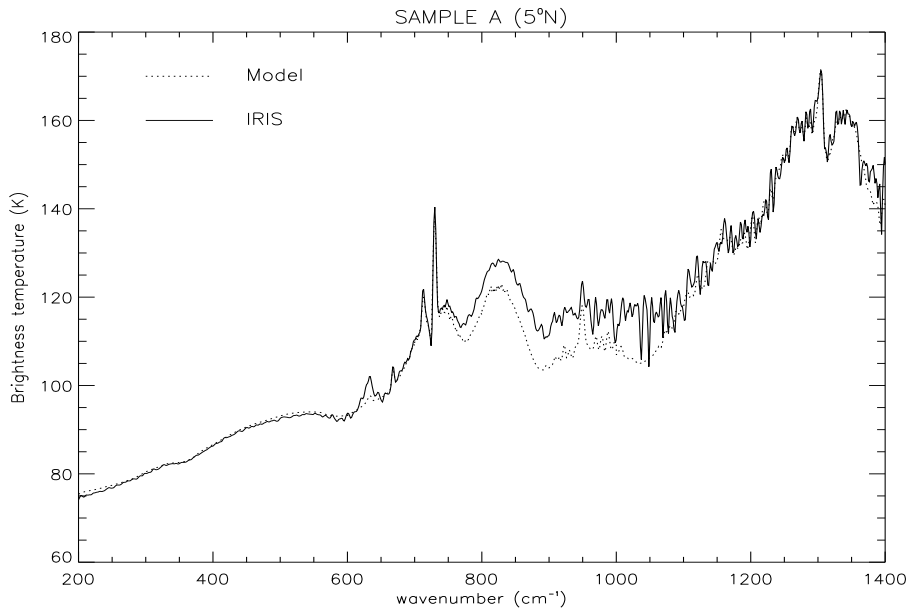

Figure 3.15: Comparison of equatorial model spectrum to IRIS Sample A spectrum over full range.

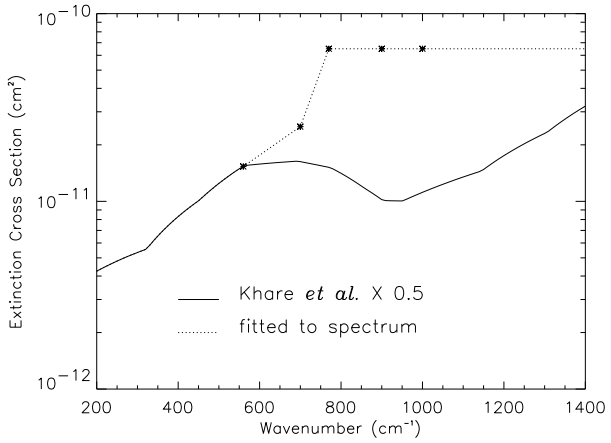

Figure 3.16: Comparison of laboratory tholin particle extinction cross-section (as measured by Khare *et al.*) with the extinction cross-section required to achieve a fit to the IRIS sample A spectrum in this model. (The scaling factor $X_{\rm IR}$=0.5 of McKay *et al.* is also included in both curves.)

calculations are likely to be different from those in Titan's atmosphere.

Note that the bands to either side of this region, *i.e.* the CH_4 band at 1304 cm^{-1} and the C_2H_2 band at 729 cm^{-1} are not affected, because the opacity is already so high that the aerosol contribution is relatively unimportant. For the other molecules: C_2H_6, C_2H_4 and C_3H_8; the gas opacity is somewhat less and so the aerosol contribution is more important.

There are several possible methods of including this continuum opacity. One method is simply to include a wavelength-dependent opacity, fitted to points of the spectrum where the gas opacity is lowest, *e.g.* at 900 and 1050 cm^{-1}. This method was used by Coustenis and Bézard (1995). I have chosen to include this extra opacity by increasing the extinction cross-section of the aerosol particles in the model to achieve a fit. The actual abundance of particles was as in the $r_{\rm c}$= 0.20 μm tholin model.

The required extinction per particle is shown in figure 3.16, compared to the optical properties for laboratory tholins. This by no means constitutes a derivation of the actual haze particle properties: it is merely a means of achieving the observed continuum level in the absence of further constraints, which must wait upon the fulfillment of Cassini-Huygens. Figure 3.17 shows the calculated spectrum compared to the data using the derived particle extinction.

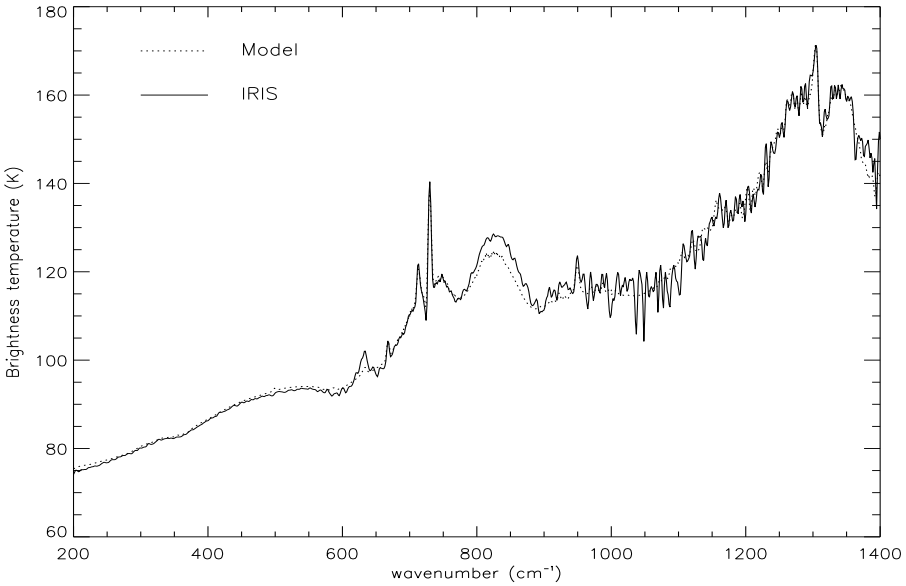

Figure 3.17: Comparison of model calculation to the IRIS sample A spectrum, when the haze extinction has been increased to fit the continuum.

There is still some residual disagreement in the ethane 850 cm band which appears to be a separate effect from the continuum opacity problem. The disagreement in the region 950–1100 is simply noise rather than missing lines: this fluctuation disappears when more spectra are summed (see figure 1 of Maguire et al., 1981).

Figure 3.18 shows the effect of increasing the mole fraction of C_2H_6 to achieve a closer fit for this band. A value of 2.6×10^{-5}, or twice the nominal value of Coustenis and Bézard (1995) would give an improved fit to the IRIS spectrum.

3.3.4 Summary

The main conclusions are as follows:

1. A tropospheric supersaturation fraction of 1.25–1.50 gives the closest fit of the model to the equatorial IRIS spectrum continuum region. This is in agreement with recent findings by Samuelson et al. (1997b).

2. When the laboratory tholin measurements of Khare et al. (1984) are used to model the haze particle optical properties then a single particle size of r_c=0.2 μm gives

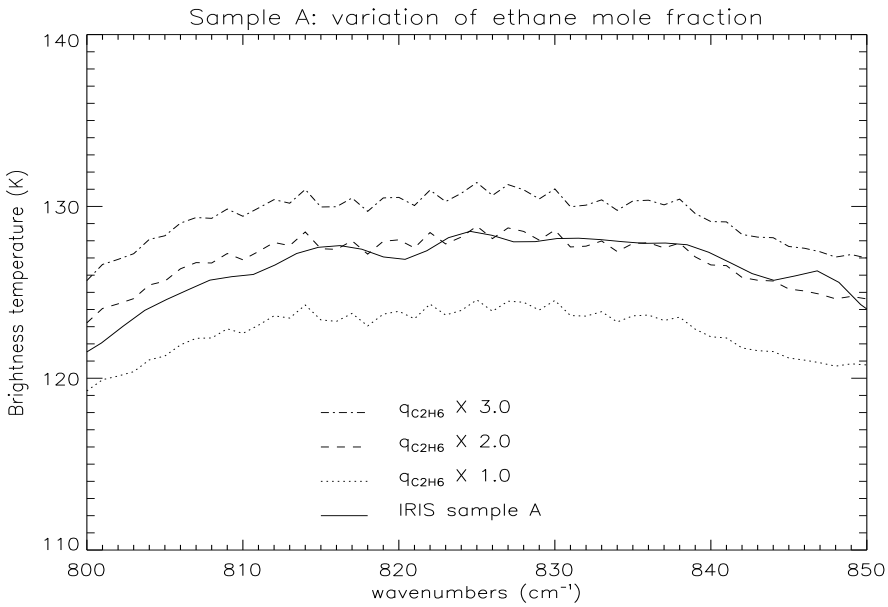

Figure 3.18: Variation of ethane abundance to improve model-data fit.

the closest match of the model calculations to the data. This estimated size is in good agreement with other studies (Rages and Pollack, 1983; McKay et al., 1989; Hutzell et al., 1996).

3. The scaling factors of McKay *et al.* applied to the Khare et al. (1984) laboratory tholin measured properties improves the agreement of the model predictions to the IRIS data.

4. The model is lacking in continuum opacity in the 730–1100 cm^{-1} spectral region, which is attributed to stratospheric haze. The continuum opacity can be raised by increasing the single particle extinction cross section to achieve a model-data match.

5. The model under-represents the emission bands of C_2H_6 and C_3H_4. This could be due to lines which are not included in the database. Some of the discrepancy is probably also due to the uncertainty in the continuum level.

Chapter 4

Calibration of CIRS 1: Determination of the MIR IFOV

Any flight instrument will almost certainly have properties which deviate to some extent from the design. Hence, it is important to measure the actual characteristics of the finished hardware, rather than relying on the design specification.

The determination of the Instantaneous Field of View (IFOV) is a crucial part of the pre-flight calibration of a spectrometer. Mathematically, the measurement of the IFOV gives the 'spatial weighting function': which is the width or extent of the object field, and any variation in response across it. Knowledge of the spatial weighting function is especially important for limb scanning measurements, when any variation across the FOV may have an effect on the retrieved parameters.

For CIRS, the individual detector fields of view are much smaller than that of the telescope. Therefore, if the telescope does not distort the FOV; each detector response $C_{\tilde{\nu}}$ to monochromatic radiation of wavenumber $\tilde{\nu}$ is equal to:

$$C_{\tilde{\nu}} = R_{\tilde{\nu}}\, \eta_{\tilde{\nu}} \int\int \{\hat{W}(\theta,\phi) I_{\tilde{\nu}}(\theta,\phi)\} \sin\theta d\theta d\phi, \tag{4.1}$$

where $I_{\tilde{\nu}}(\theta, \phi)$ is the incoming radiance from a direction (θ, ϕ) on the sky; $\eta_{\tilde{\nu}}$ is the total optical efficiency of the system; $R_{\tilde{\nu}}$ is the responsivity of the detector, and $\hat{W}(\theta, \phi)$ is the spatial weighting function normalised so that:

$$\int\int \hat{W}(\theta, \phi) \sin\theta d\theta d\phi = 1 \tag{4.2}$$

The determination of the instrument responsivity $R_{\tilde{\nu}}$ is examined in chapter 5. In this chapter, measurement of $\hat{W}(\theta, \phi)$ is considered. In CIRS, three different types of detector were used in the three different focal planes, to achieve a range of wavenumber coverage. These various detector types all have different characteristics. Measurement of the spatial weighting functions for FP3 and FP4, the mid-infrared photo-electronic detectors, was carried out for this thesis.

4.1 The FP3 and FP4 Focal Plane Assemblies

4.1.1 FP3

The FP3 array of photoconductive (PC) detectors, covering the wavenumber range 600–1100 cm^{-1}, was designed and manufactured at GSFC.

PC detectors are photon-counters, as opposed to sensing mean power like a bolometer. The detector is made from an intrinsic semiconductor, in this case HgCdTe, which has a gap between the valence and conduction bands of energy E comparable to the energy of an infrared photon (figure 4.1(a)).

When a photon strikes the material, an electron is promoted to the conduction band and the conductivity is increased. Hence, for a constant p.d. across the element, the change in current can be measured to count photons arriving. Note that, in theory, a PC detector does not directly sense the frequency of detected photons: if the photon promotes an electron to the conduction band the actual energy of the photon is not

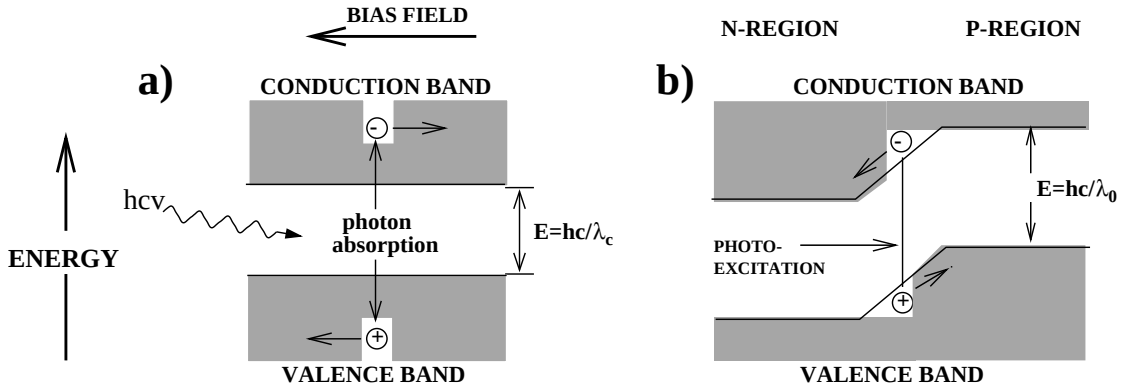

Figure 4.1: *Charge carrier generation in semiconducting materials.* (a) In an intrinsic semiconductor, the incident photon creates a photo-electron-hole pair. The electron is promoted to the conduction band and the hole drops to the valence band (after Hanel *et al.*). (b) Photoexcitation at p-n junction in a photovoltaic detector. The electron moves towards the positive ions in the n region, while the hole moves towards the negative ions in the p region (after Keyes).

measured, unlike a bolometer.

The long wavelength cut-off is determined by the size of the band gap: a longer wavelength photon has lower energy than the band gap and cannot promote an electron into the conduction band. E is given by:

$$\lambda_{\rm c}(\mu m) = \frac{1.24}{E(eV)}. \tag{4.3}$$

For the case of HgCdTe, E=0.1 eV and $\lambda_{\rm c}$=12.4 μm. A short wavelength cut-off is normally induced by other means, *e.g.* coating the detector.

The FP3 array is made from a 9 μm thick wafer of HgCdTe mounted on an alumina substrate. The wafer is etched to delineate the individual elements and metalised to provide electrical connections (see figure 4.2). The detectors are finally coated in ZnSe to reduce losses.

Each detector has a characteristic U-shape which leads to a bifurcated response. This design arises out of the need to have both electrical connections on the same side of the

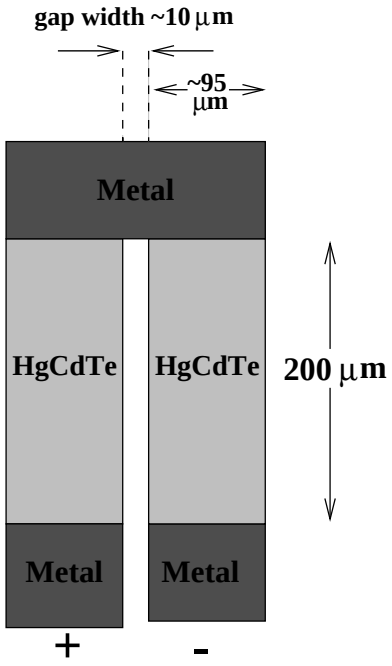

Figure 4.2: The design of an individual PC detector.

detector, due to the PV detector array being abutted against the other side.

4.1.2 FP4

The FP4 array of photovoltaic (PV) detectors, covering the wavenumber range 1100-1400 cm^{-1} was also manufactured from HgCdTe, at the CEN Saclay in France.

A PV, also called a photodiode, is composed of two types of material: p and n-doped semiconductor joined together. Because of the charge dipole, a small electric field exists across the junction. Photoelectrons produced at the junction move to the p side under the field whilst holes move to the n side, which results in a change in voltage which can be measured (see figure 4.1(b)).

Unlike the PC detectors, the PVs are regular and square in shape.

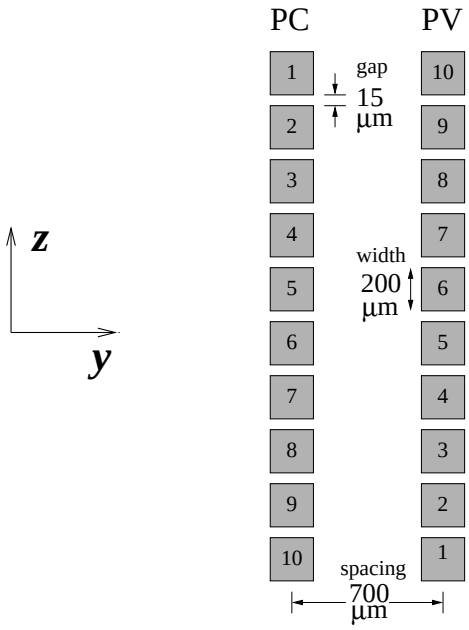

Figure 4.3: Relative positions of the ten FP3 and ten FP4 detectors.

4.1.3 Mid-IR FPA

The two focal plane arrays are mounted on metal sub-carriers (FP3=titanium; FP4=copper) which were both then attached to a pure titanium common carrier unit at AOPP. Figure 4.3 shows schematically the relative positions of the twenty mid-IR detectors. The 200 μm width of each detector translates into a 0.273 mrad FOV size on the sky.

The common carrier was in turn mounted on a titanium alloy tripod which serves to hold the detectors in a fixed position relative to the imaging lens, as well as to thermally isolate the focal planes from the rest of the instrument. The lens itself is made from diamond-turned germanium, coated in alternating layers of PbTe and ZnSe, and then in BaF_2 to improve transmission. This combination of coatings (by Reading University) gives the lens an unusually broad range of spectral transparency (figure 4.4).

The FPA is connected at the rear to an aluminium alloy 'cold finger': a thermal sink which is maintained at 70–80 K by the passive radiative cooling patch at the other end. The detectors must be maintained at low temperature to reduce the thermally generated noise.

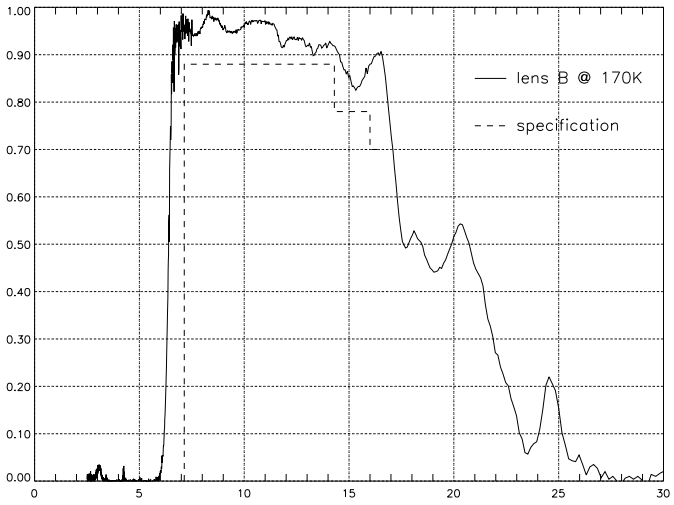

Figure 4.4: The transmission of a typical CIRS germanium lens at its nominal operating temperature of 170 K, as measured by Reading University.

4.2 Focus and Alignment Testing

During the period November 1995 to May 1996 focal plane alignment of CIRS was performed in the Space Instruments Laboratory (SIL) in AOPP; firstly the Engineering Model (EM) and subsequently the Flight Model (FMA) and back-up flight model (FMB).

There were two main tasks related to the alignment of the FPA: (i) to ensure that the lens was mounted at the correct distance from the detectors, so that the image is in focus, and (ii) to ensure that the lens was perpendicular to the optical axis, within allowable error margins.

4.2.1 Apparatus

The alignment of the FPA needed to be undertaken in an environment comparable to that which the instrument will encounter in operation at Saturn. Therefore the testing was performed in an evacuated vacuum tank and with the FPA cooled by a liquid nitrogen dewar, which took the role that the passive radiative cooler assumes in space. The Alignment Test Rig (ATR) apparatus used to align the FPA is depicted in figure 4.5.

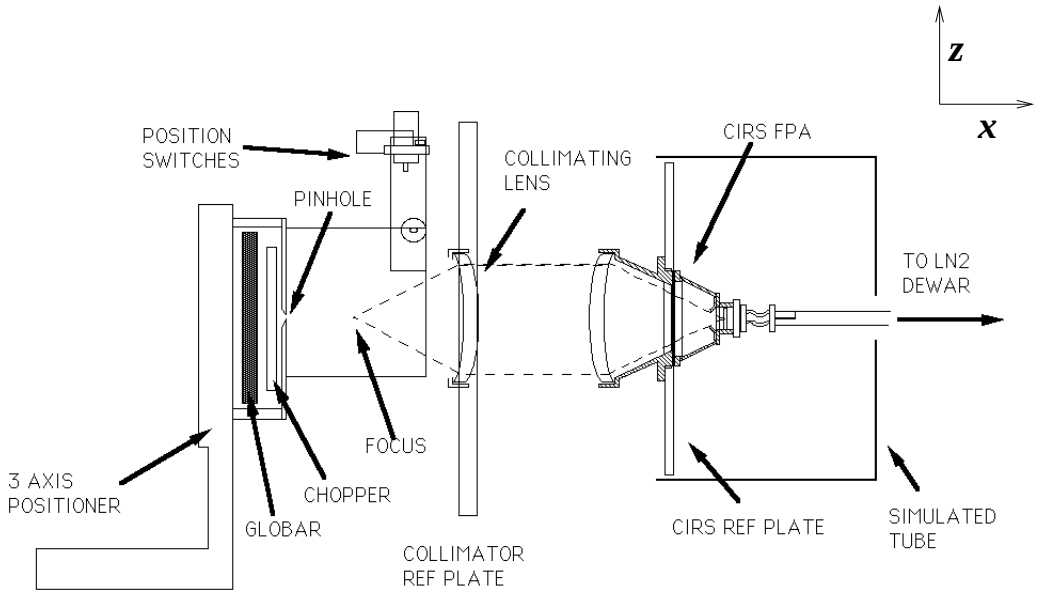

Figure 4.5: Schematic diagram of the CIRS FPA Aligment Test Rig (courtesy S. Calcutt). A pinhole in front of an infrared (globar) source, chopped using a rotating chopper, was scanned around in front of the FPA to determine the location of an image of the detector arrays. CIRS has no intermediate focus so a collimator was used to provide an image.

Radiation from a globar was chopped before passing through a pinhole, to provide a point source. CIRS has no intermediate focus, because the FPA is designed to focus the collimated radiation from the telescope and interferometer optics directly onto the detectors when in normal operation. Therefore, in the ATR, an identical lens to the FPA lens, but in reverse configuration, was used to provide a collimated beam of radiation from the image plane.[1] This 'collimating' lens was fixed in orientation relative to the FPA, although this could be adjusted between experiments. Finally, the pinhole and globar assembly was attached to a positioning mechanism which enabled it to be moved around in three orthogonal directions.

The tripod and lens assembly are attached to a precision reference plate in CIRS. Once the position of this plate was measured, a reference co-ordinate system was established. All other measured positions were then transformed to this co-ordinate system

[1]The terms 'image' and 'image plane' are used throughout this chapter to refer to the image of the detectors provided by the second, or 'collimating' lens. In normal scientific operation, the image would be the interferogram formed by the FPA lens at the detectors.

('FPA co-ordinates'). For example, the collimating lens was attached to a separate reference plate, the position of which was calculated in FPA co-ordinates.

The position measurements were made using 3-axis switches attached to the movable arm which positions the pinhole. The overall precision of positioning+switching of the arm was ± 1 μm, and its movable location was specified in the FPA co-ordinate system.

At the start of every alignment test, after the tank had been evacuated and cooled, a set of calibration measurements was made to establish a co-ordinate system. This involved using the arm to measure the relative positions and orientations of the collimator reference plate and the FPA reference plate.

4.2.2 Focusing

Achieving the focusing of the focal plane with respect to the lens was a crucial task in the flight verification of the instrument. This process involved first finding the image of the detector arrays, as imaged by the collimating lens, and then checking the magnification. Ensuring that the magnification was unity was equivalent to focusing the array.

Movement of the pinhole source in the x-direction (perpendicular to the beam) enabled the distance of the image plane from the lens to be found. This was achieved by stepping the pinhole slowly in x through the image of a particular detector.[2] At each x-position the pinhole was also scanned laterally in the z direction, perpendicular to the optical axis. At each one of these (x, z) positions the detected intensity is measured.

The result was a series of cross-sections through the detector image, or an x-z plane intensity map (figure 4.6). On either side of the image plane, the image of the detector was smeared out (*e.g.* cut 'A' and cut 'C', figure 4.7).

There were several possible algorithms for judging the image position. One possible method was to measure the FWHM of the profile: the minimum FWHM would then give the focus position. However, for the PC detectors, which have a two-lobed response

[2]Normally PC5 in the middle of the array was used. Note however that the PV array is physically offset by 77 μm in the focus direction, so the focus position would be expected to be different by that amount.

shape, the maximum value of one peak was often different from that of the other peak, so the FWHM did not necessarily have a single minimum position.

In practice, it was found that the most accurate method was to consider the slope of the response at half-maximum of one of the detectors. The maximum slope gave the image position. For the PC 5 detector depicted in figure 4.6 the focus was found to be at $x = 51250 \pm 25$ μm or 51.25 ± 0.025 mm. Tests showed that the PV detectors had a steeper slope of response than the PCs and hence gave a more accurate focus. The position of the image plane was normally determined to a precision of ± 25 μm.

Having found the image plane, the length of the array was then measured. The most accurate method was to calculate the co-ordinates of the centroids of the PV detectors at either end of the array, which could be measured to ± 2 μm. If the image size was different from the known physical size of the array by more than ± 4 μm, then a positional adjustment in the x-direction was required.

The depth of focus was estimated by ray-tracing using a computer model of the optics (carried out by Swales, a sub-contractor of GSFC). By taking into account spherical and other aberrations in the optical components and tracing rays of different frequencies, they estimated the FWHM of the peak response to be ± 40 μm.

4.2.3 Alignment

Alignment of the lens assembly optical axis to the nominal was required to a precision of ± 0.5 mrad, corresponding to an image de-centre of < 10 μm over the $\sim$50 mm focal length. This was achieved by de-mounting the tripod/lens assembly and rotating it 180° with respect to the reference plate. The image plane was then scanned again. Any movement of the detector images was then subtracted out by adjusting shims which controlled the pointing of the assembly.

The tilt (in the x-direction) of the focal plane with respect to the lens was checked by measuring the width of detectors at either ends of the arrays. The tolerance for this alignment was quite large (20 mrad) because the focusing of individual detectors could

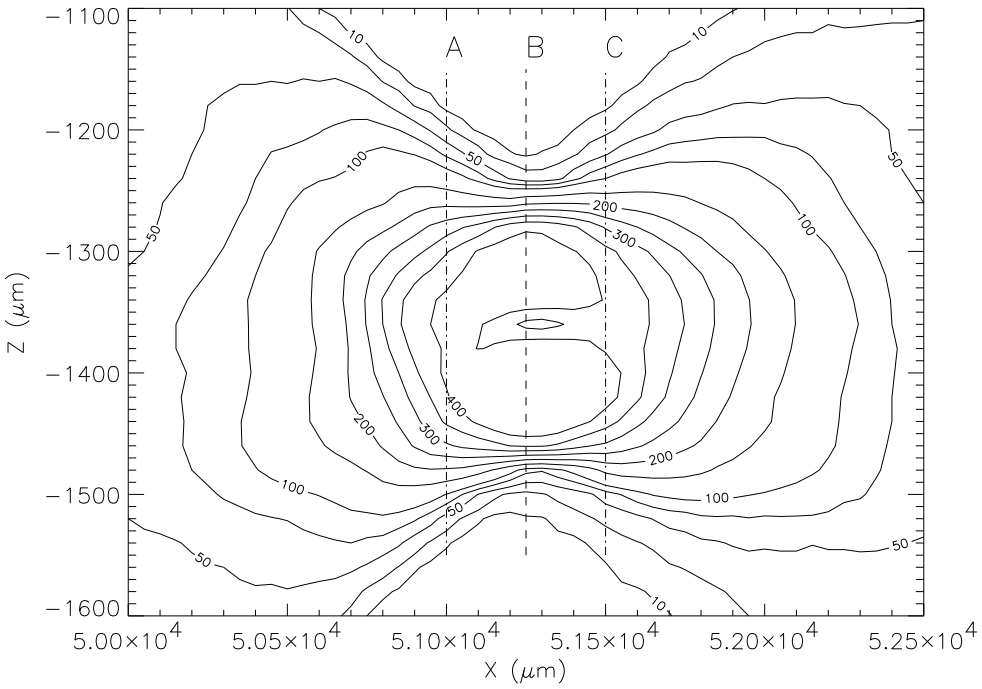

Figure 4.6: *Contour plot of the x-z plane during focusing of the PC 5 detector (02/04/97).* Data points are gathered by scanning the pinhole in the x-z plane (x: along the optical axis; z-perpendicular to the optical axis). The z-cross-section at constant x represents the spread of the dectector image. As the image plane x-co-ordinate is approached, the detector profile narrows and sharpens. The optimum x-value in this scan was a lens-image distance of 51.250 mm, indicated by the line 'B'.

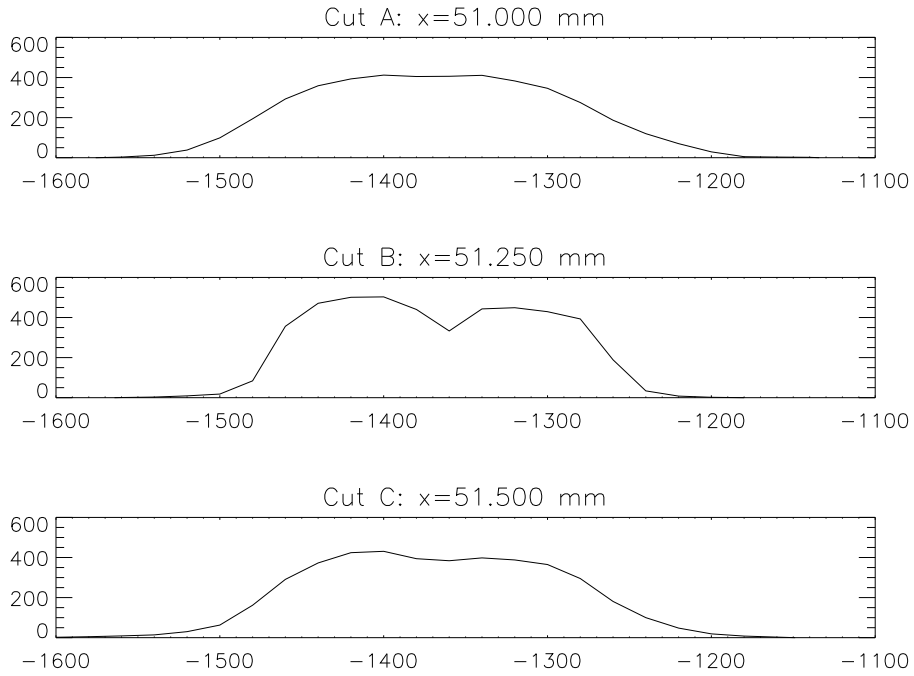

Figure 4.7: Plots of the three cuts marked A,B and C in the previous figure.

not be checked to significantly less than the depth of focus (± 40 μm).

In addition, the tilt (x-direction) and roll (y–z direction) of the FP3 array with respect to the FP4 array, their separation (decentre) and focus offset depth (-76 μm) were achieved to within tolerance limits using precision dowels and measurements.

4.3 FOV Measurements

Although the primary purpose of the ATR was to ensure correct alignment and focusing of the detectors, it was also possible to use the equipment to map the individual detector responses at high resolution, by scanning the pinhole in the y–z directions, in the plane of focus (*i.e.* constant x). The contour maps of response of the final focused detectors are shown in figures 4.8 and 4.9.

Although both arrays consist of a row of ten square detectors; the response of the PVs and PCs is qualitatively quite different. Whereas the PV detectors have a nearly uniform 'top-hat' profile in the y and z-directions, each PC detector has a twin-lobed response. Figure 4.10 is a 3-D visualisation of PC 1, one of the most strongly asymmetric detectors. This may be compared to PV 10 (figure 4.13).

By taking an average cross-section of each detector in the y-direction, it is possible to examine the response in more detail (figures 4.14 & 4.15). It can be seen that each PC has a unique profile, which moreover may be asymmetric with one 'lobe' stronger than the other. The PVs are much more uniform.

The shape of the PC detector spatial responses will clearly have an effect on any measurements made by FP3. For example, if the detectors are pointed at the planetary limb, the asymmetrical response may weight the measurement towards higher or lower altitudes, depending on relative orientation to the vertical. The importance of this effect for scientific retrievals is examined in chapter 6.

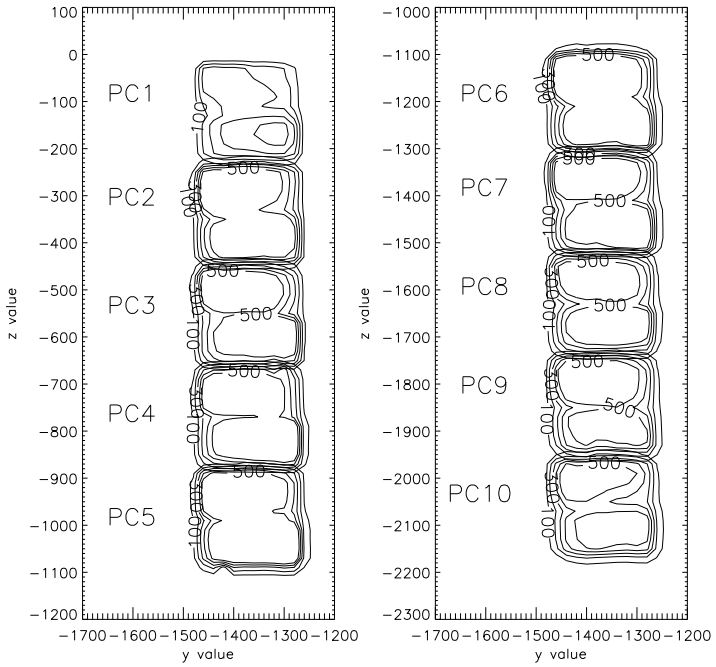

Figure 4.8: Response scans of the PC detectors dated 10/04/96 at 20 μm resolution. Contour levels are 100, 200, 300, 400, 500 'counts'.

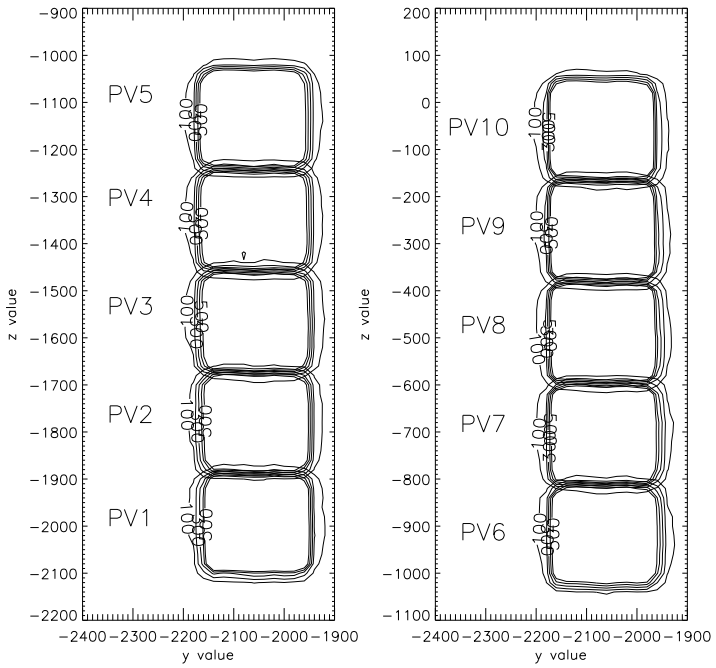

Figure 4.9: Response scans of the PV detectors dated 10/04/96 at 20 μm resolution. Contour levels are 100, 200, 300, 400, 500 'counts'.

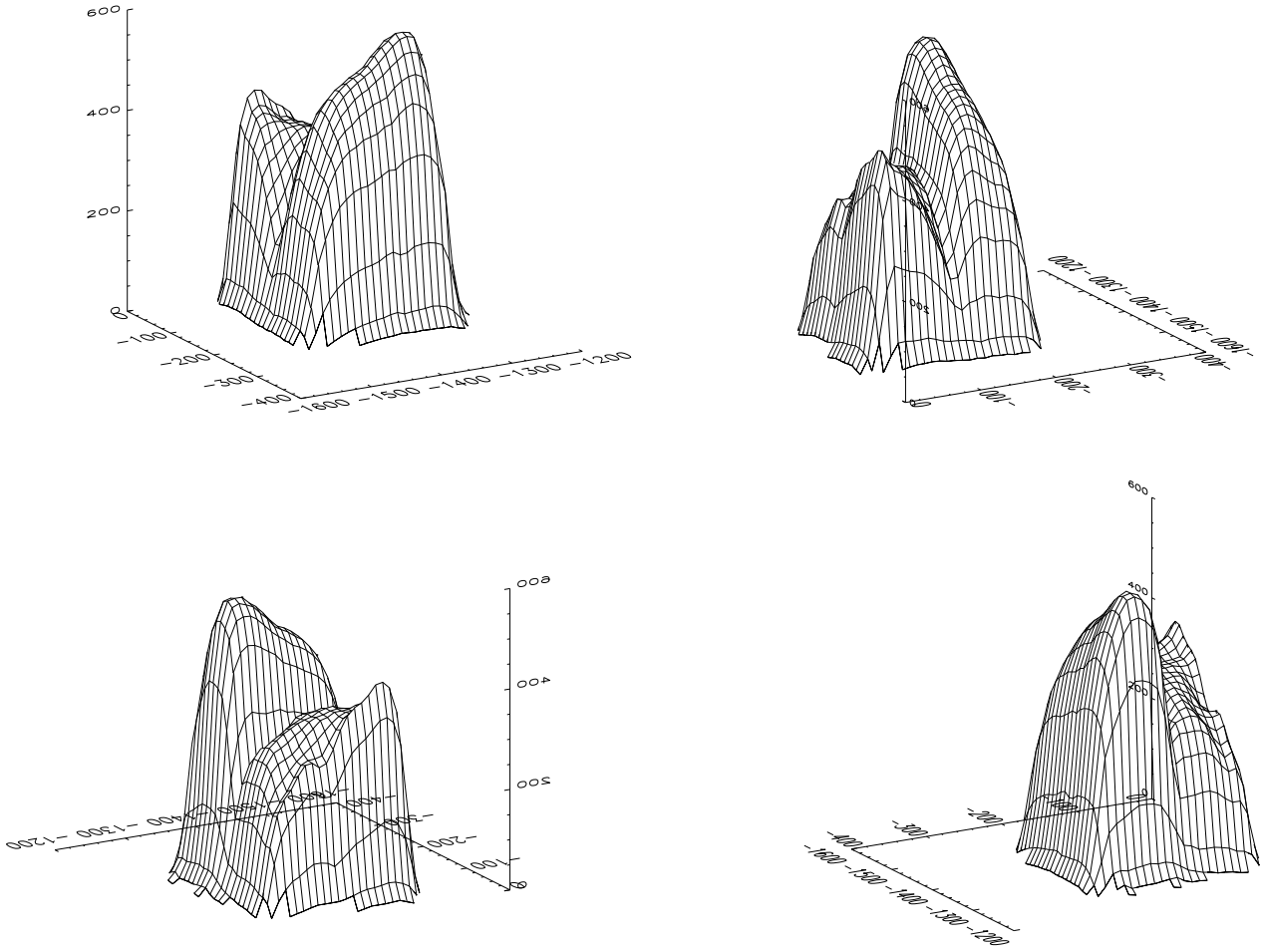

Figure 4.10: 3-D visualisations of the PC 1 detector response *(scan date: April 10th 1996)*. Each figure is rotated 90 from the previous one. Note the bifurcated twin-lobed response shape.

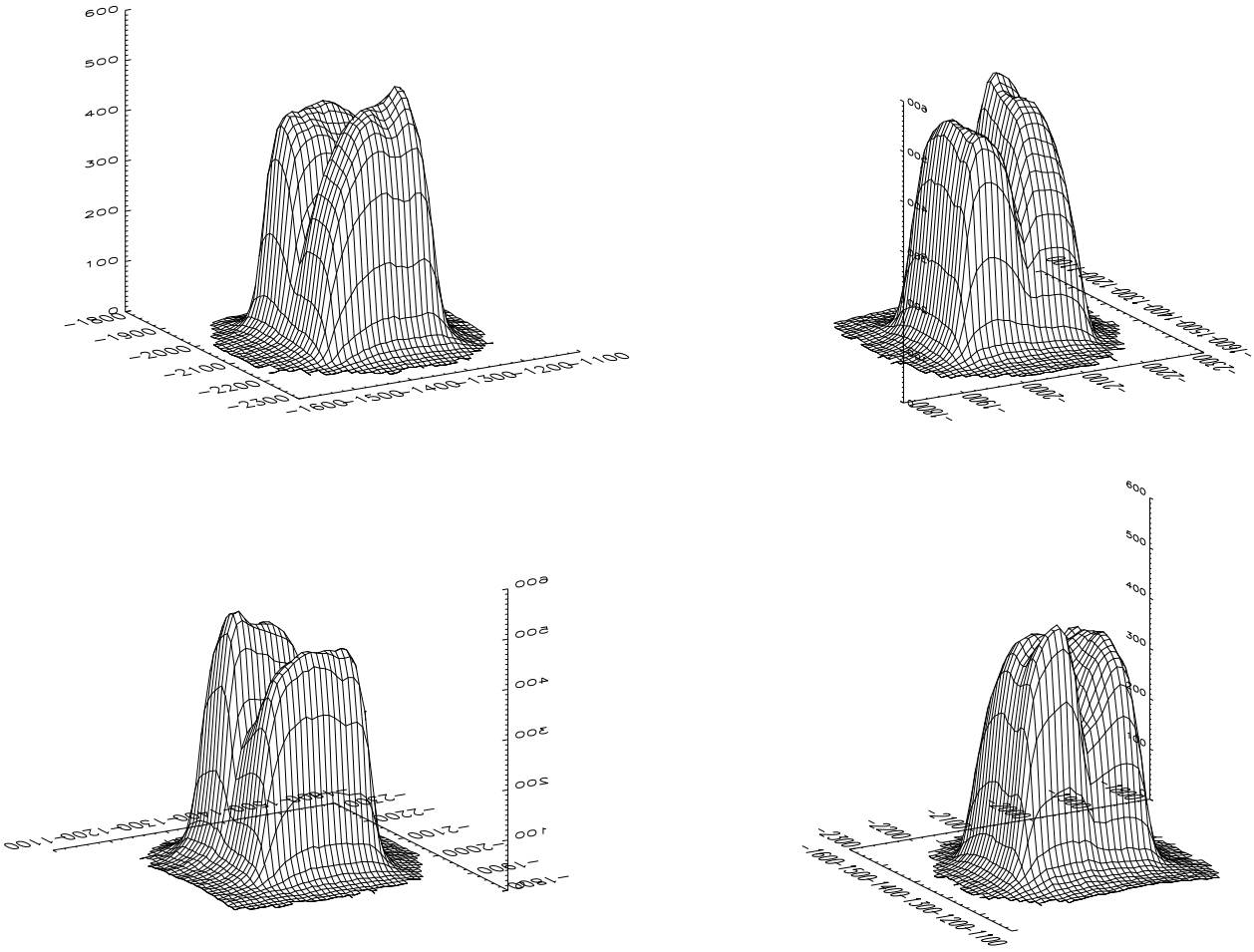

Figure 4.11: 3-D visualisations of the PC 10 detector response function *(scan date: April 10th 1996)*.

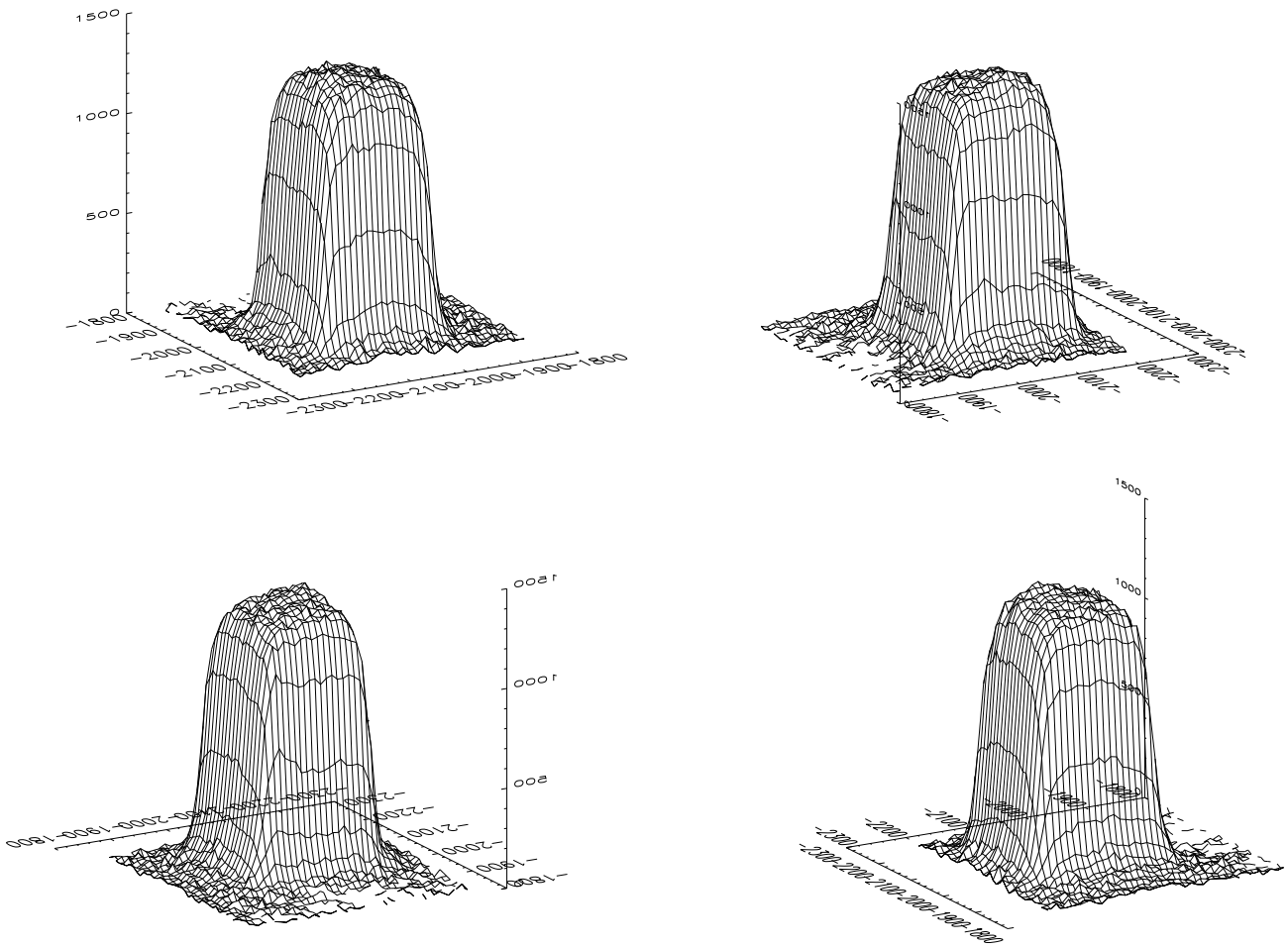

Figure 4.12: 3-D visualisations of the PV 1 detector response *(scan date: April 10th 1996)*. The function is close to a symmetric 2-dimensional 'top-hat' response. It is much more regular than the PC detectors and is not bifurcated.

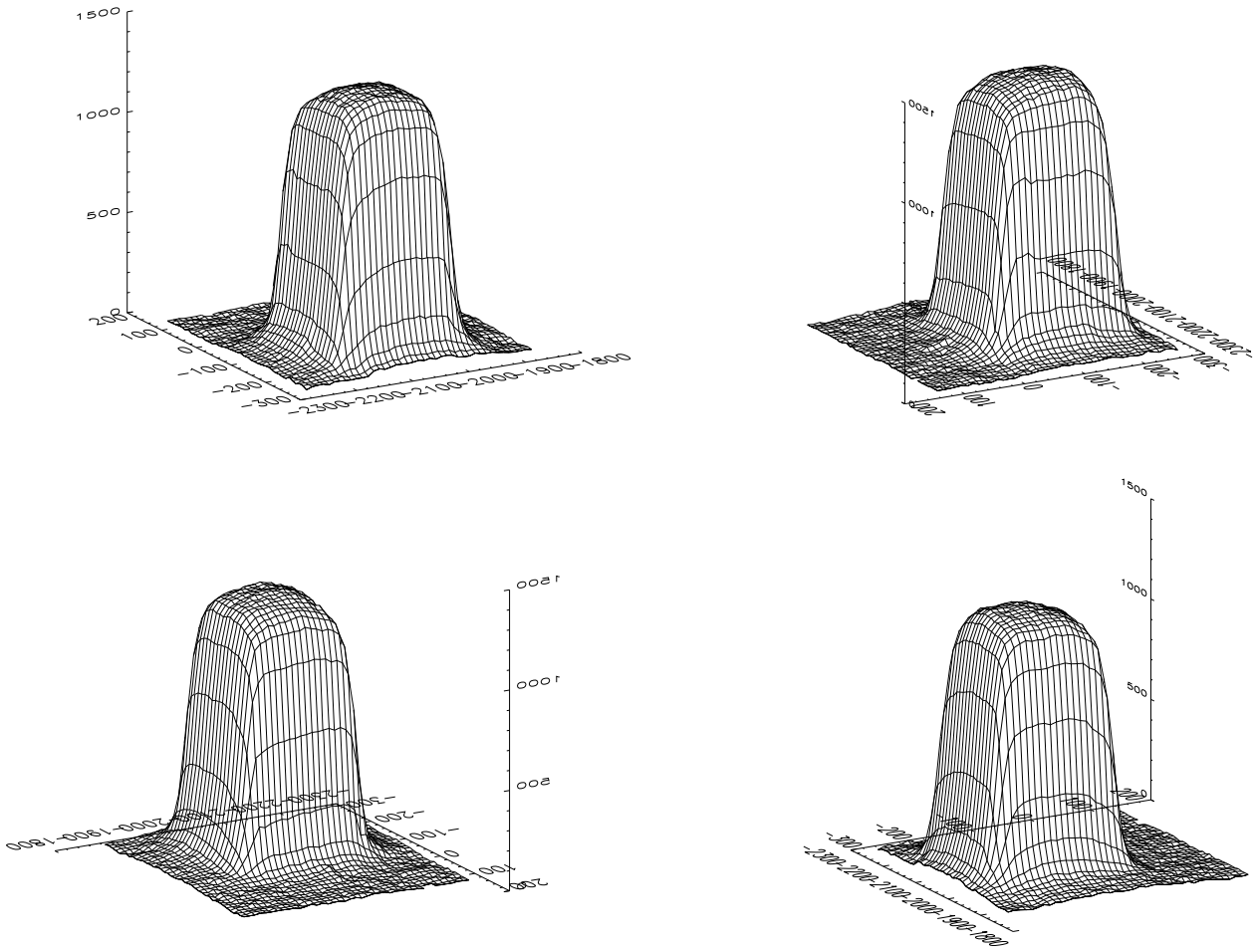

Figure 4.13: 3-D visualisations of the PV 10 detector response *(scan date: April 10th 1996)*.

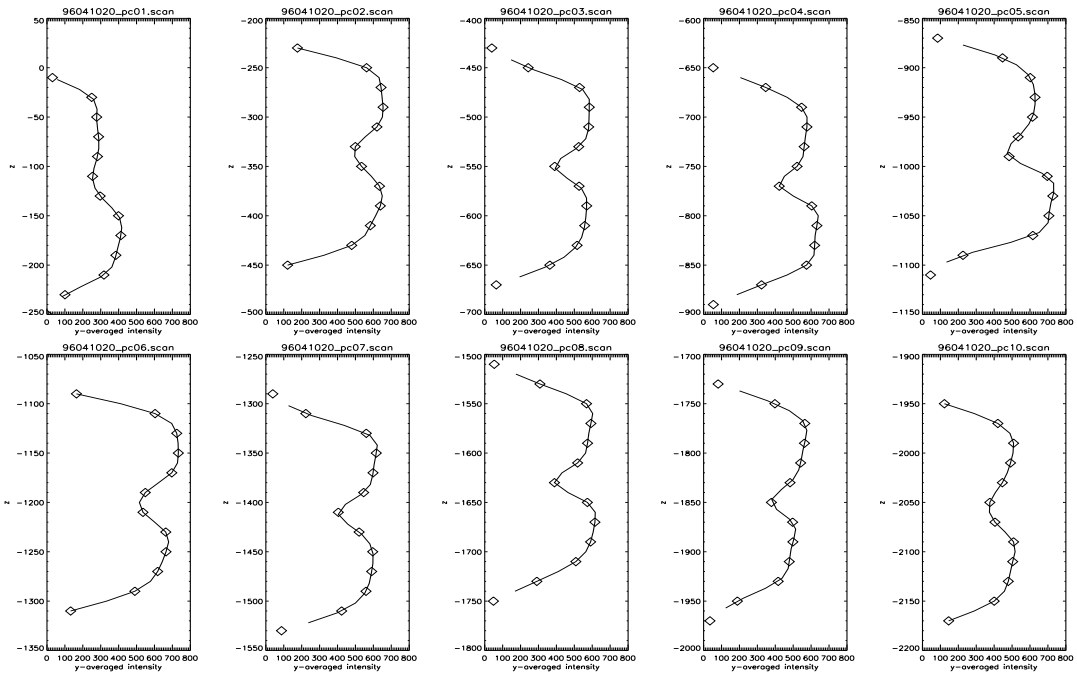

Figure 4.14: Cross-sections of individual PC detectors in the z-direction. These have been averaged across the detector (in the y-direction), to create the array of point values (diamonds) with a resolution of 20 μm. The solid line is a cubic spline fit to the points.

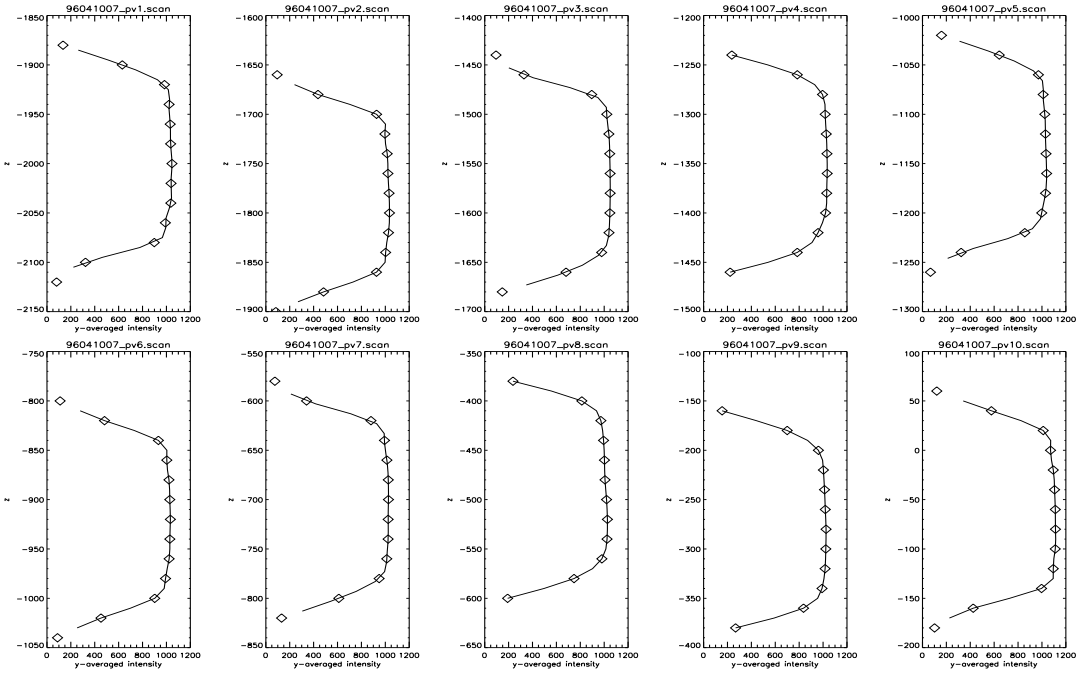

Figure 4.15: Cross-sections of individual PV detectors in the z-direction. These have been averaged across the detector (in the y-direction), to create the array of point values (diamonds) with a resolution of 20 μm. The solid line is a cubic spline fit to the points.

Chapter 5

Calibration of CIRS 2: Determination of the NESR

One of the most important parameters governing the performance of a radiometrically calibrated spectrometer like CIRS is the Noise Equivalent Spectral Radiance (NESR), which gives the noise on an observation as a function of frequency. The signal-to-noise ratio for a particular spectral feature is the spectral radiance of the signal divided by the NESR at that wavenumber.

This chapter describes the estimation of the NESR from CIRS observations of laboratory blackbody sources. The calculation divides into two distinct tasks: the production of the power spectra from interferograms, and the calculation of the NESR from series of spectra of blackbody sources at different temperatures.

The first section summarizes the theory of Fourier Transform Spectrometry which is used to transform individual interferograms into power spectra. The transform method is then applied via a new numerical code to CIRS laboratory data. Also considered are the constraints caused by finite frequency representation and apodisation, and the errors which may arise due to phase drift. The second part of this chapter shows how the NESR can be estimated from the power spectra.

5.1 Calculation of the Power Spectrum

It can be shown (e.g. Chamberlain 1979, chap. 4) that the interferogram produced at the output of an ideal Michelson two-beam interferometer is given by:

$$\mathcal{I}(x) = \int_0^\infty P(\tilde{\nu}) \cos(2\pi\tilde{\nu}x)\, d\tilde{\nu} \tag{5.1}$$

which is the Fourier cosine transform of the power spectrum, for the continuous function before sampling.

In order to maximise the spectral resolution in a given observing time, it is usual to measure only one side of the symmetric interferogram, e.g. at positive path differences. The negative path difference section contains no extra information so is not normally required (although see §5.1.3).

The physical spectrum is also one-sided, containing only positive frequencies. Therefore by symmetry arguments and using the Fourier inversion theorem it can be shown that the physical spectrum is calculated from the one-sided interferogram using:

$$P_{\mathrm{e}}(\tilde{\nu}) = 2\int_0^\infty \mathcal{I}_{\mathrm{e}}(x) \cos(2\pi\tilde{\nu}x)\, dx \tag{5.2}$$

where $\mathcal{I}_{\mathrm{e}}$ is the one-sided 'even' interferogram.

5.1.1 Apodisation

In practice, it is impossible to measure an infinite function such as $\mathcal{I}(x)$ over an infinite or semi-infinite range. If the measurement is curtailed at some path difference $x = X$, then we have effectively multiplied the infinite function $\mathcal{I}(x)$ by a boxcar function (equation A.1). This process is known as windowing. The effect of windowing on the calculated spectrum in the wavenumber ($\tilde{\nu}$) domain is convolution by the sinc function (see appendix

Function number N	Coefficients A_0	A_1	A_2	A_3	A_4	Γ	Comments
1	0.548	−0.083	0.535	0.0	0.0	0.724	Weak apod.
2	0.260	−0.155	0.895	0.0	0.0	0.844	Medium apod.
3	0.090	0.0	0.588	0.0	0.323	0.965	Strong apod.
4	0.0	0.0	1.0	0.0	0.0	0.950	Forman type
5	1.0	0.0	0.0	0.0	0.0	0.603	'Boxcar' (no apod.)

Table 5.1: The co-efficients of the three Norton & Beer apodisation functions and the corresponding co-efficients of two simpler apodisation functions for comparison. The Forman type is the simplest apodisation function which avoids discontinuities in the gradient at both $x' = 0$ and $x' = 1.0$. The numerical factor Γ which affects the resolution is described in §5.1.6.

A for derivation).

The sinc function leads to an undesired 'ripple' effect on the final spectrum. This can be alleviated by changing the form of the windowing function, so that the cut-off is not so sharp at $x = X$. However, in exchange for smaller sidelobes ('apodisation'), we must suffer a loss of resolution as the central peak widens.

Norton and Beer (1976) (hereafter N&B) have shown that there is a near-optimal class of apodising functions, from which one can be selected which has the desired level of apodisation. The set of functions has the form:

$$f_N(x') = \sum_{i=0}^{n} \mathrm{A}_i (1 - x'^2)^i; \quad \sum_{i=0}^{n} \mathrm{A}_i \equiv 1 \tag{5.3}$$

where $x' = \frac{x}{X}$ and n, the number of terms, is cut off at 4. N is the reference number of the function (see table 5.1 and figure 5.1).

In the following analysis, the N&B type 2 function has been used to apodise CIRS interferograms. This can used to set the resolution of the final output spectrum, as described in §5.1.6.

5.1.2 The Effect of Phase Delay on the Interferogram

There are several effects usually present in the measured interferogram which cause it to deviate from pure even symmetry.

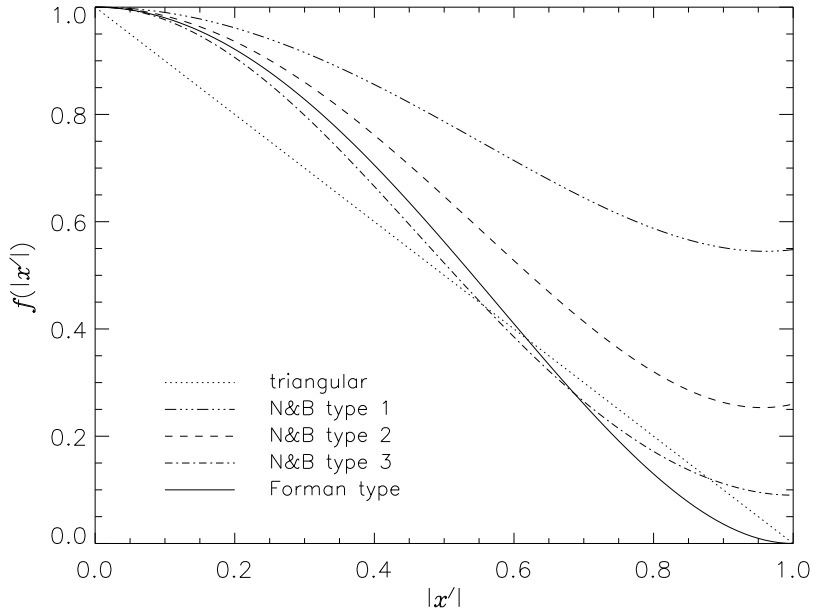

Figure 5.1: Apodising functions.

1. **Offset in sampling:** if the first data point is actually sampled before the zero path difference (ZPD) point, at $x = -\delta$, then the resultant interferogram takes the form:

$$\mathcal{I}(x) = \int_0^\infty P(\tilde{\nu}) \cos 2\pi\tilde{\nu}(x - \delta)\, d\tilde{\nu} \tag{5.4}$$

2. **Filtering:** electronic filters, designed to remove high-frequency noise from the spectrum, may have the effect of adding a wavenumber-dependent phase lag $\theta_{\tilde{\nu}}$ on each cosine component of the signal:

$$\mathcal{I}(x) = \int_0^\infty P(\tilde{\nu}) \cos(2\pi\tilde{\nu}x - \theta_{\tilde{\nu}})\, d\tilde{\nu} \tag{5.5}$$

Since any cosine wave $\cos(\alpha - \beta)$ may be expanded:

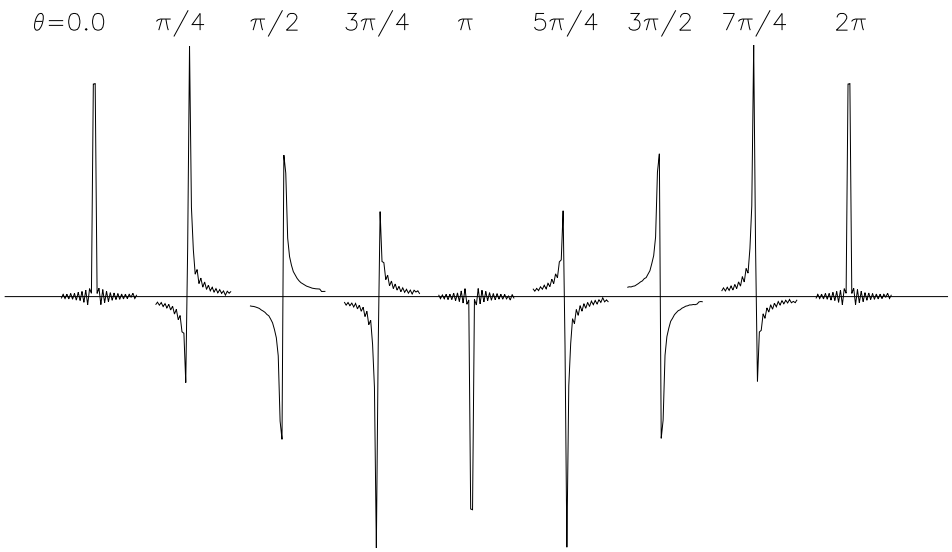

Figure 5.2: Series of ILS functions for a range of phase shifts from 0 to 2π. The $\theta = 0$ case is the FT of a pure monochromatic cosine wave. The $\pi/2$ case corresponds to the cosine transform of a sine wave. This shows that even slight phase lags can have a large effect on the final spectrum.

$$\cos(\alpha - \beta) = \cos(\alpha)\cos(\beta) + \sin(\alpha)\sin(\beta) \tag{5.6}$$

the result of adding a second term to the phase angle $2\pi\tilde{\nu}x$ is to add sine components to the cosine wave interferogram, so it is no longer evenly symmetric.

Figure 5.2 shows the effect of adding a constant phase shift to an input monochromatic cosine wave. At $\theta = 0.0$, the interferogram is pure sinc ($\cos x/|x|$), as expected from the cosine FT of a truncated cosine wave.[1] When $\theta = \pi/2$ however, the interferogram has become $\sin x/|x|$, as expected from a sine wave interferogram. In general, the resultant Instrumental Line Shape (hereafter ILS) is some combination of these two functions.

In summary, unless the unwanted sine wave artifacts can be removed from the interferogram, the final calculated spectrum will be significantly affected.

[1]For an infinite cosine wave, the FT would of course be a delta function.

5.1.3 Removal of Phase Variation

The process of removing the sine wave components from the interferogram is called phase correction. Firstly, let us define the forward and inverse complex Fourier transforms:

$$F(x) = \int_{-\infty}^{+\infty} f(\tilde{\nu}) \exp(2\pi i \tilde{\nu} x) d\tilde{\nu} \equiv \text{F.T.}[f(\tilde{\nu})] \tag{5.7}$$

$$f(\tilde{\nu}) = \int_{-\infty}^{+\infty} F(x) \exp(-2\pi i \tilde{\nu} x) dx \equiv \text{F.T.}^{-1}[F(x)] \tag{5.8}$$

where $f(\tilde{\nu})$ is some function in the frequency domain, and $F(x)$ is the corresponding function in the spatial domain. This relation can be denoted: $F(x) \overset{\text{F.T.}}{\Longleftrightarrow} f(\tilde{\nu})$. Now consider the functions:

$\mathcal{I}_{\text{e}}(x)$	the evenly symmetric, 'ideal' interferogram
$P_{\text{e}}(\tilde{\nu})$	the 'ideal' or true power spectrum
$\mathcal{I}_{\text{u}}(x)$	the unsymmetric, real measured interferogram
$P'(\tilde{\nu})$	the uncorrected power spectrum

These two pairs of functions are related by the Fourier Transform relations:

$$P_{\text{e}}(\tilde{\nu}) \overset{\text{F.T.}}{\Longleftrightarrow} \mathcal{I}_{\text{e}}(x) \tag{5.9}$$

$$P'(\tilde{\nu}) \overset{\text{F.T.}}{\Longleftrightarrow} \mathcal{I}_{\text{u}}(x) \tag{5.10}$$

P' is hence the estimate of the real power spectrum P_{e} which is derived from transforming the imperfect interferogram $\mathcal{I}_{\text{u}}$, while P_{e} would be the result of transforming the perfectly symmetric interferogram $\mathcal{I}_{\text{e}}$, which is unknown. Note that we cannot use the cosine transform because the integrand is not symmetric. Only $\mathcal{I}_{\text{u}}$ is measured. The objective is to find from this the ideal power spectrum P_{e}.

P' can be represented as:

$$P'(\tilde{\nu}) = |P_{\rm e}(\tilde{\nu})| \exp(-i\theta_{\tilde{\nu}}), \tag{5.11}$$

the product of the real magnitude spectrum times a complex angle which signifies the phase lag of each frequency component. The phase angle $\theta_{\tilde{\nu}}$ is found simply from the $P'(\tilde{\nu})$ by:

$$\theta_{\tilde{\nu}} = \tan^{-1} \frac{\mathrm{Im}(P'(\tilde{\nu}))}{\mathrm{Re}(P'(\tilde{\nu}))} \tag{5.12}$$

Re-arranging 5.9 we find that:

$$\begin{aligned} \mathcal{I}_{\rm e}(x) &= \mathrm{F.T.}[(P_{\rm e}(\tilde{\nu})e^{-i\theta_{\tilde{\nu}}})e^{+i\theta_{\tilde{\nu}}}] & (5.13)\\ &= \mathrm{F.T.}[P'(\tilde{\nu})e^{+i\theta_{\tilde{\nu}}}]. & (5.14) \end{aligned}$$

However we can apply the convolution theorem (equation A.6):

$$\begin{aligned} \mathrm{F.T.}[P'(\tilde{\nu})e^{+i\theta_{\tilde{\nu}}}] &= \mathrm{F.T.}[P'(\tilde{\nu})] * \mathrm{F.T.}[e^{+i\theta_{\tilde{\nu}}}] & (5.15)\\ \Rightarrow \mathcal{I}_{\rm e}(x) &= \mathcal{I}_{\rm u}(x) * \chi(x) & (5.16) \end{aligned}$$

In other words, the unsymmetric (measured) interferogram can be transformed into the true (symmetric) interferogram by convolution with a symmetrising function

$$\chi(x) = \mathrm{F.T.}(e^{+i\theta_{\tilde{\nu}}}). \tag{5.17}$$

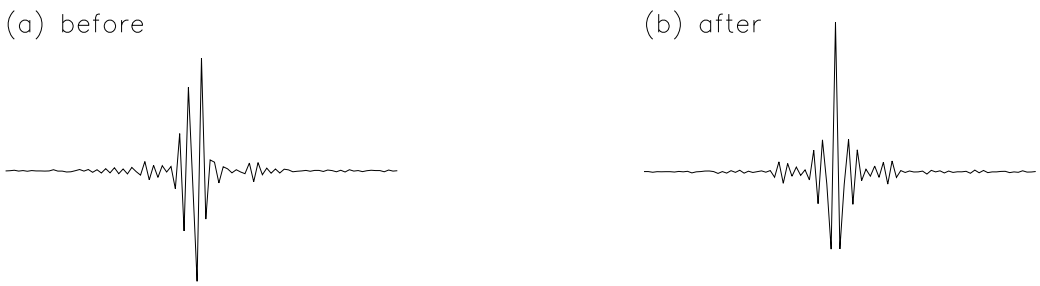

Figure 5.3: The centreburst of a typical CIRS interferogram (a) before and (b) after phase correction by the Forman method.

This is known as the **Forman Method** of phase error correction (Forman et al., 1966; Forman, 1966). Figure 5.3 shows the centreburst of a typical interferogram both before and after phase error correction. After correction, the ideal spectrum is calculated from the symmetrical interferogram using the cosine transform (equation 5.2).

5.1.4 Phase Error Correction with CIRS Spectra

In order to calculate the phase function we clearly need a two-sided interferogram: measuring the phase is equivalent to measuring the asymmetry in the interferogram. However, in a two-sided interferogram each frequency is measured twice, as $+\tilde{\nu}$ and $-\tilde{\nu}$ which is a great inefficiency in terms of measurement time, data storage space, and, in the particular case of space instruments, a factor two increase in downlink time for the same data.

In CIRS therefore a compromise measurement is made. Each interferogram contains both a short negative path-difference section and a much longer positive path-difference part. This allows a low-resolution estimate of the phase spectrum to be computed from a small two-sided interferogram symmetric about the central maximum (ZPD).

In turn, the phase correction function $\chi(x)$ is calculated, which can then be convolved with a much longer (i.e. higher resolution) one-sided, asymmetric interferogram

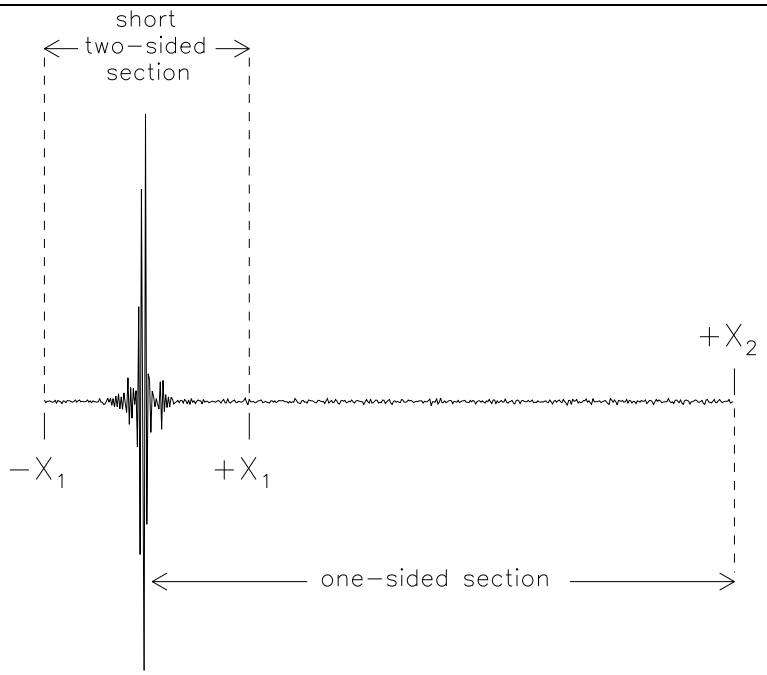

Figure 5.4: Typical measured interferogram before correction. Note the asymmetry of peaks on either side of the zero-path difference. The short, two-sided interferogram is extracted and used to estimate the phase (asymmetry) of the whole at low resolution. After correction, the long one-sided portion is used to calculate the power spectrum at maximum resolution.

to produce a corrected symmetric version $\mathcal{I}_{\rm e}$. Note however that this method of symmetrisation relies on the assumption that the phase drift is only slowly varying. Finally, $\mathcal{I}_{\rm e}$ is transformed to give the correct $P_{\rm e}$.

Consider figure 5.4. The interferogram has been measured for path differences from $-X_1$ to $+X_2$. The steps to calculating the power spectrum are as follows:

1. The short, two-sided portion from $-X_1$ to $+X_1$ is extracted: $\mathcal{I}_{\rm 2S}(x)$.

2. $\mathcal{I}_{\rm 2S}(x)$ is transformed, and the complex phase angle $\exp(i\theta(\tilde{\nu}))$ calculated.

3. $\exp(i\theta(\tilde{\nu}))$ is apodised and inverse transformed, to give $\chi(x)$ - the phase correction function.

4. $\chi(x)$ is convolved with the entire original spectrum from $-X_1$ to $+X_2$.

5. The negative path difference part is discarded, and the remaining portion from 0 to $+X_2$ is the symmetric, one-sided interferogram at high-resolution $\mathcal{I}_{\rm e}$. This is apodised and cosine-transformed to give the final estimate of $P_{\rm e}(\tilde{\nu})$.

Figure 5.5 shows some examples of phase correction applied to CIRS spectra.

5.1.5 Wavelength Calibration

Wavelength calibration in CIRS is achieved by using a reference laser beam at 783 nm which is used as a range-finder for the scan mirror. The scan mirror moves at a constant speed of 0.0208 cm s^{-1}. While the mirror is moving, data are logged every zero-crossing of the laser beam, *i.e.* every 391.5 nm of light-path difference, or every 195.75 nm of mirror travel.

Channels 3 and 4 in the mid-IR each sample from an array of five out of ten detectors (various observing modes are available; see §2.3.3). Each detector is sampled in turn, so the number of points per mid-IR spectrum is decreased relative to a FP1 spectrum by a factor of 5. Finally, all the data channels are re-sampled electronically before outputing the standard interferograms; the re-sampling factors are 18, 4.5 and 5 for channels 1, 3 and 4 respectively.[2] The re-sampling algorithm takes a consecutive sequence of points, and performs an integral average using a quadrature scheme.

Therefore the number $n_{\rm p}$ of sample points produced for an observation of duration t is:

$$n_{\rm p} = \frac{\text{light path change}}{\text{logging interval}} \times \frac{1}{\text{resample factor}} \tag{5.18}$$

$$= \frac{(2 \times 0.0208 \times t)}{(783/2 \times 10^{-7})} \times \frac{1}{(n_{\rm d} \times n_{\rm resamp})} \tag{5.19}$$

where $n_{\rm d}$ is the number of detector elements switched between and $n_{\rm resamp}$ is the re-sampling factor given above. For example, a 10 s observation with FP4 would have $n_{\rm p} = 425$.[3] The spacing of output points on the transformed power spectrum is half the

[2]Note that the Nyquist condition for sampling is relaxed when the *order* of the spectrum is second or greater. The required sampling interval is decreased from $(2\tilde{\nu}_{\rm MAX})^{-1}$ to $(2(\tilde{\nu}_{\rm MAX} - \tilde{\nu}_{\rm MIN}))^{-1}$, where $\tilde{\nu}_{\rm MAX}$ and $\tilde{\nu}_{\rm MIN}$ are the highest and lowest frequencies in the passband. It is also necessary that $(\tilde{\nu}_{\rm MAX} - \tilde{\nu}_{\rm MIN})$ is an integer fraction of $\tilde{\nu}_{\rm MAX}$.

[3]Actually, there are slightly fewer points due to the mirror flyback time.

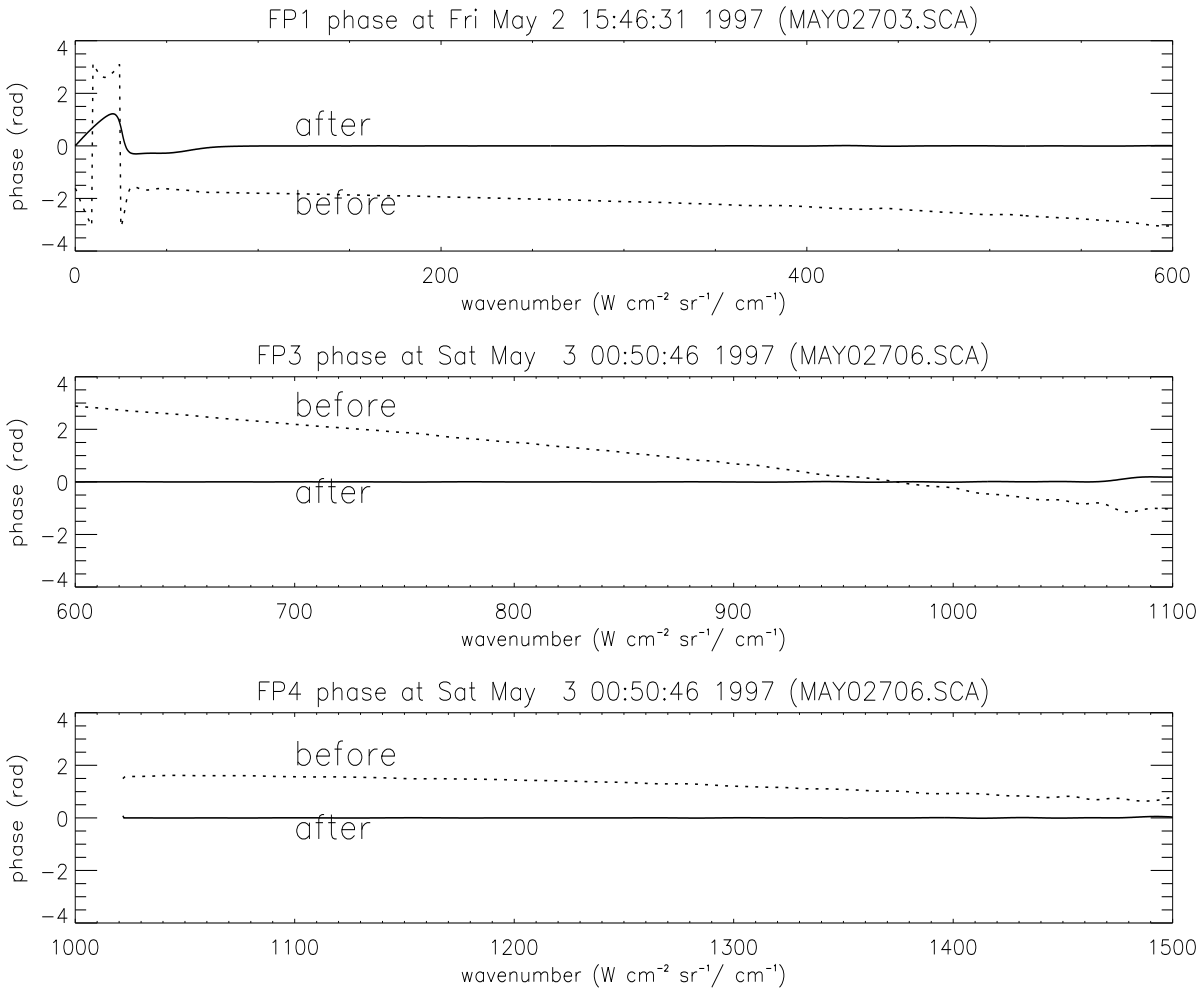

Figure 5.5: Examples of phase spectra calculated from the double-sided portion of the interferogram, both before and after correction. Top: FP1. Middle: FP3. Bottom: FP4. The phase spectra before correction exhibit a slowly varying phase drift with wavenumber. After correction, the low-order drift has been almost completely eradicated and the phase is now close to zero everywhere (some higher order phase variation still remains near zero wavenumbers for FP1). A zero phase means that the spectrum is symmetric and constructed from only cosine Fourier components.

reciprocal of the maximum path difference in the beam, X

$$\delta\tilde{\nu} = \frac{1}{2X} \tag{5.20}$$

$$X = 2 \times 0.0208 \times t \tag{5.21}$$

or alternatively, by re-arranging equation 5.19:

$$\delta\tilde{\nu} = \frac{1}{2 \times c_{\mathrm{FP}} \times n_{\mathrm{p}}} \tag{5.22}$$

which is a more useful form for the computer code, because the number of points in the interferogram is always a known figure, whereas the exact duration of the observation is not independently measured. c_{FP} is a constant factor for each focal plane defined:

$$c_{\mathrm{FP}} \equiv n_{\mathrm{d}} \times n_{\mathrm{resamp}} \times \frac{783}{2} \times 10^{-7}. \tag{5.23}$$

Taking the same example as before of a 10 s observation with FP4: the c_{FP} is 9.7875^{-4} cm, so if all the points of the interferogram were included in the transform, the output point spacing would be 1.2 cm^{-1}.

In practice, the interferogram is *zero-padded* so that it has a number of points equal to some power of two. This enables one to use the Fast Fourier Transform (FFT) or Cooley-Tukey algorithm for fast numerical calculation of the transform (Press et al., 1992, chap. 12). In the above example, the 425 data points would be placed into a 512 point data array and the remaining 87 empty spaces filled with zeroes. The power spectrum resulting would then have 512 points spaced $1.2 \times (425/512) = 1.0$ cm^{-1} apart.

5.1.6 Resolution

There are several possible definitions of the resolving power of an instrument. One method is to use the Rayleigh criterion, which judges the minimum separation of two near equal-strength lines which would allow them to be distinguished. A more general touchstone is to consider the Full Width to Half Maximum (FWHM) amplitude of the Instrumental Line Shape (ILS), *i.e.*, the width at half height which a very narrow (delta-function) spectral line would have after processing by the instrument.

This number is important because it gives some estimate of what scale spectral structure will be visible. The ILS function convolves the final spectrum, hence all lines and other features are broadened to some extent. If the ILS is much narrower than a given line, the true shape of the line will be almost unchanged. If however, the ILS is broader than the line, then it is the ILS width itself which will be dominant.

For example, consider an ILS with a FWHM of $\Delta\tilde{\nu}_i$ and a particular spectral line which has a width $\Delta\tilde{\nu}_l$. Then the resulting width of the line after convolution will be approximately:

$$\Delta\tilde{\nu}_f \simeq \left[(\Delta\tilde{\nu}_i)^2 + (\Delta\tilde{\nu}_l)^2\right]^{1/2}. \tag{5.24}$$

Note that this is strictly true only for a pair of Gaussian profiles; however, for practical purposes it provides a reasonable estimate. Assuming equation 5.24, we can put in some numbers to show how quickly the wider profile will dominate the final width. Let $\Delta\tilde{\nu}_i = 3.0$ and $\Delta\tilde{\nu}_l = 1.0$: then $\Delta\tilde{\nu}_f = 3.16$, which is only 5% different from the width of the wider profile.

In short, by controlling the width of the ILS we effectively control the output resolution. This width is determined as follows.

The FWHM of a given ILS is simply related to the width of the apodising function, or spectral window, which is imposed in the measurement (spatial) domain, before the

FT.

If X is the maximum path difference of the interferogram, then by simply solving $\mathrm{sinc}(2\tilde{\nu}X) = 0.5$, we find that the FWHM of the sinc ILS (resulting from boxcar apodisation) is $0.603/X$. This is the narrowest FWHM it is possible to have, because it uses the most information from the interferogram. In general:

$$\Delta\tilde{\nu}_{\mathrm{ILS}} = \Gamma \cdot \frac{1}{X} \tag{5.25}$$

where Γ is a numerical factor which is different for each type of apodisation. For triangle-function apodisation, the Γ of the sinc^2 ILS is 0.890, and the Γ-values for the apodisation types described in the previous section are given in table 5.1.

Finally, we are now in a position to determine how many points are required in the FT to achieve a given resolution with a given type of apodisation function. Using the definitions of equations 5.21 and 5.23 we can rearrange equation 5.19 into: $X = n_{\mathrm{p}} \times c_{\mathrm{FP}}$. Equation 5.25 can then be rearranged to show:

$$n_{\mathrm{p}} = \frac{\Gamma}{\Delta\tilde{\nu}_{\mathrm{ILS}} \times c_{\mathrm{FP}}} \tag{5.26}$$

E.g., for an observation with FP4 to have a FWHM resolution of 1 cm^{-1} using the Norton & Beer type 2 apodisation, the number of points required is: $0.844/(1.0 \times 9.7875 \times 10^{-4}) = 862$.

5.1.7 Example Calculations of CIRS Power Spectra

CIRS power spectra were calculated using a new Fourier Transform code `tran` developed for the purpose, which first uses the Forman method to symmetrise the raw standard interferograms, and then calculates the power spectra, including optional apodisation

type and resolution width. `C` code from Numerical Recipes (Press et al., 1992, chap. 12) is used to implement the necessary FFTs and convolutions.

To verify its operation, this code may be compared against the results of a similar code developed at GSFC by L. Herath. This code `wfts` has the same basic functionality as `tran` and is known to calculate CIRS power spectra correctly. Unfortunately, `wfts` was left in an incomplete and undocumented state, which necessitated the development of the present code.

Figure 5.6 shows the residual difference between spectra calculated with the two codes, which is typically 0.1% of the peak level. This difference is probably due to two differences in the calculation methods. Firstly, the new `tran` code uses the Forman method to implement the phase correction, whereas `wfts` uses the Mertz method, which corrects the spectrum in the frequency domain rather than in the spatial domain. Secondly, the apodisation functions used are slightly different although the FWHM is nominally the same.

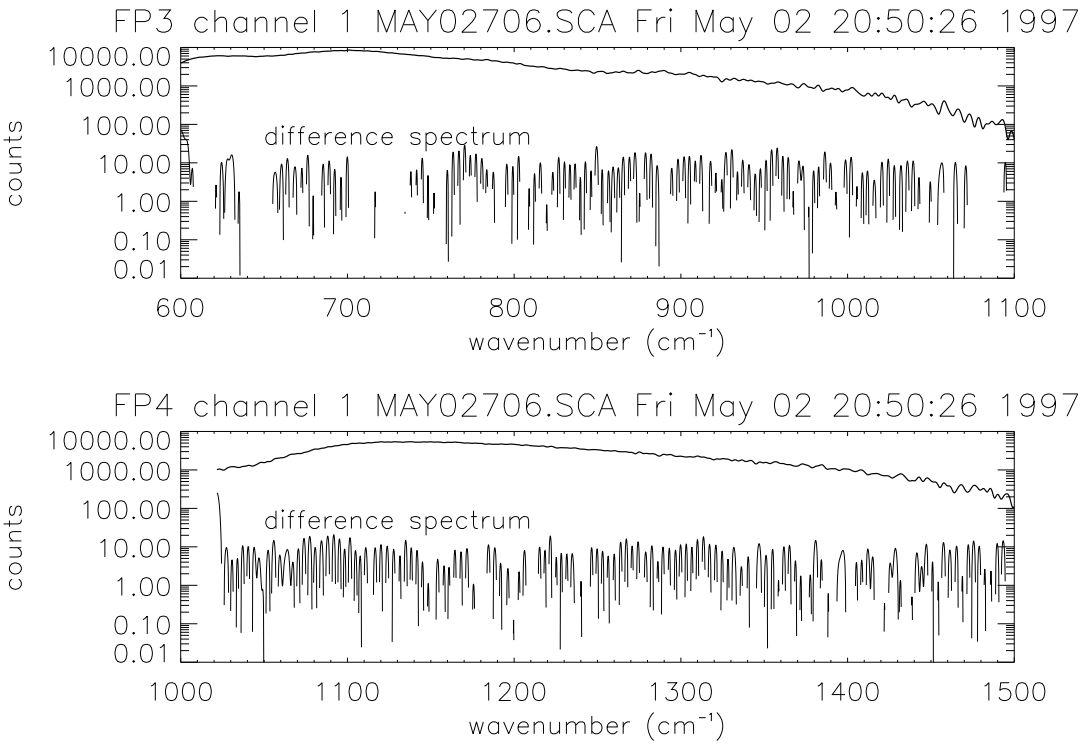

Figure 5.6: Comparison of spectra calculated with `tran` vs. the older `wfts` code, for FP3 and FP4. For each MIR focal plane, both the calculated `tran` spectrum and the difference between the `tran` and `wfts` spectrum is plotted. Spectral resolution is 3 cm^{-1}.

5.2 Radiometric Calibration and Noise

The result of any observation with CIRS, after transforming the interferogram, is a power spectrum scaled in detector 'counts':

$$C(\tilde{\nu}) = R(\tilde{\nu})[I(\tilde{\nu})_{\rm instr} - I(\tilde{\nu})_{\rm tar})] \tag{5.27}$$

where:

$C(\tilde{\nu})$ = power spectrum in counts,
$R(\tilde{\nu})$ = instrument spectral responsivity,
$I(\tilde{\nu})_{\rm instr}$ = background radiance from instrumental emissions,
$I(\tilde{\nu})_{\rm tar}$ = radiance from target.

For FP1, both the instrument (optics, telescope) and the detector are at 170 K. Most observations with CIRS will be made of targets which are typically less than 170 K, therefore $I(\tilde{\nu})_{\rm instr} = B(\tilde{\nu})_{\rm 170K} > I(\tilde{\nu})_{\rm tar}$ and the instrument is a net radiator. The signal is positive so long as the detector radiates more than it absorbs.

For FP3 and FP4, the situation is more complicated. The instrumental radiance is composed of contributions from both the 170 K optics and the 80 K focal plane, so that $I(\tilde{\nu})_{\rm instr}$ is some combination of these:

$$I(\tilde{\nu})_{\rm instr} = \beta B(\tilde{\nu})_{\rm 170K} + (1-\beta)B(\tilde{\nu})_{\rm 80K} \simeq B(\tilde{\nu})_{T_{\rm crit}}. \tag{5.28}$$

where β is a fraction between 0 and 1. This implies that there is some target temperature $80 < T_{\rm crit} < 170$ K at which $(I(\tilde{\nu})_{\rm instr} - I(\tilde{\nu})_{\rm tar}) \simeq 0$ and the net counts falls to zero. For targets either warmer or cooler than $T_{\rm crit}$ the instrument will give a negative and a

positive signal output respectively. This notion seems somewhat surprising at first glance: that the detectors, at 80 K, appear to be receiving zero signal even when the target is warmer than 80 K.

The answer lies in the interference pattern. Although the target is causing a bright central fringe to appear at the focal plane (at ZPD), the instrument is also radiating outwards, back into the interferometer at $T_{\rm crit}$. Half of this radiance goes out to space, whilst the other half comes back via the beamsplitter to the focal plane, but with a phase change of 180° and so forms dark fringes. Therefore when the source is at $T_{\rm tar} \simeq T_{\rm crit}$, the bright and dark fringes, from the target and instrument respectively, cancel out and the central fringe has minimum amplitude. After transforming, this corresponds to the minimum of output signal. At $T_{\rm tar} > T_{\rm crit}$, the net interference effect on the central fringe is for it to be bright and at $T_{\rm tar} < T_{\rm crit}$ the central fringe is dark. Note that, according to the definition of equation 5.27, a positive signal results when the instrumental contribution exceeds the target contribution (i.e. when there is a dark fringe).

An alternative view of the measurement process is to consider the electrical reponse of the detectors. These are a.c. coupled, and so only respond to signals from the interferometer. The signal from the interferometer is made of equal parts of light from both ends of the instrument, *i.e.* from the target and from the focal plane, but these are in antiphase, so it is their difference which is measured.

Note in equation 5.28 that if the response is always taken to be positive, then $C(\tilde{\nu})$ may be positive or negative. It is important to remember this sign when adding or differencing spectra of different temperatures.

The important radiometric unknowns are $R(\tilde{\nu})$ and $I(\tilde{\nu})_{\rm instr}$. With accurate knowledge of these two quantities, the measured $C(\tilde{\nu})_{\rm target}$ can be used to find $I(\tilde{\nu})_{\rm target}$. Hence, a minimum of two known temperature calibration targets are required.

5.2.1 Ground vs. Inflight Calibration

It is well known that the absolute calibration of instruments may not remain constant during launch and long exposure to the space environment. In order to obtain correctly characterised observations therefore it is important to measure key instrument parameters before and after any set of in-flight observations.

In space, this is achieved slightly differently for the MIR and the FIR planes. For the FIR, the two temperature sources are:

1. Deep Space: the 2.73 K background is effectively a zero-radiance source; so $C(\tilde{\nu})_{\text{deepspace}} = R(\tilde{\nu}) \cdot I(\tilde{\nu})_{\text{instr}}$.

2. A second target is not required: the instrument (optics and detector) temperature is reliably thermostated to 170 K, hence we know that it must have zero net signal when it views a 170 K blackbody. Importantly, we do not actually need to make any measurement. In other words, by accurately controlling the instrument temperature we can say with certainty that: $I(\tilde{\nu})_{\text{instr}} = B(\tilde{\nu})_{170\text{K}}$.

For the MIR:

1. Once again, deep space is the zero-radiance source so $C(\tilde{\nu})_{\text{deepspace}} = R(\tilde{\nu}) \cdot I(\tilde{\nu})_{\text{instr}}$.

2. The second target is an internal black shutter which will be at the same temperature as the instrument and telescope. It is therefore equivalent to an external blackbody at the same temperature as the instrument, and $I(\tilde{\nu})_{\text{tar}} = B(\tilde{\nu})_{170\text{K}}$. The net counts in this case are non-zero.

Calibration of the instrument with only two temperature sources makes an assumption that the responsivity is linear: that it is the same at two different temperatures. This may not be the case. Hence the essence of the ground radiometric testing is to fully characterise the instrument in terms of the following parameters:

1. **Responsivity:** The spectral responsivity of the instrument observing a target at temperature T is defined as the output counts minus counts at zero radiance (the background and offset), divided by the input radiance, as a function of wavenumber. It is usually impractical to measure $C_{\tilde{\nu}}(T{=}0)$ in the laboratory, however the responsivity may be calculated by observing a second blackbody target at a different temperature T_0 and using the formula:

$$R_{\tilde{\nu}}(T) = \left| \frac{C_{\tilde{\nu}}(T) - C_{\tilde{\nu}}(T_0)}{B_{\tilde{\nu}}(T) - B_{\tilde{\nu}}(T_0)} \right| . \tag{5.29}$$

2. **Linearity:** The formula for responsivity given above assumes that the the net number of counts $\Delta C_{\tilde{\nu}}(T)$ increases linearly with $\Delta I_{\tilde{\nu}}(T)$. In fact, this must be assessed by observing several target temperatures and plotting the responsivity (see §5.2.3).

3. **NESR:** The Noise Equivalent Spectral Radiance at a given wavelength is the 1σ random fluctuation on the signal, calibrated in radiance units. This is equivalent to the noise in counts, divided by the responsivity, assuming that the measurements are uncorrelated.

During the commissioning of the CIRS instrument at GSFC, a substantial number of spectra of various cold-body sources were taken. The next section outlines how the data were collected. Subsequent sections describe the analysis of the data, using the Fourier transform program for calculation of power spectra, to determine the above parameters.

5.2.2 Data Aquisition

The radiometric performance of the fully assembled CIRS flight instrument was assessed twice: during August 1996 and again in May 1997. The measurements were made at GSFC by a scientific team led by V. Kunde. During the 9-month interim between the

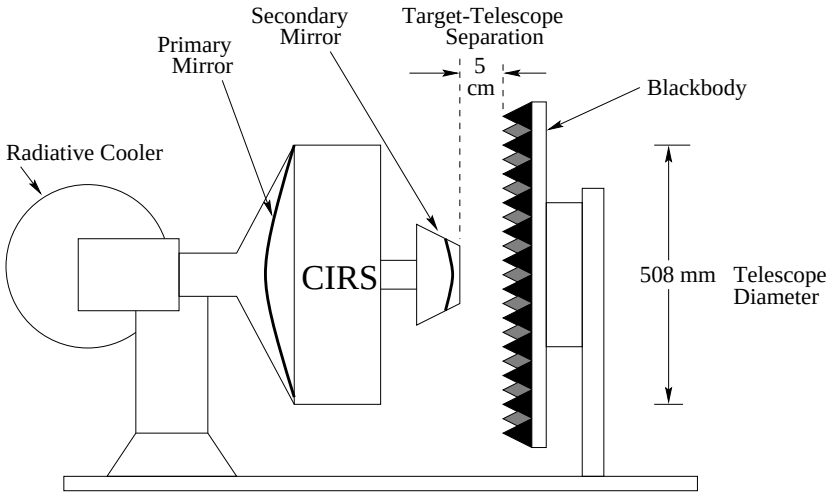

Figure 5.7: Diagram of the apparatus used at GSFC to measure the radiometric performance of CIRS. The entire apparatus was placed in a large evacuated vacuum tank and cooled (see text).

two radiometric tests, the instrument was disassembled and reassembled, and the gains of the amplification stages changed (see results following).

Figure 5.7 shows the apparatus used for the measurements. CIRS operated in flight configuration, and the optics were cooled to the flight operating temperature of 170 K. The passive radiative cooler was pointed at a 25 K target cooled by LHe which allowed the MIR detectors to cool to ∼80 K. A full aperture blackbody radiator was placed directly in front of the main telescope, completely filling the instrument FOV. This was also cooled by LN2 to the required target temperature.

The temperature of the mid-IR detectors was varied from 77 K to 85 K. During the May 1997 calibration there were also some measurements made at $T_{\rm FPA}$=90 K, although the FP4 detectors were not active at this higher temperature. For each $T_{\rm FPA}$, the temperature of the target was varied from ∼82 K to ∼170 K incrementally. Tables 5.2 and 5.3 show the dates and temperature settings.

For each setting of ($T_{\rm FPA}$, $T_{\rm TAR}$) four blocks of measurements were taken, switching between the ODD and EVEN detection modes in the mid-IR, and with the MIR shutter

$T_{\rm FPA}$	$T_{\rm TAR}$(K)=82	125	150	160	170
77-78 K	82.5–85.0 K (aug13601.sca)	124.2 K (aug13603.sca)	150.0 K (aug13604.sca)	160.0 K (aug13605.sca)	170.2–170.1 K (aug13606.sca)
80-81 K	81.9 K (aug14601.sca)	125.2 K (aug14602.sca)	151.5–152.2 K (aug14603.sca)	160.0–159.6 K (aug14604.sca)	170.0–169.6 K (aug14605.sca)
85 K		124.2–126.7 K (aug15601.sca)		159.8 K (aug15602.sca)	169.7 K (aug16601.sca)

Table 5.2: The target and FPA temperatures of the 1996 radiometric calibration

$T_{\rm FPA}$	$T_{\rm TAR}$(K)=82	110	130	150	160	170
78.5 K	80.5–80.6 (may05706.sca)	112.4–112.5 (may04702.sca)				170.2 (may06701.sca)
80 K	81.0–85.0 K (may02703.sca)	108.7–109.0 K (may03702.sca)	128.2–128.3 K (may03703.sca)	153.5–154.0 K (may02704.sca)	161.8–162.0 K (may02705.sca)	172.3 K (may02706.sca)
85 K	83.4–83.5 K (may04701.sca)	110.7–110.9 K (may03705.sca)	128.6 K (may03704.sca)	147–149 K (may06703.sca)	161.8 K (may06702.sca)	170.6–170.9 K (may04703.sca)
90 K	83.6–83.9 K (may06704.sca)					170.2–170.3 K (may07701.sca)

Table 5.3: The FPA and target temperatures of the 1997 radiometric calibration

OPEN and then CLOSED (see table 5.4 and section 2.3).[4] Each block of measurements consisted of at least 30 individual 20-second scans recorded simultaneously on the three FPs.

5.2.3 Responsivity and Linearity

Method

The first step in the data analysis was to calculate the responsivity $R(\tilde{\nu})$, which allows the spectra to be calibrated in physical units. This was a two stage process, for which two new `C` codes were written.

The first stage was to transform individual interferograms into power spectra, and to

[4]The shutter closed measurements were taken primarily to assess the efficacy of in-flight calibration using the shutter as a 170 K black body.

Block	Shutter	FP1	FP3	FP4
A	OPEN	ON	EVEN	EVEN
B	OPEN	ON	ODD	ODD
C	CLOSED	ON	EVEN	EVEN
D	CLOSED	ON	ODD	ODD

Table 5.4: Instrument settings during each calibration run.

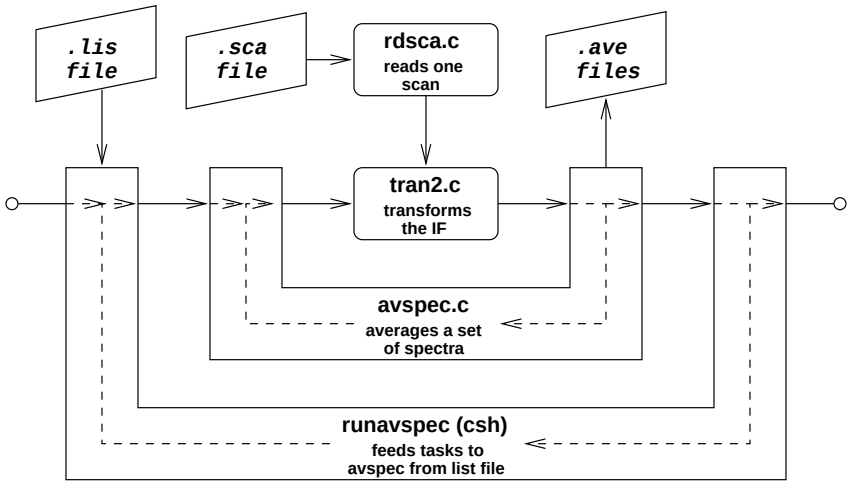

Figure 5.8: Schematic diagram of the averaging procedure, showing the interaction of data files and program modules. The core program is `tran` which performs the transform and apodisation of standard interferograms. Power spectra taken at the same target and focal plane temperature were averaged by the code `avspec`. The details of which scan files contained which interferograms and at which temperatures were stored in a list file. A batch processing program (`runavspec`) was used to automate the data reduction, by sending averaging 'jobs' to the averaging program, which used the transform program as a subroutine.

co-add and average the ∼30 power spectra corresponding to a particular $T_{\rm FPA}$ and $T_{\rm TAR}$ for each detector. The spectra were apodised during the transform to the desired width. This process is illustrated by figure 5.8.

The second task was to subtract cold from warm mean spectra, and divide by the difference in Planck functions, to obtain the responsivity, as given by equation 5.29. This method assumes that the responsivity varies linearly with temperature. As a check on this, the responsivity was calculated twice using two different warm temperatures for the mid-IR detectors, namely 160 K and 170 K. The cold temperature was 82 K. For the far-

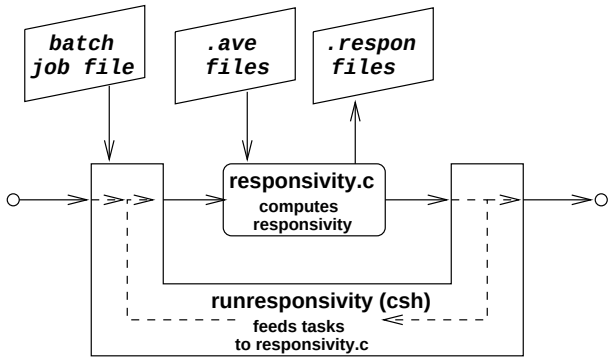

Figure 5.9: Schematic diagram of the responsivity calculation, showing the interaction of data files and program modules.

IR, which has a greater response at lower temperatures, the responsivity was calculated twice using different cold temperatures, namely 82 K and 125–130 K. Figure 5.9 shows how the calculation was automated. The result was a set of responsivity spectra for each detector, at a range of target and FPA temperatures.

Discussion of Mean Spectral Response

The two main sequences at constant T_{FPA} from each year were analysed: 1996 T_{FPA}= 78 K, 80 K; and 1997 T_{FPA}= 80 K, 85 K.

Some examples of mean power spectra from the 1997 T_{FPA}= 80 K sequence are plotted in figures 5.10–5.12, for FP1, FP3 detector 2 and FP4 detector 2, all at 3 cm^{-1} resolution and apodised using the Norton & Beer type 2 function which gives a medium level of apodisation. These show how the responses vary with target temperature differently for the three focal planes.

For FP1, it can be seen that the magnitude of the power spectra decreases with increasing temperature. This is because the response is proportional to the difference between the target temperature and the instrument temperature (170 K) as given by equation 5.27. Hence, the maximum response is to the 80 K target, and the response decreases to almost zero at 170 K.

For FP3 and FP4 the response does not continuously increase with temperature, as described in §5.2.3. As the temperature increases from ∼80 K, the magnitude of the

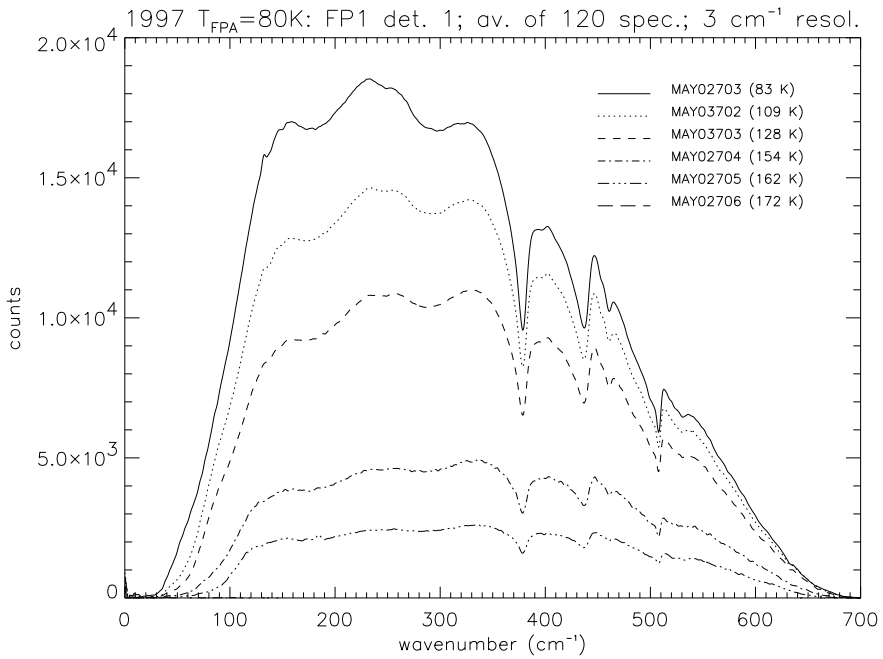

Figure 5.10: FP1 sequence of mean power spectra for various target temperatures and at a constant detector temperature of 170 K. Each mean spectrum is an average of 120 spectra, recorded 02-03/05/97.

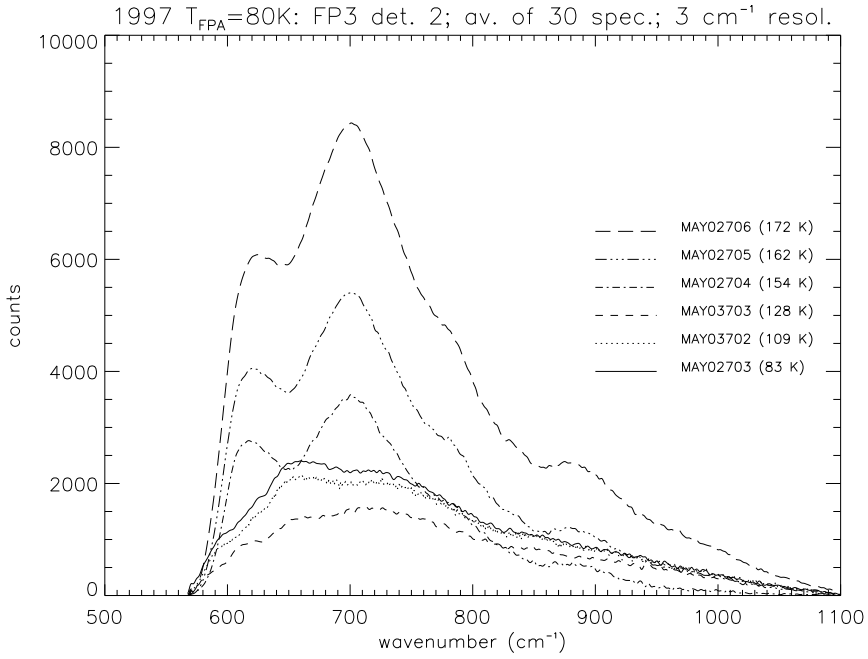

Figure 5.11: FP3 detector 2 sequence of mean power spectra for various target temperatures and at a constant detector temperature of 80 K. Each mean spectrum is an average of thirty spectra, recorded 02–03/05/97.

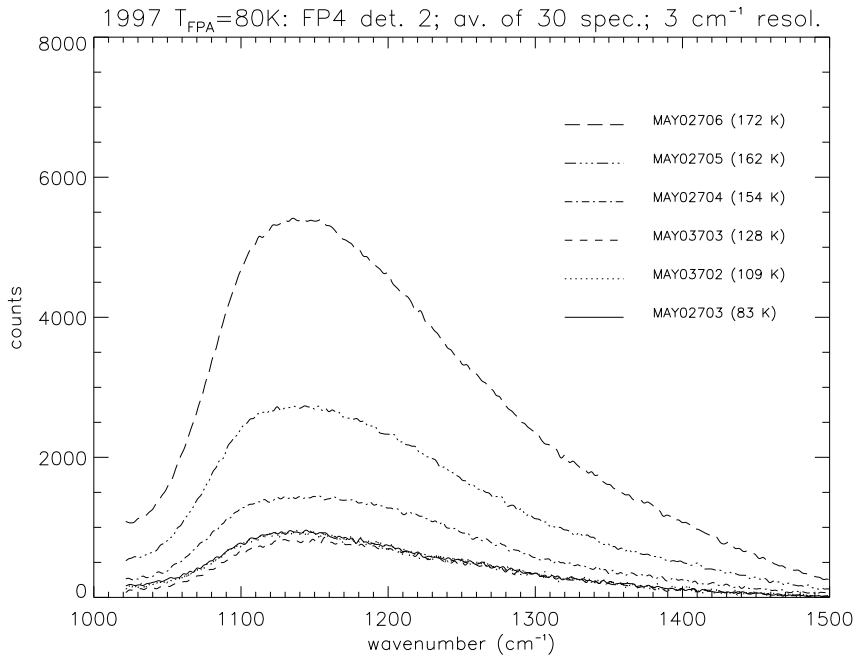

Figure 5.12: FP4 detector 2 sequence of mean power spectra for various target temperatures and at a constant detector temperature of 80 K. Each mean spectrum is an average of thirty spectra, recorded 02–03/05/97.

response initially decreases, becomes close to zero when $T_{\rm TAR} \simeq T_{\rm crit}$, somewhere between 130 and 150 K, and then increases again. In fact, by inspection of equation 5.27, we see that when the $T_{\rm TAR}$ is above $T_{\rm crit}$, the sign of the response should be negative.

In order to be able to add or subtract spectra, which is required to calculate the responsivity and linearity, we must add back in to the spectra the sign information which has been lost during the Fourier Transform. In principle, it is possible to determine the sign of the response from the phase (polarity) of the ZPD of the interferogram. A positive signal at ZPD should indicate the detector is hotter than the source, and vice versa, with a sharp reversal at $T_{\rm TAR}=T_{\rm crit}$.

In practice however the phase of the ZPD has been found to drift from positive to negative along the pixel elements of each array, even when the target temperature is the same. This drift is not well understood at present, but may be related to the resampling of the interferogram in the instrument, which reduces the data rate. In addition, the polarity has shown unpredictable behaviour near $T_{\rm TAR}=T_{\rm crit}$. This may at least in part be due to a contribution to the radiance from the beamsplitter which may have a fixed

phase angle offset relative to the other beams, known as the Revercomb effect (Revercomb et al., 1988).

Although the ZPD of the interferogram has proved to be unreliable when determining the absolute sign of the IFM, it is possible to use the fact that we expect the response to be linear against net radiance (to first order) to determine where the sign reversal occurs.

The method used was to choose a wavenumber near the middle of the range for each array (FP3 and FP4), where the counts are high, and to plot the counts against blackbody radiance for each value of T_{TAR}. For each point, there is in principle an uncertainty in the sign of the response in counts. However, we may reasonably assume that the T_{TAR}= 170 K point lies at negative counts, whilst the T_{TAR}= 80 K point lies at positive counts. Then, by requiring that the remaining intervening points lie approximately on a straight line joining these two extrema, the sign of the intervening points is easily fixed.

This process was repeated four times for each focal plane, once for each sequence of T_{TAR} at fixed T_{FPA} (figures 5.14 and 5.15). In addition, a similar process was used to arrange linearly the responses of the FP1 detector for various T_{TAR}; note however in this case that the response is always positive and does not cross the x-axis (figure 5.13). A straight line fit has been applied to the data points, using a 'robust' least-square deviation method from the data analysis package `IDL`.

For FP3 and FP4, the 'break-even' or 'fold' point temperature T_{crit} is indicated on each figure: this was determined by inverting the Planck spectral radiance at the x-axis intercept of the line, to obtain the equivalent brightness temperature. Also marked on the figures is the gradient of the straight line fit dC/dI, the magnitude of which is equivalent to the responsivity of the detector at that wavenumber.

Figure 5.15 shows that FP4 has a $T_{\mathrm{instr}} \simeq 149$ K in 1996 and 142 K in 1997, independent of T_{FPA}. If $B(\tilde{\nu})_{80\mathrm{K}} << B(\tilde{\nu})_{T_{\mathrm{crit}}}$, which is the case in the mid-IR, then equation 5.28 becomes approximately:

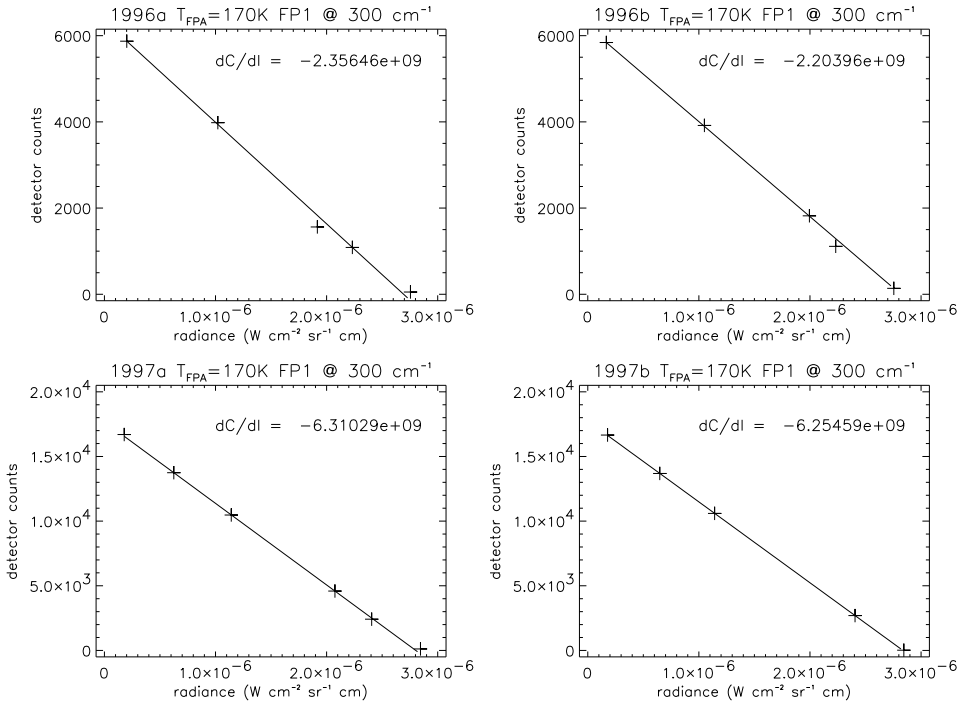

Figure 5.13: Response linearity of the FP1 detector at 300 cm^{-1}, near the peak of the blackbody measured spectrum. The magnitude of the gradient dC/dI of the straight line fit to the response is the responsivity. The gradient of the line is negative, as the counts decrease with increasing radiance from 80 K to 170 K. The response does not cross the x-axis, as the target temperature never exceeds the detector temperature.

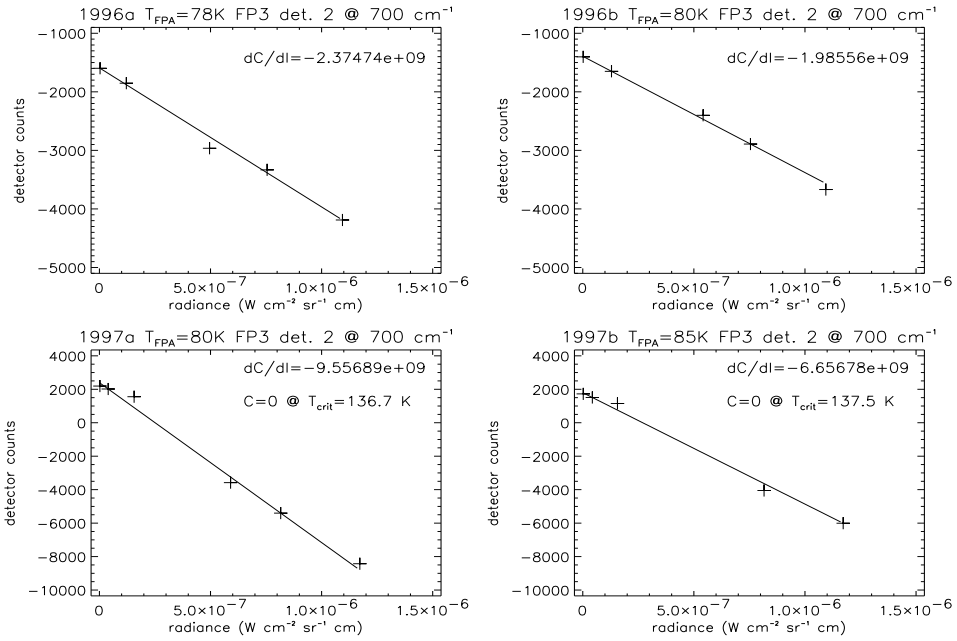

Figure 5.14: Response linearity of the FP3 detector 2 at 700 cm^{-1}, near the peak of the blackbody measured spectrum. The magnitude of the gradient dC/dI of the straight line fit to the response is the responsivity. The gradient of the line is negative, as the counts decrease with increasing radiance from 80 K to 170 K. Where the straight line crosses the x-axis is the fold point, the temperature of which (T_{crit}) is determined by inverting the Planck spectral radiance at this point. Note that in 1996 no fold point occurs; suspected reasons for this are outlined in the text.

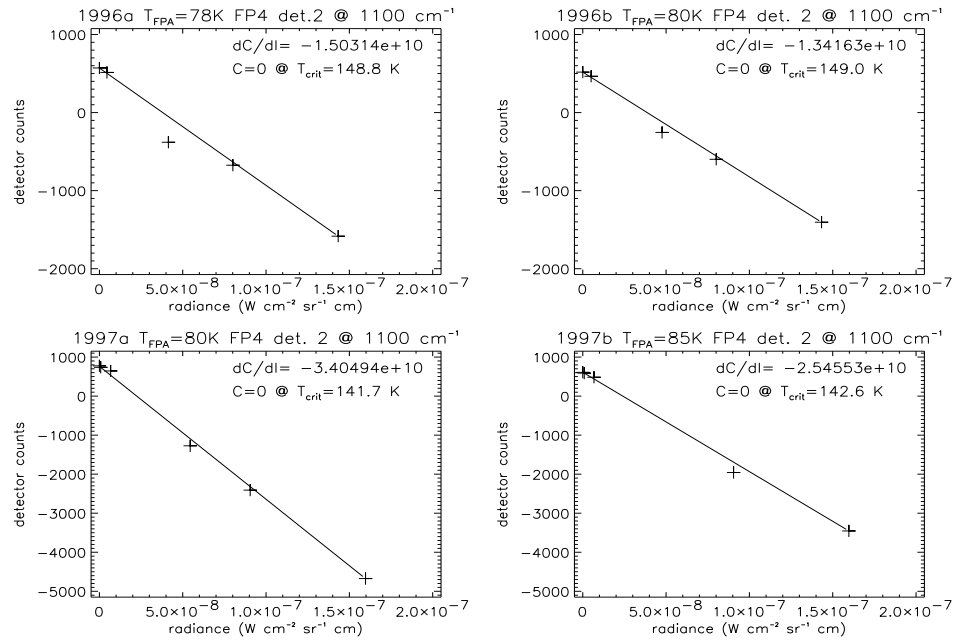

Figure 5.15: Response linearity of the FP4 detector 2 at 1100 cm^{-1}, near the peak of the blackbody measured spectrum. The magnitude of the gradient dC/dI of the straight line fit to the response is the responsivity. The gradient of the line is negative, as the counts decrease with increasing radiance from 80 K to 170 K. Where the straight line crosses the x-axis is the fold point, the temperature of which (T_{crit}) is determined by inverting the Planck spectral radiance at this point.

$$\beta B(\tilde{\nu})_{170\mathrm{K}} \simeq B(\tilde{\nu})_{T_{\mathrm{crit}}}. \tag{5.30}$$

and we find that β is 0.27 and 0.16 for FP4 in 1996 and 1997 respectively. This is the same as saying that in 1997 the instrumental background emission could be approximated by a 170 K blackbody filling 16% of the detector FOV.

For FP3 however, the 1996 data is unusual. If the points at colder T_{TAR} are given a positive sign, and the warmer points a negative sign, then there is no apparent straight-line fit at all. If however, all the points are assumed to be at negative counts then an obvious straight-line fit ensues (upper two plots of figure 5.14). If this is the case, then there is no crossing of the x-axis, i.e. there is no fold point and T_{crit} is undetermined. To add to the confusion, the 1997 data does not show this problem, and a T_{crit} of $\simeq$137 K is indicated, giving β=0.24. In short, it appears that in 1996, there was a problem in the data acquisition which somehow caused the cool T_{TAR} points to appear warm, but only for FP3. How is a coherent picture then to be drawn from these data?

It is difficult to determine exactly the cause of the problem without a more detailed knowledge of the experimental procedure. One strong possibility however, follows from a memorandum received by the author from the instrument P.I. (V. Kunde, private communication) which states that the mid-IR calibration shutter was known to 'droop' into the instrumental field of view during the ground calibration tests. This problem occurs simply due to the Earth's gravity: the shutter has been designed to work normally in space. In addition, this problem is known to affect the FP3 FOV more than that of FP4.

This then may explain the unusual data: the response of FP3 when viewing a cool target appears to be anomalously high, because some substantial fraction of the field of view was actually seeing the 170 K shutter. It appears that the contribution of the shutter was great enough to cause the apparent source radiation (*i.e.* 'real' source

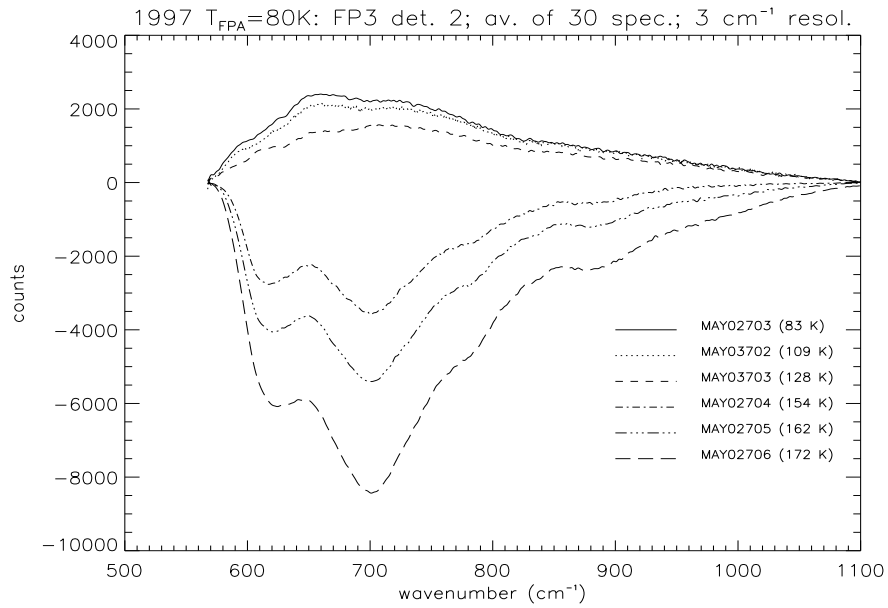

Figure 5.16: FP3 detector 2 sequence of mean power spectra for various target temperatures and at a constant detector temperature of 80 K. Each mean spectrum is an average of thirty spectra, recorded 02–03/05/97. The sign of the response has been added, so that the spectra form a monotonically decreasing sequence with increasing $T_{\rm TAR}$.

radiation plus shutter contribution) to always exceed the instrumental background, and hence the recorded response was always negative. Therefore the straight-line fit to this data did not pass through the x-axis. The 1997 data for FP3 however does show a break-even point, so if the problem persisted in 1997 it must have been at a much smaller level.

Figures 5.16 and 5.17 show the sequences of spectra for FP3 and FP4 in 1997 after the sign of the response has been included.

A complete set of mean spectra sequences for all the observed temperatures, for FP1 and detectors 2 and 10 from FP3 and FP4, is plotted in appendix B.1.

Results: Responsivity

The wavelength varying responsivities $R(\tilde{\nu})$ were calculated for all 21 detectors. In the mid-IR, the $T_{\rm TAR}$=82 K spectrum was used as the cold or baseline spectrum, and the responsivity was calculated for warm targets at 160 K and 170 K, at $T_{\rm FPA}$=78, 80, 85 K. For FP1, the 170 K spectrum was used as the baseline (zero-response), and the responsivity was calculated for targets at ∼82 K and ∼125 K. Figures 5.18–5.20 show

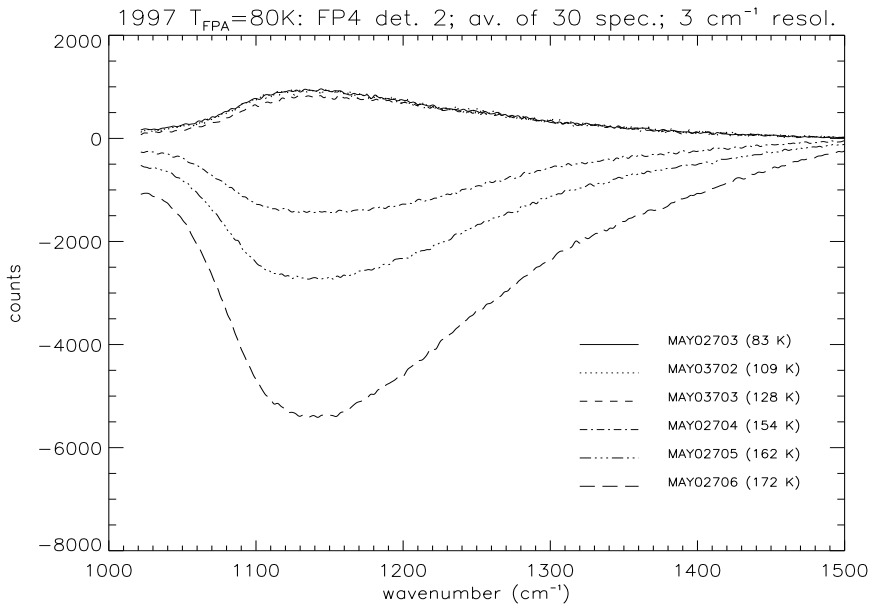

Figure 5.17: FP4 detector 2 sequence of mean power spectra for various target temperatures and at a constant detector temperature of 80 K. Each mean spectrum is an average of thirty spectra, recorded 02–03/05/97. The sign of the response has been added, so that the spectra form a monotonically decreasing sequence with increasing T_{TAR}.

some sample results. The full set of results appear in B.2.

Change in Gain 1996–1997

The gain of the amplification stages was increased from 1996 to 1997; by factors 2.74, 2.09 and 2.95 respectively for FP1, FP3 and FP4.

This can be checked by comparing the responsivity for the same T_{FPA} and T_{TAR} from 1996 to 1997, at a given wavenumber. For FP1, at T_{FPA}=170 K and T_{TAR}=83 K, we find an increase factor of 2.79, close to that expected. For FP4, the measured increase factor from responsivity at 1100 cm^{-1} was 2.6, which is also in reasonable agreement with expectations.

For FP3 at 700 cm^{-1} the measured increase factor was 4.36 for 1996 and 1997 T_{FPA}=80 K datasets, which is clearly incompatible with increase in amplifier gain. The reason for this is quite simply because of the anomalous low-temperature spectra in the 1996 data, thought be due to the shutter droop. This causes the the low T_{TAR} spectra to be at negative, rather than positive radiances, and so the responsivity is greatly reduced.

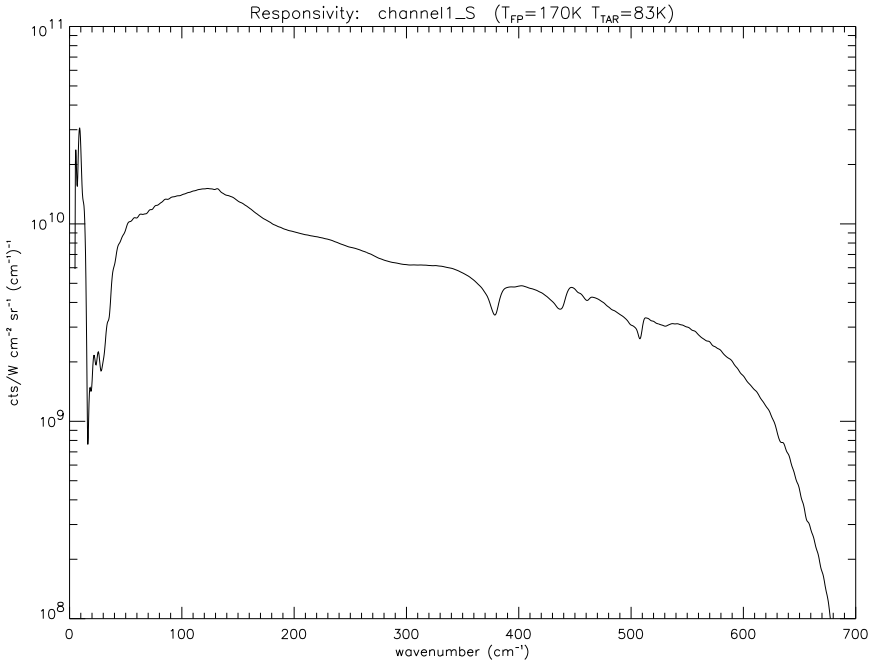

Figure 5.18: Responsivity of FP 1 detector at $T_{\rm FPA}$=170 K, and $T_{\rm TAR}$=83 K. Date 02/05/97 (file ref: MAY02703).

This does not occur with the 1997 data.

If however, instead of responsivity we consider simply the counts at 700 cm^{-1} for a 170 K target, the increase factor is 2.30, much closer to expectations.[5]

Variation of Response with Focal Plane Temperature

We can now check how the response of FP3 and FP4 varies with $T_{\rm FPA}$, by comparing the responsivity at a given wavenumber for the same $T_{\rm TAR}$.[6] The responsivity $R_{\tilde{\nu}}$ is expected to decline as the focal plane temperature rises, which is readily seen on the plots.

With the 1996 data, we can calculate the responsivity decrease from $T_{\rm FPA}$=78 K to $T_{\rm FPA}$=80 K. FP3 at 700 cm^{-1} decreased by a factor 0.87±0.01, and FP4 response at 1100 cm^{-1} decreased by 0.89±0.01. At the same wavenumbers, in 1997, the responses

[5]The difference between considering total counts and considering responsivity is that it is not quite accurate to expect the total counts on the hot spectrum to increase by the gain change factor when the baseline cold spectrum has not been subtracted. The cold spectrum cannot be utilised when analysing the 1996 FP3 data because it is probably polluted with warm shutter radiation.

[6]FP1 was always at the instrument temperature of 170 K.

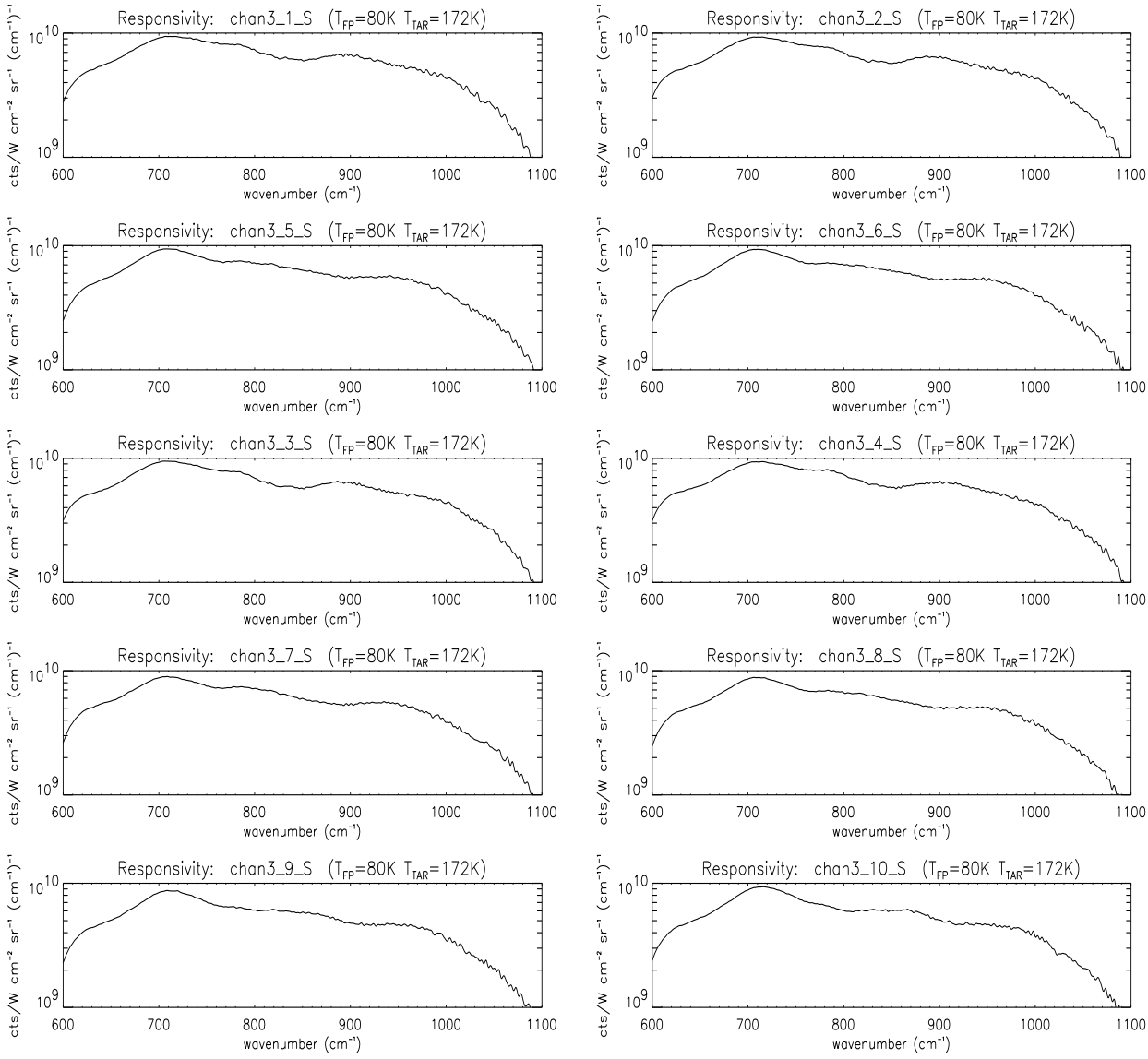

Figure 5.19: Responsivities of FP 3 detectors at T_{FPA}=80 K, shutter open and T_{TAR}=172 K. Date 02/05/97 (file ref: MAY02706).

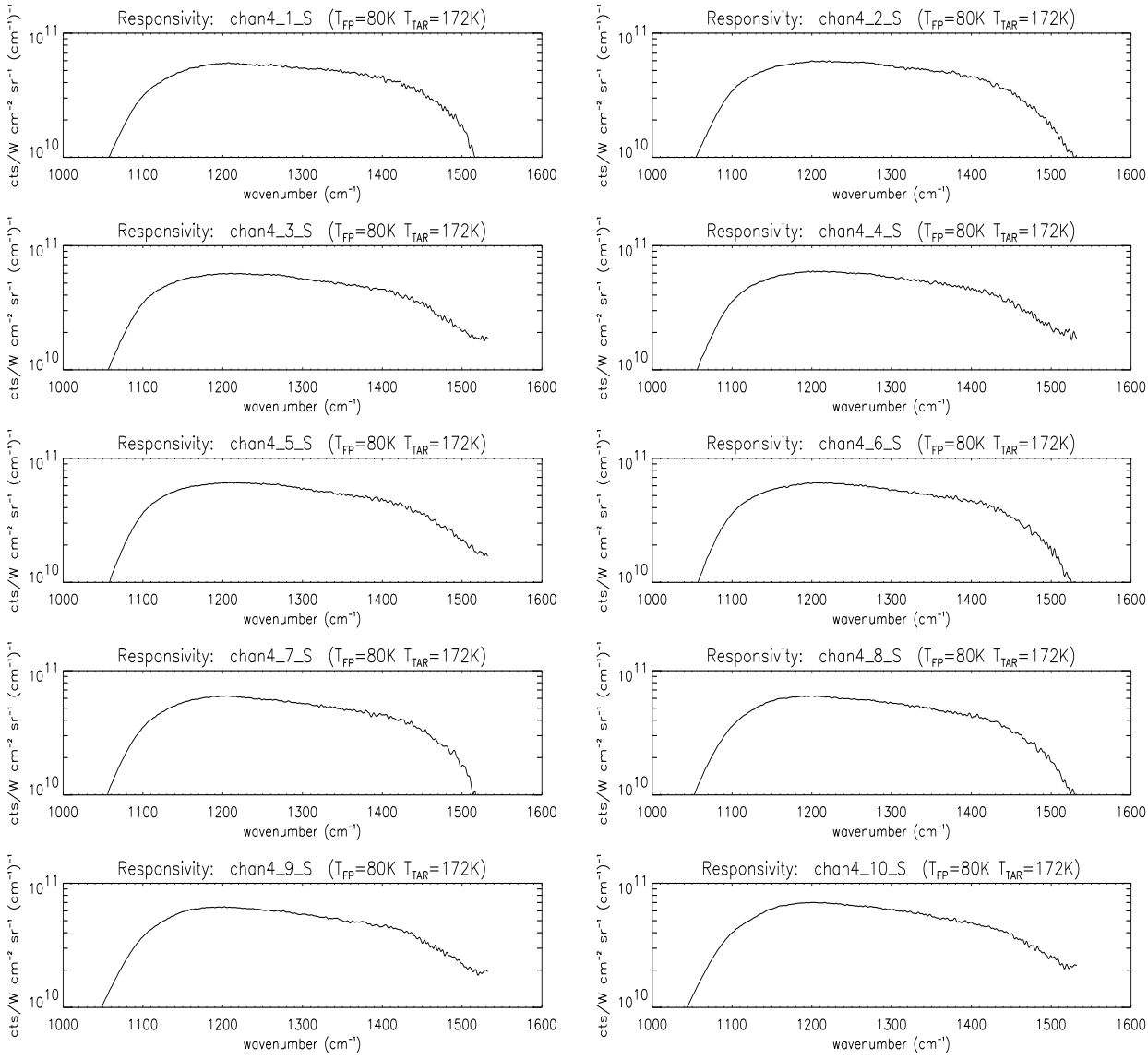

Figure 5.20: Responsivities of FP 4 detectors at T_{FPA}=80 K, shutter open and T_{TAR}=172 K. Date 02/05/97 (file ref: MAY02706).

dropped by factors 0.73 and 0.75 respectively from $T_{\rm FPA}$=80 K to $T_{\rm FPA}$=85 K. A rough linear fit through this data would therefore indicate that $\sim$ 5-6% of peak response is lost per K increase in $T_{\rm FPA}$, in the range 78–85 K.

Some measurements exist of the responsivity for the FP3 array, and its variation with temperature, which were made at the commissioning of the PC detectors at GSFC in 1995. These numbers indicate that $R_{\tilde{\nu}}$ at $T_{\rm FPA}$= 85 K is expected to be 0.77 of its value at $T_{\rm FPA}$= 80 K. The 5% difference from the present results is likely to be due to the $\sim \pm 0.5$ K error in $T_{\rm FPA}$ and $\sim \pm 2$ K error in $T_{\rm TAR}$ due to temperature drift during the experiment.

5.2.4 Noise Equivalent Spectral Radiance (NESR)

Having determined the responsivity of the instrument to incoming radiation, the noise on an observation can now be estimated. In this section, firstly, the instrumental NESR is defined from a theoretical standpoint, and then the measurement of the NESR for CIRS is described.

Definition

The performance of infrared detectors is always limited by noise. For a given type of detector, the usual area-independent figure of merit is D^* defined:

$$D^* = \frac{\sqrt{A_{\rm D}}}{\rm NEP} \tag{5.31}$$

where $A_{\rm D}$ is the detector area, and NEP is the Noise Equivalent Power, defined as the incident radiation power which would give a detector signal equal to the noise signal. D^* can be predicted theoretically, and is also usually measured by the manufacturer and supplied with the component.

When an interferogram is measured, we may define the *effective* total integration

time (scan time, excluding mirror flyback time) as:

$$t_{\mathrm{e}} = n_{\mathrm{p}} \times \delta t_{\mathrm{e}} \tag{5.32}$$

where n_{p} is the number of output points and δt_{e} is the *effective* integration time per sample point in the IFM. The effective integration time per point is the actual dwell time at each logging interval, multiplied by n_{resamp}. The actual dwell time δt is simply the logging interval divided by the mirror travel speed: 195.75 nm/ 0.0208 cm s^{-1}= 9.41×10^{-4} s (see 5.1.5).

If we integrate the NEP over the effective total integration time, then we find the RMS noise level is:

$$\mathrm{Noise} = \sqrt{A_{\mathrm{D}} t_{\mathrm{e}}} / D^{*}. \tag{5.33}$$

Similarly, the integrated signal power is:

$$\mathrm{Signal} = \eta_{\tilde{\nu}} I_{\tilde{\nu}} A\Omega \delta\tilde{\nu} t_{\mathrm{e}} \tag{5.34}$$

where $\eta_{\tilde{\nu}}$ is the efficiency of the optical system plus detectors, and $A\Omega$ is the étendue. $\delta\tilde{\nu}$ is the output spectral point spacing or bin size, in the absence of zero-padding. $\delta\tilde{\nu}$ is directly proportional to the resolution $\Delta\tilde{\nu}$ as defined in §5.1.6, with a constant of proportionality equal to $1/2\Gamma$.

If the spectrum is zero-padded before taking the transform, then the output spectral grid size becomes smaller by a factor $n_{\mathrm{p}}/n_{\mathrm{FFT}}$, where n_{FFT} is the padded length used in the FFT. The spectral resolution however does not improve, because the effect of zero-padding is merely to interpolate the output spectrum onto a finer grid, without any

qualitative change in the information contained.

Hence, the signal to noise ratio is:

$$\mathrm{S/N} = \frac{\eta_{\tilde{\nu}} I_{\tilde{\nu}} A \Omega \delta\tilde{\nu} D^* \sqrt{t_\mathrm{e}}}{\sqrt{A_\mathrm{D}}} \tag{5.35}$$

The Noise Equivalent Spectral Radiance is the radiance which would correspond to a S/N of unity:

$$\mathrm{NESR} = \frac{I_{\tilde{\nu}}}{\mathrm{S/N}} = \frac{\sqrt{A_\mathrm{D}}}{A \Omega \delta\tilde{\nu} D^* \sqrt{t_\mathrm{e}}} \tag{5.36}$$

Notes:

1. The spectral output spacing $\delta\tilde{\nu} \propto (t_\mathrm{e})^{-1}$ by equations 5.20 and 5.21, and therefore NESR $\propto \sqrt{t_\mathrm{e}}$ or $\propto 1/\sqrt{\delta\tilde{\nu}}$. This leads to the slightly counter-intuitive result that as scan time increases, the NESR goes up and the S/N ratio decreases. This is exactly the opposite to the case in a non-interferometer spectrometer. Note however that the spectral resolution improves by a factor equal to the increase in scan time. See figure 5.21.

2. The usual results for co-adding or re-binning spectra apply, namely that:

   (a) when two similar spectra are co-added, the NESR reduces by a factor $\sqrt{2}$ (S/N goes up by $\sqrt{2}$), and

   (b) re-binning a spectrum of n_p points by co-adding every two points together increases S/N by $\sqrt{2}$ (there are then $n_\mathrm{p}/2$ independent points).

3. By combining the results above, it can easily be demonstrated that it is possible to arrive at the same spectral resolution in the same observing time, but with a different NESR depending on how the observing time is utilised. Consider spectrum

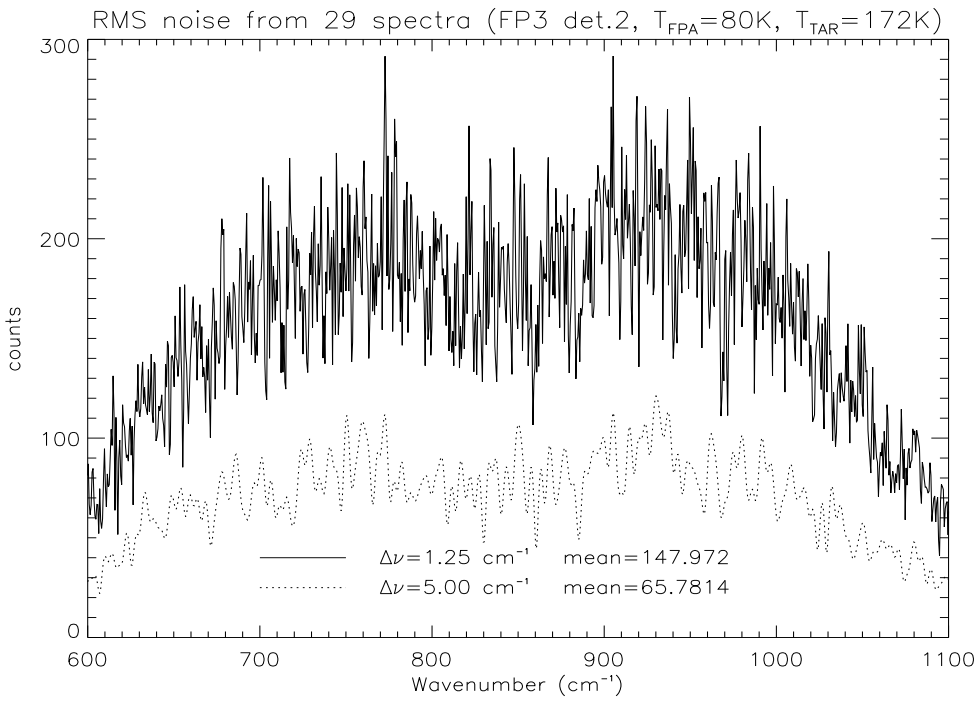

Figure 5.21: FP3 RMS noise variation on spectra at two different resolutions. In both cases the RMS noise has been averaged over 29 spectra at constant $T_{\rm FPA}$ and $T_{\rm TAR}$. The solid line shows the noise calculated from spectra resulting from transforming the original IFMs (scan time 20 s and resolution 1.25 cm^{-1}). In the second case, the lower resolution was obtained by taking the same 29 IFMs and cutting their length by a factor 4, to increase $\delta\tilde{\nu}$ by the same factor. These 'cut' IFMs were then transformed to power spectra and the noise calculated as before. The mean noise level has now dropped by a factor 2.

1 which has a binsize of $\delta\tilde{\nu}_1$, arising from a scan of time t_1. The NESR on this scan is N_1. Now consider that two scans of time $t_1/2$ are made, each having an NESR of $N_2 = N_1/\sqrt{2}$. Co-adding these two scans together results in single spectrum of NESR=$N_1/2$ and having binsize $2 \times \delta\tilde{\nu}_1$. Re-binning the first spectrum by a factor two also gives a spectrum of binsize $2 \times \delta\tilde{\nu}_1$ but an NESR=$N_1/\sqrt{2}$, a factor $\sqrt{2}$ higher than the co-added scans, but from the same total time. Therefore it is always best to observe at the final resolution required, rather than an initial higher resolution.

Noise Sources in CIRS Detectors

The physical origins of noise on CIRS observations are now outlined. Note however that it was not the objective of this thesis to devise a detailed theoretical model of the noise arising in different components, which has in any case been extensively modelled and measured during the development phase. The objective was to measure the final noise of CIRS viewed as a complete system. Nevertheless it is important to bear in mind the sources of the noise, so a brief description of the expectations from a physical standpoint is given here.

There are three possible sources of noise on a given CIRS interferogram observation: noise in the detectors, noise from inherent fluctuations in the arriving stream of radiation, and noise in the post-detection electronic circuits of the signal amplifiers. By careful design the amplifier noise may be reduced to below the limits imposed by detector noise and photon noise. Hence, this noise is assumed to be negligible compared to other noise sources on CIRS observations. The other two types of noise are discussed with reference to the individual detector arrays.

Focal Plane 1 Bolometer Detector

A bolometer is a thermal detector: changes in the incident radiation field cause changes in the temperature of the detector, which in turn affects the resistance. The resistance change can be measured by applying a p.d. across the detector and monitoring the change

in current or voltage.

There are four main internal noise sources for a thermal detector. Firstly, Johnson (or Nyquist) noise which arises due to the random motion of electrons in the conducting material, which manifests itself as a fluctuating electrical potential. This occurs even when the temperature is constant. Secondly, the temperature of the detector will also fluctuate continuously to a small degree: this also converts into an electrical signal. Thirdly, radiative heat exchange between the detector and its housing contributes a photon exchange noise. Another form of noise, called $1/f$ power law noise, occurs at low frequencies and it thought to occur due to potential barriers at the contacts, interior or surface of the semiconductor.

In addition to internal noise, there is the external noise due to radiation falling on the detector, both from the source, and the background from the instrument.[7] Noise occurs due to random fluctuations in the incident radiative power. Mathematical expressions for all these noise sources are given in the standard texts (e.g. Keyes, 1977).

Focal Plane 3 and 4 Photo-Electronic Detectors

Photovoltaic and photoconductive detectors work by direct conversion of incident photons into conducting electrons, with a quantum efficiency $Q_{\rm D}$. The principles of operation of the photo-electronic detectors were described in §4.1.

Johnson noise and $1/f$ noise also occur in photo-electronic detectors. A further noise source is generation-recombination (g-r) noise, which occurs due to fluctuations in the rates of thermal generation and recombination of free carriers in a semiconducting material. This gives rise to a randomly varying amount of charge carriers, which translates into a resistance variation, and hence a varying voltage. Additionally, in photo-voltaic detectors (FP4) there is noise due to the bias voltage, called shot noise. A detailed discussion of these effects can be found in Keyes (1977, chap. 4).

[7] A subtle distinction is made here between the second source of internal noise, which occurs due to a physical joining of the detector to its housing and leads to a radiative conductance, and the external noise due to photons arriving from other parts of the instrument, which are not necessarily in thermal equilibrium with the detector.

External noise also occurs for photo detectors, due to the incident radiation from the source and background. In this case, the noise may be understood in terms of random fluctuations in the number of photons arriving per second.

The incident photons obey Poisson statistics, so that for any given point (*i.e.* path difference X) in the interferogram, the probability $\Pr(N)$ of detecting N photons is given by:

$$\Pr(N) = \frac{(\overline{N})^N \exp(-\overline{N})}{N!} \tag{5.37}$$

where $\overline{N}$ is the long-term average number of photons which would be detected in a fixed observing time t, if we made very many observations and took the mean value. The rms fluctuation about the long-term mean value N is $\Delta N = (N)^{1/2}$. We may assume that the noise on sucessive points on the interferogram is uncorrelated, so that once the Fourier transform has occured to compute the power spectrum, the noise from all the different points on the interferogram is spread evenly amongst all the frequency channels. Strictly this is true only when the spectrum is totally unapodised: otherwise, a correlation exists between neighbouring frequency bins. In this work the objective is soley to obtain a low-order fit to the broad noise spectrum, so the low levels of apodisation used have an insignificant effect. However, apodisation would be an important consideration if we were attempting a formal retrieval (inversion) on a planetary spectrum.

The various forms of internal noise, and the external photon noise due to the background are independent of the target in the field of view. The most important noise sources for FP3 are Johnson noise and g-r noise, and for FP4 are photon noise from the background and Shot noise in the detectors. For the all the mid-IR detectors, most of the 2π sr FOV is shielded from the warmer instrumental background by a small aperture maintained at the focal plane temperature, through which only a solid angle $\sim$0.75 sr of external radiation enters. Hence, most of the background radiation comes from the lens

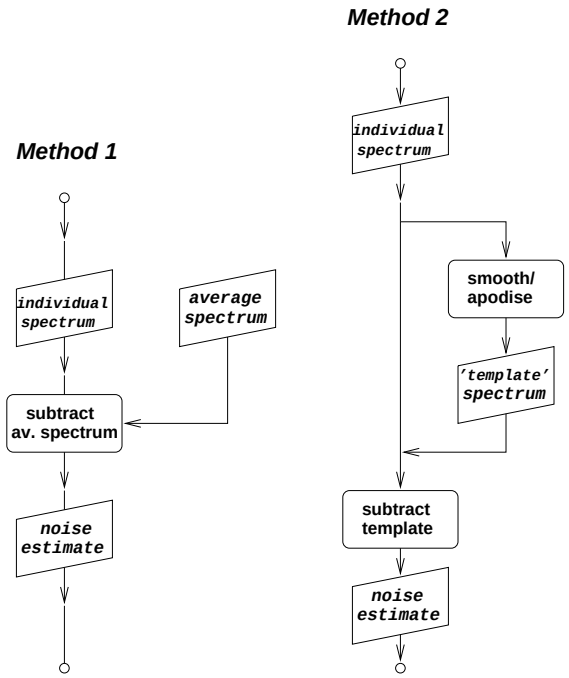

Figure 5.22: Two alternative methods for noise estimation on a single spectrum.

at 170 K, through the window, but there will be a certain proportion which should vary with the focal plane temperature.

The remainder of this section describes the estimation of the NESR on each focal plane from the radiometric test data.

Noise Measurement

Figure 5.22 shows two possible algorithms for estimating the fluctuation in counts on a particular spectrum.[8]

- **Method 1.** Each individual spectrum is calculated using `tran` as before, including apodisation to the desired resolution. Then, the 30-spectrum mean (calculated as described in §5.2.3) at the same T_{FPA} and T_{TAR} is subtracted point-by-point to find the fluctuation on the individual spectrum, as a function of wavenumber.

- **Method 2.** The individual spectrum is calculated at the desired resolution (typically 1-5 cm^{-1}). The same spectrum is also calculated at a much lower resolution,

[8] Other methods exist which were not investigated in this thesis, for example, measuring the time-dependent signal at the detectors without scanning the mirror.

i.e. it is apodised to a wider FWHM (typically 5-15 cm^{-1}). Now, the fluctuation can be estimated by subtraction of the low-resolution spectrum from the high-resolution one.

In both the above cases, the smoother spectrum (either the mean, or the more apodised version) is taken to be a smooth 'fit' through the noisy points of the high-resolution spectrum. In practice, it was found that method 2 was preferable; it was a more reliable 'fit'.[9]

Each of these methods has its drawbacks. Method 1 works well when the series of spectra to be analysed are very homogeneous. If there is any drift in the underlying shape throughout the sequence, *e.g.* due a variation in the target temperature or responsivity, then there will be a larger variance about the mean shape, and the mean shape will be a less accurate template for the individual spectra.

There is also a potential problem inherent in Method 2. The very practice of apodisation, by curtailing the interferogram, reduces the number of counts which go into the final spectrum. Therefore, the amplitude of the power spectrum goes down according to how much apodisation is used. This means that the low-resolution spectrum would be slightly scaled down in peak value compared to the higher resolution one, and therefore its veracity as a smooth fit to the data is impinged.

In practice however, most of the counts in the interferogram occur in the centreburst, whereas apodisation tends to cut off the low-amplitude, long path-difference oscillations. The actual decrease in peak value for the moderate amounts of apodisation used to create the 'low-resolution' spectrum is much smaller than the noise fluctuation being measured and therefore the effect is negligible. [10]

[9]The word 'fit' is used loosely: it does not imply a polynomial or other calculated curve fit to the data points.

[10]Note added in proof: a potentially more serious problem with method 2, is that it is equivalent in the IFM domain to taking a high-resolution IFM (length X), cutting its length substantially to reduce the resolution (now length X', where $X' << X$), subtracting the short IFM from the long one, and taking the difference to be noise. This assumes (1) that there is no noise in the first part of the IFM from 0 to X', and (2) that there is no signal in the portion from X' to X. A much safer method of estimation is to take the difference of successive spectra, subtracting each spectrum in the sequence of

Figure 5.23 illustrates the noise Method 2. In each figure of the sequence a high-resolution (1.25 cm^{-1}) spectrum is overplotted on a low-resolution ('fit') spectrum. Smooth spectra at FWHM=5, 10, 15 cm^{-1} are shown.

In the following analysis, a smooth spectrum of FWHM=10 cm^{-1} was used to estimate the noise fluctuation on 1.25 cm^{-1} spectra.

Each individual fluctuation or 'difference' spectrum is squared and then square-rooted to find the RMS deviation, for each detector. However, in order to obtain more reliable statistics the square deviation of each of the thirty spectra in each series were co-added, and the RMS calculated as:

$$\Delta C_{\mathrm{RMS}}(\tilde{\nu}) = \left[\frac{1}{30}\sum_{i=1}^{30}(C_i(\tilde{\nu}) - C_i'(\tilde{\nu}))^2\right]^{\frac{1}{2}} \tag{5.38}$$

where $C_i(\tilde{\nu})$ and $C_i'(\tilde{\nu})$ are the 'unsmoothed' and 'smooth' versions of the i^{th} spectrum respectively. The fact of constant T_{FPA} and T_{TAR} is taken as implicit for all the quantities in the equation. Figure 5.24 shows the computational procedure used to co-add the fluctuations and determine the RMS noise in counts on a set of spectra.

Finally, the calibrated noise is simply the noise in counts divided by the detector responsivity:

$$\mathrm{NESR}(\tilde{\nu}) = \frac{\Delta C_{\mathrm{RMS}}(\tilde{\nu})}{R(\tilde{\nu})} \tag{5.39}$$

The noise was calculated for each of the 21 detectors individually. The overall noise calculation algorithm is illustrated in figure 5.25.

30 from its predecessor and attributing any difference to noise. This makes no assumptions about the shape of the signal, and again a simple expression can be derived for the NESR. This method was used to check the 'method 2' algorithm utilised in this thesis, and the difference was ~ 5 % for a 2.5 cm^{-1} scan and < 1 % at 1.25 cm^{-1} resolution.

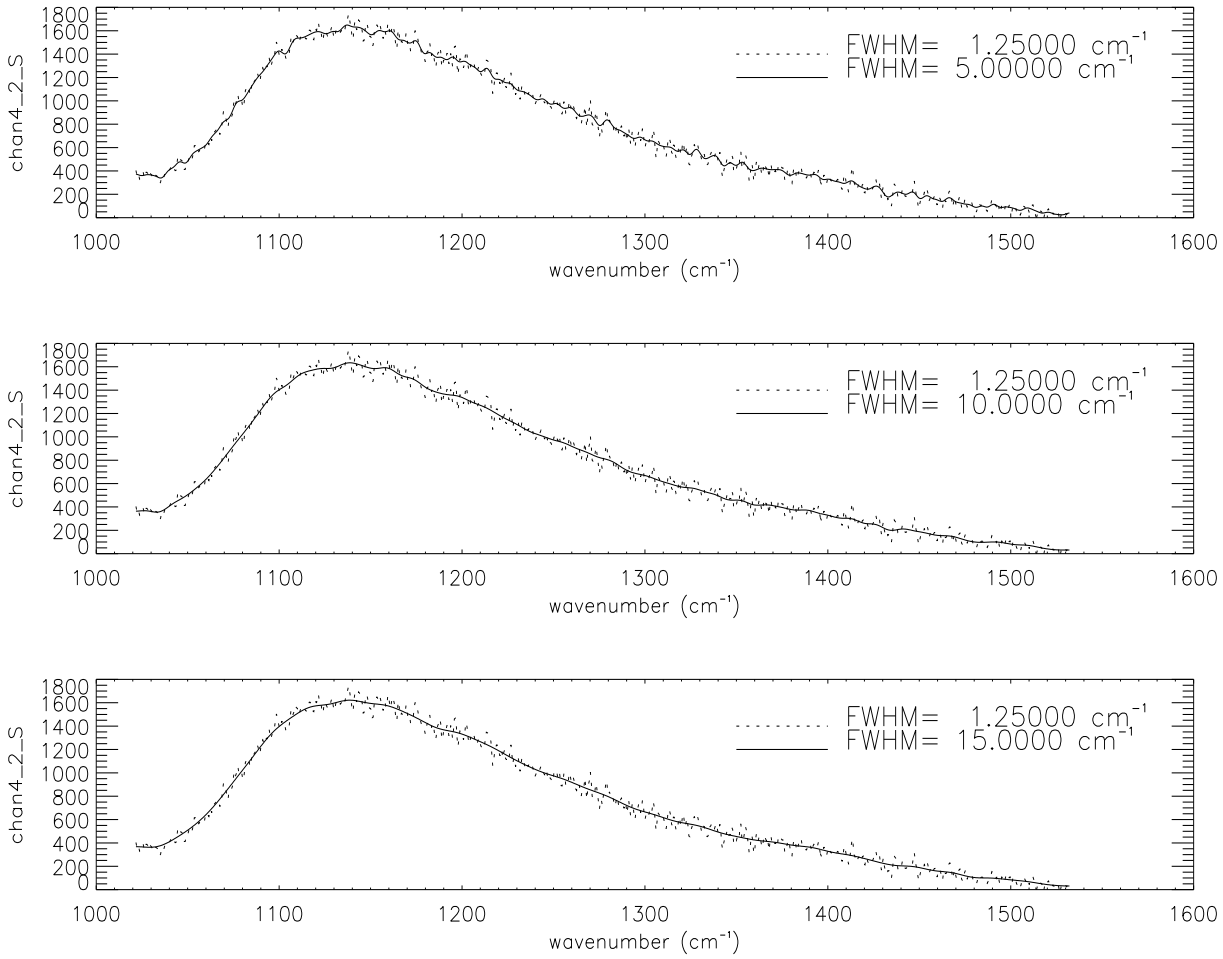

Figure 5.23: Spectrum at 1.25 cm^{-1} resolution over-plotted on various 'smoother' (i.e. more heavily apodised spectra). Subtraction of the 'noisy' spectrum from the 'smooth' spectrum gives the noise in counts. (FPA 3, det. 2; T_{FPA}= 80 K, T_{TAR}= 170 K; file ref: AUG14605 Time: 02:00:14).

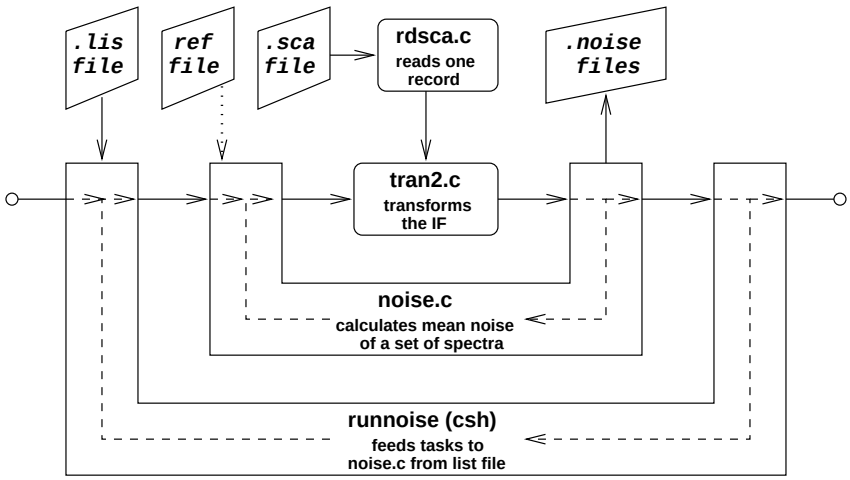

Figure 5.24: Schematic diagram of the procedure for calculating the mean noise on a set of similar spectra, showing the interaction of files and program modules.

NESR: Results

Figures 5.26–5.28 compare the NESRs derived by the above method to those calculated by L. Herath, using a different Fourier Transform code but a similar noise analysis method. All the calculated NESRs have been scaled to the level of a 3 cm^{-1} resolution observation to enable comparison with Herath's calculations. To obtain the NESRs at 3 cm^{-1} resolution, the NESRs at 1.25 cm^{-1} are scaled by a factor $\sqrt{\delta\tilde{\nu}_1/\delta\tilde{\nu}_2}$ = $\sqrt{1.25/3.00}$=0.645 to account for the difference in resolution (see equation 5.36).

For all focal planes, the comparison to Herath's results is close. Note however that the large deviations ('spikes') seen above the mean level on the FP1 NESR spectrum are not real, but due to a systematic error in the calculation method. The problem is that the low-order fit to the noisy spectrum cannot match the sharp features seen at these wavenumbers.

The reason for a slight residual deviation between Herath's results and the present findings may be due to differences in the methods used to calculate the responsivity and noise of the detectors. Herath's method is not known, but it is thought that he subtracted interferograms, then transformed to get a difference spectrum, rather than subtracting the final spectra. The reason for subtracting in the spatial rather than the

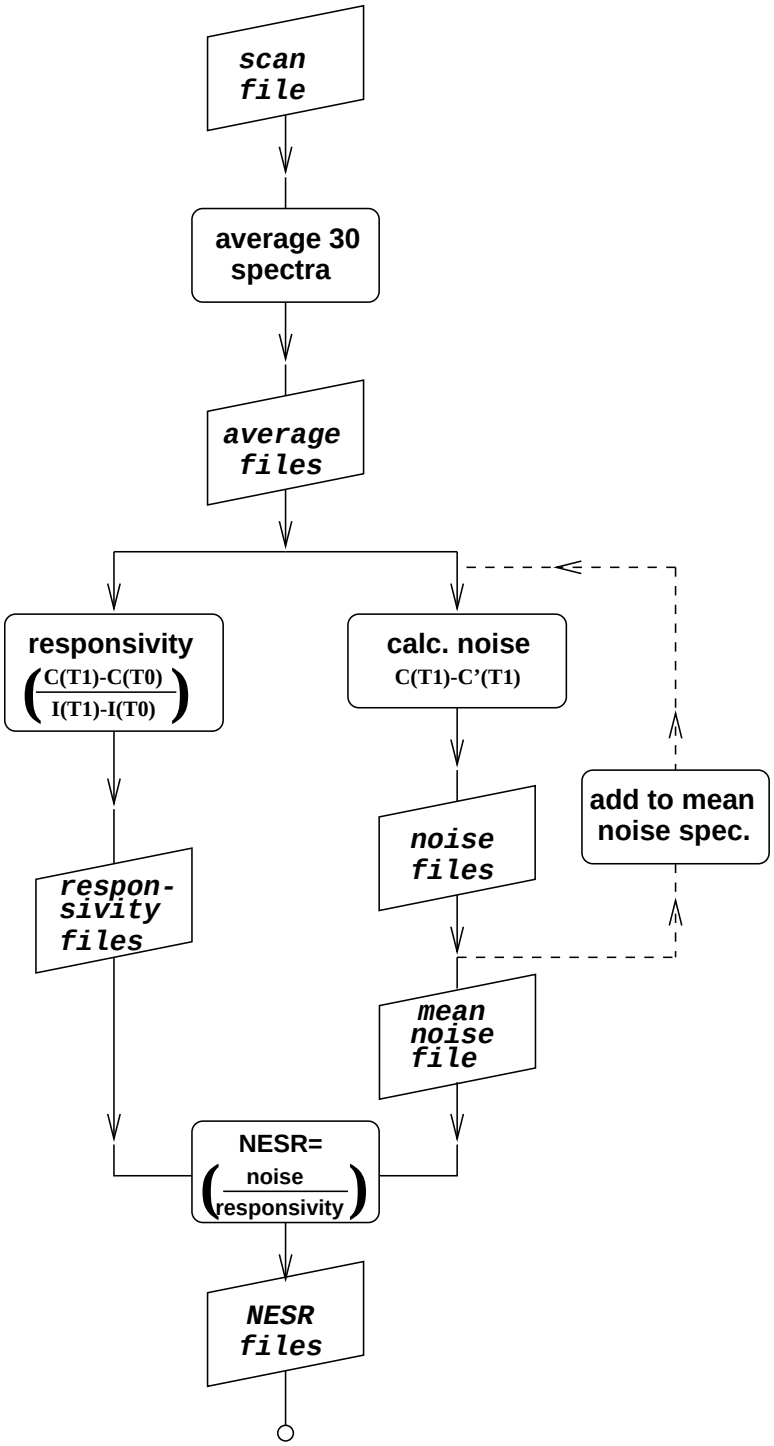

Figure 5.25: Flow chart of the overall noise calculation algorithm for CIRS spectra.

spectral domain is to eliminate any constant phase effect due to the beamsplitter, which should be the same on spectra taken at different temperatures. The effect of this on radiometric calibration of FTIRs is described by Revercomb et al. (1988). It is not yet certain which method gives a more accurate calibration for CIRS.

Also shown on these plots is the original instrument requirement NESRs, which were imposed at the design stage. In the far-IR, the NESR is roughly a factor 3 higher than requirement, and in the mid-IR the NESR is a factor 5–10 higher than the requirement. The reasons for this loss in performance are not clear, however throughput testing at GSFC appears to indicate that there is a greater than anticipated loss in the optics, due to losses at coatings on reflectors and beamsplitters. In addition, the proposal seems to have been too optimistic about the NESR in final instrument. The implications of the NESR levels for CIRS science are examined in the next chapter.

It is also possible to investigate the noise variation with target and focal plane temperature using this dataset.

Figures 5.29 and 5.30 show the noise in counts for a single detector on focal planes 3 and 4, at a constant focal plane temperature of 80 K in the 1997 dataset, but for varying target temperatures. No systematic variation in level is seen, indicating as expected that the source radiance is not the dominant contribution. For FP1, a similar lack of variation was noted.

Figure 5.31 shows the variation of the NESR with focal plane temperature for FP4. The noise in this case has been calibrated to allow intercomparison, as the responsivity of the detectors varies with T_{FPA}. The NESR is seen to increase monotonically with focal plane temperature. A power law fit to this progression was attempted, but the actual value derived was found to vary substantially with wavenumber, between $\sim$3 and $\sim$7.

Figure 5.32 shows the NESR variation of FP3 with focal plane temperature. In this case, it can be seen that the 1996 and 1997 data for 80 K, which should be the same, are systematically displaced, with the 1996 data being higher. The reason for this is due to the residual uncertainty in the responsivity calculation for FP3 in 1996.

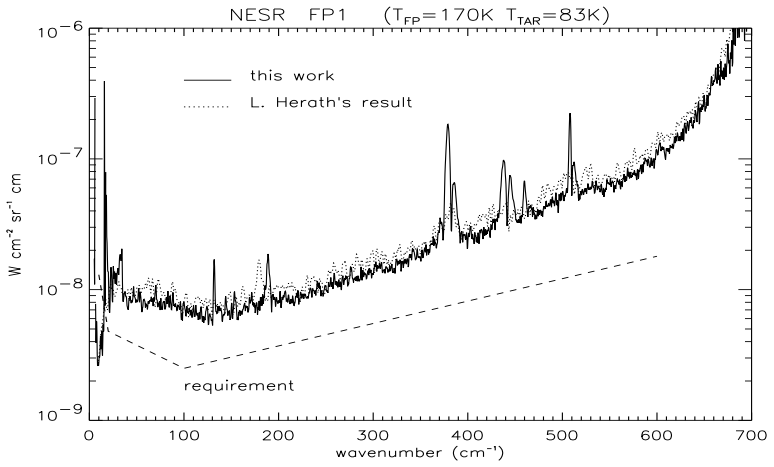

Figure 5.26: FP 1 detector; comparison of calculated noise spectrum with that of L. Herath (GSFC).

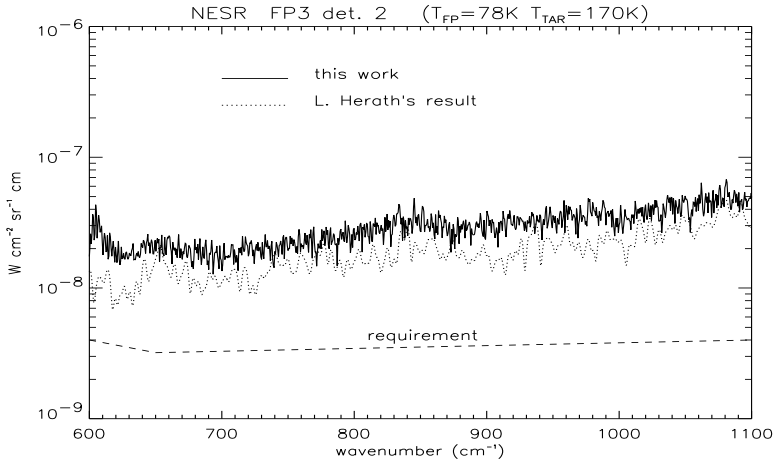

Figure 5.27: FP 3 detector 2; comparison of calculated noise spectrum with that of L. Herath (GSFC).

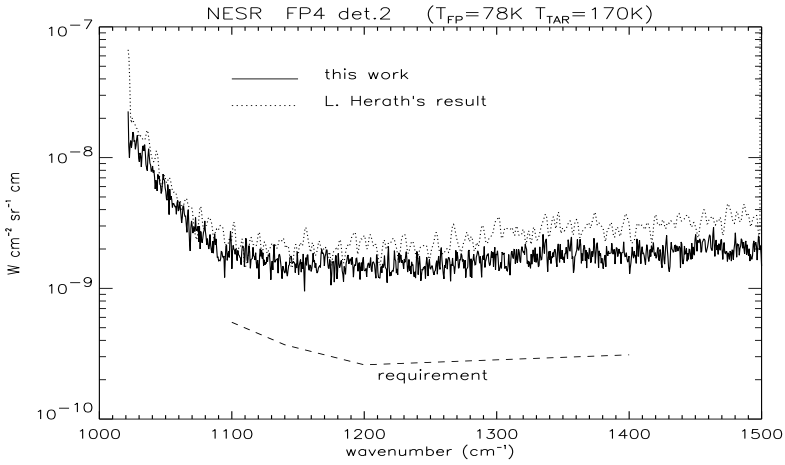

Figure 5.28: FP 4 detector 2; comparison of calculated noise spectrum with that of L. Herath (GSFC).

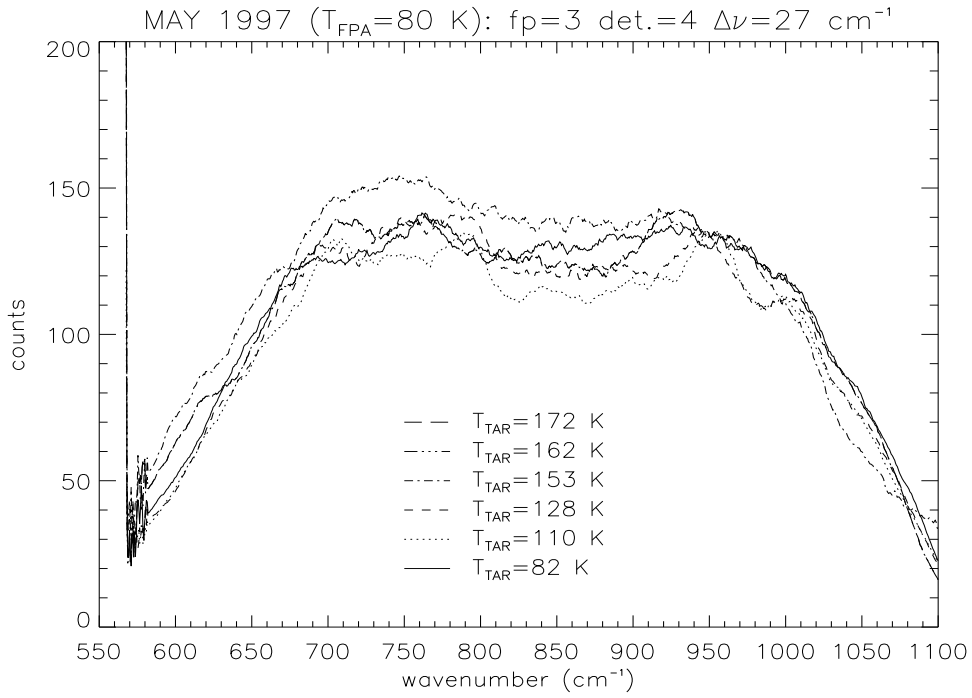

Figure 5.29: FP3 noise variation with target temperature.

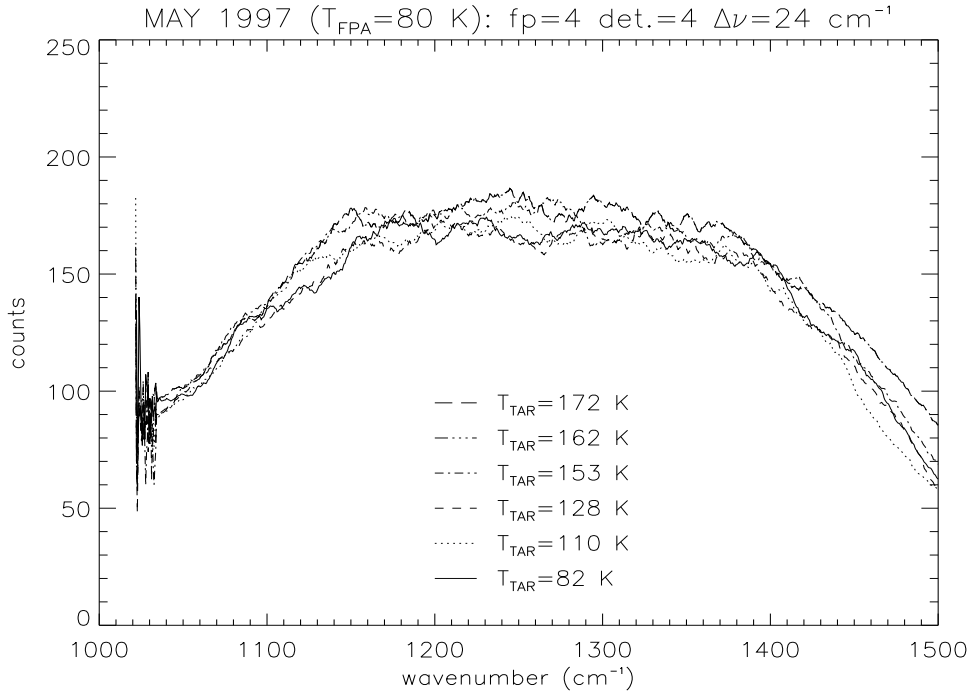

Figure 5.30: FP4 noise variation with target temperature.

Considering only the 1996 data, the 80 K noise is higher than the 78 K noise, and considering only the 1997 data, the 85 K noise is higher than the 80 K noise. A rough power law fit again indicates a T^m dependence where $m \sim 3$–7 depending on wavelength.

The full set of NESRs for the various detectors at various ($T_{\rm FPA}$, $T_{\rm TAR}$) are supplied in appendix B.3.

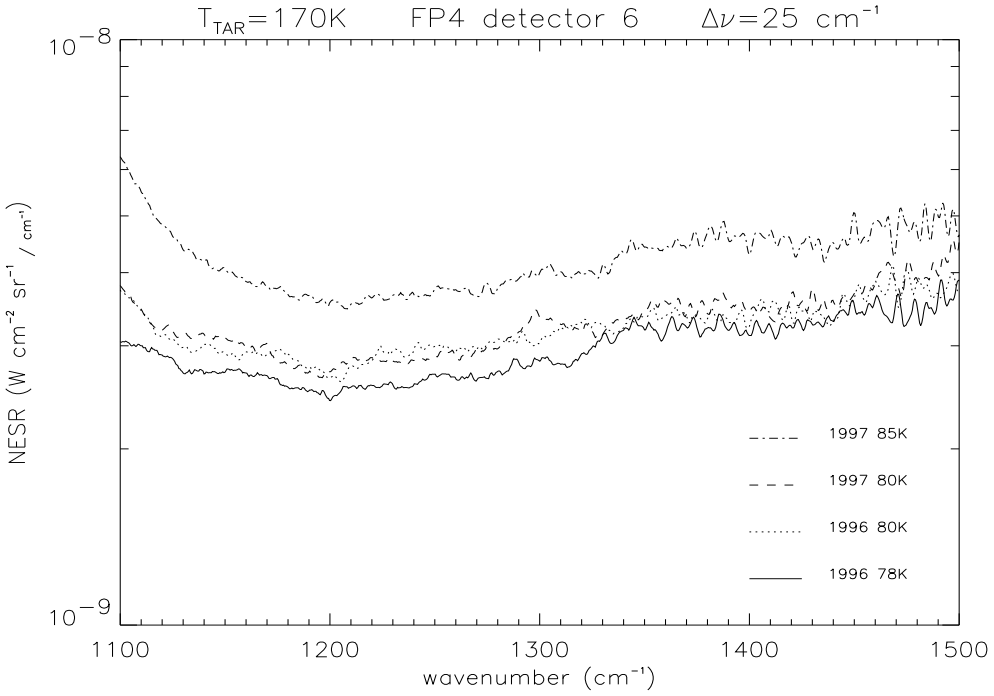

Figure 5.31: FP4 noise variation with focal plane temperature.

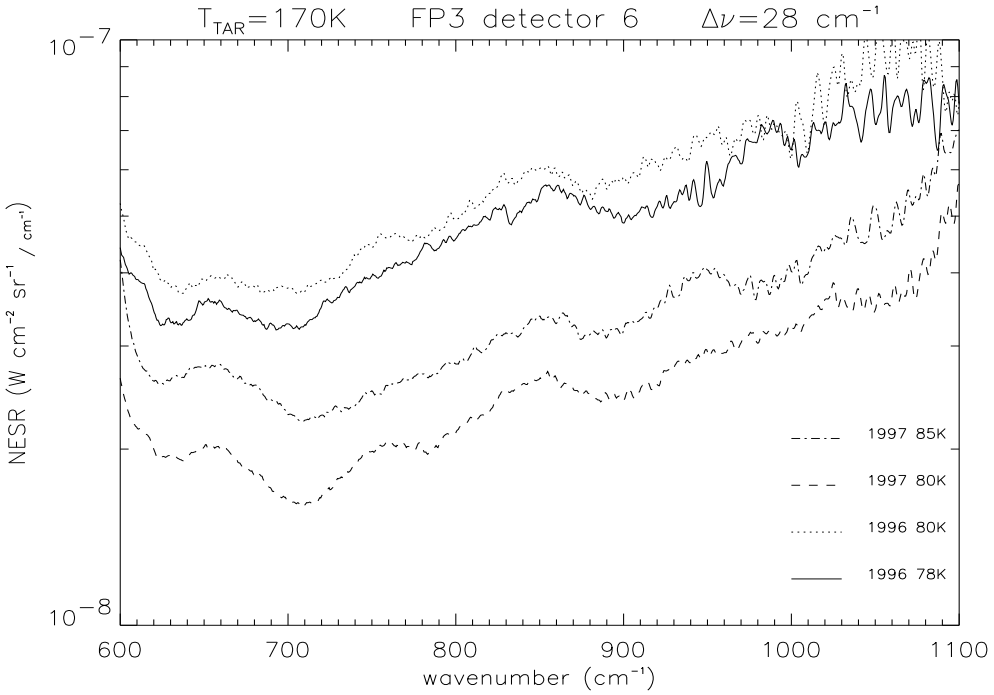

Figure 5.32: FP3 noise variation with focal plane temperature.

Chapter 6

Scientific Observations with CIRS

In previous chapters, the performance of the flight model of CIRS has been quantified, in terms of the instantaneous field of view (chapter 4) and the noise equivalent spectral radiance (chapter 5). In this chapter, the effect of the measured performance on the ability of CIRS to obtain scientific results is considered. Use is made here of the atmospheric model and radiative transfer code which was described in chapter 3.

Three of the principal measurements which CIRS will make are as follows (I have also indicated parenthetically how these measurements are interdependent with measurements to be made by other CIRS instruments):

1. **The vertical temperature and pressure profile.** Retrieval is primarily via the ν_4 band of CH_4 at $\sim$7.7 μm, the collision-induced absorption band of N_2–N_2 at 10–100 cm^{-1}, and the rotational band of methane at 50–150 cm^{-1}. *(The interpretation of these measurements will be greatly strengthened when there are radio occultation measurements of refractivity at the same points on the planet.)*

2. **The vertical profiles of gases.** These will be deduced by modelling their respective emission bands and employing retrieval algorithms. *(The retrievals will be strengthened when independent measurements of other bands of the same gases are made at shorter wavelengths by the other Cassini spectrometers, UVIS and/or VIMS.)*

3. **The vertical variation of hazes and condensates**. This will be deduced in the infrared from CIRS measurements of the continuum. *(In addition,* in situ *measurements of the aerosols by the ACP and other Huygens instruments, as well as optical wavelength measurements from the ISS and VIMS on the orbiter will be informative in the analysis of CIRS data.)*

These three types of observations will be repeated many times during the mission to give full spatial and temporal coverage of the satellite.

The practical modes of viewing and operation of CIRS are now discussed. Different remote-sounding scenarios are used for different types of investigation, and they each have particular benefits and drawbacks. Following this, it is shown how these operational modes are used to measure spectra for specific scientific purposes.

6.1 Viewing Geometries and Switching Modes

Any remote sounding instrument has two principal viewing geometries of an atmosphere: along a surface-intercepting line-of-sight, called nadir viewing, whether strictly vertical or along a slant-path; or through the limb of the atmosphere, where the line-of-sight passes through a minimum altitude of atmosphere called the tangent point.

These two modes of observation give rise to emphasis of different spectral regions. For example, on Titan, a limb-viewing mode greatly increases the strength of weak, optically thin lines of minor gases such as C_2N_2, because the radiation is coming from a much greater column-number of molecules. However surface-sensing can only be achieved in nadir mode.

To derive the maximum scientific potential from CIRS observations, it will be necessary to have extensive global coverage, both in nadir and limb sensing mode, and also to repeat the coverage at different times in the mission.

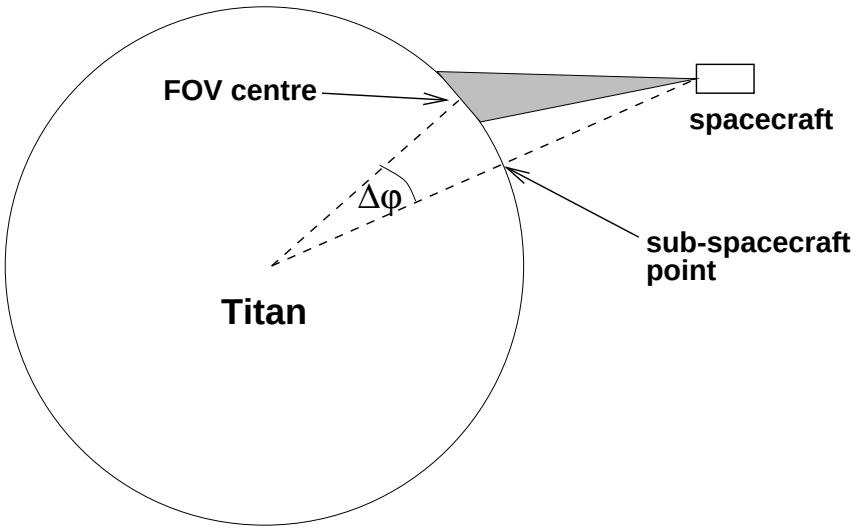

Figure 6.1: Geometry of nadir viewing. The angle $\Delta\phi$ is defined as the angle subtended at the centre of the planet by the sub-spacecraft point and the centre of the field fo view.

6.1.1 Nadir Viewing

Spatial Resolution

Figure 6.2 shows the spatial resolution for FP1 and for a single element of FP3 or FP4, at various distances from the planet and for various values of $\Delta\phi$, defined as the angle subtended at the centre of the planet between the sub-spacecraft point and the centre of the field of view (see figure 6.1).

To map the disk with a certain resolution, the size of the projected FP1 FOV is the constraining factor. For example, to achieve a resolution of $\leq 10^\circ$ in latitude or longitude, the spacecraft must be closer than $\sim$70,000 km ($\sim$25 R_T), assuming that the maximum $\Delta\phi$ of observation is 45° (*i.e.* that the centre of the field of view is no more than 45° away from the sub-spacecraft point). The resolution of the MIR detectors is much finer: provided the spacecraft is at a distance of 100,000 km or less, the spatial resolution of the disk is less than one degree of latitude/longitude on Titan.

What spatial resolution on the disk is required for scientific studies? It is not easy to answer this question, because at present only very large scale features have been seen. In the atmosphere, these include the hemispheric asymmetry, North Polar Hood and collar observed by the Voyager spacecraft. On the surface, the bright areas on the leading

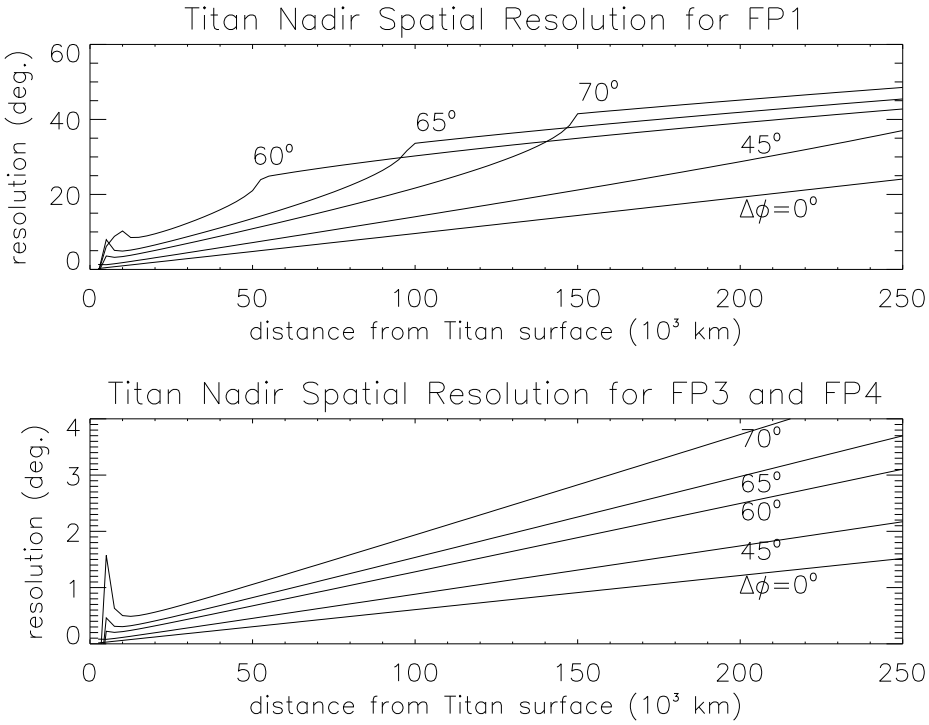

Figure 6.2: CIRS nadir FOV. The labeled angles on the curves correspond to different values of the $\Delta\phi$ (see figure 6.1). The cusp in the curves for the larger values of $\Delta\phi$ seen for FP1 occurs when one edge of the field of view expands past the edge of the planet, so that some of the limb or deep space is included in the FOV.

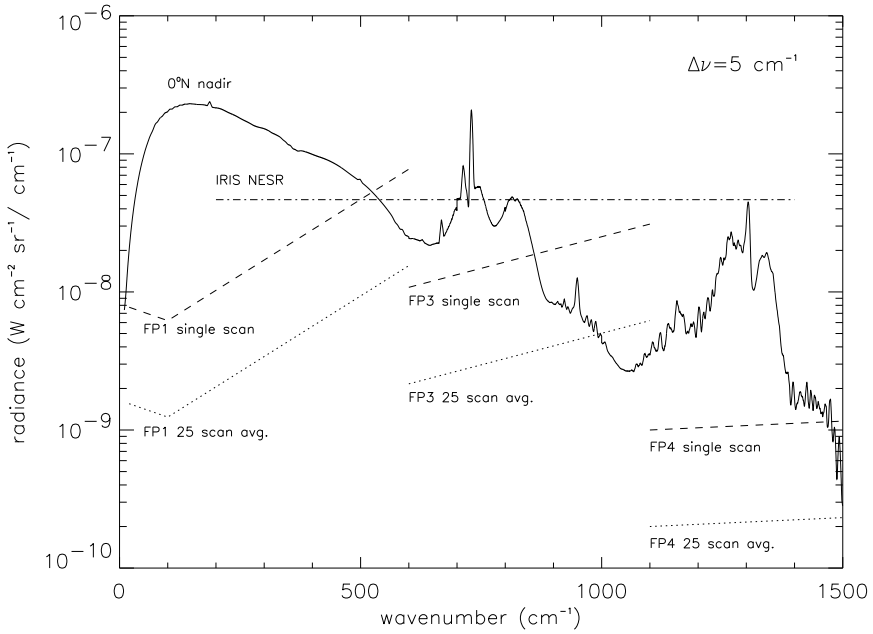

Figure 6.3: Comparison of synthetic spectrum at 5 cm^{-1} resolution (5 s scan) with the measured NESR of CIRS. Both single-scan and 25-scan average NESRs are indicated. The Voyager IRIS NESR is also shown for comparison.

hemisphere have only been studied with a resolution of several tens of degrees.

CIRS will be able to provide much higher resolution observations than are presently available. By viewing at different wavelengths, any region from the surface to high in the stratosphere may be sensed. It is safe to say that an angular resolution of 10° or less will be desirable, because we know of variations on this length scale from the existing data.

NESR of Nadir Viewing

Figure 6.3 shows a synthetic nadir spectrum for Titan's equator at 5 cm^{-1} resolution. Over-plotted are the new measured NESRs of CIRS from chapter 5, for (i) a single 5 s scan; and (ii) an average of 25 scans; for all three focal planes. Also shown is the Voyager NESR, adjusted to the same resolution. Note that a 25-scan average can be obtained in only five times the observing time of a single scan in the mid-IR, if the five detectors which observe simultaneously are co-added.

The lowest (worst) signal-to-noise ratio is obtained in the 1000–1100 cm^{-1} spectral region observed by FP3. Even for a 25-scan average, the S/N will still be less than unity,

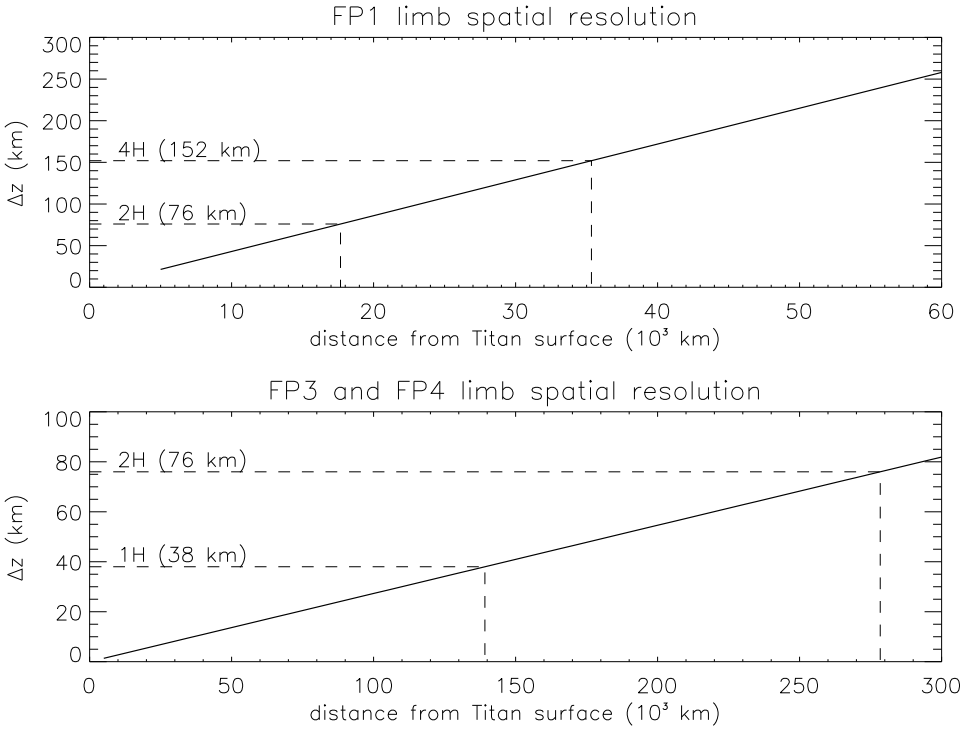

Figure 6.4: CIRS limb spatial resolution.

so if the C_2H_4 and CH_3D lines of this region are to be distinguished from the noise then many more spectra must be summed ($\sim$200).

6.1.2 Limb Viewing

Spatial Resolution

Figure 6.4 shows the variation in the spatial resolution on Titan's limb for a variety of spacecraft distances. Again, the larger field of view of FP1 is the constraining factor in observations if the FIR region is to be observed. Indicated on the upper plot is the distance required to obtain resolutions of 2 and 4 scale heights (in the stratosphere) on the limb. The spacecraft is currently planned to approach closely enough for resolution of less than one scale height by FP1 (at $d < 9000$ km), but the observing time at these distances will be short, and more problematic is the fact that constant correction to the spacecraft pointing will be required to maintain a target area in the field of view.

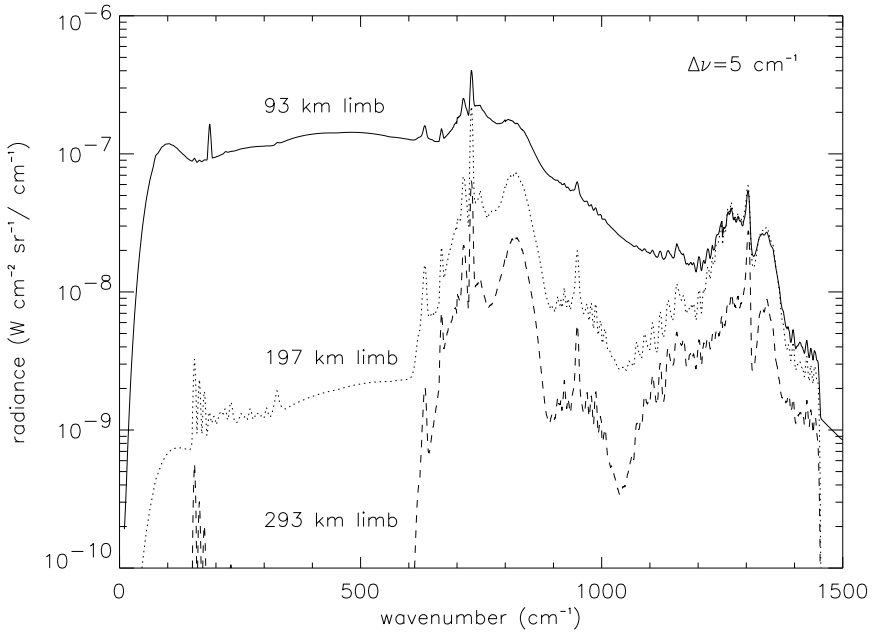

Figure 6.5: Synthetic limb spectra for three different heights, which correspond to the lower stratosphere, upper stratosphere and lower mesosphere, at low resolution. The gas band at 200–300 cm^{-1} which becomes increasingly prominent at higher altitudes is due to methane.

Spatial Weighting Function for FP3 and Noise

Figure 6.5 shows the relative radiances of three limb sightlines at different altitudes.

CIRS like all instruments has a finite field of view. For nadir viewing, each pixel will see a relatively homogeneous area; that is to say, the radiance originating from different places within the field of view will be of nearly equal magnitudes. Therefore, in the final spectrum which is recorded by the pixel, the gaseous abundances and temperatures for all points within the field of view are represented more or less equally.

For limb viewing however, the radiance is much greater lower down in the atmosphere, hence the mean spectrum resulting is biased towards the lower altitudes.[1] This means that, when modelling a limb observation, individual spectra for various heights must be calculated, and the whole set integrated over the projected field of view. Account must be taken for the shape of the field of view (square for FP3 and FP4, circular for FP1). Additionally, for FP3, the response across the field of view varies substantially, as described in chapter 4. This effect is now analysed to see under what circumstances

[1]This is less true for FP1, which has a circular FOV, which is hence wider in the middle of the FOV than at the top and bottom, than for FP3 and FP4 which have a square FOV.

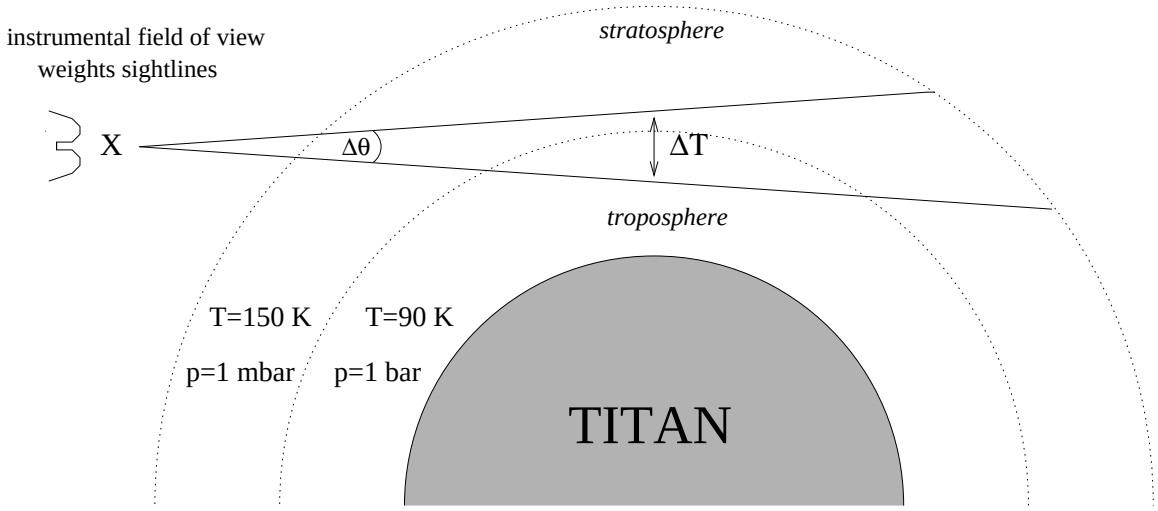

Figure 6.6: Schematic diagram of PC detector limb viewing.

it may be important.

The first step was to calculate multiple spectra for various altitudes. The nominal equatorial model and radiative transfer code described in chapter 3 were employed. Then, the detector field of view was projected onto the limb. Finally, the field of view response, or spatial weighting function, was multiplied with the limb spectra at different heights and the mean of these constituted the detector response (see figure 6.6). The spectra were interpolated using a cubic spline to attain more altitude points. The free parameters in this test were the altitude of the centre of the field of view, the width of the projected field of view, and the actual spatial weighting function used, which varied from detector to detector.

Figure 6.7 shows the difference between the actual spectrum calculated for the PC1 detector, which was the most 'anomalous' detector, and the response calculated for a hypothetical square detector of the same FOV width, but having a perfectly uniform flat response across its area. In this sequence, the projected FOV for each altitude z_{cen} is one scale height in width (the scale height varies with altitude according to the physical profile).

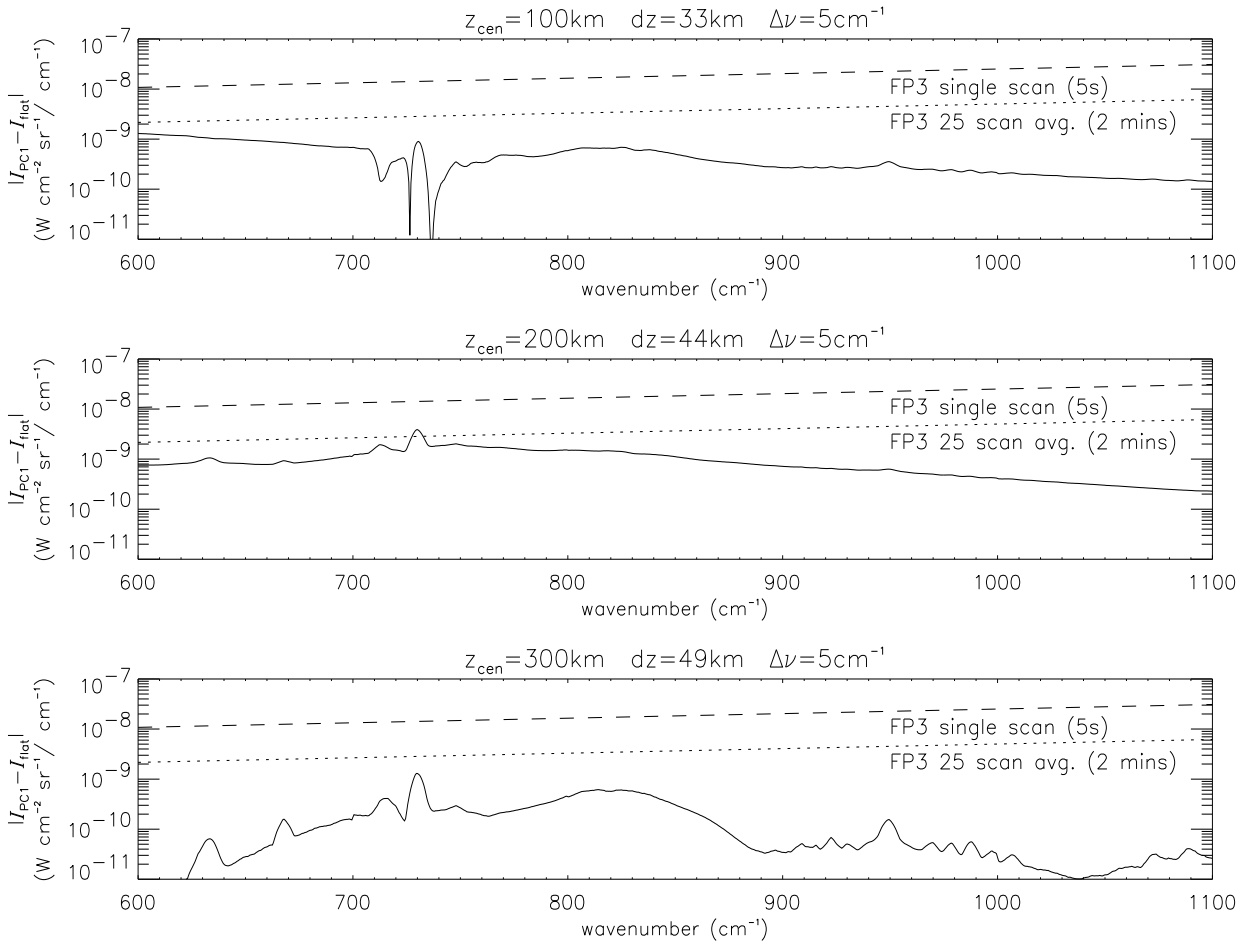

Figure 6.7: Plots showing in each case the difference between synthetic limb-view spectra calculated for two different spatial response functions : (i) actual PC1 detector response and (ii) 'ideal' detector with flat reponse across the FOV. The sequence shows results for three different limb tangent heights in the atmosphere at 5 cm^{-1} resolution, where the instrument field of view subtends one scale height.

If the detectors are assumed to have a uniform spatial weighting function, then a systematic error will be introduced into a subsequent retrieval calculation. To enable the magnitude of this error to be compared to the random error on a spectrum, the NESR for two different integration times is over-plotted on figure 6.7: the upper line is the NESR for a single spectrum, and the lower for a 25x5s-spectrum average (2 minute) observation.

To consider which of these errors will be the more important, we must consider their effect on a retrieval, for example, of a gas abundance from limb viewing. If a single spectral element, say from 815–816 cm^{-1} in the ν_9 band of ethane, is used to retrieve the mixing ratio q_v, assumed to be constant in the stratosphere, then the error on the retrieved quantity δq_v will be related to the error on the spectral element δI by the formula:

$$\delta q_\mathrm{v} = \frac{\mathrm{d}q_\mathrm{v}}{\mathrm{d}I} \cdot \delta I, \tag{6.1}$$

for both systematic and random error. In this case, if the systematic error, which adds quadratically to the random error, is much the smaller of the two, then it can safely be neglected. For example, when two numbers add together quadratically (i.e. the resultant is root of the sum of the squares) if the larger number is seven times bigger than the smaller number, then the quadratic sum of the two is only 1% different from the larger number.

If however the retrieval, rather than using a single spectral element uses a spectral region, for example, ten elements of equal size from 810–820 cm^{-1} in the ethane retrieval, then random errors tend to produce an increasingly smaller resultant error on the answer, the more spectral elements are used. If N spectral elements are used, and if each has a similar weighting in the retrieval, then the error on the retrieved quantity tends to reduce by $\sim\sqrt{N}$.

Systematic errors on the other hand do not tend to reduce when more elements are used, and produce an approximately constant error on the retrieved quantity (assuming the magnitude of the systematic error does not vary substantially over the spectral region): there is no $\sqrt{N}$ reduction.

Therefore, it seems safe to say that as a rule of thumb, if the systematic error is less than the random error divided by $\sqrt{N}$, where N is the number of spectral elements used, then the random error will dominate. However, in figure 6.7 it is already apparent that the systematic noise is approaching the single-element NESR, which is higher than the N-element NESR, for the two-minute integrations.

Figure 6.8 is similar to 6.7 but for a wider field of view: for each altitude the detector samples two scale heights of atmosphere. In this case, the systematic noise is even larger, and at some wavelengths is greater than the single-element, 2-minute NESR. Note however that all these calculations pertain only to the PC1 detector; for the other PC detectors the asymmetry in the field of view is less, and hence so also will be the expected systematic error.

In summary, the least-error approach to retrievals using limb-view spectra from focal plane 3 will always be to explicitly use the measured spatial weighting functions to weight sightlines in the field of view, and hence avoid systematic error which may result if uniformity is assumed.

6.1.3 CIRS Switching Modes

CIRS has four switchable modes of operation for the mid-IR detectors (see §2.3.3). Selecting the most suitable mode for an observation can be used to enhance the scientific return.

The two complementary modes 'odd pixels' and 'even pixels' are used to attain narrow spatial resolution over a wide field of view in the mid-IR. In these mode, the overall spatial coverage of the five detectors is of comparable width to the FOV of the FP1 detector. These would be used, for example, for nadir-viewing when the spacecraft is close to the

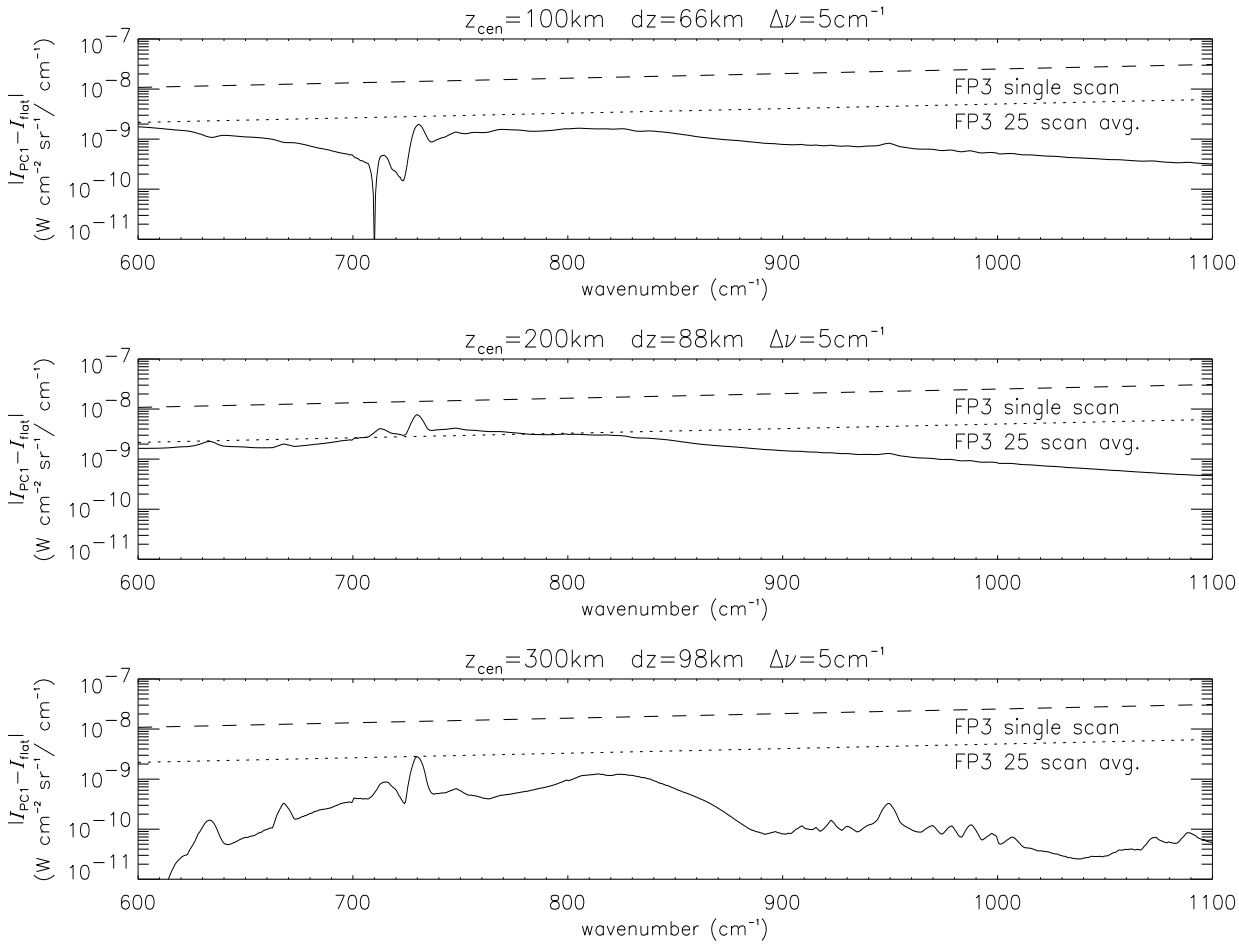

Figure 6.8: Plots showing in each case the difference between synthetic limb-view spectra calculated for two different spatial response functions : (i) actual PC1 detector response and (ii) 'ideal' detector with flat reponse across the FOV. The sequence shows results for three different limb tangent heights in the atmosphere at 5 cm^{-1} resolution, where the instrument field of view subtends two scale height.

planet, to achieve greater latitudinal coverage, or to achieve wider coverage of the limb.

The 'centre pixels' mode would be used to achieve a narrower field of view. For example if the five resulting spectra were to be later co-added to increase signal-to-noise, then a closer spacing for greater homogeneity may be desirable.

The 'pixel pairs' modes is very useful, because in this mode alone the flux received at all the pixels is utilised, and therefore offers the greatest signal-to-noise in a fixed observing time. The cost of this greater S/N is that the FOV of each resolution element is effectively doubled, and hence may be too great for good resolution on the planetary limb. However, it may be invaluable for trying to detect new trace gases.

6.2 Measurement of Gaseous Abundances

Gas abundances may be retrieved from observations by a method of calculating synthetic spectra, and then comparing the predicted radiances in the gas bands to the measured radiances. If a discrepancy is found, then the model gas abundances are adjusted, and the new synthetic spectrum calculated. This process is then iterated until the desired accuracy is reached. This method has been used to determine stratospheric gas abundances from IRIS data (e.g. Coustenis and Bézard, 1995).

The accuracy of the retrieval is limited by the noise on the observational data, the NESR, and also by errors in the model. The retrieval is iterated until model converges with the data to within an amount set by the combined errors from the model and data.

The NESR has been measured as described in chapter 5. We are now in a position to use this to set the limitations on CIRS science in two separate respects:

1. A 'simulated' retrieval can be done, which uses current estimates of the VMRs for gases in the atmosphere. The NESR can then be used to estimate the abundance errors on a typical retrieval.

2. The minimum observable VMR on a spectrum can estimated, by comparing the

calculated radiances to the the background continuum level plus the NESR of the observation.

The estimation of these values is now described.

6.2.1 Error Bars on Nominal Abundances

Method

Firstly, a 'nominal' spectrum was calculated, and the radiance measured at the centre of various gaseous bands (as listed in table 3.3). The nominal spectrum used the equatorial model described in chapter 3, including the gas abundances of table 1.2. Then, for each band, the 'NESR$^+$' radiance was calculated by adding the 25-scan average NESR shown on figure 6.3 to the nominal radiance at that wavenumber.

Subsequently, the abundances for each gas were increased by small increments and the spectrum recalculated near the band centres, until the radiance reached the level of the NESR$^+$ radiance. The difference between the gas abundance at that radiance and the nominal abundance then gave the expected 1-σ error on the abundance measurement for that gas. The same process was then repeated except that the gas abundances were decreased, and the final radiance level (the 'NESR$^-$' radiance) was equal to the nominal level minus the NESR.

Note that this a fairly crude method and is intended only to give a rough order-of-magnitude estimate of the error. A rigorous analysis would include a simulated retrieval of the gas abundance from synthetic data, in which normally more than just a single spectral element (as used here, at the band centre) would be included.

Nadir Viewing Measurements

The results for the VMR measurement error for some of the stronger gas bands for an equatorial nadir spectrum are given in table 6.1. The NESR in all cases is for 25 co-added 5 cm^{-1} resolution scans, corresponding to a total observing time of 2 minutes for a single detector.

mole-cule	band centre (cm^{-1})	NESR W cm^{-2} sr^{-1} $/cm^{-1}$	Approx. S/N	nominal VMR & 1-σ error	$t_{S/N=50}$ (mins)
CO_2	667	2.49×10^{-9}	4.8	$1.40^{+0.55}_{-0.45}\times10^{-8}$	226
HCN	713	2.74×10^{-9}	24	$1.70^{+0.35}_{-0.32}\times10^{-7}$	9.1
C_2H_2	730	2.84×10^{-9}	68	$3.00^{+0.10}_{-0.20}\times10^{-6}$	
C_3H_8	748	2.95×10^{-9}	14	$5.00^{+3.00}_{-3.00}\times10^{-7}$	26
C_2H_6	821	3.44×10^{-9}	10	$1.30^{+0.23}_{-0.20}\times10^{-5}$	52
C_2H_4	950	4.52×10^{-9}	1.7	$1.50^{+1.40}_{-1.00}\times10^{-7}$	1763
CH_4	1304	2.16×10^{-10}	206	$2.48^{+0.07}_{-0.06}\times10^{-2}$	

Table 6.1: Estimates of errors on derived CIRS abundances from equatorial nadir spectra, based on the nominal stratospheric values of Coustenis & Bézard (1995) and NESRs for 25 co-added 5 s scans (5 cm^{-1} resolution) measured in chapter 5.

The table also shows an estimate of the signal-to-noise ratio of the band measurement, defined as:

$$\mathrm{S/N}(\tilde{\nu}) = \frac{I(\tilde{\nu})_{\mathrm{gas+continuum}} - I(\tilde{\nu})_{\mathrm{continuum}}}{\mathrm{NESR}(\tilde{\nu})}, \tag{6.2}$$

the difference between the radiance with the gas band and continuum radiances present, minus the radiance due to the continuum alone (surface emission and stratospheric haze, at these wavelengths), divided by the NESR. Also indicated, for the cases where S/N is less than 50, is the observing time required to reach a signal-to-noise of 50.

This sensitivity study was also attempted for several weaker bands in the far-IR; the 50 cm^{-1} band of CO, and the 203 cm^{-1} band of H_2O. However, these lines were much too weak to be measured with any useful accuracy from a 25×5 s summation. Longer integration times are considered in §6.2.2.

mole-cule	band centre (cm^{-1})	NESR W cm^{-2} sr^{-1} $/cm^{-1}$	Approx. S/N	nominal VMR & 1-σ error	$t_{S/N=50}$ (mins)
CO_2	667	2.49×10^{-9}	7.1 ↑	$1.40^{+0.77}_{-0.56}\times10^{-8}$ ↑	102 ↓
HCN	713	2.74×10^{-9}	25 ∼	$1.70^{+0.35}_{-0.22}\times10^{-7}$ ∼	8.3 ∼
C_2H_2	730	2.84×10^{-9}	78 ↑	$3.00^{+0.15}_{-0.10}\times10^{-6}$ ∼	
C_3H_8	748	2.95×10^{-9}	18 ↑	$5.00^{+1.00}_{-0.95}\times10^{-7}$ ↓	16 ↓
C_2H_6	821	3.44×10^{-9}	19 ↑	$1.30^{+0.15}_{-0.14}\times10^{-5}$ ↓	14 ↓
C_2H_4	950	4.52×10^{-9}	3.9 ↑	$1.50^{+0.90}_{-0.65}\times10^{-7}$ ↓	339 ↓
CH_4	1304	2.16×10^{-10}	266 ↑	$2.48^{+0.13}_{-0.11}\times10^{-2}$ ↑	

Table 6.2: Estimates of errors on derived CIRS abundances from limb viewing at z_{cen}=200 km and Δz=44 km, based on the nominal stratospheric values of Coustenis & Bézard (1995). NESRs are for 25 co-added 5 s scans (5 cm^{-1} resolution) measured in chapter 5.

Limb Viewing

Table 6.2 shows the results of abundance error estimation for limb viewing measurements. Again, the nominal equatorial model was used to calculate the synthetic spectra. The detector field of view was centred on an altitude of 200 km, and the width of the MIR field of view was 1 scale height (44 km). No spatial weighting function was applied for the FP3 detectors (600–1100 cm^{-1} range), to avoid losing some of the generality of the result, by choosing a particular detector. The NESR was for 25 co-added 5 s scans, as in the nadir case described above.

Also indicated on the table, for the S/N, 1-σ error and $t_{S/N=50}$ is whether these figures have increased (↑), decreased (↓), or stayed approximately the same (∼) compared to the nadir-viewing case. For the gases C_3H_8, C_2H_6 and C_2H_4 a marked improvement in sensitivity is seen. This is particularly important for C_2H_4 measurements, because the time required to reach a S/N of 50 has decreased from a 29-hour observation to a much more practical 4.4 hours. However, for HCN and C_2H_2, the retrieval error is similar to the nadir-viewing case, and for CH_4 and CO_2 it has actually increased.

Strictly, these results apply only to the tangent height of the calculation (200 km) and

will vary considerably with altitude. Assuming that the band centre remains optically thin, then the following behaviour will be expected. At higher limb-viewing altitudes in the stratosphere, the radiance received in each band will decrease, which will hence reduce the S/N ratio and lead to a bigger error on the abundance. At lower tangent heights, the radiance may initially increase, increasing the S/N and decreasing the retrieval error, but at some point the band centre will become optically thick, after which point the errors will become very large.

Note that in limb viewing, so long as the emission remains unsaturated, the weighting function peaks at the tangent height of the observation, so information about the vertical distribution of the gas is automatically obtained. This is in contrast to nadir viewing, where the vertical distribution must be retrieved mathematically from the relative strengths of various lines of the gas at different wavenumbers.

The observing times considered were, as in the nadir case, much too short to make useful measurements of CO or H_2O in the far-IR.

6.2.2 Minimum Detectable Abundances

The spectral synthesis code was also used to estimate the minimum detectable abundances for minor gaseous species in Titan's atmosphere. The method used was first, to calculate the continuum in the absence the gas band, which included contributions from the surface, the haze, and the collision-induced continuum. The minimum detectable radiance for a single gas line was hence defined as the continuum level at that wavenumber, plus the appropriate NESR of the observation. Therefore the atmospheric model was calculated with the gas present, and the stratospheric abundance adjusted until the required radiance level was attained.

Table 6.3 shows results for a number of minor species. Species which are easily detectable on a single scan (methane, HCN, ethane, propane, acetylene) were not computed. The spectral resolution in this calculation was 0.5 cm^{-1} and the total observing time was 1 hr, corresponding to 70 scans co-added, in nadir viewing geometry. This is a

molecule	wavenum. (cm^{-1})	NESR W cm^{-2} sr^{-1} / cm^{-1}	min. detect. VMR	notes
CO	50.0	2.7×10^{-9}	1.0×10^{-5}	100% UKIRT*
H_2O	202.7	3.9×10^{-9}	2.7×10^{-10}	67% ISO†
C_2N_2	234.1	4.6×10^{-9}	8.6×10^{-10}	4% IRIS 70°N
C_4H_2	627.9	4.3×10^{-9}	5.2×10^{-10}	2% IRIS 7°N
C_3H_4	633.1	4.4×10^{-9}	2.3×10^{-9}	46% IRIS 7°N
HC_3N	663.3	4.7×10^{-9}	7.8×10^{-10}	2% IRIS 70°N
CO_2	667.5	4.7×10^{-9}	5.0×10^{-10}	4% IRIS 7°N
C_2H_4	949.4	8.5×10^{-9}	1.3×10^{-8}	9% IRIS 7°N

Table 6.3: Minimum detectable abundances for some minor species in Titan's atmosphere. Calculation is for 0.5 cm^{-1} resolution scans (52 s) in nadir viewing mode with a total observing time of 1 hr (70 scans co-added). The reference abundances used for comparison in the last column are all from Coustenis & Bézard (1995) except: * Coustenis *et al.* (1998); † Noll *et al.* (1996).

typical amount of time which the instrument might be able to be pointed continuously at one spot on the disk.

In the final column of the table, the minimum detectable abundances are expressed as a fraction of the known abundances of the species in Titan's atmosphere at present. Note that while the calculation presented here is for an equatorial thermal profile, some species such as C_2N_2 and HC_3N have only been detected so far on polar spectra by Voyager, so the comparison in the case of these gases must be treated with a degree of caution. In summary, the detection of most minor species at a S/N level above unity seems certain, with the exception of CO and H_2O which are only marginally detected.

Table 6.4 shows the minimum detectable abundances for a number of other minor species, as yet undetected on Titan. This table is an updated version of Table II from Coustenis *et al.* (1993), derived by simply taking the NESR values used by those authors, and updating them to the new measured values. Then, by assuming that the radiances are linearly dependent on abundance, the estimated minimum detectable VMRs (as-

gas name	molecule	wavenum. (cm^{-1})	predicted VMR	NESR W cm^{-2} sr^{-1} $/cm^{-1}$	min. det. VMR
Allene	CH_2=C=CH_2	356.0	1.6×10^{-8}	8.5×10^{-9}	4×10^{-9}
		845.0		6.8×10^{-9}	1×10^{-8}
Benzene	C_6H_6	673.5	1.8×10^{-9}	4.8×10^{-9}	5×10^{-10}
Acetonitrile	CH_3-C≡N	363.0	4.6×10^{-9}	8.8×10^{-9}	9×10^{-8}
		717.0		5.2×10^{-9}	2×10^{-8}
Acrylonitrile	CH_2=CH-C≡N	241(R)	1.3×10^{-9}	4.8×10^{-9}	3×10^{-8}
		221(P)		4.3×10^{-9}	3×10^{-8}
Propionitrile	CH_3CH_2-C≡N	211(R)	3.2×10^{-9}	4.1×10^{-9}	2×10^{-8}
		202(P)		3.9×10^{-9}	2×10^{-8}
Cyanopropyne	CH_3-C≡C-C≡N	338.0	$< 1.0\times10^{-9}$	7.8×10^{-9}	9×10^{-9}
		499.0		1.8×10^{-8}	2×10^{-8}
Crotonitrile	CH_3CH=CH-C≡N	148(P)	$\leq\times10^{-9}$	3.0×10^{-9}	3×10^{-8}
		165(R)		3.2×10^{-9}	2×10^{-8}
		728.0		5.3×10^{-9}	1×10^{-8}
Butanenitrile	$CH_3(CH_2)_2$-C≡N	728.0		2.1×10^{-8}	3×10^{-7}
Isobutyronitrile	$(CH_3)_2$-CHC≡N	538.0	7.5×10^{-11}	2.1×10^{-8}	3×10^{-7}
Cyclopropane-	△-C≡N	928.0	$<\times10^{-9}$	8.1×10^{-7}	2×10^{-6}
carbonitrile		1046.0		1.0×10^{-8}	5×10^{-7}

Table 6.4: Updated version of Table II of Coustenis *et al.* (1993), showing the measured NESRs and the new estimates for minimum detectable abundances. Sources for the predicted VMRs are given in Coustenis *et al.* (1993).

sumed constant in stratosphere) have been revised accordingly. For a description of the method used to estimate the radiances, and also references for the predicted VMRs in the atmosphere (column 4 in this work), see Coustenis *et al.* (1993).

For all these species the estimated minimum detectable VMRs have been revised upwards from the earlier estimates, due to the measured NESRs being higher than estimates made at the design stage. Comparison of the estimated detection limits with the predicted abundances from chemical and photochemical modelling shows that only allene and benzene are likely to be detected on a 1-hour integration. For the remaining molecules, an increase in S/N ratio by a factor 10 or more will be required for them to be detected in nadir viewing, if the amounts predicted in the models are accurate. However, limb viewing with long pathlengths will greatly increase the radiances for these minor species.

6.2.3 More Advanced Retrievals

The actual errors from a rigorous retrieval algorithm may be significantly less than the estimates above. This is because, in the case of wide bands, the retrieval can simultaneously use information from multiple wavelengths of the band. In this case, it may be worth increasing the spectral resolution at the sacrifice of signal to noise ratio, for a fixed observing time.

6.3 Temperature Sounding

The inverse problem of retrieving atmospheric temperature from remote sounding spectral data has been discussed extensively in the literature Rodgers (1976, and references therein). A thorough investigation of the use of the of CIRS for temperature retrievals is beyond the scope of this thesis, however, it is possible to make some estimates of the accuracy which may be attained by making some simplifying assumptions.

In the stratosphere, temperatures can be inferred by modelling the strong ν_4 band of methane at 7.7 μm. In order to use this band, the vertical abundance distribution of methane must be known, or assumed by other means. Figure 6.9 shows some contribution functions (C.F.s) for the P-branch of the band, for various limb viewing heights. The atmosphere has been split into 20 vertical layers by equal increment of ln$p$, and the view in each case passes through a distinct 'lowest layer' of the model atmosphere. The contribution function is defined as the weighting function times the spectral radiance at each height:

$$\text{C.F.}_{\tilde{\nu}}(z) = B_{\tilde{\nu}}(T(z)) \cdot \frac{d\tau_{\tilde{\nu}}}{dz}(z) \tag{6.3}$$

and the individual C.F.s have been normalised to a peak value of unity. Using the 7.7 μm band, the atmosphere may be sounded from altitudes of $\sim$400 km down to

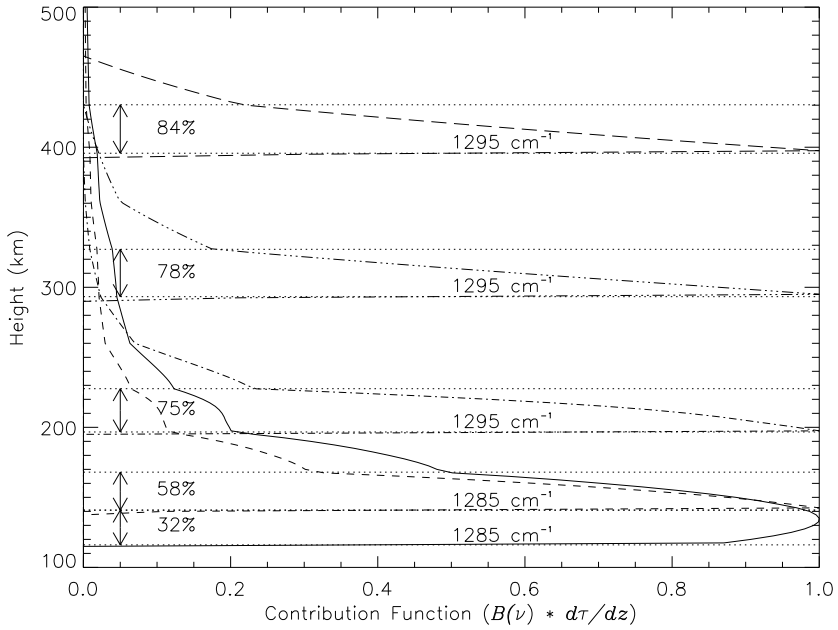

Figure 6.9: Normalised contribution functions in the P-branch of the methane ν_4 band for limb viewing at various tangent heights in the stratosphere. The atmosphere has been split into 20 layers by equal increment of log pressure. The faint dotted lines indicate the breadth of the lowest layer for each limb view. The percentages marked on the plots indicate the proportion of the overall contribution which arises in the lowest layer, for each calculation.

$\sim$150 km. Lower altitudes cannot be sampled in this spectral region, because for lower tangent heights, the atmosphere becomes optically thick before the tangent point. This is illustrated by the lowest C.F. in the figure, which shows a peak above the nominal tangent height of 116 km, and also does not have a sharp peak, as occurs when the path is optically thin.

To reach the lower stratosphere and upper troposphere, a different spectral region must be considered. There are in fact several possibilities in the far-IR.

One possibility is the N_2–N_2 collision-induced absorption band at 10–100 cm^{-1}. Figure 6.10 shows the contribution functions at 90 cm^{-1} near the peak of the band in the far-IR. This band can be used from 80 km down to 60 km in limb-sounding mode, and perhaps even lower in nadir viewing mode (not shown) for the longest wavelengths. It may also be possible to sound using the CIA bands of CH_4 and H_2, assuming the vertical abundances are known.

A second possibility is the pure rotational lines of methane from $\sim$50 to 150 cm^{-1}.

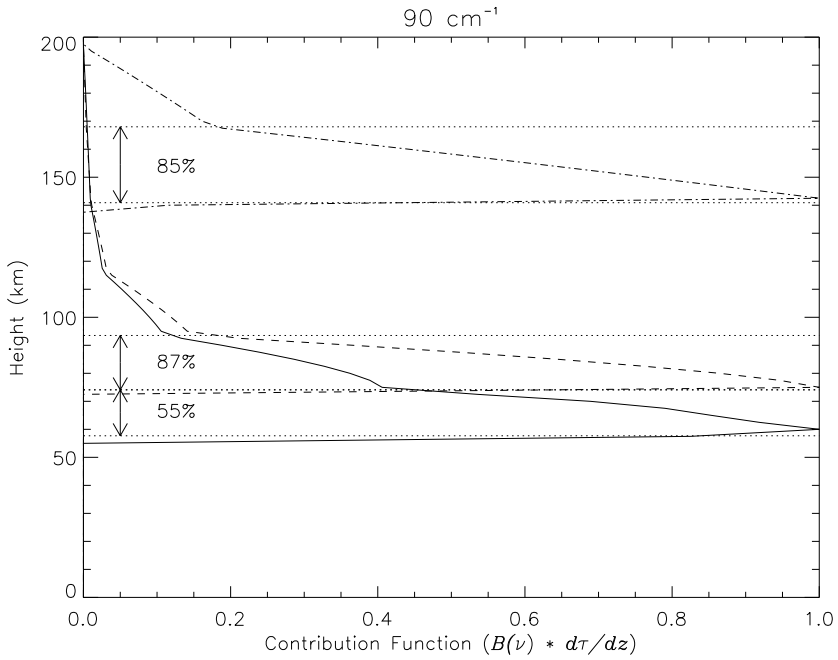

Figure 6.10: Normalised contribution functions at 90 cm^{-1} in the N_2–N_2 CIA band for limb viewing at various tangent heights in the stratosphere. The atmosphere has been split into 20 layers by equal increment of log pressure. The faint dotted lines indicate the breadth of the lowest layer for each limb view. The percentages marked on the plots indicate the proportion of the overall contribution which arises in the lowest layer, for each calculation.

These lines are detectable in Titan's atmosphere because of the large amounts of methane in the lower atmosphere. Figure 6.11 shows the normalised contribution functions for one line centre at 104 cm^{-1}, which shows that temperature sounding in limb viewing mode is possible down to ∼70 km.

I have attempted to estimate the accuracy within which the temperature measurements may be made, by making the simplifying assumption that all the emission at a particular wavenumber comes from a region very close to the tangent height of the limb view.

Consider figure 6.12, which shows the geometry of limb viewing. The atmosphere is divided up into equal layers as described above, and the field of view of a single pixel[2] includes exactly one layer at the point of tangent. Although the radiance received at the detector comes from all layers n and above, in fact most of the radiance will come

[2]Note that only the detectors from FP4 and FP1 are used in temperature sounding, due to the spectral locations of the gaseous bands used in the sounding, and hence the spatial weighting function is assumed to be flat.

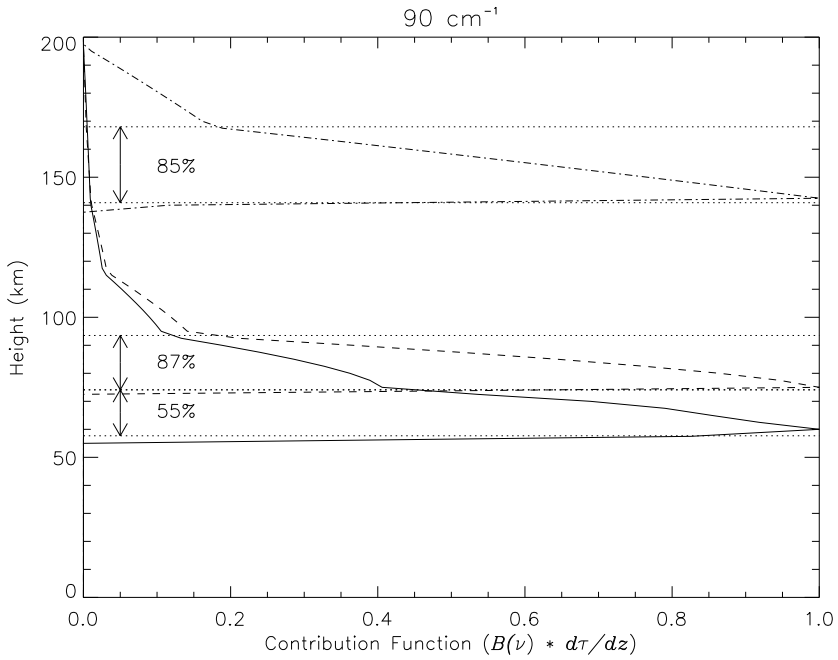

Figure 6.11: Normalised contribution functions at 104 cm^{-1} in the CH_4 pure rotational (forbidden) band for limb viewing at various tangent heights in the stratosphere. The atmosphere has been split into 20 layers by equal increment of log pressure. The faint dotted lines indicate the breadth of the lowest layer for each limb view. The percentages marked on the plots indicate the proportion of the overall contribution which arises in the lowest layer, for each calculation.

from the lowest layer seen (n) if the path remains optically thin. Hence, in the following treatment, it is assumed that *all* the emission at a particular wavenumber comes from a particular layer, within which the continuous temperature distribution is represented as a mean temperature.

The validity of this assumption may be assessed by calculating how much of the overall contribution comes from just the lowest layer. These figures are indicated as the percentages on figures 6.9–6.11. I have only considered the approximation to be valid when the percentage contribution of the lowest layer is 50% or more of the the total.

This allows a rough estimate of the temperature measurement error to be made, using a process analogous to the method used in the previous section to estimate gas abundance errors. Again, only a single spectral element has been used at the indicated wavenumber, but this could be extended to cover multiple elements.

Firstly, a nominal equatorial temperature profile is used to calculate the radiance at the appropriate wavenumber. Then, the temperature profile is adjusted slightly by

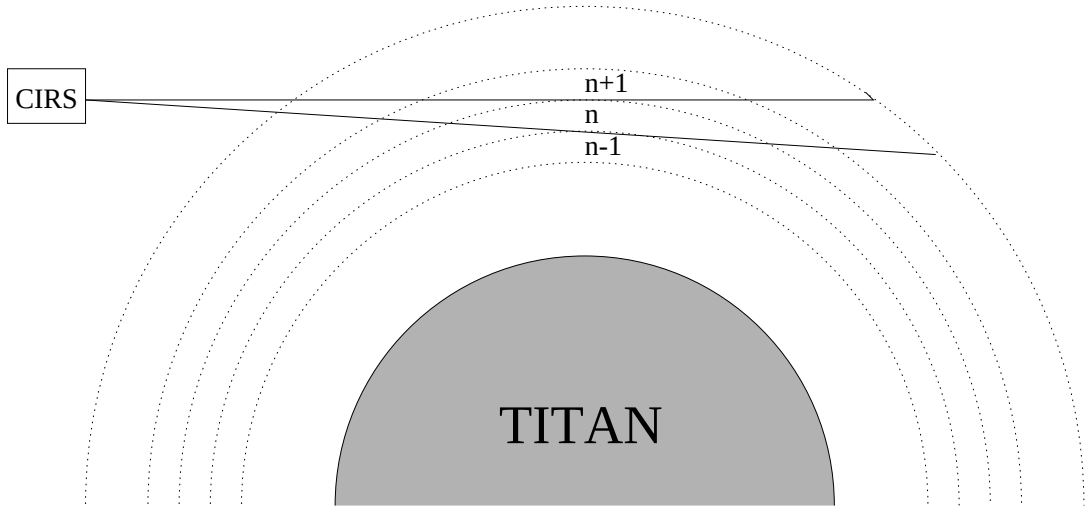

Figure 6.12: Illustration of limb viewing for temperature sounding. The field of view of one pixel covers exactly one layer of the atmosphere (as defined in the 20-layer log$p$ model) at the tangent point.

adding a small increment ΔT, but only in the altitude range of the bottom layer of the limb calculation. This process is iterated until the radiance has changed by an amount equal to the NESR at that wavenumber. As before, the NESR level used was equivalent to a 2-minute integration, or 25×5 s scans. This ΔT is equivalent to the expected measurement error. The process was repeated to find the ΔT required to reduce the radiance by the NESR amount. The results are shown in table 6.3.

Although these figures must be treated with some caution in view of the approximations being made, some general trends seem to be established. The temperature retrieval error for all three types of sounding increases at higher tangent altitudes: this is clearly due to the fall in radiance with height, whilst the NESR level stays constant.

Above 140 km, and up to 300–400 km (depending on integration time and desired accuracy), the strong ν_4 band of methane will give the most accurate temperature information. Below 140 km however, this band becomes too optically thick to be useful. Below 140 km, the rotational lines of methane around 100 cm^{-1} give the most accurate results, and can sound down to ∼70 km before saturating.

The N_2-N_2 collisional band can be used for sounding in a relatively narrow alti-

emission type	wavenumber (cm^{-1})	tangent height (km)	FOV width [H] (km)	layer T
CH_4 ν_4 (P)	1295	396	34 [50]	$169.4^{+2.5}_{-3.1}$
CH_4 ν_4 (P)	1295	293	34 [49]	$177.7^{+0.5}_{-0.5}$
CH_4 ν_4 (P)	1295	197	31 [44]	$173.9^{+0.2}_{-0.2}$
CH_4 ν_4 (P)	1295	140	27 [38]	$157.4^{+0.3}_{-0.3}$
CH_4 rot.	104	116	25 [36]	$150.5^{+1.1}_{-1.2}$
CH_4 rot.	104	93	23 [32]	$140.0^{+0.5}_{-0.3}$
CH_4 rot.	104	74	19 [26]	$120.4^{+0.1}_{-0.1}$
N_2–N_2 (CIA)	90	93	23 [32]	$140.0^{+5.2}_{-6.5}$
N_2–N_2 (CIA)	90	74	19 [26]	$120.4^{+1.9}_{-1.6}$

Table 6.5: Estimated errors on temperature retrievals from limb viewing of Titan. In the stratosphere, the ν_4 band of methane is sounded in the mid-IR. In the lower stratosphere and troposphere, both the collision-induced opacity of N_2–N_2 collisions, and a methane rotational band are sounded in the far-IR. The tangent height is the altitude of the bottom of the lowest layer in the path calculation. The thickness of the bottom layer is indicated in column 4, which is the same as the FOV width at the tangent height. This is followed by the scale height [in square brackets]. The temperature indicated in column 5 is the Curtis-Godson, or pressure-weighted mean tempature of the layer. The error on the temperature has been derived as described in the text, for the NESR of a 2-minute integration.

tude region from ∼60–80 km, depending on wavenumber. Temperature retrievals using this continuum will not be as accurate as from the methane rotational band, however retrievals using the nitrogen continuum may be used to check the methane results.

Error estimates such as these may be of value when designing observational sequences for the instrument (see §7.2). Finally, it will always be valuable to derive a temperature profile in the lower atmosphere independently via radio occultation.

6.4 Methane Saturation

In the range 200–400 cm^{-1}, the continuum radiance is largely due to collision-induced opacity of N_2–CH_4 and CH_4–CH_4 pairs. By varying the surface humidity and maximum amount of saturation of methane in the troposphere model, the continuum level can be raised or lowered in the synthetic spectra. In chapter 3, the model was compared to an IRIS equatorial spectrum to derive an estimate of the amount of methane supersaturation.

This nominal model is now used to estimate the accuracy of CIRS measurements of the supersaturation fraction. The method is similar to that used in §6.2 to estimate the error on gaseous abundance measurements. Firstly, a nominal synthetic spectrum was calculated using $s = 1.5$, and the radiance measured at 200, 300 and 400 cm^{-1}. Then, the $NESR^+$ radiance was calculated at these three points, by adding on the NESR expected for a 2-minute integration. Then, the amount of supersaturation was *decreased* in the model until the radiance matched the $NESR^+$ level. A separate match was obtained at the three different wavenumbers.

Then, the $NESR^-$ level was calculated at the three points and the corresponding amounts of supersaturation required to match these again determined. This process resulted in an estimate of the expected error in the supersaturation fraction when determined from each of these three wavenumber points.

Table 6.4 shows the results. The 200 cm^{-1} point gives the smallest error of the

Wavenumber (cm^{-1})	S/N	s.s. (%) and error
200	105	50^{+14}_{-11}
300	45	50^{+15}_{-12}
400	18	50^{+63}_{-38}

Table 6.6: Error on estimates of the percentage supersaturation of methane from the far-IR continuum.

three: this is due to a combination of lower NESR in this region and higher signal level combining to give the greatest S/N ratio, which is reflected in the smallest errors on the supersaturation.

This test shows that errors of ∼10 % are routinely achievable; and by co-adding more spectra, much smaller errors will be possible. In addition, using a χ^2-minimisation over a whole spectral region, *e.g.* 200–300 cm^{-1} will in principle enable a much more accurate determination to be made by using more information from the spectral data. If the NESR on the spectrum is the limiting factor determining the error on the retrieval, then by using 20 elements of width 5 cm^{-1} instead of a single element, the error on the supersaturation will be reduced by a factor $\sqrt{20}$.

Chapter 7

Summary and Conclusions

In this chapter I first summarize the principal results of this thesis (§7.1), and then consider how this information may affect the planning of scientific observations over the mission (§7.2). Finally, suggestions for ways in which this current study might be extended are proposed (§7.3).

7.1 Summary

7.1.1 Radiative Transfer Model of Titan's Atmosphere

The model atmosphere and radiative transfer code have been largely successful in reproducing the observed equatorial spectrum from IRIS. In particular, the strong bands of methane, acetylene and HCN are well represented, as is the collision-induced continuum at $\lambda < 400$ cm^{-1}. This has led to an estimate for the maximum super-saturation ratio of methane in the troposphere of 125–150%, for a surface humidity of 60%.

One key drawback of the model is its failure *a priori* to predict the observed continuum level for the region 750–1100 cm^{-1}, due to stratospheric haze. Although I have used just a single particle size, in fact the shape of the extinction curve does not change with particle size, and hence the laboratory tholins are not a good analogue for the haze extinction in this region. Rannou et al. (1997) have shown that aggregate (fractal)

particles can be used to improve the model of scattered light at Titan's limb observed by Voyager 2, so the reliance on purely spherical particles in the model may have to be removed.

7.1.2 Detector Fields of View and Spatial Weighting Functions

The spatial weighting functions of all 20 mid-IR detectors have been measured, for the flight model detectors. The PV detectors (FP4) as expected have a uniform response cross-section in both the y and z axes, and moreover all these detectors show a similar level of response (see figures 4.9 and 4.15).

The PC detectors of FP3 however have an unusual response characteristic, all showing a bifurcated weighting function, which is expected due to their physical design (figure 4.8). However, some of the detectors, in particular numbers 1 and 5, show significant asymmetry of response between the two lobes (figure 4.8). In addition, the level of reponse varies significantly along the array, tailing off towards both ends. The lowest response is detector 1, which has a mean response of $\sim$50% that of detector 6.

Often when observing with FP3, the 'odd pixels only' or 'even pixels only' modes will be used. In this event, if there are no other considerations todecide between the two possibilities, the even pixels should be used, which exhibit less variation from detector to detector than the odd pixels.

In any event, the fact that the spatial weighting functions for all detectors have been quantified will allow the instrumental weighting effect to be compensated for and removed when analysing data collected in by the mid-IR interferometer.

7.1.3 NESR of the Detectors

A new Fourier Transform code has been written which performs phase correction to CIRS interferograms and transforms the IFMs to apodised power spectra. The spectra produced with this code are in close agreement to the spectra produced with an older

CIRS code. However, the new code has the advantage of being non-interactive and hence can be used to process much larger volumes of data than was previously possible, which will be important once Cassini begins to return scientific data.

The code has been used to transform pre-flight radiometric calibration data, which have subsequently been analysed to deduce the responsivity and noise equivalent radiance for all 21 detectors, for a range of focal plane operating temperatures. The measured NESRs are somewhat (∼3–10) higher than the original specification, and this is thought to be mainly due to higher than predicted losses in the optics.

7.1.4 Measurement Capability of CIRS

A preliminary sensitivity study for CIRS retrievals of key scientific quantities including: the abundances for major and minor gases; atmospheric temperature; and supersaturation amount; has been completed. This made use of the experimental NESRs to estimate the expected errors on the measured quantities. In addition, the expected minimum detectable abundances of minor constituents, including some as yet undetected, have been calculated, for a net integration time of 1 hour.

For temperature sounding, it has been shown how different spectral regions may be used to sound different levels in the atmosphere. Sounding below ∼50 km in the infrared may not be possible, and so coupled analysis of CIRS data with radio occultation measurements will be important.

The effect of the FP3 spatial weighting function on measured spectra has also been investigated. The results indicate that the non-uniform response of the PC detectors may have a noticeable effect for integration times over 2 minutes in length, and may become increasingly important when more spectral elements are used in the retrieval.

7.2 Review of Current Observing Proposals

Six 'typical' sequences of observations were proposed in the pre-launch period (designed by F.M. Flasar, G.L. Bjoraker, R.E Samuelson and R. Courtin). These are intended to cover a broad range of investigations, using both limb and nadir viewing, and various switching modes of the mid-IR detectors. It is now appropriate to revisit these sequences (sometimes referred to as 'links') in light of the results of this thesis, and consider what modifications, if any, might need to be made. In each case, the current parameters of the sequence are described first (*italic text*) followed by a commentary.

1. **Mid-IR Limb Temperature Map.** *Limb sounding with FP3 and 4 at intervals of 5° latitude. Pressure levels 2–0.01 mbar. Vertical resolution 1 scale height. Spectral resolution 20 cm^{-1}. Observing time 10s at low latitudes, corresponding to a S/N =90 at 1304 cm^{-1}. Derived ΔT=0.2 K at 0.01 mbar. Total duration ∼2 hrs.*

   At 0.01 mbar ($z \simeq$350 km), the results of §6.3 indicate that a ΔT of ∼2 K would be achieved from a 30s observation, if the decrease in resolution from 5 to 20 cm^{-1} is taken into account. This is an order of magnitude greater than in the proposal, which was based on pre-construction theoretical values for the NESR. Indeed, it can be seen from figure 5.28 that the NESR is indeed an order of magnitude greater at 1304 cm^{-1} than predicted. Therefore, a factor 100 increase in observation time would be required to achieve a ΔT=0.2 K, or about 1 hour of integration at each point on the limb.

   In practice, this may not be realistic, and either a greater ΔT or a decrease in spatial resolution may have to be accepted. The latter could be achieved by using the pixel pairs mode to co-add detectors, or fewer latitudes could be sounded. One possibility may be firstly to map a wide range of latitudes relatively quickly, and with a fairly low accuracy (ΔT=1 K would require a factor ∼4 increase in observing time, keeping the rest of the sequence as before), and then, perhaps on a separate

encounter at a later time, to make a smaller number of high S/N observations at selected latitudes (e.g. 0, 30°N, 30°S, 75°N and 75°S) with the highest vertical resolution (ΔT=0.2 K would require ∼5 hrs).

2. **Mid-IR Hydrocarbon Quick-Map.** *Limb sounding with FP3 and FP4 at intervals of 5° latitude, primarily of HCN and C_2H_2. Pressure levels 20–0.04 mbar. Vertical resolution 1 scale height. Spectral resolution 3 cm^{-1}. S/N 7–50 for 20s observations. Total time 58 mins for 1/4 limb.*

   As in the previous case, the integration time will need to be substantially increased (×25) to compensate for the factor ∼5 increase in NESR at 700–800 cm^{-1} since the proposal. This is probably impractical during a single pass of Titan; hence a decrease in S/N or in vertical resolution may have to be accepted.

3. **Far-IR Nadir Temperature and Aerosol Map.** *Map temperatures in the upper troposphere (15–100 cm^{-1}), the surface (540 cm^{-1}) and stratospheric haze and CIA continuum (200–600 cm^{-1}). Spectral resolution 20 cm^{-1}. Spatial resolution on the disk is ∼11°. S/N >30. Individual observations=86 s. Total time: 3 hrs.*

   The increase in NESR since the proposal is least for FP1, therefore an increase by a factor 9 in the total observing time will be sufficient to achieve the intended S/N. It is probably undesirable to reduce the spatial resolution further, as 11° is already quite coarse. Instead, it may be preferable to map a smaller portion of the planet on each pass and retain the original FOV size and S/N. Later in the mission, the inclination of orbit of Cassini is increased, so it may be desirable to concentrate on mapping the equatorial regions in the early mission, and map the polar regions later.

4. **FIR Limb Integration.** *Obtain HCN and CH_4 mixing ratios (100–250 km) detect H_2O, CO, and $H^{13}CN$ emissions. Vertical resolution 180 km. Spectral resolution 0.5 cm^{-1}. S/N >10. Dwell time: 1890 s. Total sequence time: 2 hrs.*

The integration times required to detect CO and H_2O emissions in the far-IR are likely to be much longer than was thought during the early mission planning. Observations of 4–5 hrs will probably be needed to detect the emissions at low spectral resolution (5 cm^{-1}), with correspondingly longer times to achieve high spectral resolution. The best strategy is probably to begin by integrating continuously on the equatorial limb for as long as possible during an early encounter, without moving the instrument footprint. Then, when the equatorial detection is certain, the observations can progress to other latitudes.

5. **FIR and MIR Nitrile/Hydrocarbon Nadir Map.** *Globally map stratospheric mixing ratios of nitriles and hydrocarbons (z=100–250 km). Spatial resolution is ∼7.5° (FP1) and ∼0.9° (FP3 and 4). Spectral resolution 3 cm^{-1}. S/N 2–200. Total time 2.7 hrs.*

   In this link, the FOVs of all the focal planes are swept backwards and forwards across the face of the disk, with the FP1, FP3 and FP4 arrays all centred on the same latitude during each sweep. The primary modification which needs to be made is to slow down the sweep rate, from 0.197 mrad s^{-1} to allow for a greater integration time at each latitude. The current scheme allows for 16 latitudes to be mapped during each encounter. It will probably be desirable to reduce this to four or fewer latitudes, and trade off some spectral resolution to increase the S/N in the early days of the mission. Later in the mission, it may be possible to co-add spectra taken on later passes to increase the S/N and still have a medium (3 cm^{-1}) spectral resolution. FP3 and FP4 are required to operate in the 'reduced resolution' or 'pixel pairs' mode. Alternatively, the 'centre pixels' mode could be used and all five pixel spectra co-added to increase the S/N at the expense of some horizontal resolution.

6. **MIR Nitrile/Hydrocarbon Map.** *Globally map stratospheric mixing ratios of nitriles and hydrocarbons (z=100–250 km) with FP3 in 'pixel-pairs' or reduced*

resolution mode. Spatial resolution is ∼3.0°. Spectral resolution 3 cm^{-1}. S/N 2–300. Total time 3.4 hrs.

This sequence is very similar to the previous one; although designed to take place at much greater distances from Titan. The commentary appended to the previous sequence also applies here, except that it will probably not be possible to reduce the spatial resolution by going to the 'centre pixels' mode. Both this sequence and the previous one are intended to be repeated at least six times during the mission (beginning, middle and end, both day and night sides).

All these observational sequences are intended to be repeated on multiple passes of Titan, so as to also obtain information on the temporal variation of abundances, temperature, and so on.

Figure 7.1 depicts the two main observing orientations of the mid-IR FOV, with respect to the planet. The left-hand figure shows the 'stepping' mode which is intended for limb viewing. This geometry has the advantage of sampling the widest range of altitudes for each position of the FOV, however this requires quite precise tracking of the spacecraft in both the x and z directions. The 'comb' mode is designed for nadir measurements, which requires only sweeping in the z-direction.

S. Calcutt has raised the point that spacecraft pointing may not ultimately be reliable and repeatable enough to accurately perform limb measurements in the (a) scenario. In this event, the comb method could also be applied to the limb, with the sweep speed suitably reduced.

7.3 Further Work

The following suggestions are made for follow-up study to this work:

- **Atmospheric Model.** The model of the continuum due to aerosol opacity requires improvement. Other types of particles should be considered, including aggregates.

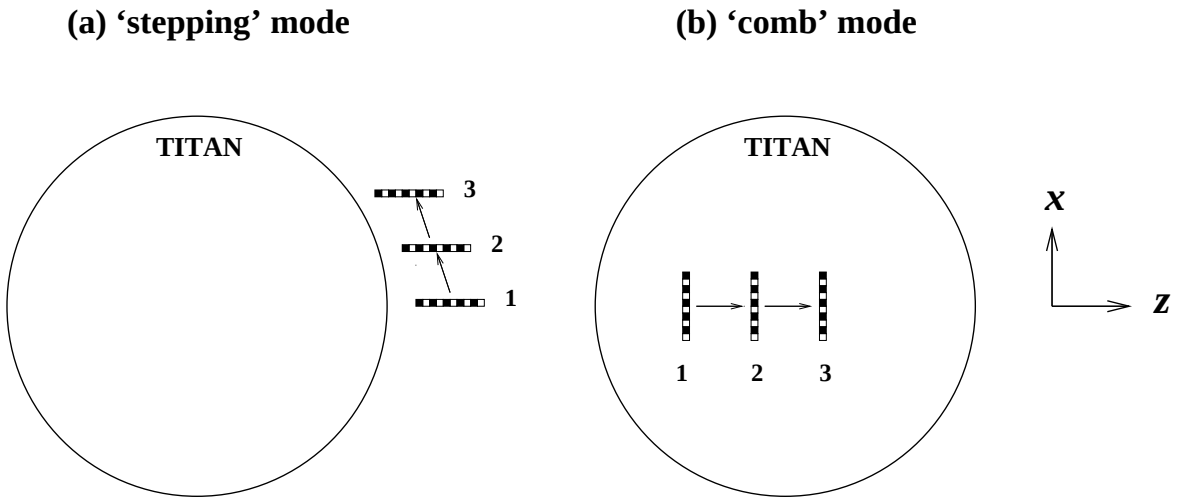

Figure 7.1: CIRS field of view movement on Titan's disk.

An alternative would be to remove the use of an actual particle distribution, and instead to model the resulting opacity only. The Voyager data for other latitudes could also be modelled, and the atmospheric model should be extended to include latitudinal variation. This would enable predictions to be made for S/N at polar regions. In addition, a microphysical condensation model should be developed to increase accuracy of methane profiles in the troposphere.

- **Radiative Transfer Code.** One way to extend the power of the predictive code would be to add line data where possible for a wider range of molecules than is currently the case. For example, the molecules benzene and allene are expected (Yung et al., 1984; Coustenis et al., 1993), and also a wide range of heavier hydrocarbon molecules, although at smaller mole fractions. Predictions for the minimum detectable abundances of these molecules have been made (§6.2.2) but in the event that emissions from these gases is seen, a more accurate lin-by-line treatment will be required to model the spectrum and perform retrievals accurately.

- **Fourier Transform Code and NESR Calculation.** The current NESR calculations could be checked by using other noise estimation methods. For example, instead of subtracting the final spectra, one can subtract the individual interfero-

grams before transforming. This would provide an independent check of the data analysis method.

- **Sensitivity study of errors.** The methods used to estimate the errors on the gas abundances and temperatures retrieved from CIRS data were simplistic. Fuller account needs to be taken of errors in the model (such as the profile) and the effect of utilising information from multiple spectral elements, when estimating the errors on retrieved quantities. Completing a full simulated retrieval will be essential to obtain accurate information for mission planning.

In addition, there are many other pre-mission activities which will be important. One of the most crucial will be to continue the investigation into laboratory tholins; the variation of tholin which is produced under different reaction conditions, and an analysis of the chemical and physical nature of the final substrates.

Appendix A

Windowing and Apodisation: Mathematical Description

A.1 Spectral Windowing

Consider the case where we can measure I in the range $0 < x < X$. This is equivalent to multiplying $I(x)$ by a boxcar or 'top-hat' function $\sqcap_1(x)$ defined as:

$$\sqcap_1\left(\frac{x}{X}\right) = \begin{cases} 1 & 0 \leq x \leq X \\ 0 & x < 0, x > X \end{cases} \tag{A.1}$$

This is called the **windowing function**, because it restricts the range of another function. The Fourier Transform of $\sqcap_1$ is:

$$2\int_0^\infty \sqcap_1\left(\frac{x}{X}\right)\cos(2\pi\tilde{\nu}x)dx = 2X\mathrm{sinc}(2\tilde{\nu}X) \tag{A.2}$$

where $\mathrm{sinc}(x) = \sin(\pi x)/(\pi x)$ is the **apparatus function**, also written as $A_0(\tilde{\nu})$.

Now if we take the FT of the restricted interferogram:

$$P_{\rm e}^{\rm c}(\tilde{\nu}) = 2\int_0^\infty \left(\sqcap_1\left(\frac{x}{X}\right)\mathcal{I}_{\rm e}(x)\right)\cos(2\pi\tilde{\nu}x)dx \tag{A.3}$$

where the super-script 'c' denotes that the result is a 'computed', rather than 'true' power spectrum, we see that we have lost some information in the measurement process through windowing. $P_{\rm e}^{\rm c}$ can be re-written as the full infinite FT:

$$P_{\rm e}^{\rm c}(\tilde{\nu}) = 2\int_{-\infty}^\infty \left(\sqcap_2\left(\frac{x}{X}\right)\mathcal{I}_{\rm e}(x)\right)e^{-2\pi\tilde{\nu}x}dx \tag{A.4}$$

where

$$\sqcap_2\left(\frac{x}{X}\right) = \begin{cases} 1 & |x| \leq X \\ 0 & |x| > X \end{cases} . \tag{A.5}$$

The **convolution theorem** states that:

$$F.T.[A(x)\cdot B(x)] = a(\tilde{\nu}) * b(\tilde{\nu}) \tag{A.6}$$

(see e.g. Arfken, 1985, p811 for derivation) hence equation A.4 can be re-written as:

$$P_{\rm e}^{\rm c}(\tilde{\nu}) = B_e(\tilde{\nu}) * A_0(\tilde{\nu}X). \tag{A.7}$$

In other words, when we window a spectrum by restricting its range in one domain, then the Fourier Transform of the original function is convolved by the Apparatus function A_0 in the other domain. In physical terms, two things have happened: there has been

a reduction in resolution, and also spurious features ('ripples') have been introduced.

A.2 Weighting and Apodisation

There is nothing that can be done about the loss of resolution, which has its origin in the loss of information incurred by not measuring the high spatial frequencies, however we can take some steps to mitigate the effect of the ripples.

We can generalise equation A.7 to the case where a general **weighting function** multiplies the interferogram:

$$P_{\mathrm{e}}^{\mathrm{c}}(\tilde{\nu}) = 2\int_{-\infty}^{\infty}\left(W\left(\frac{x}{X}\right)\mathcal{I}_{\mathrm{e}}(x)\right)e^{-2\pi\tilde{\nu}x}dx \tag{A.8}$$

$$= \mathcal{B}_{\mathrm{e}}(\tilde{\nu}) * A(\tilde{\nu}X). \tag{A.9}$$

Note the the function $W(\frac{x}{X})$ is assumed to include the boxcar function $\sqcap(\frac{x}{X})$, and $W(\frac{x}{X}) \overset{F.T.}{\Longleftrightarrow} A(\tilde{\nu})$. Now, we are free to choose weighting functions W which give us an **apodisation function** A which has any desired properties, *e.g.* fewer ripples than A_0. This is not a free lunch however: we pay for the smaller sidelobes by incurring a wider central lobe, *i.e.* further loss of resolution.

If instead of using a boxcar weighting function we choose the triangular or 'sawtooth' function defined:

$$\bigwedge\left(\frac{x}{X}\right) = \begin{cases} 1 - \frac{|x|}{X} & |x| \leq X \\ 0 & |x| > X \end{cases} \tag{A.10}$$

we find that the corresponding weighting function is:

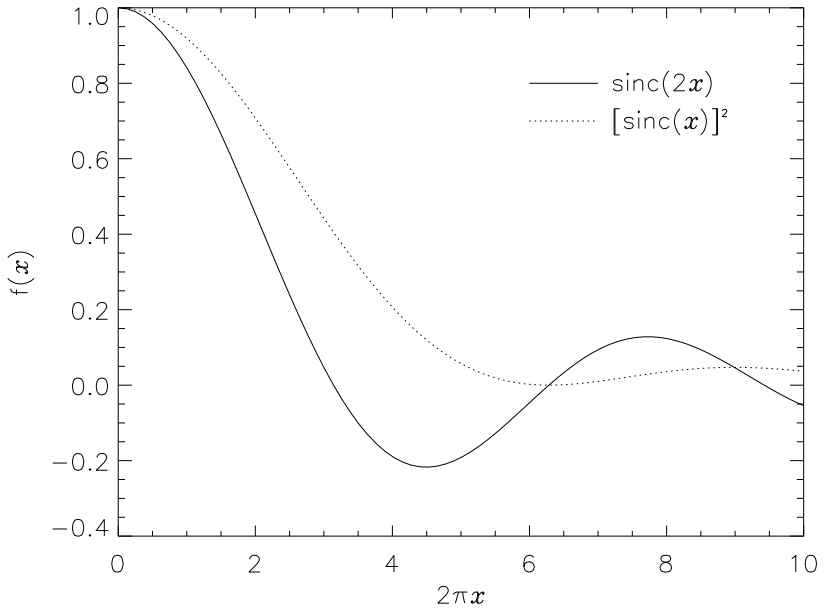

Figure A.1:

$$A(\tilde{\nu}X) = X[\mathrm{sinc}(\tilde{\nu})]^2. \tag{A.11}$$

Figure A.1 illustrates the comparison between the sinc function resulting from the boxcar weighting, and the sinc^2 weighting resulting from the triangular weighting. Although the sinc^2 function has a more rapid attenuation ($\propto \frac{1}{x^2}$ rather than $\propto \frac{1}{x}$) the FWHM is 1.47 times greater. Resolution has been traded off in exchange for apodisation.

See section 5.1.1 for a further discussion of apodisation functions.

Appendix B

Radiometric Calibration Plots

B.1 Mean Spectra Plots

Plots of means of similar spectra at 3 cm^{-1} resolution (see §5.2.3 for discussion). For FP1, the means are of 120 spectra. For FP3 and FP4, the means are of 30 spectra. The data is presented in order: FP1, FP3, FP4; and in order of $T_{\rm FPA}$ for each focal plane.

#	Date	$T_{\rm FPA}$(K)	FP	detector
B.1	02–03/05/97	80	1	1
B.2	03–06/05/97	85	1	1
B.3	02–03/05/97	80	3	2
B.4	02–03/05/97	80	3	10
B.5	03–06/05/97	85	3	2
B.6	03–06/05/97	85	3	10
B.7	02–03/05/97	80	4	2
B.8	02–03/05/97	80	4	10
B.9	03–06/05/97	85	4	2
B.10	03–06/05/97	85	4	10

Table B.1: Index of the mean spectra plots.

(See also table 5.3). For FP3 and FP4 the data pertaining to detectors 2 and 10 is plotted. These detectors are taken to be representative of each array of ten detectors, being almost at opposite ends of the arrays.

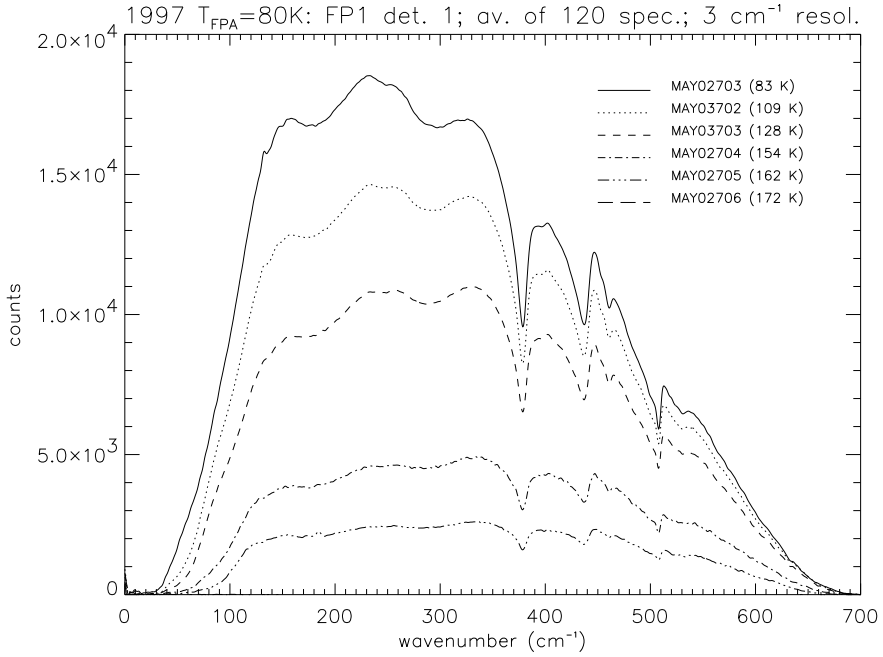

Figure B.1: FP 1: averages of 120 spectra, recorded 02–03/05/97.

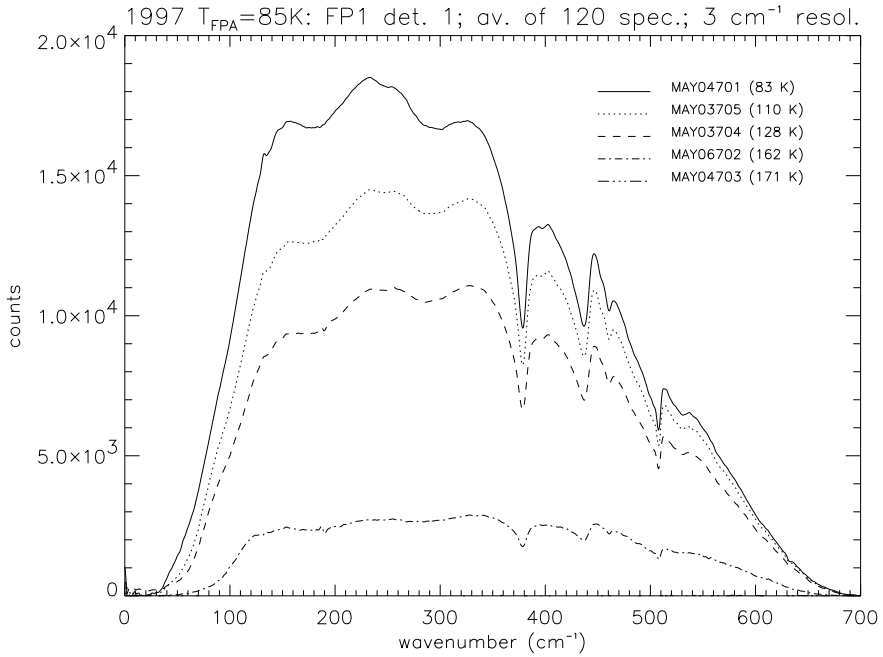

Figure B.2: FP 1: averages of 120 spectra, recorded 03–06/05/97.

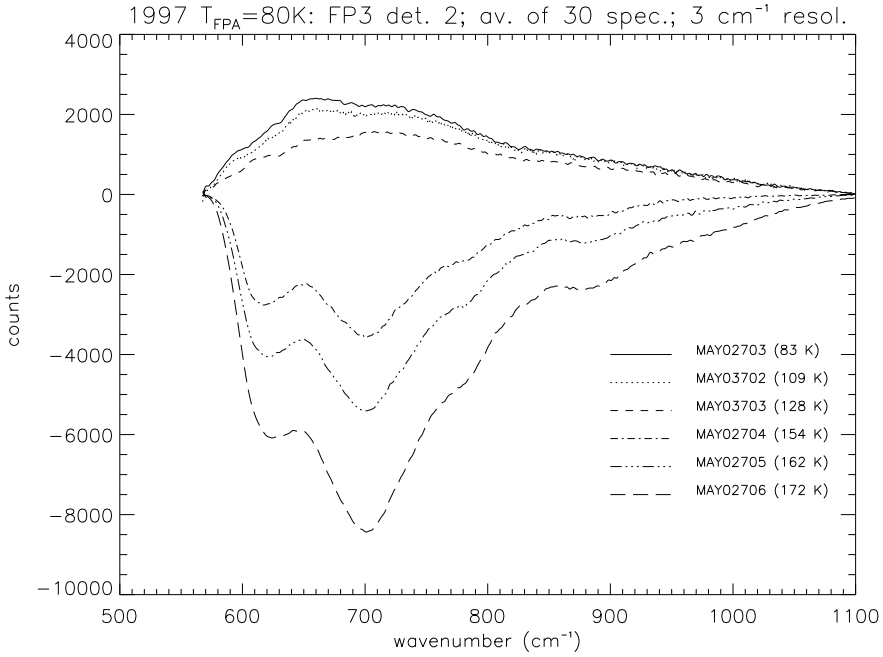

Figure B.3: FP 3 detector 2: averages of thirty spectra, recorded 02–03/05/97.

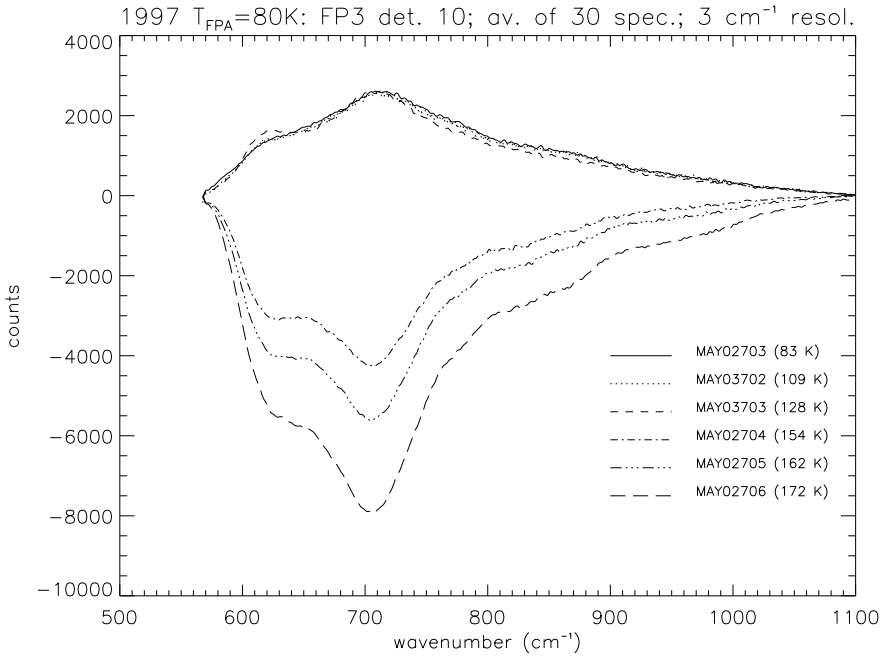

Figure B.4: FP 3 detector 10: averages of thirty spectra, recorded 02–03/05/97.

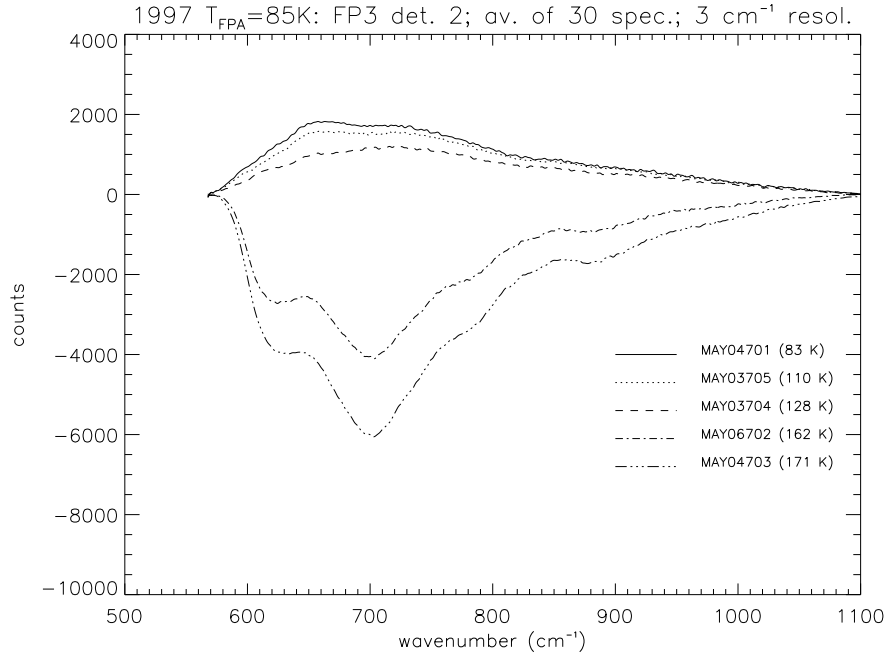

Figure B.5: FP 3 detector 2: averages of thirty spectra, recorded 03–06/05/97.

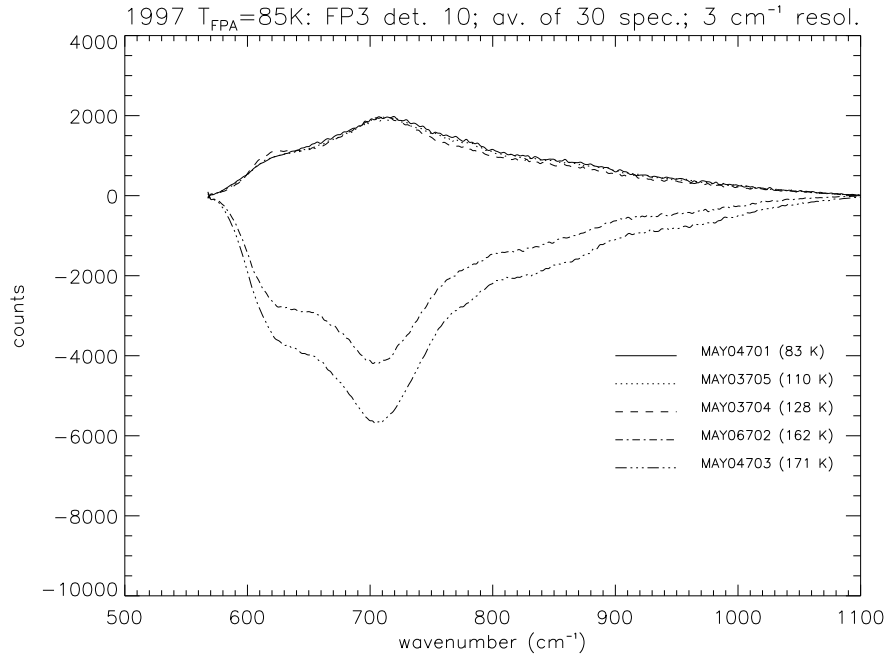

Figure B.6: FP 3 detector 10: averages of thirty spectra, recorded 03–06/05/97.

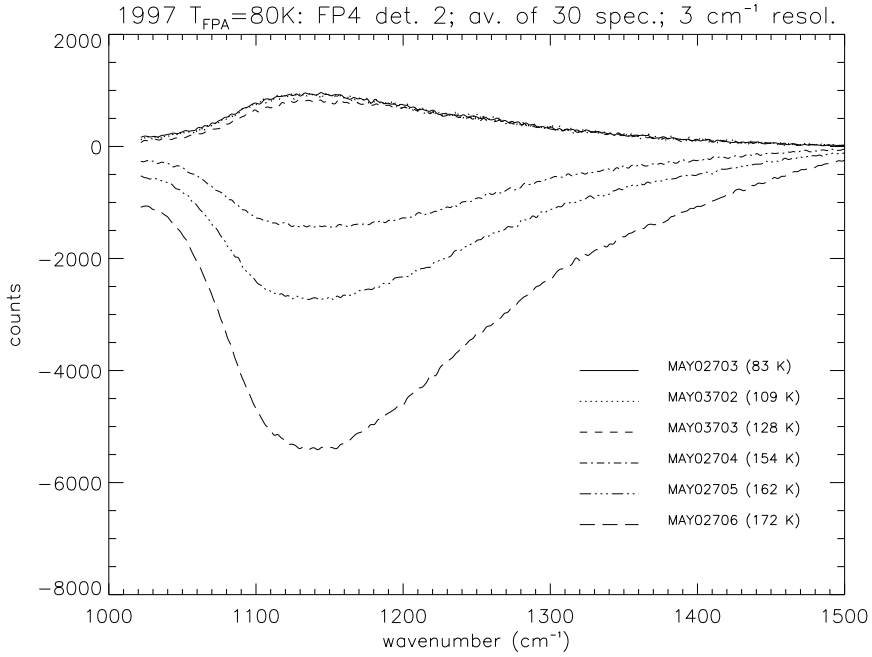

Figure B.7: FP 4 detector 2: averages of thirty spectra, recorded 02–03/05/97.

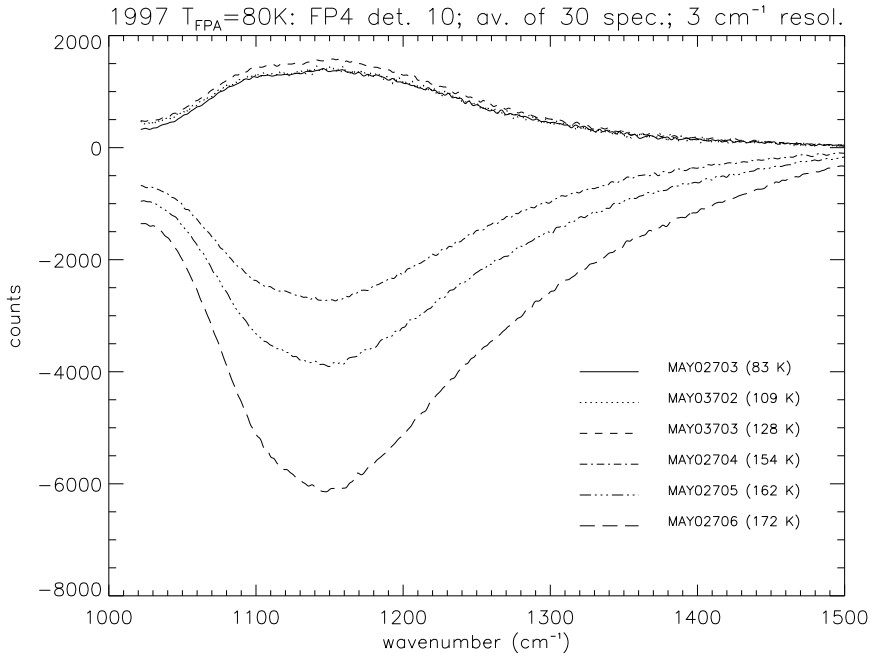

Figure B.8: FP 4 detector 10: averages of thirty spectra, recorded 02–03/05/97.

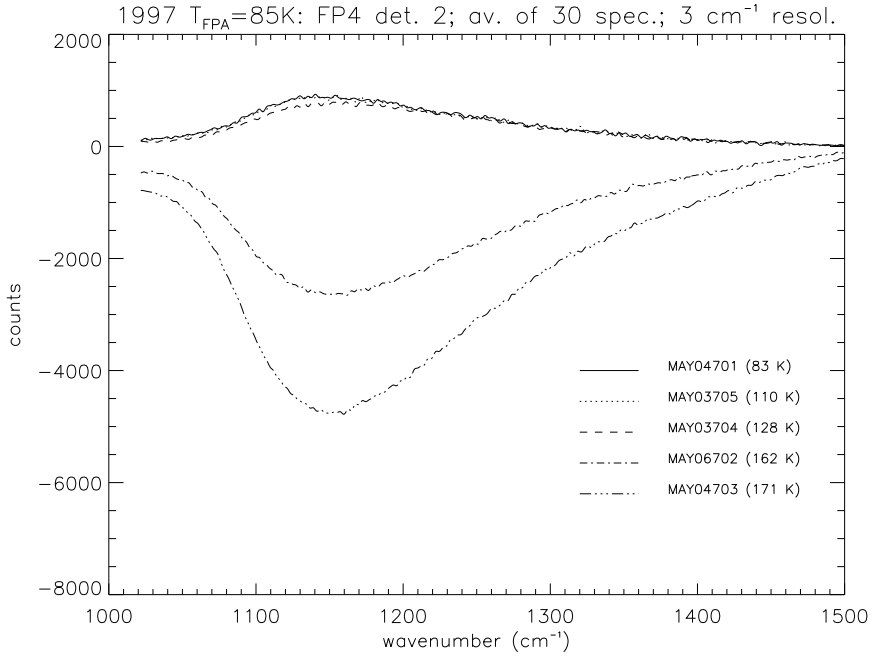

Figure B.9: FP 4 detector 2: averages of thirty spectra, recorded 03–06/05/97.

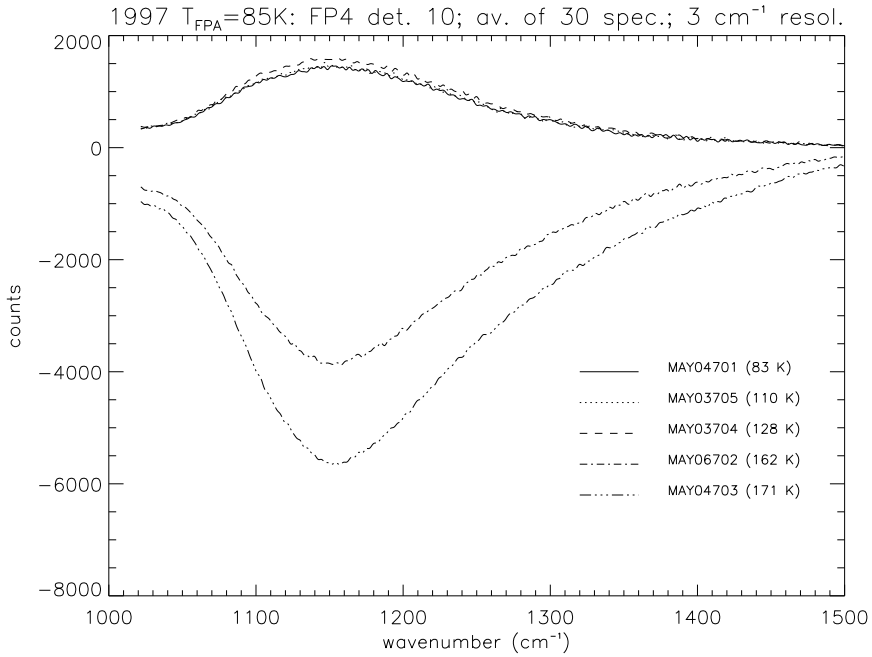

Figure B.10: FP 4 detector 10: averages of thirty spectra, recorded 03–06/05/97.

B.2 Detector Responsivity Plots

A series of plots of detector responsivities for all detectors, derived from FWHM=3 cm^{-1} mean spectra plots (see §B.1). The data is presented in order: FP1, FP3, FP4; and in order of $T_{\rm FPA}$ for each focal plane. See §5.2.3 for discussion.

#	Date	$T_{\rm FPA}$(K)	$T_{\rm TAR}$(K)	FP
B.11	02/05/97	170	83	1
B.12	03/05/97	170	128	1
B.13	04/05/97	170	83	1
B.14	03/05/97	170	129	1
B.15	02/05/97	80	162	3
B.16	02/05/97	80	172	3
B.17	06/05/97	85	162	3
B.18	06/05/97	85	172	3
B.19	02/05/97	80	162	4
B.20	02/05/97	80	172	4
B.21	06/05/97	85	162	4
B.22	06/05/97	85	172	4

Table B.2: Index of the responsivity plots.

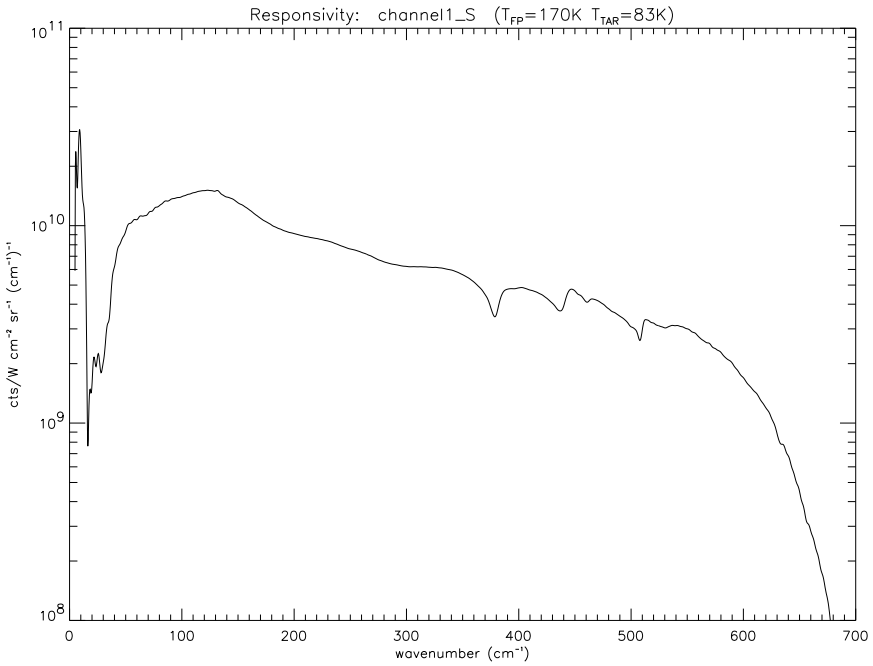

Figure B.11: Responsivity of FP 1 detector at $T_{\rm FPA}$=170 K, and $T_{\rm TAR}$=83 K. Date 02/05/97 (file ref: MAY02703).

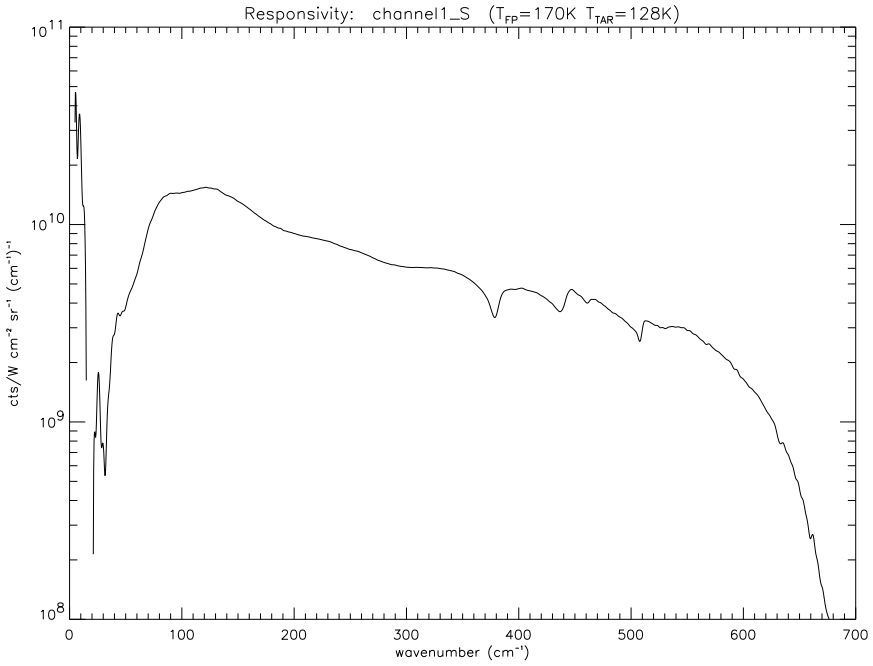

Figure B.12: Responsivity of FP 1 detector at $T_{\rm FPA}$=170 K, and $T_{\rm TAR}$=128 K. Date 03/05/97 (file ref: MAY03703).

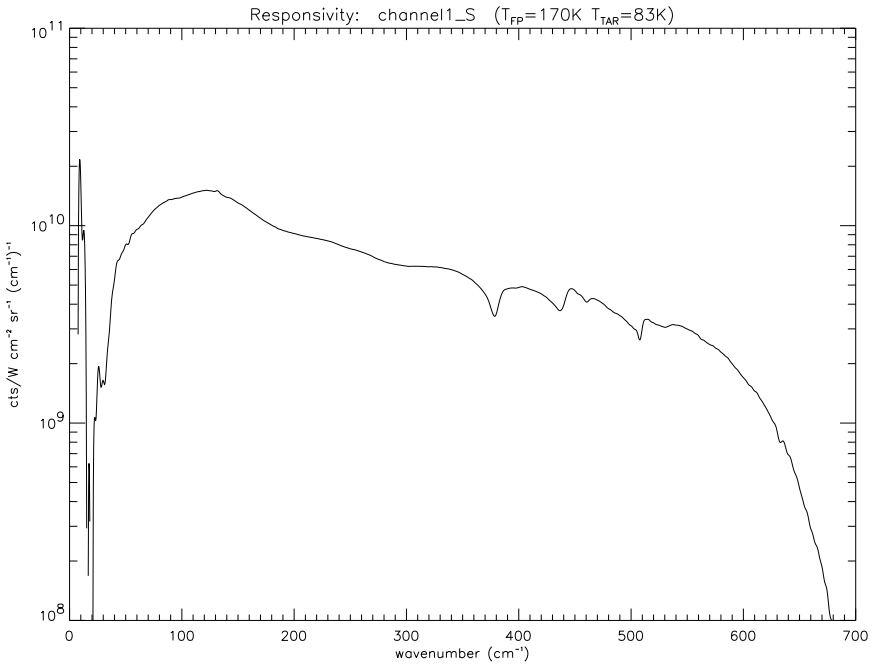

Figure B.13: Responsivity of FP 1 detector at $T_{\rm FPA}$=170 K, and $T_{\rm TAR}$=83 K. Date 04/05/97 (file ref: MAY04701).

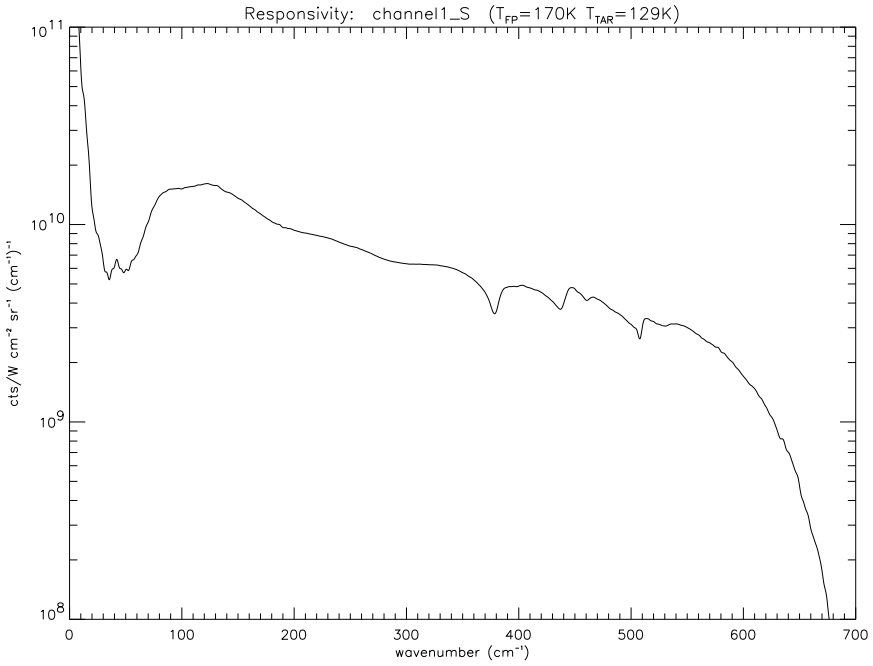

Figure B.14: Responsivity of FP 1 detector at $T_{\rm FPA}$=170 K, and $T_{\rm TAR}$=129 K. Date 03/05/97 (file ref: MAY03704).

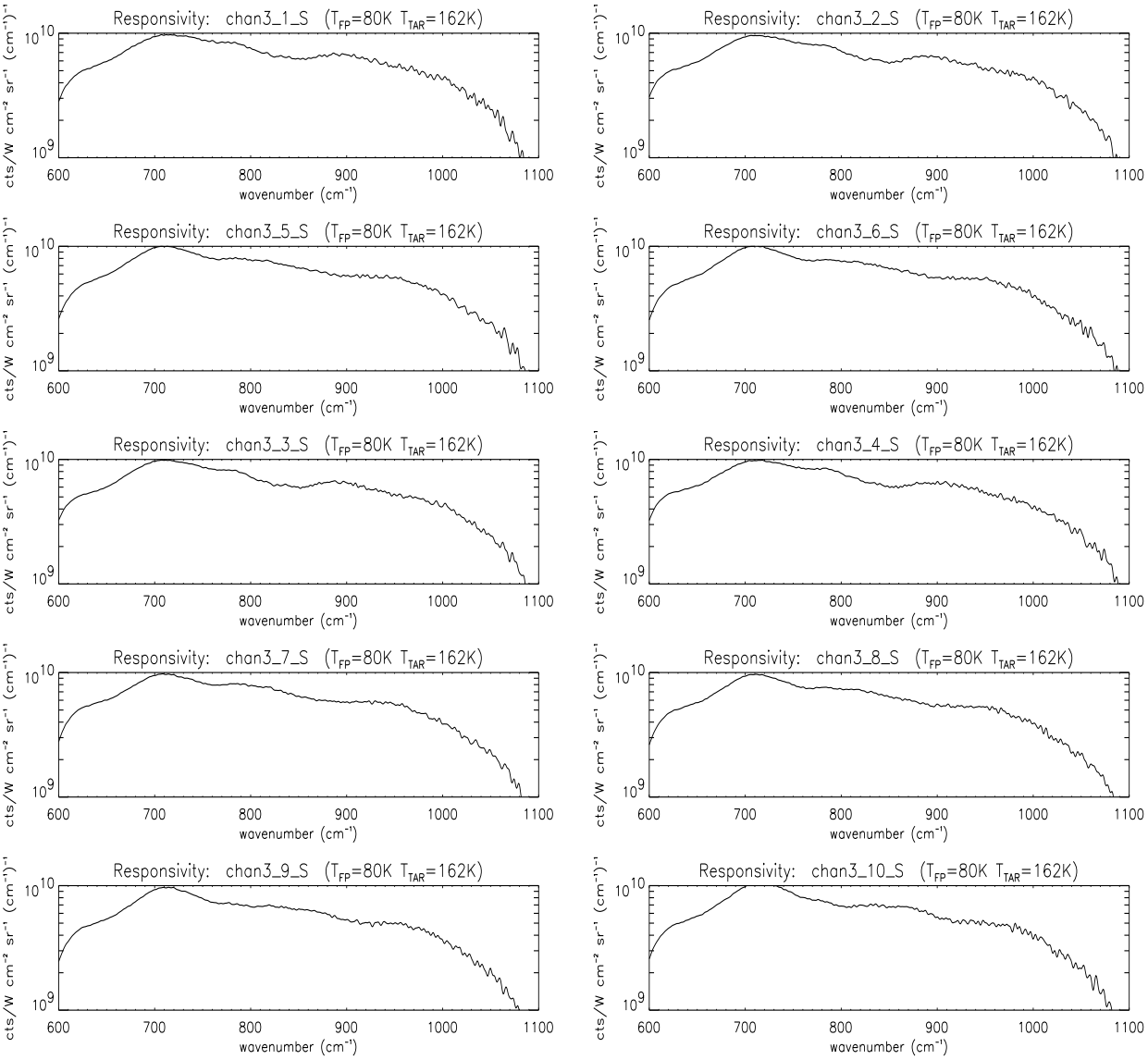

Figure B.15: Responsivities of FP 3 detectors at T_{FPA}=80 K, shutter open and T_{TAR}=162 K. Date 02/05/97 (file ref: MAY02705).

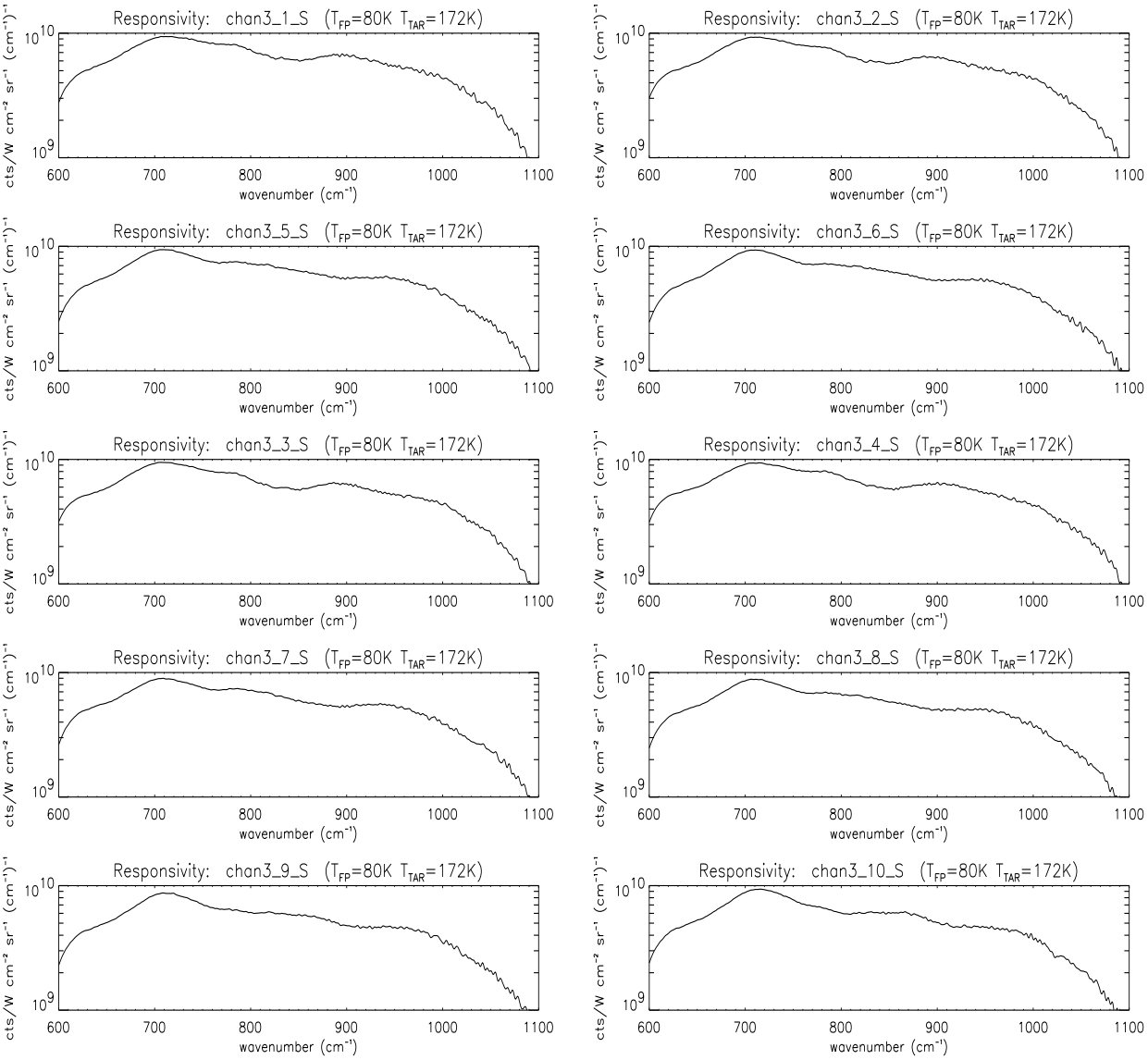

Figure B.16: Responsivities of FP 3 detectors at T_{FPA}=80 K, shutter open and T_{TAR}=172 K. Date 02/05/97 (file ref: MAY02706).

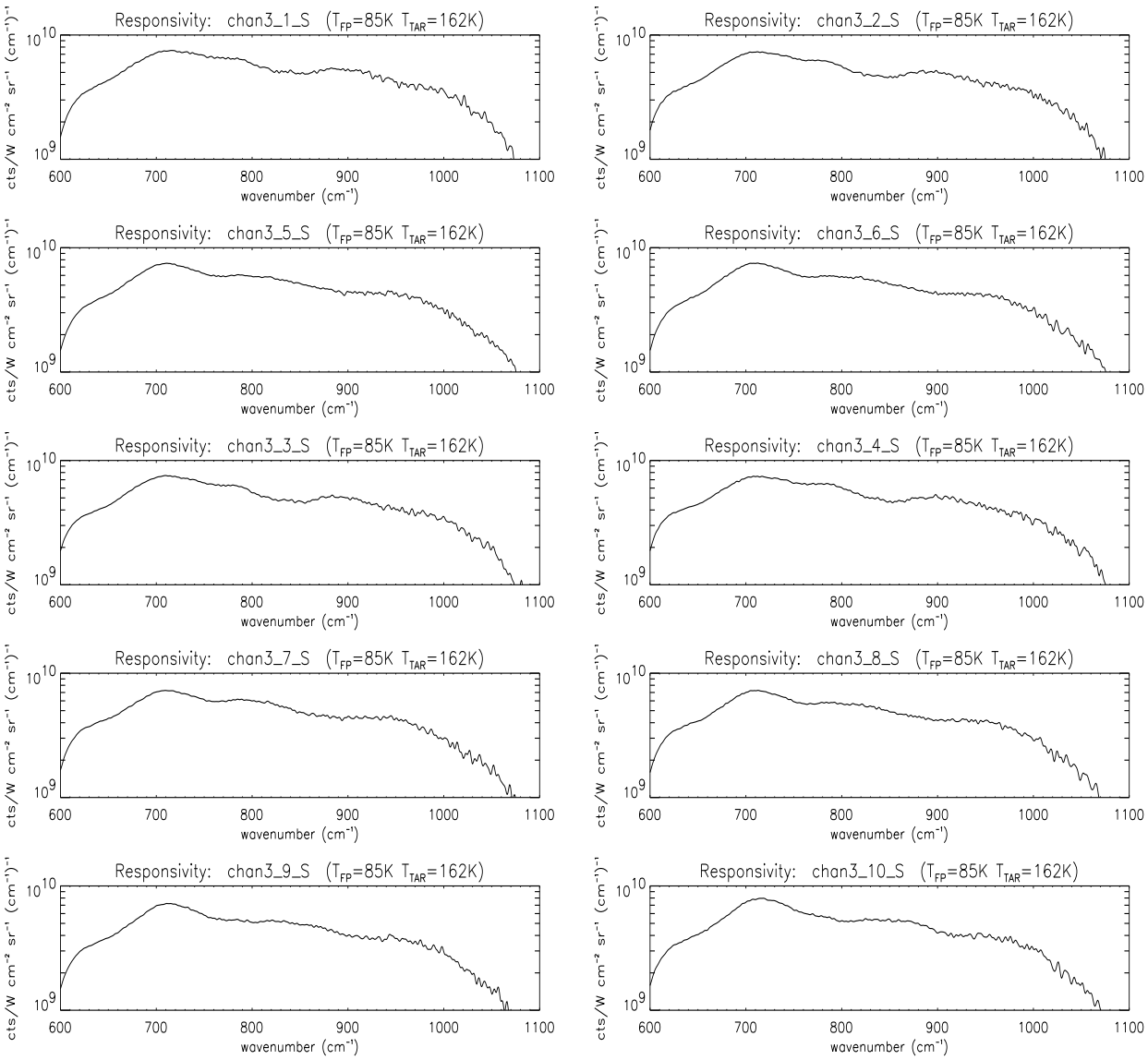

Figure B.17: Responsivities of FP 3 detectors at T_{FPA}=85 K, shutter open and T_{TAR}=162 K. Date 06/05/97 (file ref: MAY06702).

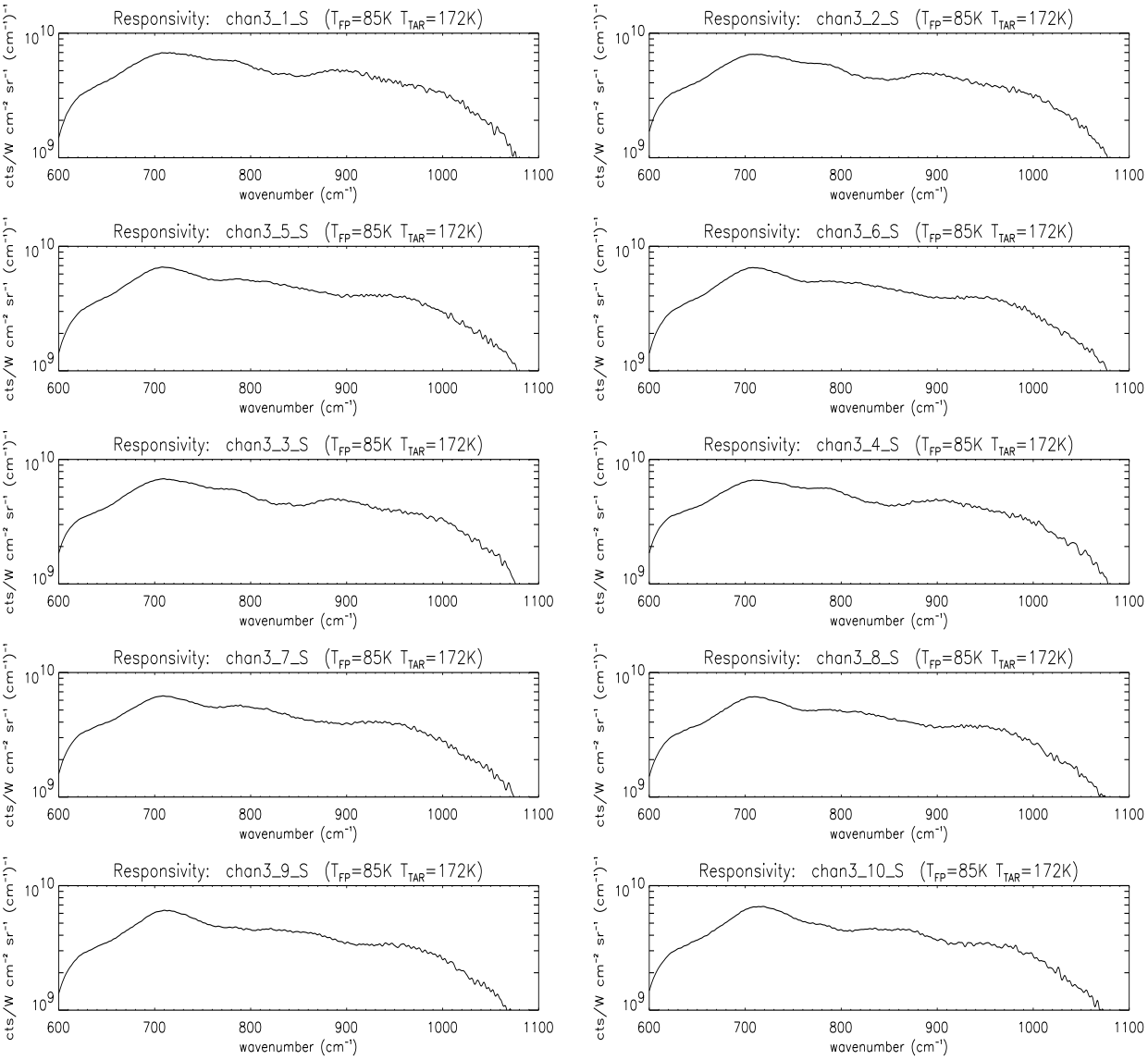

Figure B.18: Responsivities of FP 3 detectors at T_{FPA}=85 K, shutter open and T_{TAR}=172 K. Date 04/05/97 (file ref: MAY04703).

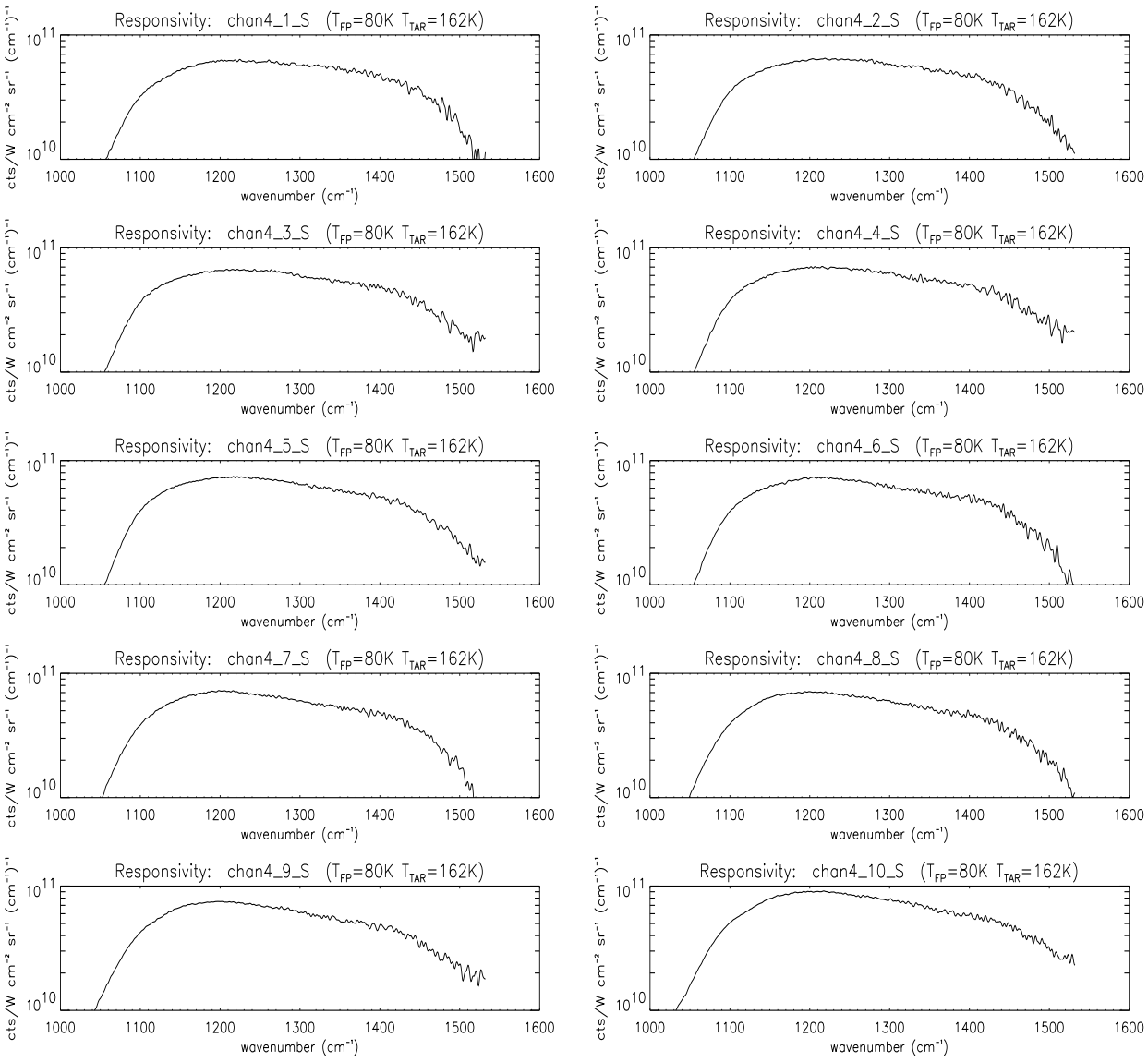

Figure B.19: Responsivities of FP 4 detectors at T_{FPA}=80 K, shutter open and T_{TAR}=162 K. Date 02/05/97 (file ref: MAY02705).

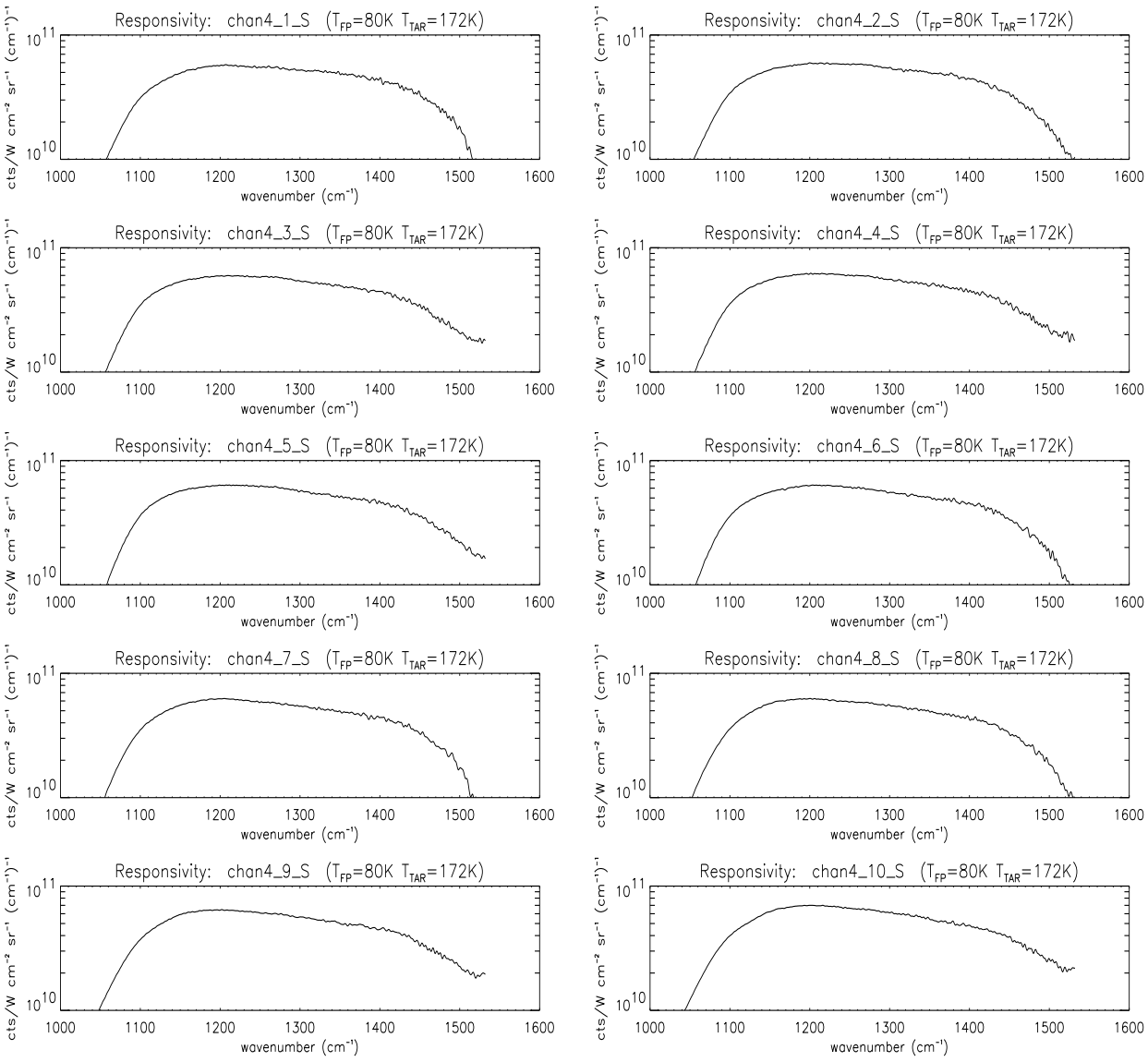

Figure B.20: Responsivities of FP 4 detectors at T_{FPA}=80 K, shutter open and T_{TAR}=172 K. Date 02/05/97 (file ref: MAY02706).

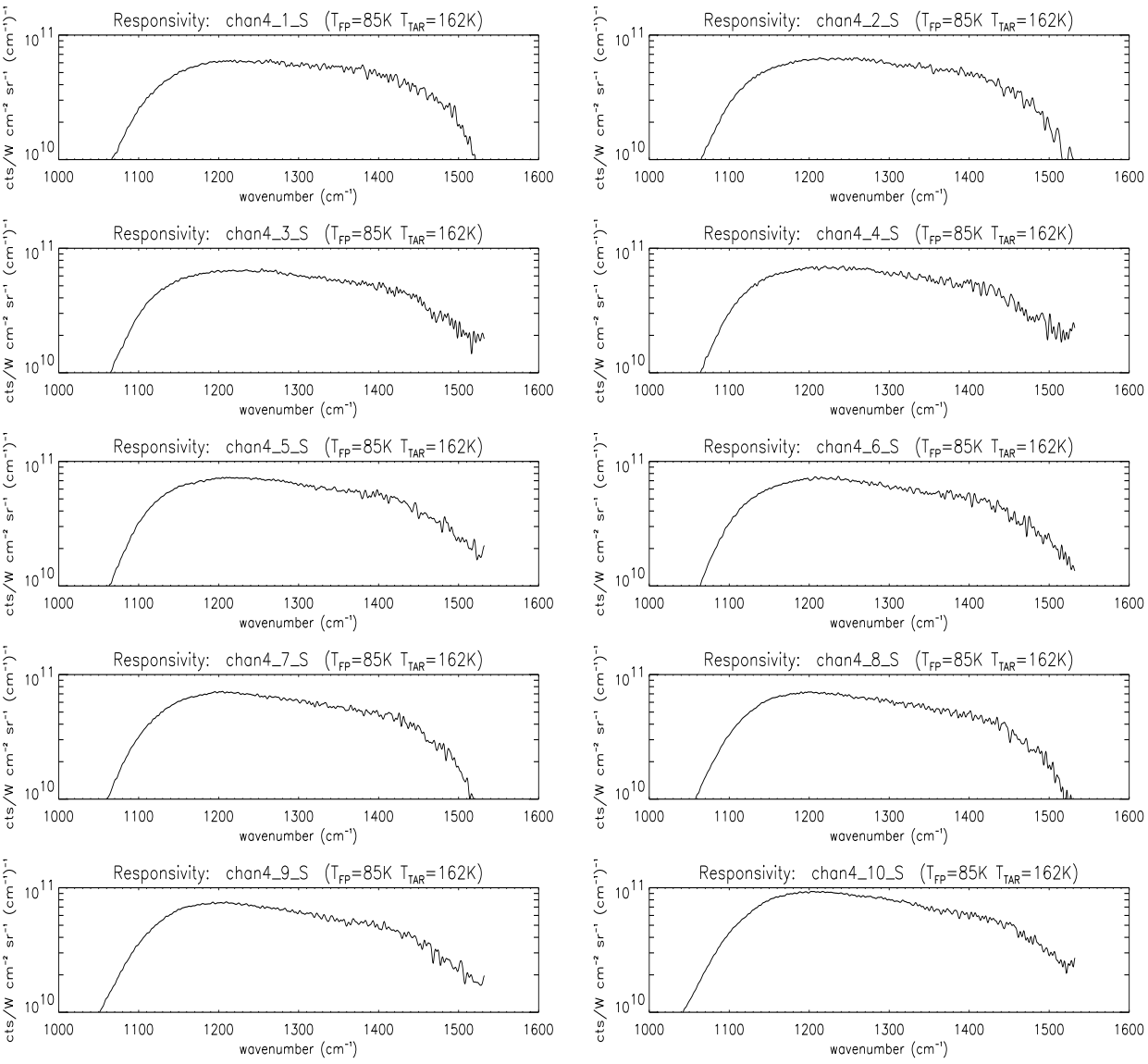

Figure B.21: Responsivities of FP 4 detectors at T_{FPA}=85 K, shutter open and T_{TAR}=162 K. Date 06/05/97 (file ref: MAY06702).

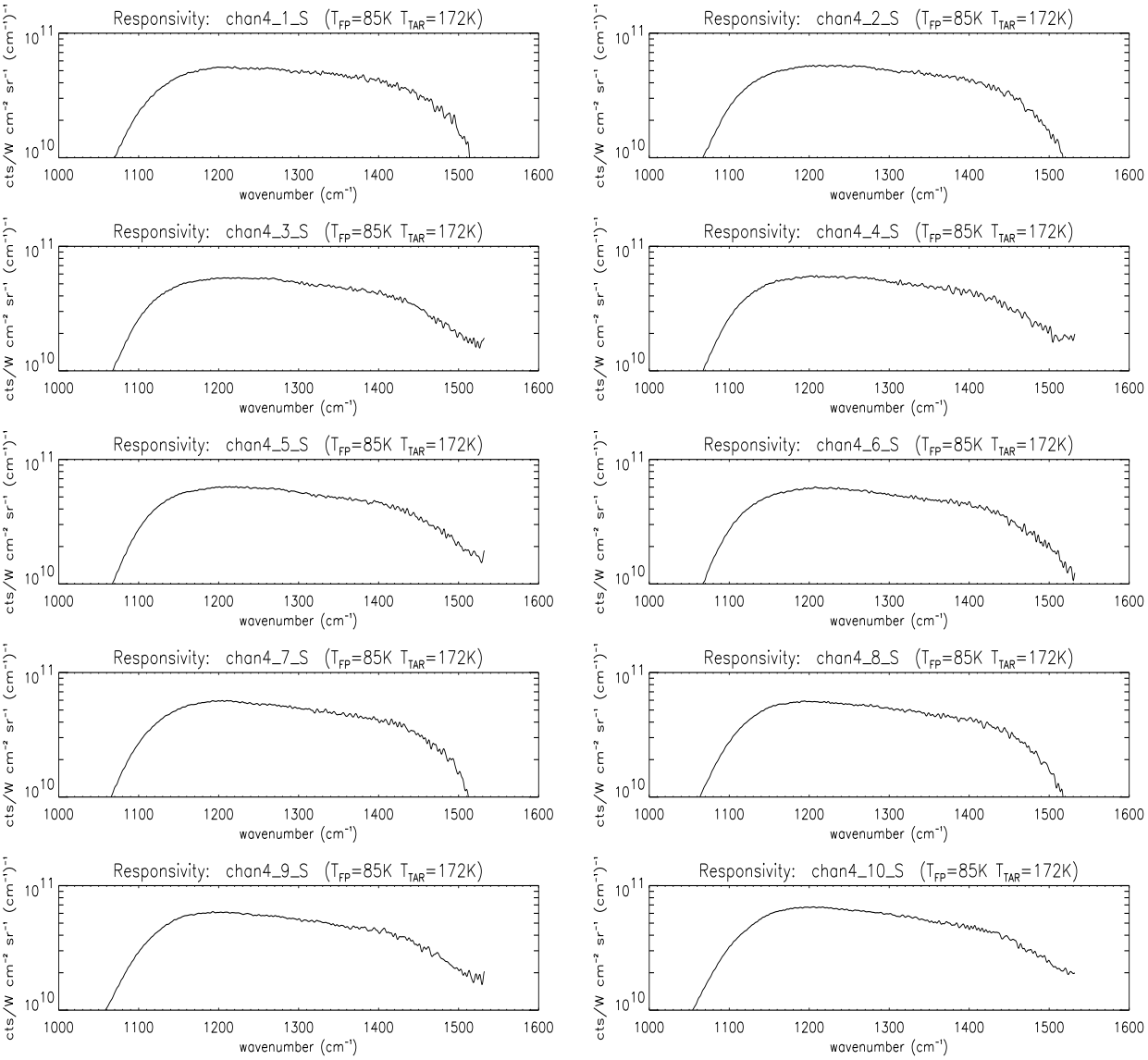

Figure B.22: Responsivities of FP 4 detectors at T_{FPA}=85 K, shutter open and T_{TAR}=172 K. Date 04/05/97 (file ref: MAY04703).

B.3 NESR Plots

A series of plots of calibrated NESR for all detectors. The data is presented in order: FP1, FP3, FP4; and in order of increasing $T_{\rm FPA}$ for each focal plane. The NESR level has been adjusted to 3 $\rm cm^{-1}$ resolution. See §5.2.4 for discussion.

#	Date	$T_{\rm FPA}$(K)	$T_{\rm TAR}$(K)	FP
B.23	02/05/97	170	83	1
B.24	03/05/97	170	128	1
B.25	04/05/97	170	83	1
B.26	03/05/97	170	129	1
B.27	02/05/97	80	162	3
B.28	02/05/97	80	172	3
B.29	06/05/97	85	162	3
B.30	06/05/97	85	172	3
B.31	02/05/97	80	162	4
B.32	02/05/97	80	172	4
B.33	06/05/97	85	162	4
B.34	06/05/97	85	172	4

Table B.3: Index of the calibrated NESR plots.

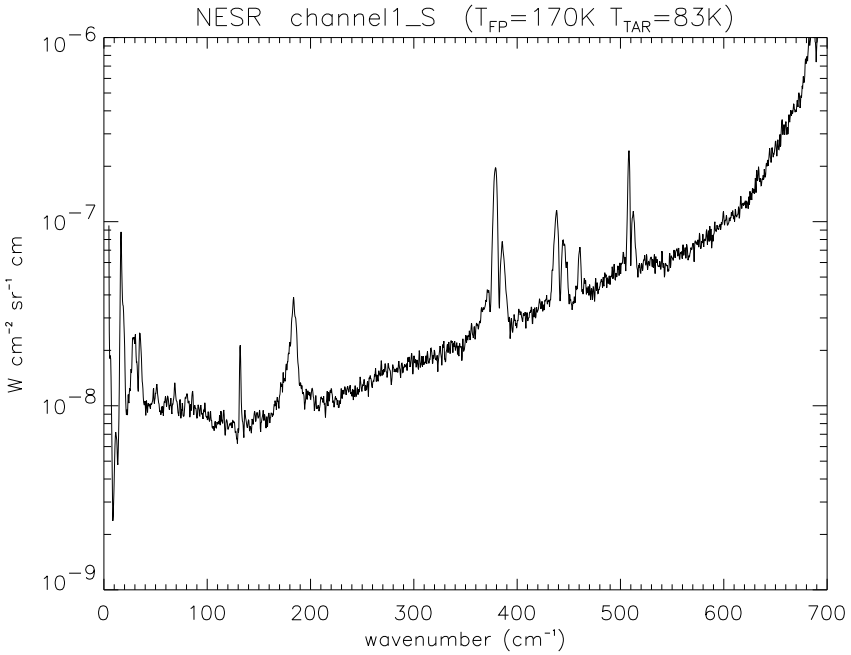

Figure B.23: NESR of FP 1 detector at $T_{\rm FPA}$=170 K, and $T_{\rm TAR}$=83 K. Date 02/05/97 (file ref: MAY02703).

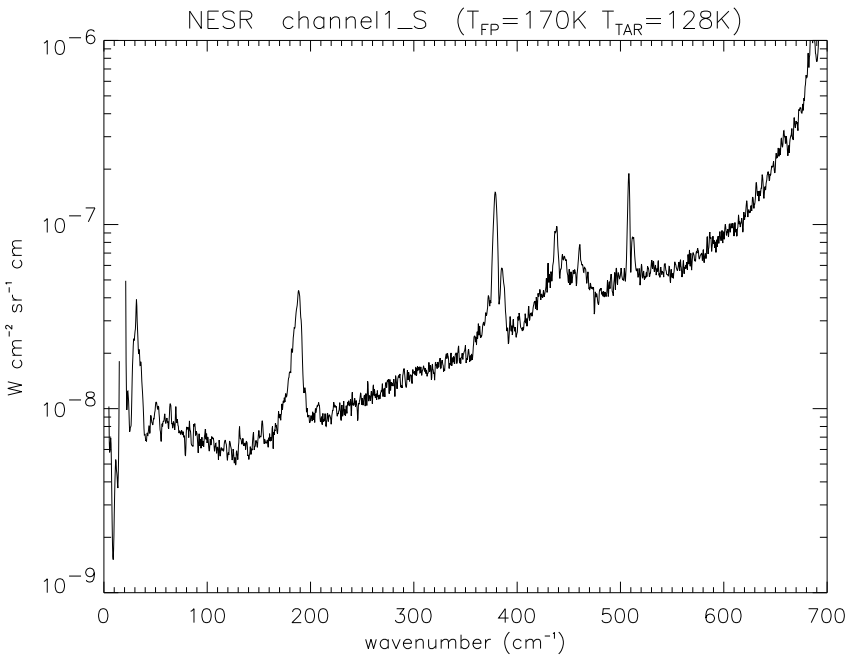

Figure B.24: NESR of FP 1 detector at $T_{\rm FPA}$=170 K, and $T_{\rm TAR}$=128 K. Date 03/05/97 (file ref: MAY03703).

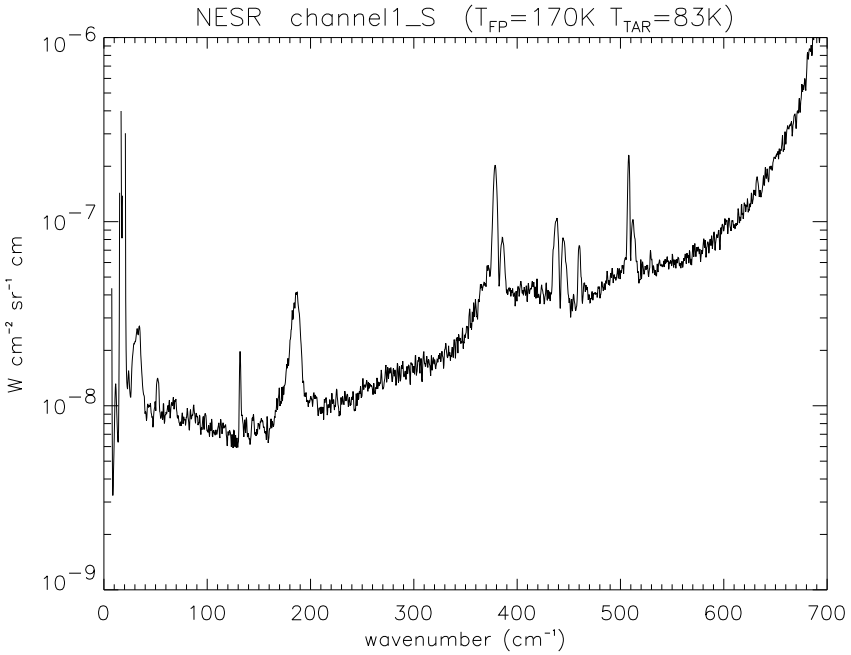

Figure B.25: NESR of FP 1 detector at $T_{\rm FPA}$=170 K, and $T_{\rm TAR}$=83 K. Date 04/05/97 (file ref: MAY04701).

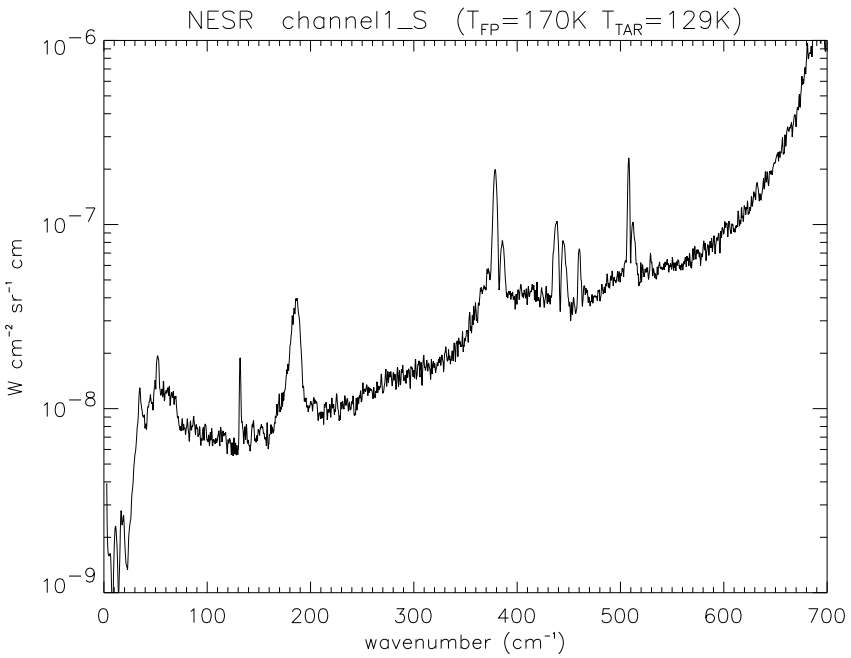

Figure B.26: NESR of FP 1 detector at $T_{\rm FPA}$=170 K, and $T_{\rm TAR}$=129 K. Date 03/05/97 (file ref: MAY03704).

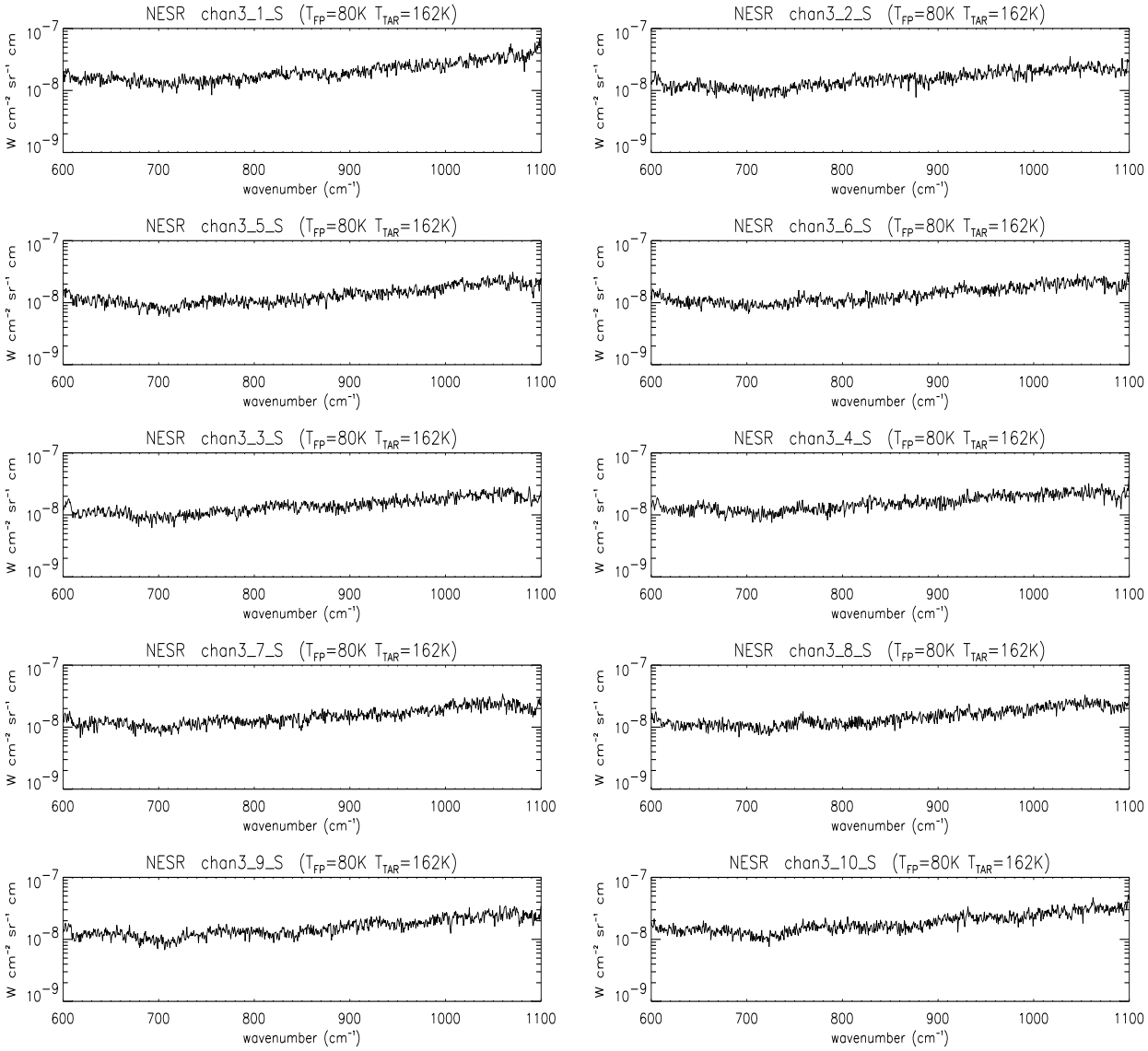

Figure B.27: NESR of FP 3 detectors at T_{FPA}=80 K, shutter open and T_{TAR}=162 K. Date 02/05/97 (file ref: MAY02705).

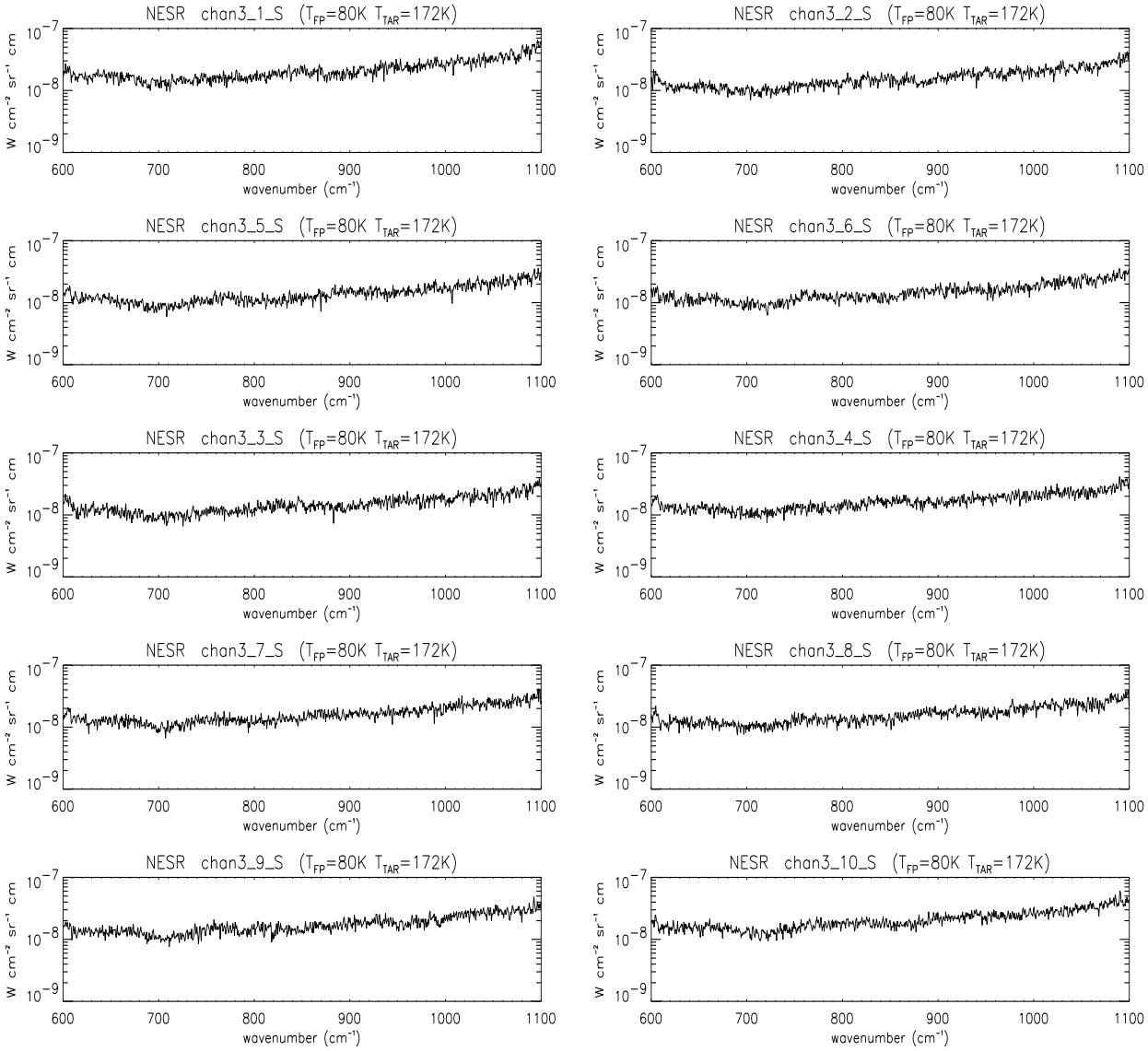

Figure B.28: NESR of FP 3 detectors at T_{FPA}=80 K, shutter open and T_{TAR}=172 K. Date 02/05/97 (file ref: MAY02706).

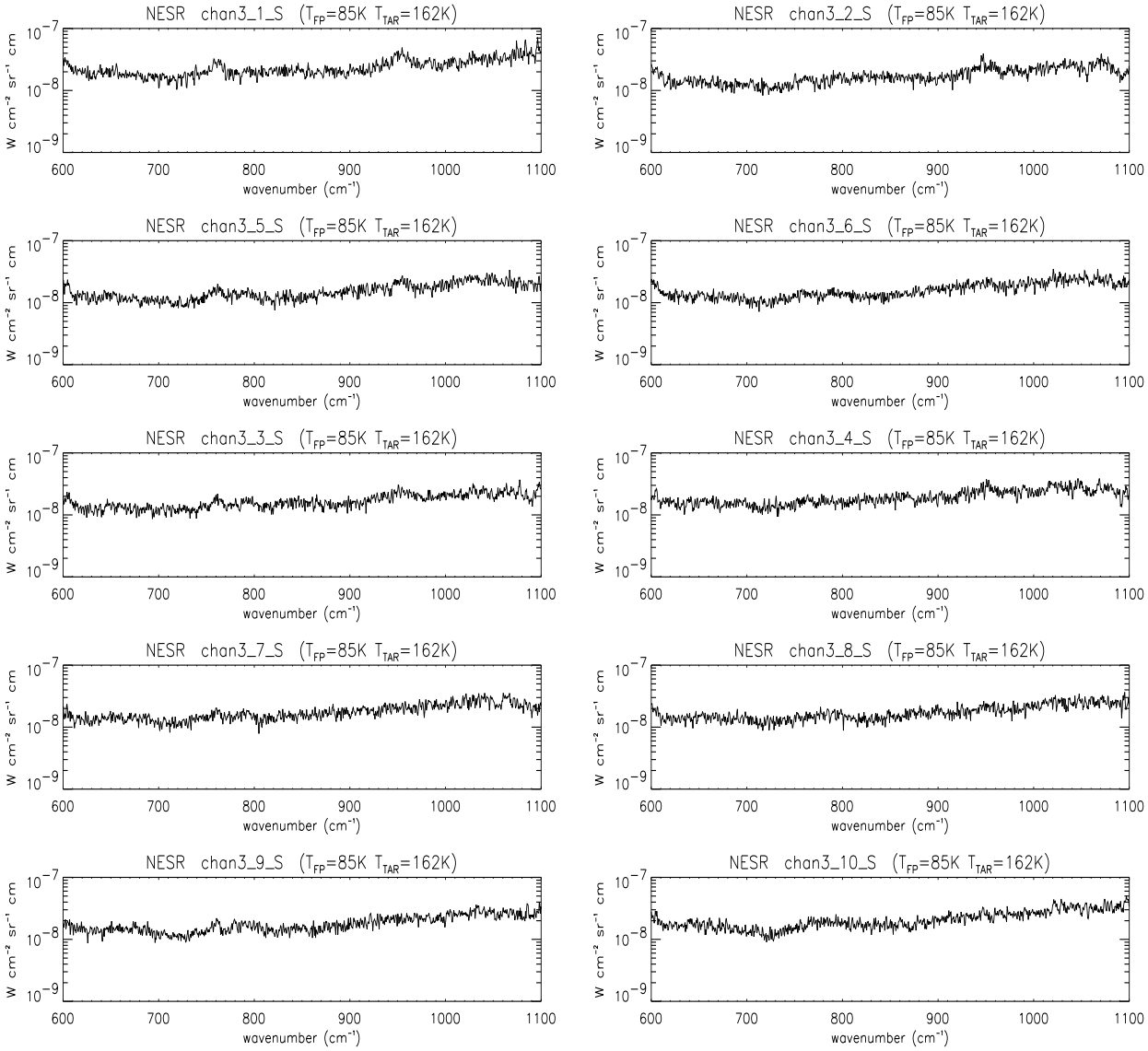

Figure B.29: NESR of FP 3 detectors at T_{FPA}=85 K, shutter open and T_{TAR}=162 K. Date 06/05/97 (file ref: MAY06702).

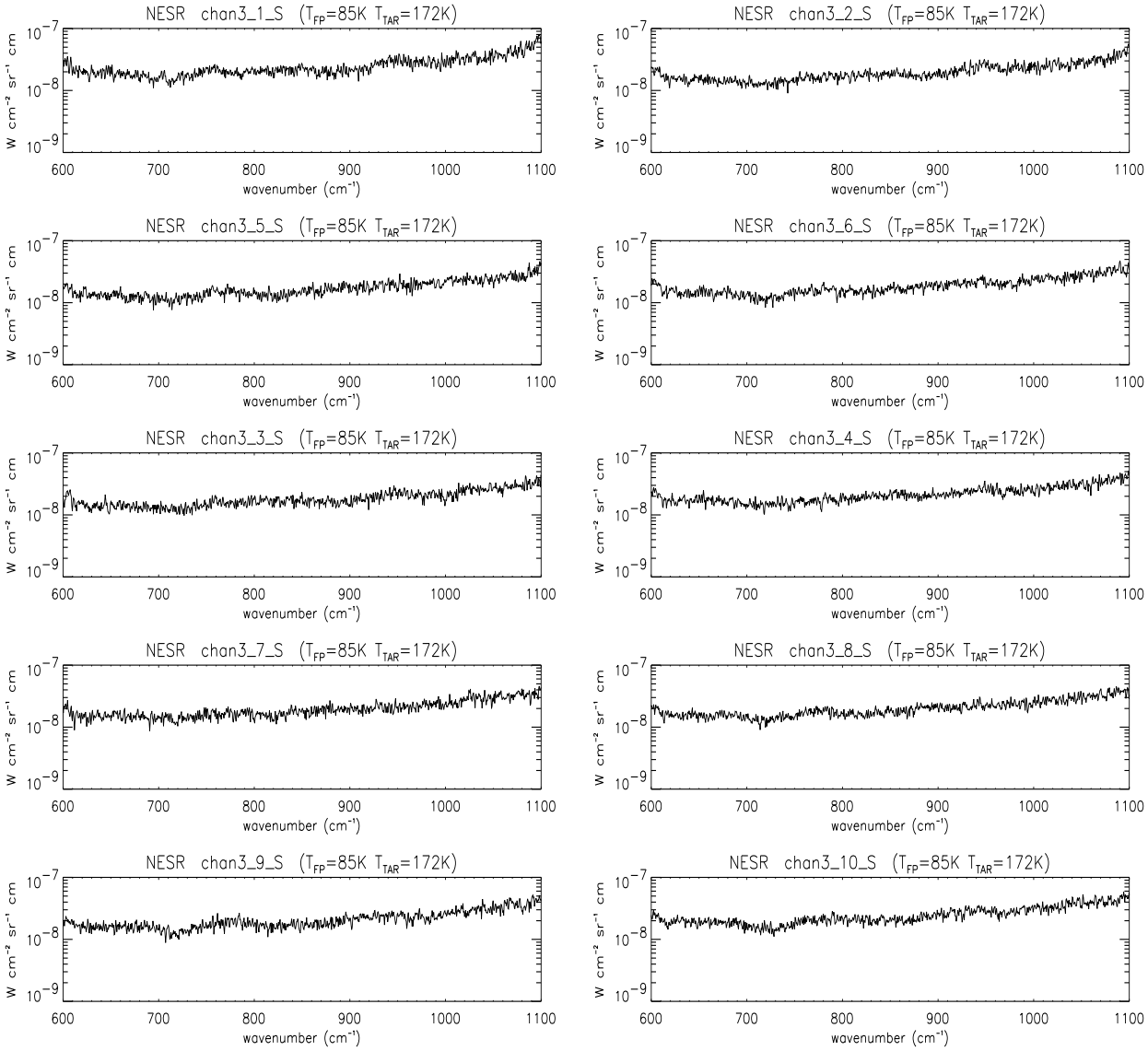

Figure B.30: NESR of FP 3 detectors at T_{FPA}=85 K, shutter open and T_{TAR}=172 K. Date 04/05/97 (file ref: MAY04703).

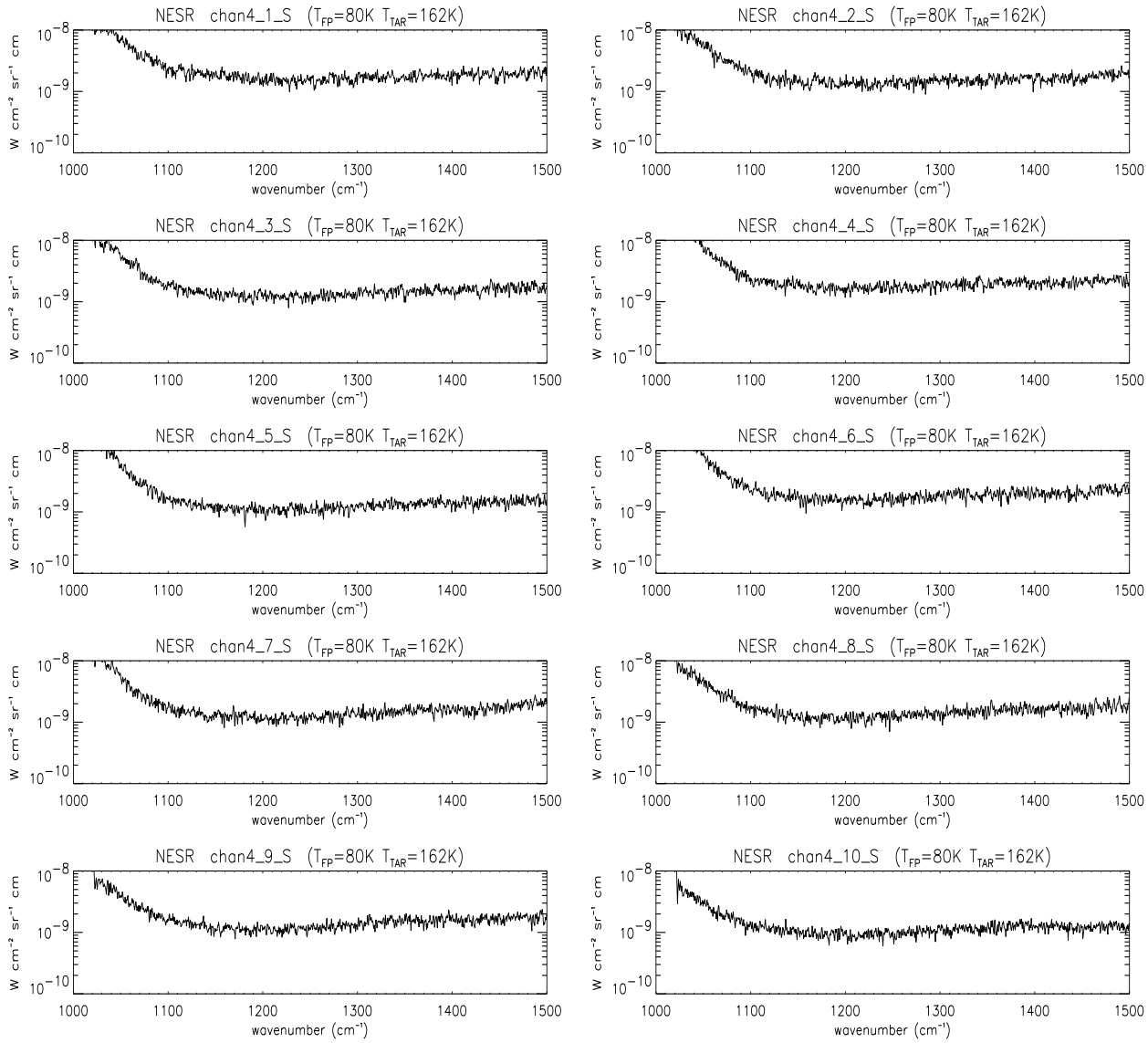

Figure B.31: NESR of FP 4 detectors at T_{FPA}=80 K, shutter open and T_{TAR}=162 K. Date 02/05/97 (file ref: MAY02705).

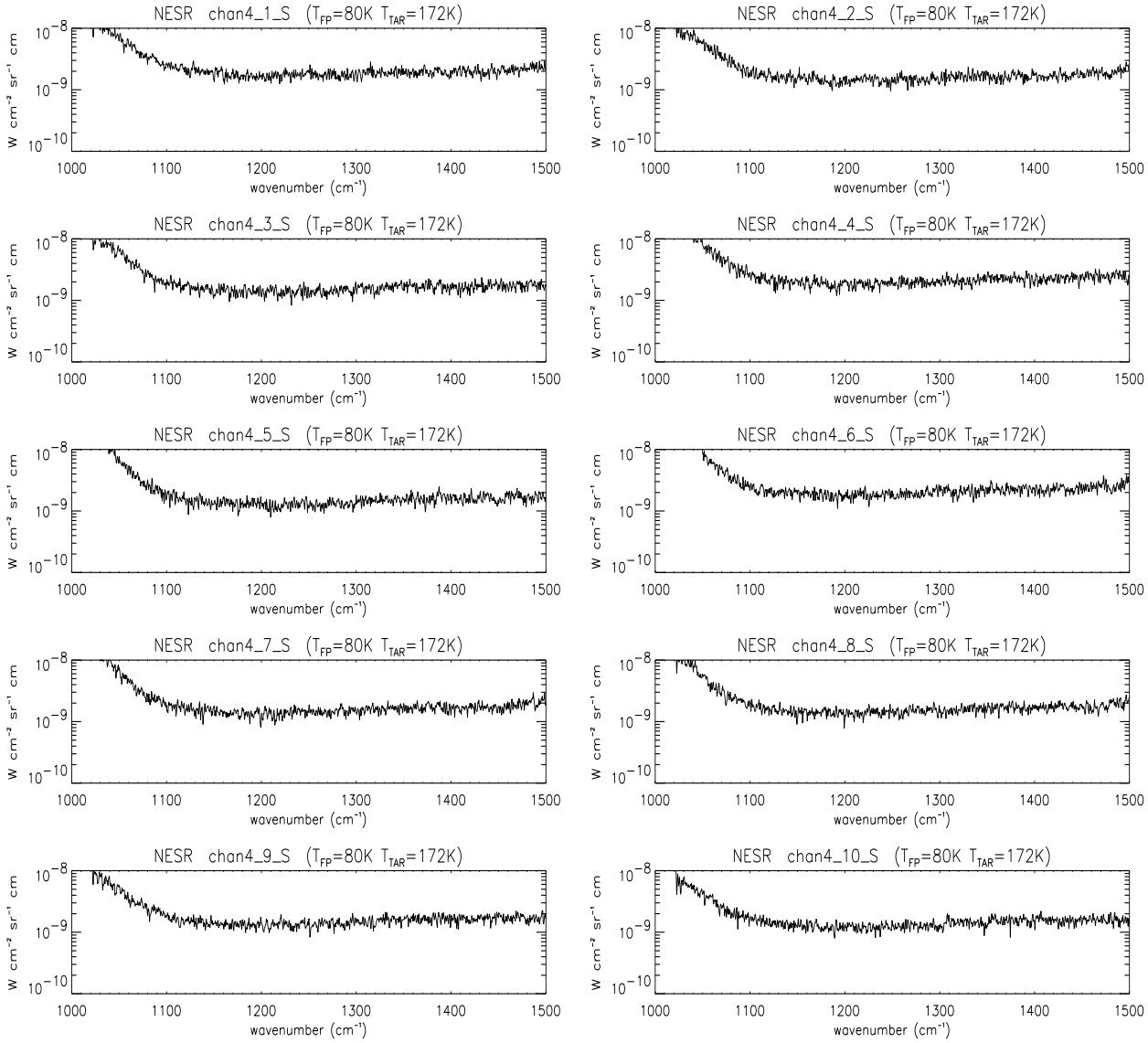

Figure B.32: NESR of FP 4 detectors at T_{FPA}=80 K, shutter open and T_{TAR}=172 K. Date 02/05/97 (file ref: MAY02706).

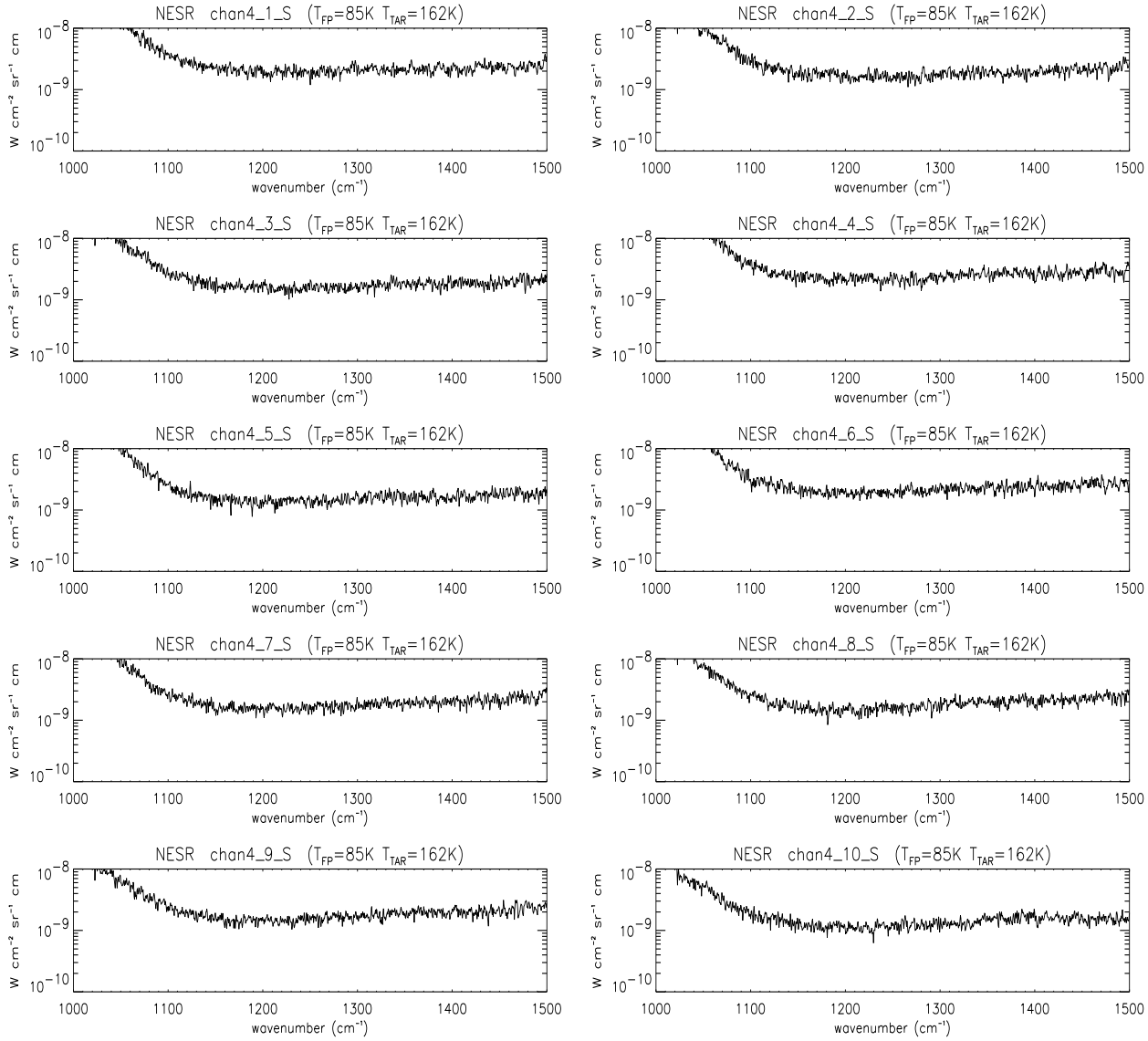

Figure B.33: NESR of FP 4 detectors at T_{FPA}=85 K, shutter open and T_{TAR}=162 K. Date 06/05/97 (file ref: MAY06702).

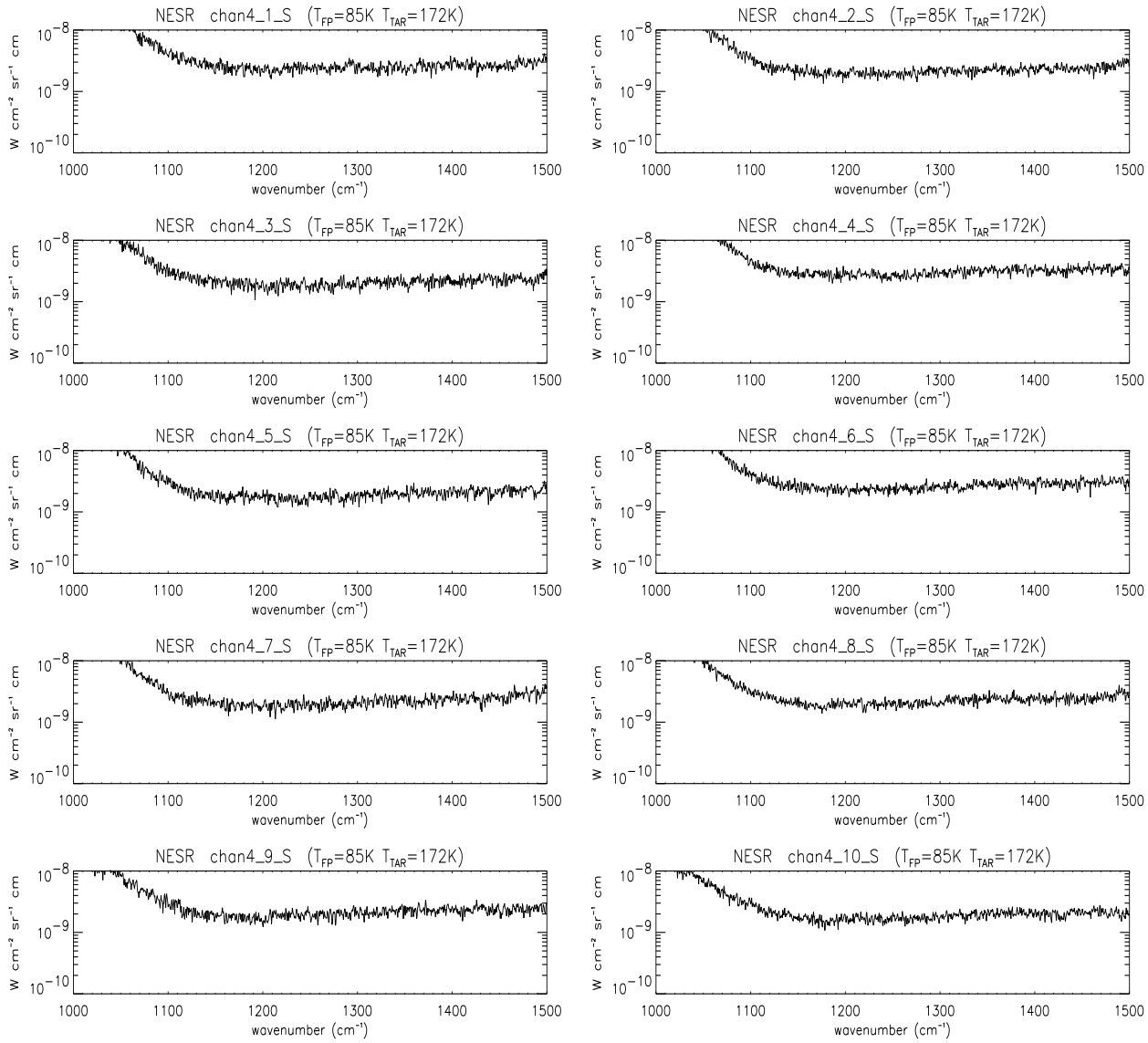

Figure B.34: NESR of FP 4 detectors at T_{FPA}=85 K, shutter open and T_{TAR}=172 K. Date 04/05/97 (file ref: MAY04703).

Bibliography

G. Arfken. *Mathematical Methods for Physicists*. Academic Press, London, Third edition, 1985.

G.T. Armstrong, F.G. Brickwedde, and R.D. Scott. Vapour pressures of the methanes. *J. Res. Nat. Bur. Stan.*, 55(1):39–52, 1955.

P.W. Atkins. *Molecular Quantum Mechanics*. Oxford Univ. Press, Oxford, Second edition, 1983.

S.K. Atreya, T.M. Donahue, and W.R. Kuhn. Evolution of a nitrogen atmosphere on Titan. *Science*, 210:611–613, 1978.

A. Bar-Nun, I. Kleinfield, and E. Ganor. Shape and optical properties of aerosols formed by photolysis of acetylene, ethylene and hydrogen cyanide. *J. Geophys. Res.*, 93(D7): 8383–8387, 1988.

B. Bézard, A. Coustenis, and C.P. McKay. Titan's stratospheric temperature asymmetry: A radiative origin? *Icarus*, 113:267–276, 1995.

A. Borysow. Modelling of collision-induced infrared-absorption spectra of H_2–H_2 pairs in the fundamental band at temperatures from 20K to 300K. *Icarus*, 92(2):273–279, 1991.

A. Borysow. Modelling of collision-induced infrared-absorption spectra of H_2–H_2 pairs in the fundamental band at temperatures from 20 to 300K (vol. 92 pg. 273, 1991). *Icarus*, 106(2):614, 1993.

A. Borysow and L. Frommhold. Collision-induced rototranslational absorption spectra of N_2–N_2 pairs for temperatures from 50 to 300K. *Astrophys. J.*, 311:1043–1057, 1986a.

A. Borysow and L. Frommhold. Theoretical collision-induced rototranslational absorption spectra for modeling Titan's atmosphere: H_2–N_2 pairs. *Astrophys. J.*, 303:495–510, 1986b.

A. Borysow and L. Frommhold. Theoretical collision-induced rototranslational absorption spectra for the outer planets: H_2–CH_4 pairs. *Astrophys. J.*, 304:849–865, 1986c.

A. Borysow and L. Frommhold. Collision-induced rototranslational absorption spectra of CH_4–CH_4 pairs at temperatures from 50 to 300K. *Astrophys. J.*, 318:940–943, 1987.

A. Borysow and C. Tang. Far infrared CIA spectra of N_2–CH_4 pairs for modeling of Titan's atmosphere. *Icarus*, 105:175–183, 1993.

A. Borysow, L. Trafton, L. Frommhold, and G. Birnbaum. *Astrophys. J.*, 296:644–654, 1985.

A.L. Broadfoot et al. Extreme ultraviolet observations from Voyager 1 encounter with Saturn. *Science*, 212:206–211, 1981.

S. Calcutt, F. Taylor, P. Ade, V. Kunde, and D. Jennings. The Composite Infrared Spectrometer. *J. Brit. Interplan. Soc.*, 45:811–816, 1992.

J. Chamberlain. *The Principles of Interferometric Spectroscopy.* Wiley, 1979.

P. Coll, D. Coscia, M.C. Gazeau, E. de Vanssay, J.C. Guillemin, and F. Raulin. Organic chemistry in Titan's atmosphere: new data from laboratory simulations at low temperature. *Adv. Space Res.*, 16(2):93–103, 1995.

J. Comas-Solá. *J. Br. Astron. Assoc.*, 19:151, 1908.

M. Combes, L. Vapillon, E. Gendron, A. Coustenis, O. Lai, R. Wittemberg, and R. Sirdey. Spatially resolved images of Titan by means of adaptive optics. *Icarus*, 129(2):482–497, 1997.

R. Courtin. The spectrum of Titan in the far-infrared and microwave regions. *Icarus*, 51:466–475, 1982.

R. Courtin, D. Gautier, and C. McKay. Titan's thermal emission spectrum: Reanalysis of the Voyager infrared measurements. *Icarus*, 114:144–162, 1995.

A. Coustenis and B. Bézard. Titan's atmosphere from Voyager infrared observations. IV latitude variations of temperature and composition. *Icarus*, 115:126–140, 1995.

A. Coustenis, B. Bézard, and D. Gautier. Titan's atmosphere from Voyager infrared observations. 1: The gas composition of Titan's equatorial region. *Icarus*, 80:54–76, 1989.

A. Coustenis, B. Bézard, D Gautier, and A. Marten. Titan's atmosphere from Voyager infrared observations. 3: Vertical distributions of hydrocarbons and nitriles near Titan's north pole. *Icarus*, 89:152–167, 1991.

A. Coustenis, Th. Encrenaz, B. Bézard, G. Bjoraker, G. Graner, M. Dang-Nhu, and E. Arié. Modelling Titan's thermal infrared spectrum for high resolution space observations. *Icarus*, 102:240–260, 1993.

A. Coustenis, Th. Encrenaz, A. Salama, E. Lellouch, G. Bjoraker, R.E. Samuelson, R. Wittenberg, Th. de Grauw, M.F. Kestler, D. Gautier, and G. Orton. ISO observations of Titan with SWS/grating. 1998a. In preparation.

A. Coustenis, E. Lellouch, and C.P. Maillard, J.P.and McKay. Titan's surface: Composition and variability from the near-infrared albedo. *Icarus*, 118:87–104, 1995.

A. Coustenis, A. Salama, E. Lellouch, Th. Encrenaz, G.L. Bjoraker, R.E. Samuelson, Th. de Graauw, H. Feuchtgruber, and M.F. Kessler. Evidence for water vapour in Titan's atmosphere from ISO/SWS data. *Astron. Astrophys.*, 336:L85–L89, 1998b.

S.F. Dermott and C. Sagan. Tidal effects of disconnected hydrocarbon seas on Titan. *Nature*, 374:238–240, 1995.

C. Emiliani. *Planet Earth: Cosmology, Geology and the Evolution of Life and Environment.* Cam. Univ. Press, Cambridge, 1992.

F.M. Flasar. Oceans on Titan? *Science*, 221:55–57, 1983.

F.M. Flasar and B.J. Conrath. Titans' stratospheric temperatures: A case for dynamical inertia? *Icarus*, 85:346–354, 1990.

F.M. Flasar, R.E. Samuelson, and B.J. Conrath. Titan's atmosphere: Temperature and dynamics. *Nature*, 292:693–698, 1981.

M.L. Forman. *J. Opt. Soc. Am.*, 56:978, 1966.

M.L. Forman, W.H. Steele, and G.A. Vanasse. *J. Opt. Soc. Am.*, 56:59, 1966.

G.S. Golitsyn. Another look at atmospheric dynamics on Titan and some of its general consequences. *Icarus*, 24:70–75, 1975.

G. Graner and G. Wagner. High-resolution infrared spectrum of propyne: the 30 μm region. *J. Mol. Spectrosc.*, 144:389–415, 1990.

C.A. Griffith. Evidence for surface heterogeneity on Titan. *Nature*, 511:511, 1993.

C.A. Griffith, T. Owen, and R. Wagener. Titan's surface and troposphere investigated with ground-based near-infrared observations. *Icarus*, 93:362–378, 1991.

M.A. Gurwell and D.O. Muhleman. CO on Titan: evidence for a well-mixed vertical profile. *Icarus*, 117:375–382, 1995.

R. Hanel, B. Conrath, F.M. Flasar, V. Kunde, W. Maguire, J. Pearl, J. Pirraglia, R. Samuelson, L. Herath, M. Allison, D. Gautier, P. Gierasch, L. Horn, R. Koppany, and C. Ponnamperuma. Infrared observations of the Saturnian system from Voyager 1. *Science*, 212:192–200, 1981.

R.A. Hanel, B.J. Conrath, D.E. Jennings, and R.E. Samuelson. *Exploration of the Solar System by infrared remote sensing.* Cam. Univ. Press, Cambridge, UK, 1992.

T. Hidayat, A. Marten, B. Bézard, D. Gautier, T. Owen, and G. Matthews, H.E.and Paubert. Millimeter and submillimeter heterodyne observations of Titan, retrieval of the vertical profile of HCN and the C^{12}/C^{13} ratio. *Icarus*, 126(1):170–182, 1997.

T. Hidayat, A. Marten, B. Bézard, D. Gautier, T. Owen, H.E. Matthews, and G. Paubert. Millimeter and submillimeter heterodyne observations of Titan, the vertical profile fo carbon dioxide in its stratosphere. *Icarus*, 133(1):109–133, 1998.

F. Hourdin, O. Talagrand, R. Sadourny, R. Courtin, D. Gautier, and C.P. McKay. Numerical simulation of the general circulation of the atmosphere of Titan. *Icarus*, 117: 358–374, 1995.

Hubbard et al. The occultation of 28 Sgr by Titan. *Astron. Astrophys.*, 269:541–563, 1993.

W.B. Hubbard, D.M. Hunten, H.J. Reitsema, N. Brisch, Y. Nevos, E. Carrera, F. Rossi, and L.H. Wasserman. Results for Titan's atmosphere from its occultation of 28 Sagittari. *Nature*, 343:353, 1990.

D.M. Hunten. The escape of H_2 from Titan. *J. Atmos. Sci.*, 30:726–732, 1973.

D.M. Hunten, M.G. Tomasko, F.M. Flasar, R.E. Samuelson, D.F. Strobel, and D.J. Stevenson. Titan. In T. Gehrels and M.S. Matthews, editors, *Saturn*, Space Science Series, pages 671–759, Tuczon, Arizona, 1984. The University of Arizona Press.

W.T. Hutzell, C.P. McKay, and O.B. Toon. Effects of time-varying haze production on Titan's geometric albedo. *Icarus*, 105:162–174, 1993.

W.T. Hutzell, C.P. McKay, O.B. Toon, and F. Hourdin. Simulations of Titan's brightness by a two-dimensional haze model. *Icarus*, 199:112–129, 1996.

Ip. Meteoroid ablation processes in Titan's atmosphere. *Nature*, 345:511, 1990.

P.G.J. Irwin and S.B. Calcutt. *Radtran*. Planetary Sciences Group, Atmospheric Physics, Oxford, 1995.

P.G.J. Irwin, S.B. Calcutt, and F.W. Taylor. Radiative transfer models for Galileo NIMS studies of the atmosphere of Jupiter. *Adv. Space Res.*, 18:1149–1158, 1997.

R.J. Keyes. *Optical and Infrared Detectors*. Topics in Applied Physics. Springer-Verlag, Berlin, 1977.

R.K. Khanna, M.A. Perera-Jarmer, and M.J. Ospina. Vibration infrared and Raman spectra of dicyanoacetylene. *Spectrochem. Acta*, 43A:421–425, 1987.

B.N. Khare, C. Sagan, E.T. Arakawa, F. Suits, T.A. Callcott, and M.W. Williams. Optical constants of organic tholins produced in a simulated Titanian atmosphere: From soft X-rays to microwave frequencies. *Icarus*, 60:127–137, 1984.

B.N. Khare, C. Sagan, H. Ogino, B. Nagy, C. Er, K.H. Schram, and E.T. Arakawa. Amino acids derived from Titan tholins. *Icarus*, 68:176–184, 1986.

G.P. Kuiper. Titan: A satellite with an atmosphere. *Astrophys. J.*, 100:378, 1944.

V. Kunde et al. Infrared Fourier spectroscopy of Saturn and Titan from the Cassini orbiter. Technical report, NASA, 1990. A proposal submitted to the NASA Office of Space Science and Applications (A.O. No. OSSA-1-89).

V. Kunde et al. Cassini infrared Fourier spectroscopic investigation. *Proc. Soc. Photo-Opt. Instrum. Eng.*, 2803:162–177, 1996.

L.M. Lara, E. Lellouch, J.J. López-Moreno, and R. Rodrigo. Vertical distribution of Titan's atmospheric neutral constituents. *J. Geophys. Res.*, 101(E10):23261–23283, 1996.

J.-P. Lebreton and D.L. Matson. An overview of the Cassini mission. *Nuovo Cimento Della Societa Italiana Di Fisica C-Geophysics and Space Physics*, 15(6):1137–1147, 1992.

E. Lellouch, A. Coustenis, D. Gautier, F. Raulin, N. Dubouloz, and C. Frère. Titan's atmosphere and hypothesised ocean: A reanalysis of the Voyager 1 radio-occultation and IRIS 7.7 μm data. *Icarus*, 79:328–349, 1989.

E. Lellouch, D.M. Hunten, G. Kockarts, and A. Coustenis. Titan's thermosphere profile. *Icarus*, 83:308–324, 1990.

M.T. Lemmon, E. Karkoschka, and M. Tomasko. Titan's rotation: Surface feature observed. *Icarus*, 103:329–332, 1993.

M.T. Lemmon, E. Karkoschka, and M. Tomasko. Titan's rotational light curve. *Icarus*, 113:27–38, 1995.

J.S. Lewis. Icarus. *Satellites of the outer planets: Their physical and chemical nature*, 15:174–185, 1971.

D.R. Lide and H.V. Kehiaian. *CRC Handbook of Thermophysical and Thermochemical Data*. CRC Press, 1994.

G.F. Lindal, G.E. Wood, H.B. Hotz, D.N. Sweetnam, V.R. Eshleman, and G.L. Tyler. The atmosphere of Titan: An analysis of the Voyager 1 radio occultation measurements. *Icarus*, 53:348–363, 1983.

R.D Lorenz, P.H. Smith, M.T. Lemmon, E. Karkoschka, G.W. Lockwood, and J. Caldwell. Titan's north-south asymmetry from HST and Voyager imaging: Comparison with models and ground-based photometry. *Icarus*, 127:173–189, 1997.

J.I. Lunine. Does Titan have an ocean? A review of current understanding of Titan's surface. *Rev. Geophys.*, 31:133–149, 1993.

J.I. Lunine, D.J. Stevenson, and Y.L. Yung. Ethane ocean on Titan. *Science*, 222: 1229–1230, 1983.

B.L. Lutz, C. de Bergh, and T. Owen. Titan: Discovery of carbon monoxide in its atmosphere. *Science*, 220:1374–1375, 1983.

W.C. Maguire, R.A. Hanel, D.E. Jennings, V.G. Kunde, and R.E. Samuelson. C_3H_8 and C_3H_4 in Titan's atmosphere. *Nature*, 292:683–686, 1981.

A. Marten, D. Gautier, L. Tanguy, A. Lecacheux, C. Rosolen, and G. Paubert. Abundance of carbon monoxide in the stratosphere of Titan from millimeter heterodyne observations. *Icarus*, 1988:558–562, 1988.

D.H. Martin and E. Puplett. Polarized interferometric spectroscopy for the millimeter and submillimeter spectrum. *Infrared Physics*, 10:105–109, 1969.

G.D. McDonald, W.R. Thompson, M. Heinrich, B.N. Khare, and C. Sagan. Chemical investigation of Titan and Triton tholins. *Icarus*, 108:137–145, 1994.

C.P. McKay. Elemental composition, solubility, and optical properties of Titan's organic haze. *Plan. & Space Sci.*, 44(8):741–747, 1996.

C.P. McKay, S.C. Martin, C.A. Griffith, and R.M. Keller. Temperature lapse rate and methane in Titan's troposphere. *Icarus*, 129:498–505, 1997.

C.P. McKay, J.B. Pollack, and R. Courtin. The thermal structure of Titan's atmosphere. *Icarus*, 80:23–53, 1989.

C.P. McKay, J.B. Pollack, and R. Courtin. The greenhouse and antigreenhouse effects on Titan. *Science*, 253:1118–1121, 1991.

W. Meyer, A. Borysow, and L. Frommhold. Absorption spectra of H_2–H_2 pairs in the fundamental band. *Phys. Rev. A*, 40(12):6931–6949, 1989.

W. Meyer, A. Borysow, and L. Frommhold. Collision-induced 1st overtone band of gaseous hydrogen from 1st principles. *Phys. Rev. A*, 47(5B):4065–4077, 1993.

D.O. Muhleman, A.W. Grossman, B.J. Butler, and M.A. Slade. Radar reflectivity ot Titan. *Science*, 248:975–980, 1990.

J.S. Neff, T.A. Ellis, J. Apt, and J.T. Bergstralh. Bolometric albedos of Titan, Uranus and Neptune. *Icarus*, 62:425–432, 1985.

K.S. Noll, T.R. Geballe, R.F. Knacke, and Y.J. Pendleton. Titan's 5 μm spectral window: carbon monoxide and the albedo of the surface. *Icarus*, 124:625, 1996.

R.H. Norton and R. Beer. New apodising functions for Fourier spectrometry. *J. Opt. Soc. Am.*, 66(3):259–264, 1976.

G. Paubert, D. Gautier, and R. Courtin. The millimeter spectrum of Titan: detectability of HCN, HC_3N and CH_3CN and the CO abundance. *Icarus*, 60:599–612, 1988.

W.H. Press, S.A. Teukolsky, W.T. Vetterling, and B.P. Flannery. *Numerical Recipes in* `C`. Cam. Univ. Press, Cambridge, U.K., Second edition, 1992.

K. Rages and J.B. Pollack. Vertical distribution of scattering hazes in Titan's upper atmosphere. *Icarus*, 55:50–62, 1983.

K. Rages, J.B. Pollack, and P.H. Smith. Size estimates of Titan's aerosols based on Voyager high-phase-angle images. *J. Geophys. Res.*, 88(A11):8721–8728, 1983.

P. Rannou, M. Cabane, R. Botet, and E. Chassefière. A new interpretation of scattered light measurements at Titan's limb. *J. Geophys. Res.*, 102(E5):10997–11013, 1997.

F. Raulin, A. Accaoui, M. Razaghi, M. Dang-Nhu, A. Coustenis, and D. Gautier. Infrared spectra of gaseous organics: Application to the atmospheres of Titan. II. infrared

intensities and frequencies of C_4-alkanenitriles and benzene. *Spectrochem. Acta*, 46: 671–683, 1990.

H.E. Revercomb, H. Bujis, H.B. Howell, D.D. Laporte, W.L. Smith, and L.A. Sromovsky. Radiometric callibration of IR Fourier transform spectrometers: solution to a problem with the high-resolution interferometer sounder. *Applied Opt.*, 27(15):3210–3218, 1988.

C.D. Rodgers. Retrieval of atmospheric temperature and composition from remote measurements of thermal radiation. *Rev. Geophys. Space Phys.*, 14(4):609–624, 1976.

C. Sagan. Organic chemistry in the atmosphere of Titan. In D. Hunten, editor, *The Atmosphere of Titan*, number 340 in SP, pages 134–142. NASA, 1974.

C Sagan and W.R. Thompson. Production and condensation of organic gases in the atmosphere of Titan. *Icarus*, 59:133–161, 1984.

R.E. Samuelson. Radiative equilibrium model of Titan's atmosphere. *Icarus*, 53, 1983.

R.E. Samuelson. Clouds and aerosols of Titan's atmosphere. In *The Atmospheres of Saturn and Titan*, number 241 in ESA SP, pages 99–107. ESA, 1985.

R.E. Samuelson, R.A. Hanel, V.G. Kunde, and W.C. Maguire. Mean molecular weight and hydrogen abundance of Titan's atmosphere. *Nature*, 292:688–693, 1981.

R.E. Samuelson, W.C. Maguire, R.A. Hanel, V.G. Kunde, D.E. Jennings, Y.L. Yung, and A.C. Aikin. CO_2 on Titan. *J. Geophys. Res.*, pages 8709–8715, 1983.

R.E. Samuelson, L.A. Mayo, M.A. Knuckles, and R.J. Khanna. C_4N_2 ice in Titan's north polar stratosphere. *Plan. & Space Sci.*, 45(8):941–948, 1997a.

R.E. Samuelson, N.R. Nath, and A. Borysow. Gaseous abundances and methane supersaturation in Titan's troposphere. *Plan. & Space Sci.*, 45(8):959–980, 1997b.

B. Sicardy et al. Probing Titan's atmosphere by stellar occultation. *Nature*, 343:350, 1990.

B.A. Smith et al. Encounter with Saturn: Voyager 1 imaging science results. *Science*, 212:163–191, 1981.

B.A. Smith et al. A new look at the Saturn system: The Voyager 2 images. *Science*, 215:504–537, 1982a.

G.R. Smith, D.F. Strobel, A.L. Broadfoot, R. Sandel, D.E. Shemansky, and J.B. Holbe. Titan's upper atmosphere: Composition and temperature from the EUV solar occultation results. *J. Geophys. Res.*, 87(A3):1351–1359, 1982b.

P.H. Smith, M.T. Lemmon, R.D. Lorenz, L.A. Sromovsky, J.J. Caldwell, and M.D. Alison. Titan's surface, revealed by HST imaging. *Icarus*, 119:336–349, 1996.

D.F. Strobel. Chemistry and evolution of Titan's atmosphere. *Plan. & Space Sci.*, 30 (8):839–848, 1982.

D.F. Strobel and D.E. Shemansky. EUV emission from Titan's upper atmosphere. *J. Geophys. Res.*, 87(A3):1361–1368, 1982.

W.R. Thompson, T.J. Henry, J.M. Schwartz, B.N. Khare, and C. Sagan. Plasma discharge in N_2+CH_4 at low pressures: Experimental results and applications to Titan. *Icarus*, 90:57–73, 1991.

W.R. Thompson and C. Sagan. Titan: Far-infrared and microwave remote sensing of methane clouds and organic haze. *Icarus*, 60:236–259, 1984.

O.B. Toon, C.P. McKay, R. Courtin, and T.P. Ackerman. Methane rain on Titan. *Icarus*, 75:255–284, 1988.

O.B. Toon, C.P. McKay, C.A. Griffith, and R.P. Turco. A physical model of Titan's aerosols. *Icarus*, 95:24–53, 1992.

D. Toublanc, J.P. Parisot, J. Brillet, D. Gautier, F. Raulin, and C.P. McKay. Photochemical modeling of Titan's atmosphere. *Icarus*, 113:2–26, 1995.

G.L. Tyler, V.R. Eshleman, J.D. Anderson, G.S Levy, G.F. Lindal, G.E. Wood, and T.A. Croft. Radio science investigations of the Saturn system with Voyager 1: Preliminary results. *Science*, 212:201–206, 1981.

R.V. Yelle. Non-LTE models of Titan's upper atmosphere. *Astrophys. J.*, 383:380–400, 1991.

Y.L. Yung. An update of nitrile photochemistry on Titan. *Icarus*, 72:468–472, 1987.

Y.L. Yung, M. Allen, and J.P. Pinto. Photochemistry of the atmosphere of Titan: Comparison between model and observations. *Astrophys. J. Supp.*, 55:465–506, 1984.

C. Zheng and A. Borysow. Modelling of collision-induced infrared-absorption spectra of H_2 pairs in the first overtone band at temperatures from 20K to 500K. *Icarus*, 113(1): 84–90, 1995.